

# **Machine Learning-enhanced feasibility studies on the production of new particles with preferential couplings to third generation fermions at the LHC**

Thesis submitted in partial fulfillment  
of the requirements for the degree of  
**Doctor in Sciences - Physics**

**Presented by:**  
Cristian Fernando Rodríguez Cruz

**Directed by:**  
Prof. Andrés Florez (advisor)  
Universidad de los Andes  
Prof. Joel Jones-Perez (co-advisor)  
Pontificia Universidad Católica del Perú

Uniandes - High Energy Physics Research Group  
Phenomenology of Particle Physics

**Universidad de los Andes**  
Faculty of Sciences  
Department of Physics  
Bogotá D.C., Colombia  
November 8, 2025. Pre-alpha version



## Abstract

The Standard Model (SM) of particle physics is the most successful framework for describing the subatomic world. It is continuously tested in experiments worldwide, with the Large Hadron Collider (LHC) being the flagship project in this endeavor. One of the primary goals of the LHC is to precisely measure SM parameters and search for deviations that could signal new physics.

In recent years, reported anomalies, such as those in B-meson decays from LHCb, BaBar, and Belle experiments, along with the potential discrepancy in the muon's magnetic moment ( $g - 2$ ) from Fermilab, suggest a violation of lepton flavor universality (LFU). These observations provide a compelling window into physics beyond the SM. Among the proposed SM extensions to explain LFU violation, many introduce new particles with preferential couplings to third and second-generation fermions. Popular candidates include heavy states such as  $Z'$  bosons,  $\phi'$  scalars, and leptoquarks (LQs), among others.

This work presents two phenomenological studies proposing different strategies to probe new models, such as the 4321 [1],  $U(1)_{T_R^3}$  [2], that extend the SM particle content to explain clues on LFU violation. The studies use benchmark scenarios in which the structure of the model and the couplings of the new particle fields determine preferential interactions with second- and third-generation SM fermions. The hypothetical signal and background samples are generated using Monte Carlo simulations, emulating the current running conditions of the LHC and the performance of the CMS detector. The expected sensitivity for the different signal models under study is obtained by performing a detailed analysis of the available (non-excluded) experimental phase-space, boosted by machine learning (ML) techniques to optimize the discovery potential for these exotic states.



---

## CONTENTS

Abstract	iii
Contents	v
INTRODUCTION	1
1 STANDARD MODEL OF PARTICLE PHYSICS	5
1.1 Fields . . . . .	5
1.1.1 Interactions and Symmetries . . . . .	7
1.2 Standard Model . . . . .	14
1.2.1 Particle Content and Gauge Group . . . . .	15
1.2.2 Gauge Bosons . . . . .	17
1.2.3 Matter Fields . . . . .	19
1.2.4 Electroweak Symmetry Breaking . . . . .	21
1.3 Deficiencies of SM and New Physics . . . . .	27
1.3.1 Phenomenological problems . . . . .	28
1.3.2 Theoretical problems . . . . .	29
1.3.3 Cosmological problems . . . . .	30
1.4 Lepton Universality: Tests and Anomalies . . . . .	32
2 PHENOMENOLOGICAL FRAMEWORK	35
2.1 Detectors and Subsystems . . . . .	36
2.1.1 Collision Parameters . . . . .	41
2.2 Jets Reconstruction . . . . .	43
2.2.1 Jet algorithms . . . . .	45
2.2.2 $\tau$ Tagging at Multipurpose Detectors . . . . .	46
2.2.3 B Tagging at Multipurpose Detectors . . . . .	47
2.3 The CMS Detector . . . . .	49
2.4 Phenomenological Pipeline . . . . .	51
2.5 Measurement of the Power of an Analysis . . . . .	55
2.6 ML enhanced signal-background discrimination . . . . .	59
2.6.1 XGBoost: Optimized Gradient Boosting . . . . .	65
2.6.2 Standard ML Analysis Workflow . . . . .	68
3 $U(1)_{T_R^3}$ GAUGE EXTENSION OF THE STANDARD MODEL	71
3.1 The Minimal $U(1)_{T_R^3}$ Model . . . . .	73
3.1.1 The Universal Seesaw Mechanism . . . . .	76
3.1.2 Minimal UV-complete Theory . . . . .	77
3.2 Current Exclusion Limits on Vector-Like Quarks . . . . .	77
3.3 Strategy, Samples and Simulation . . . . .	79
3.4 Data Analysis Using Machine Learning . . . . .	85
3.5 Results . . . . .	87
3.6 Discussion . . . . .	94
4 ON VECTORIAL LEPTOQUARKS SENSITIVITY AT THE LHC	97
4.1 A Simplified Model for the $U_1$ Leptoquark . . . . .	100
4.2 Search strategy and simulation . . . . .	104

4.3	Results . . . . .	111
4.4	Discussion and conclusions . . . . .	117
5	CONCLUSIONS AND OUTLOOK	121
5.1	Summary . . . . .	121
5.2	Methodological insights . . . . .	123
5.3	Outlook and Future Directions . . . . .	125
5.3.1	Extended Phenomenology of the $U(1)_{T_R^3}$ Model . .	125
5.3.2	Leptoquark Phenomenology Beyond the LHC . . .	126
5.3.3	Advanced Analysis Techniques . . . . .	126
5.4	Closing Remarks . . . . .	128
A	ON THE UNIVERSAL SEESAW MECHANISM	131
A.1	Single chiral fermion: The Core Mechanism . . . . .	131
A.1.1	Mass Matrix Setup and Diagonalization . . . . .	131
A.1.2	Mixing Angles and Explicit Parameter Relations .	132
A.1.3	Perturbativity Constraints for the Top Quark . . .	135
A.2	Extension to Quarks, Leptons, and Neutrinos . . . . .	136
A.2.1	Quark Sector: Full Flavor Structure . . . . .	137
A.2.2	Three Generations and the CKM Matrix . . . . .	138
A.2.3	Lepton and Neutrino Sectors . . . . .	139
B	THE 4321 MODEL	141
	BIBLIOGRAPHY	151

---

## INTRODUCTION

---

The pursuit of a fundamental description of nature’s building blocks and their interactions is a central endeavor of modern physics. This quest has led to the development of the Standard Model (SM) of particle physics, a quantum field theory that encapsulates our current understanding of the subatomic world. With breathtaking precision, the SM describes the electromagnetic, weak, and strong nuclear forces, and classifies all known elementary particles. Its triumphs are undeniable, crowned by the landmark discovery of the Higgs boson at the Large Hadron Collider (LHC) in 2012, which confirmed the mechanism for generating the masses of elementary particles, and represented the final piece of the SM puzzle.

Yet, for all its success, the SM is universally acknowledged to be an incomplete theory. It offers no candidate for dark matter, does not explain the origin of small neutrino masses, cannot account for the matter–antimatter asymmetry in the universe, does not incorporate gravity, and leaves the mass of the Higgs boson itself unnaturally unstable under quantum corrections—a problem known as the hierarchy problem. These profound theoretical shortcomings provide a clear motivation for physics beyond the SM (BSM). However, the most compelling guide for this search has always come from experimental data itself.

The primary mission of the LHC is not only to consolidate the SM but to probe its boundaries and search for new physics. While no direct evidence of new particles has been found so far, a series of subtle but persistent discrepancies—termed “anomalies”—have emerged from experiments worldwide, suggesting a potential crack in the SM’s foundation.

A particularly intriguing set of these anomalies points towards a violation of Lepton Universality (LU). In the SM, the electroweak force couples with identical strength to the three charged leptons (electrons, muons, and taus), a fundamental principle known as LU. The most significant and long-standing hints of LU violation come from measurements of semileptonic  $B$ -meson decays. The ratios  $R(D^{(*)}) = \mathcal{B}(B \rightarrow D^{(*)}\tau\nu_\tau)/\mathcal{B}(B \rightarrow D^{(*)}\ell\nu_\ell)$ , where  $\ell$  is a muon or electron, have been measured by the BaBar, Belle, and LHCb collaborations to consistently exceed the SM predictions by a combined significance of approximately  $3\sigma$ – $4\sigma$ . This deviation suggests that  $B$  mesons are more likely to decay to a final state containing a tau lepton than the SM allows, providing a compelling hint of new physics that couples preferentially to the third generation fermions. Furthermore, the longstanding discrepancy in the muon’s anomalous magnetic moment ( $g - 2$ ), recently confirmed with increased precision by the Fermilab experiment, adds another layer of intrigue, as it also hints at new physics potentially coupled preferentially to the second generation.

*Recent theoretical updates of the Standard Model prediction for the muon anomalous magnetic moment, including improved lattice-QCD results for the hadronic vacuum polarization, indicate that the discrepancy with experiment appears less significant; see [3]. However, this is still a subject of ongoing debate.*

While each anomaly individually requires careful scrutiny, their collective persistence has generated significant excitement, as they seem to point towards new physics that breaks lepton universality, potentially involving enhanced couplings to heavier fermions.

The pattern of these LU-violating anomalies has inspired a vast landscape of theoretical models extending the SM. A common thread among the most promising explanations is the introduction of new heavy particles that mediate interactions with non-universal couplings to the different generations of fermions. This generational hierarchy is crucial to evade tight constraints from precision measurements on electrons (first generation) while affecting processes involving muons and taus.

In this thesis, we contextualize and present two of our phenomenological studies that propose different strategies to probe new physics models, such as the 4321 [1] and  $U(1)_{T_R^3}$  [2] models, which extend the SM particle content to explain the hints of LU violation. These models introduce new particles with preferential couplings to second and third-generation fermions, making them prime candidates for explaining the experimental anomalies.

The experimental challenge lies in probing these models at the LHC. The proposed new particles are often heavy, leading to low production rates, and their decay signatures are complex and overwhelmed by enormous backgrounds from SM processes. Given the immense number of theoretical possibilities and the finite resources available to experimental collaborations, it is impossible to pursue every potential signature with equal vigor. This is where **phenomenological feasibility studies** becomes critical. They provide a vital bridge between theory and experiment by performing a detailed *a priori* assessment of the discovery potential for a given signal model. By using Monte Carlo simulations to emulate the detector response and analysis chain, these studies can identify the most promising signatures, optimize event selection criteria, and estimate the sensitivity achievable with the available data. This process is essential for prioritizing the experimental program, justifying the dedication of significant computing and human resources to a particular search, and ultimately guiding the LHC experiments towards the most well-motivated and detectable signals of new physics.

This thesis contributes to this effort by presenting two dedicated phenomenological studies that propose and develop novel strategies to probe signatures typical of the 4321 and  $U(1)_{T_R^3}$  models at the LHC. The work is situated at the intersection of theoretical model-building and experimental high-energy physics, with the explicit goal of assessing the feasibility of these searches.

The core methodology of this research involves:

1. Defining **benchmark scenarios** within each model, selecting specific mass points and coupling structures that explain the LU anomalies while remaining experimentally viable.

2. Using **Monte Carlo simulation** to accurately generate the hypothetical signal processes alongside the dominant SM background processes, emulating the run conditions of the LHC and the performance of the CMS detector.
3. Performing a detailed analysis of the available experimental phase-space. Given the high-dimensionality of the final states (e.g., involving multiple jets, leptons, and missing energy) and the complex, overlapping kinematical distributions of signal and background, traditional “cut-and-count” analyses are often sub-optimal. To overcome this, we employ advanced **Machine Learning (ML) techniques**, specifically supervised learning algorithms such as Boosted Decision Trees (BDTs) or Deep Neural Networks (DNNs). These algorithms are trained to learn the complex, non-linear correlations between many kinematic variables (e.g., invariant masses, angular separations, transverse momenta) to construct powerful discriminators that optimally separate the rare signal events from the large and diverse SM backgrounds. This ML-enhanced approach significantly boosts the analysis sensitivity, allowing for the detection of weaker signals or the setting of more stringent limits than would otherwise be possible.
4. Deriving the **expected sensitivity** for each model, establishing the exclusion limits or discovery potential that the LHC experiments could achieve with the current dataset. This final step is the ultimate quantitative measure of the search’s feasibility.

The structure of this thesis is as follows. We begin by establishing the theoretical foundation with a review of the SM in Chapter 1. Then, Chapter 2 details the experimental context, describing the LHC and the CMS detector, and introduces the general analysis techniques employed, including a discussion on the application of Machine Learning in high-energy physics. The original phenomenological work of this thesis is presented in the subsequent chapters: Chapter 3 details a search for new physics in the process  $pp \rightarrow t\bar{t}\mu^+\mu^-$ , while Chapter 4 presents a search for vector leptoquarks in the process  $pp \rightarrow \tau^+\tau^- + b\text{-jets}$ . Finally, Chapter 5 concludes by summarizing our findings and discussing their implications for the field, along with an outlook on future prospects.



# 1

---

## STANDARD MODEL OF PARTICLE PHYSICS

---

The Standard Model (SM) of particle physics is a quantum field theory (QFT) that describes matter as fermionic particles and their fundamental interactions. The forces are incorporated through the gauge principle, where force-carrying particles—vector bosons with spin one, arising from the adjoint representation of symmetry groups (*gauge groups*)—mediate the interactions between matter particles [4, 5]. However, this elegant formulation is not sufficient to account for particle masses. These are generated through Yukawa interactions, which are scalar-fermion couplings between the Higgs field and the fermion fields. While the Yukawa interactions themselves are not gauge interactions, their allowed structure—specifically, which fermions they can couple and their transformation properties—is strictly dictated by the gauge symmetry of the theory. This combined framework of gauge and Yukawa sectors successfully describes three of the four fundamental forces in nature.

In this chapter, we contextualize the SM by introducing the basic concepts of quantum field theory, including the notion of fields and symmetries. We then present the particle content of the SM, its gauge group, and the Lagrangian density that describes its dynamics. The Higgs mechanism and its role in providing mass to the weak gauge bosons and fermions are also discussed. Finally, we address the main deficiencies of the SM and review the experimental evidence that motivates the search for physics beyond the SM.

### 1.1 FIELDS

---

Relativistic quantum fields are degrees of freedom in QFT. Formally, they are *operator-valued functions on spacetime that transform under a representation of the Lorentz group on an invariant subspace* [6]. The different representations of the Lorentz group are mainly characterized by their spin, and their fields obey a different equation of motion (see table 1.1).

In classical field theory, a variational principle is established which generates the equations that govern the dynamics of the different fields in a theory, *the equations of motion*. Hamilton’s principle, or principle of minimal action, indicates that all possible physical configurations for a set of fields  $\varphi^I$ , with  $I = 1, 2, 3, \dots, n$ , are those for which the action  $S$  is minimal [7, 8]:

$$S = \int \mathcal{L}(\varphi^I, \partial_\mu \varphi^I) d^4x. \quad (1.1)$$

Here,  $d^4x = dx^0 dx^1 dx^2 dx^3$  and  $x \equiv (ct, x^1, x^2, x^3) \equiv (x^0, x^1, x^2, x^3) \in \mathcal{M}^4$ , are the space-time coordinates in the Minkowskian spacetime ( $\mathcal{M}^4$ ), and the function  $\mathcal{L}(\varphi^I, \partial_\mu \varphi^I)$  is called *the Lagrangian density* of a theory [4, 7]. The problem in classical field dynamics is to find the functions  $\varphi^I(x)$  in a space-time  $\mathcal{M}^4$ , fixing their boundary conditions. The solution to this classical problem is given by the Euler-Lagrange equations:

$$\frac{\partial \mathcal{L}}{\partial \varphi^I} - \frac{\partial}{\partial x^\mu} \frac{\partial \mathcal{L}}{\partial (\partial_\mu \varphi^I)} = 0, \quad (1.2)$$

and they are used to obtain the equations of motion of the set of fields  $\varphi^I$  [8].

While in classical field theory the Euler-Lagrange equations directly determines the dynamics of the system, in QFT the approach changes: if we adopt the path-integral formulation [9, 10], the idea of an equation of motion vanishes and we move on to searching for correlations between free particle states. However, the notion of action remains the cornerstone in the description of these observables.

Explicitly, the correlation functions are calculated through the Lehmann-Symanzik-Zimmermann (LSZ) reduction formula, which connects these correlators with physical scattering amplitudes. These are computed from the path integral [11, 12]:

$$\begin{aligned} Z[J] &= \langle \text{out}, 0|0, \text{in} \rangle \\ &= \mathcal{N} \int \mathcal{D}(\varphi, \bar{\varphi}) e^{iS[\varphi]} e^{i \int J_1 \varphi^I d^4x} \\ &= \mathcal{N} \int \mathcal{D}(\varphi, \bar{\varphi}) e^{i \int d^4x \mathcal{L}} e^{i \int J_1 \varphi^I d^4x}, \end{aligned} \quad (1.3)$$

taken over the space of fields  $\varphi$  with an appropriate measure  $\mathcal{D}(\varphi, \bar{\varphi})$  and normalized by  $\mathcal{N}$ . The quantity  $Z$  is known as the partition function of the theory and gives the transition amplitude from the initial vacuum  $|0, \text{in}\rangle$  to the final vacuum  $|0, \text{out}\rangle$  in the presence of a source  $J(x)$  producing particles [13].

Name	Field	Spin	Free-Lagrangian
Klein-Gordon	$\phi$	0	$\mathcal{L} = \frac{1}{2} (\partial^\mu \phi \partial_\mu \phi - m^2 \phi \phi)$
Dirac	$\chi$	1/2	$\mathcal{L} = \bar{\chi} (i \gamma^\mu \partial_\mu - m \mathbf{1}) \chi$
Proca (Massive Vector)	$A^\mu$	1	$\mathcal{L} = -\frac{1}{4} F^{\mu\nu} F_{\mu\nu} + \frac{1}{2} m^2 A^\mu A_\mu$

**Table 1.1:** Some relevant representations of the Lorentz group in 4-dimensional space-time. In this notation  $\eta_{\mu\nu} = \text{diag}(1, -1, -1, -1)$ ,  $\gamma^\mu$  are the Dirac matrices,  $F_{\mu\nu} = \partial_\mu A_\nu - \partial_\nu A_\mu$  is the abelian field strength tensor. All equations are written in natural units with  $c = \hbar = 1$ . Fields are shown in their standard representations.

Therefore, the dynamics, at both the classical and quantum levels, are entirely determined by the Lagrangian density. For free fields (i.e., non-interacting), the Lagrangian is quadratic in the fields and the path integral

can be evaluated exactly. Tab. 1.1 records the Lagrangian density for these free fields. However, to describe physics, we must include interactions, which render the path integral impossible to compute exactly.

The framework of *perturbation theory* addresses this by expanding the interaction part of the Lagrangian as a power series. This expansion is organized using *Feynman diagrams*, which provides a pictorial representation of each term, and a set of *Feynman rules*, which provides a precise dictionary to translate these diagrams into mathematical expressions for scattering amplitudes [10, 12]. The importance of these rules cannot be overstated, as they are the practical computational tools of perturbative QFT.

In this paradigm, our task is to propose a Lagrangian density for a set of fields that correctly models the propagation and interactions of fundamental particles. The free part defines the particle content and propagators, while the interaction part defines the vertices and possible scattering processes.

### 1.1.1 INTERACTIONS AND SYMMETRIES

The structure of the Lagrangian density in a quantum field theory is not arbitrary; it is constrained by fundamental principles that ensure the theory is physically consistent and mathematically well-defined. These principles act as “rules” that guide the construction of viable theories. In what follows, we systematically develop these constraints, starting from the practical requirements of perturbation theory and building up to the fundamental symmetry principles.

To perform calculations, we typically split the Lagrangian into a free part, which describes non-interacting fields, and an interaction part:

$$\mathcal{L} = \mathcal{L}_0 + \mathcal{L}_{\text{int}}. \quad (1.4)$$

This splitting is the starting point for perturbation theory. In the path integral formulation, the generating functional  $Z[J]$  can then be expressed as an operator acting on the free functional  $Z_0[J]$ :

$$Z[J] = \mathcal{N} \exp \left[ i \int d^4x \mathcal{L}_{\text{int}} \left( -i \frac{\delta}{\delta J(x)} \right) \right] Z_0[J]. \quad (1.5)$$

The exponential operator generates an infinite series known as the perturbation series. The  $n$ -point correlation function is found by taking functional derivatives of  $Z[J]$  with respect to the sources  $J(x_i)$  and setting  $J = 0$ . Each term in this series is represented by a **Feynman diagram**, whose components are:

- **External Lines:** Represent incoming and outgoing physical particles.
- **Internal Lines:** Represent virtual particles propagating between interactions, corresponding to the free-field propagators derived from  $\mathcal{L}_0$ .

- **Vertices:** Represent interactions, derived from the terms in  $\mathcal{L}_{\text{int}}$ . Each vertex has an associated coupling constant and enforces momentum conservation.

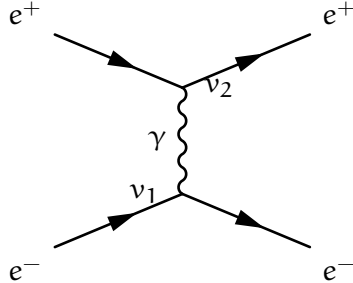


**Figure 1.1:** Example of a Feynman diagram for  $e^+e^- \rightarrow e^+e^-$  scattering. **External lines** (solid arrows at the edges) represent the incoming and outgoing electrons and positrons. The **internal line** (wavy line) represents the virtual photon propagator. The **vertices** ( $v_1$  and  $v_2$ ) represent the electromagnetic interaction points where the coupling constant  $e$  (electric charge) enters and momentum is conserved.

For this perturbation series to be a predictive computational tool, it must yield finite physical results. However, individual terms in the series (i.e., individual Feynman diagrams) often lead to divergent integrals when loop corrections are included. The key is that in a *renormalizable* theory, these divergences from all diagrams can be systematically absorbed into a finite number of parameters (like masses and coupling constants) through a redefinition procedure known as renormalization. It is important to note that while individual Feynman diagrams may diverge, the requirement is that the combination of all contributions at a given order yields finite, physically meaningful results after renormalization.

This requirement of renormalizability imposes a powerful constraint on the form of  $\mathcal{L}_{\text{int}}$ . Through power-counting arguments, one finds that only operators of mass dimension  $\leq 4$  lead to renormalizable interactions. In natural units, where  $\mathcal{L}$  has dimension [mass]<sup>4</sup>, this means that  $\mathcal{L}_{\text{int}}$  can be expressed as a truncated polynomial containing only terms up to dimension 4. Specifically, this allows Yukawa couplings (dim 4), quartic scalar interactions (dim 4), and gauge interactions (dim 4), while forbidding non-renormalizable operators like  $\phi^6$  (dim 6). Higher-dimensional operators are still allowed in effective field theories, but they correspond to interactions that are suppressed at low energies and signal the presence of new physics at higher scales [10, 12].

This is why we express  $\mathcal{L}_{\text{int}}$  as a truncated polynomial: renormalizability demands that we include only a finite set of operators with dimension  $\leq 4$ , ensuring that the theory remains predictive at all accessible energy scales.

An additional crucial requirement is the *stability of the vacuum*. For a theory to be physically meaningful, it must possess a stable ground state. This is ensured by demanding that the scalar potential, which governs the self-interactions of scalar fields, is bounded from below. If the potential were unbounded, the system could lower its energy indefinitely by evolving

toward field configurations of ever-greater magnitude, meaning no stable vacuum would exist.

For a renormalizable theory, the scalar potential can contain at most quartic terms. The stability condition requires that the quartic couplings satisfy certain positivity constraints to ensure that the potential raises with the scalar fields in any direction in field space. This is why the scalar potential is a polynomial of at most order four: renormalizability forbids higher-order terms, and stability demands that the quartic terms dominate at large field values with the correct sign.

It is important to note that this condition must hold not just at tree level but also at the quantum level, as running couplings can change sign at different energy scales, potentially leading to metastability or instability of the vacuum.

A fundamental requirement from quantum mechanics is *Hermiticity*: the Lagrangian density must be Hermitian to ensure that observables are real and the time evolution of the theory is unitary [12, 14]. This is the most basic constraint that quantum theory imposes on the Lagrangian. Without Hermiticity, the theory would predict complex-valued probabilities and violate the fundamental probabilistic interpretation of quantum mechanics.

Beyond the quantum mechanical requirement of Hermiticity, special relativity imposes a fundamental constraint: *Poincaré invariance*. This symmetry demands that the equations of motion remain the same in all inertial frames. Mathematically, this is implemented by requiring the action to be globally invariant under Poincaré transformations [14]. Equivalently, the Lagrangian density must transform as a Lorentz scalar and may change under translations at most by a total derivative [8].

This constraint is extremely powerful: it eliminates all possible interaction terms that would depend on the choice of reference frame. For instance, terms that explicitly depend on spacetime coordinates or preferred directions are forbidden. Furthermore, *dimensional analysis* places additional restrictions. In natural units,  $\mathcal{L}$  carries dimensions of mass to the fourth power ( $[\mathcal{L}] = [\text{mass}]^4$ ), which corresponds to an energy density. Combined with Lorentz invariance, this means that the interaction terms must be constructed from Lorentz-covariant combinations of fields and their derivatives, with the correct overall mass dimension.

The symmetries discussed so far—Poincaré invariance, Hermiticity, and dimensional analysis—are universal requirements that any relativistic quantum field theory must satisfy. However, they still leave a vast array of possible interaction terms. To further constrain the Lagrangian and to describe the fundamental forces of nature, we must consider *internal symmetries*: transformations that act on the fields' internal degrees of freedom rather than on spacetime coordinates.

Internal symmetries can be either *global* (where the transformation parameters are constant throughout spacetime) or *local* (gauge symmetries, where the parameters can vary from point to point). The procedure for constructing gauge theories—where global symmetries are “promoted”

*In QFT, Poincaré invariance is assumed to be global. Promoting it to a local symmetry leads to gravity, with spin-2 fields (the graviton) as mediators. Perturbatively, such a theory is not renormalizable, so it lacks predictivity at high energies, although it can still be understood as an effective field theory.*

to local ones by introducing gauge fields—is systematic and will be described in detail below. This gauge principle has proven to be the most powerful organizing principle in particle physics, determining not only which interactions are realized in nature but also their precise mathematical structure.

A classical symmetry of the Lagrangian may not always survive the process of quantization. If it fails to do so, it is said to be anomalous. *Chiral anomalies*, specifically, arise from the regularization of fermion loops in triangle diagrams and can break gauge symmetries at the quantum level. Since gauge symmetry is the very principle that dictates the form of interactions and removes unphysical states, its violation would destroy the renormalizability and unitarity of the theory. Therefore, the particle content must be carefully chosen so that these potential anomalies cancel among fermions, a non-trivial condition famously satisfied by the quarks and leptons of the Standard Model [10, 12, 15].

In summary, the construction of a consistent relativistic quantum field theory proceeds through a hierarchy of constraints:

1. **Perturbative renormalizability:** power-counting arguments restrict operators to mass dimension  $\leq 4$ , ensuring  $\mathcal{L}_{\text{int}}$  is a truncated polynomial.
2. **Vacuum stability:** the scalar potential must be bounded from below, requiring appropriate positivity conditions on quartic couplings.
3. **Hermiticity:** quantum mechanics demands  $\mathcal{L}$  be Hermitian for real observables and unitary evolution.
4. **Poincaré invariance:** special relativity requires the action to be invariant under Lorentz transformations and translations, eliminating frame-dependent terms.
5. **Internal symmetries:** global and gauge symmetries further constrain the form of interactions and determine the structure of fundamental forces.
6. **Anomaly cancellation:** the particle content must be chosen such that chiral anomalies cancel, preserving gauge symmetry at the quantum level.

These constraints drastically reduce the number of possible terms in the Lagrangian. The renormalizable interaction structures that survive are limited to: Yukawa couplings between fermions and scalars, quartic scalar self-interactions, and gauge interactions between matter/scalar fields and vector bosons. The precise form of these interactions is then determined by the internal (gauge) symmetries of the theory, which we now describe in detail.

### Gauge theories

The procedure is systematic: first, the spin-0 and spin-1/2 fields are organized into representations of a unitary (gauge) group  $G$ , such that the Lagrangian density is globally invariant under  $G$ . This global symmetry is then “promoted” to a *local symmetry* (where the group parameters can vary in spacetime) by replacing the ordinary derivatives  $\partial_\mu$  with *covariant derivatives*  $\mathcal{D}_\mu$  that incorporate new *gauge fields*  $B_\mu^A$  [5, 16–19]. This “promotion” is described in more detail below.

Given a Lagrangian density  $\mathcal{L}(\varphi^I, \partial_\mu \varphi^I)$ , where  $I$  is an index enumerating the different fields  $\varphi^I$  in the model, it is said to be *globally symmetric* under unitary transformations if the action remains invariant under field variations. At infinitesimal level, these variations are given by:

$$\delta_G \varphi^I = i\theta^A (T_A)^I_J \varphi^J, \quad (1.6)$$

where  $\theta^A$  are constant parameters of the transformation and the  $T_A$  are the generators of the group  $G$  in the appropriate representation. The corresponding finite unitary transformation is

$$U_G \equiv U(\theta) = \exp(i\theta^A T_A). \quad (1.7)$$

Note that the  $T_A$  generators satisfy the same Lie algebra of the group  $G$ :

$$[T_A, T_B] = i f_{AB}^C T_C, \quad (1.8)$$

where  $f_{AB}^C$  are the structure constants of  $G$ .

To promote the global symmetry to a local one ( $\theta^A \rightarrow \theta^A(x)$ ), the ordinary derivative  $\partial_\mu$  is replaced by a *covariant derivative*  $\mathcal{D}_\mu$ . This new derivative is designed to transform covariantly under the gauge group, meaning  $\mathcal{D}_\mu \varphi \rightarrow U(x)(\mathcal{D}_\mu \varphi)$ , so that the kinetic terms  $\mathcal{L}_{\text{kin}} \sim (\mathcal{D}_\mu \varphi)^\dagger (\mathcal{D}^\mu \varphi)$  remain invariant. This is achieved by introducing a gauge field  $B_\mu^A$  for each generator  $T_A$  and defining:

$$\mathcal{D}_\mu = \partial_\mu - ig B_\mu^A T_A, \quad (1.9)$$

where  $g$  is the gauge coupling constant. The transformation law for the gauge fields that ensures the covariant transformation of  $\mathcal{D}_\mu$  is:

$$\delta B_\mu^A = \frac{1}{g} \partial_\mu \theta^A + f_{BC}^A \theta^B B_\mu^C. \quad (1.10)$$

The introduction of the gauge fields  $B_\mu^A$  requires the addition of a kinetic term for them to the Lagrangian. This is constructed from the *field strength tensor*  $F_{\mu\nu}^A$ , defined as the curvature of the covariant derivative:

$$F_{\mu\nu}^A T_A = -\frac{i}{g} [\mathcal{D}_\mu, \mathcal{D}_\nu] = \partial_\mu B_\nu^A - \partial_\nu B_\mu^A + g f_{BC}^A B_\mu^B B_\nu^C. \quad (1.11)$$

The gauge-invariant kinetic Lagrangian is then:

$$\mathcal{L}_{\text{gauge}} = -\frac{1}{4} \delta_{AB} F_{\mu\nu}^A F^{\mu\nu B}. \quad (1.12)$$

A general, archetypal Lagrangian, embodying these structures, can be written as:

$$\mathcal{L} = -\frac{1}{4}F_{\mu\nu}^A F^{A\mu\nu} + i\bar{\psi}^i \gamma^\mu \mathcal{D}_\mu \psi^i + (\bar{\psi}_L^j \Gamma_k^j \Phi \psi_R^k + h.c.) + |\mathcal{D}_\mu \Phi|^2 - V(\Phi) \quad (1.13)$$

The terms correspond to: the kinetic term for gauge fields ( $F_{\mu\nu}^A$ ), the kinetic term for fermions  $\psi^i$ , the Yukawa interactions between left- and right-handed fermions and scalars ( $\Gamma_k^j$  is a Yukawa coupling matrix and  $\Phi$  is a scalar field), the kinetic term for scalars, and the scalar potential  $V(\Phi)$ . For a renormalizable and stable theory  $V(\Phi) = \mu^2|\Phi|^2 + \lambda|\Phi|^4$  with  $\lambda > 0$ .

Note the absence of explicit mass terms for the gauge fields ( $\sim M^2 B_\mu B^\mu$ ) and fermions ( $\sim m\bar{\psi}\psi$ ). These are forbidden by gauge invariance and for chiral fermions. Mass terms can be generated via spontaneous symmetry breaking, as discussed below.

It is important to emphasize that while the Yukawa interactions do not involve gauge bosons directly, their structure is nonetheless *completely determined by the gauge symmetry*. Specifically, gauge invariance dictates which fermion fields can couple to which scalar fields, and constrains the form of the coupling matrix  $\Gamma_k^j$ . For a Yukawa term to be gauge-invariant, the product  $\bar{\psi}_L^j \Phi \psi_R^k$  must be a singlet under the gauge group. This requirement arises because the left-handed and right-handed fermions typically transform in different representations of the gauge group, and the scalar field  $\Phi$  must carry the appropriate quantum numbers to make the overall combination invariant. In the Standard Model, for instance, the left-handed fermions are  $SU(2)_L$  doublets while the right-handed fermions are singlets, and the Higgs doublet provides the necessary quantum numbers to form gauge-invariant Yukawa couplings. Thus, even though Yukawa interactions are scalar-mediated rather than gauge-mediated, the gauge principle is the fundamental organizing principle that determines their allowed structure.

### Example

*Note that for this vector-like  $U(1)$  theory, the explicit fermion mass term  $m\bar{\psi}\psi$  is gauge-invariant. This will not be the case for chiral gauge theories like the Standard Model.*

To illustrate these concepts, let us consider a renormalizable theory with a real scalar  $\phi$  and a Dirac spinor  $\psi$ , and suppose that this theory is globally invariant under  $U(1)$  phase transformations, i.e. the fields  $\varphi \in \{\phi, \psi\}$  transform as  $\varphi \mapsto e^{i\theta}\hat{Q}\varphi$  such that  $\hat{Q}\psi = q\psi$  and  $\hat{Q}\phi = 0$ . The free Lagrangian density is

$$\mathcal{L}_{\text{free}} = \frac{1}{2}\partial^\mu\phi\partial_\mu\phi - \frac{1}{2}\mu^2\phi^2 + \bar{\psi}(i\gamma_\mu\partial^\mu - m)\psi. \quad (1.14)$$

To add globally symmetric interaction terms, we must consider operators of mass dimension  $\leq 4$ . The most general renormalizable Lagrangian, invariant under the global  $U(1)$  symmetry, is

$$\mathcal{L}_{\text{global-int}} = k_1\phi\bar{\psi}\psi - \underbrace{\left(\frac{\alpha}{3!}\phi^3 + \frac{\lambda}{4!}\phi^4\right)}_{V(\phi) - \frac{1}{2}\mu^2\phi^2} \quad (1.15)$$

Here,  $V(\phi)$  is the scalar potential containing both the mass term ( $\mu^2\phi^2$ , which is part of the free theory) and the self-interaction terms ( $\phi^3$  and  $\phi^4$ , which are genuine interactions). All terms in  $V(\phi)$  are allowed because  $\phi$  is a real scalar field and thus a U(1) singlet (charge 0). However, for stability of the potential, we require  $\lambda > 0$ . With  $\mu^2 > 0$  as shown, the vacuum is unique at  $\langle \phi \rangle = 0$ . The sign of  $\mu^2$  will become crucial for spontaneous symmetry breaking in the Higgs mechanism. Finally, the Yukawa coupling  $k_1\phi\bar{\psi}\psi$  is also gauge-invariant since the charges of  $\bar{\psi}$ ,  $\phi$ , and  $\psi$  sum to zero ( $-q + 0 + q = 0$ ).

Promoting the global symmetry to a local one ( $\theta \rightarrow \theta(x)$ ) requires introducing a gauge field  $A_\mu$  and replacing ordinary derivatives with covariant derivatives:

$$\mathcal{D}_\mu\phi = (\partial_\mu - igA_\mu\hat{Q})\phi \implies \begin{cases} \mathcal{D}_\mu\phi = \partial_\mu\phi, & \text{(since } \hat{Q}\phi = 0) \\ \mathcal{D}_\mu\psi = (\partial_\mu - igqA_\mu)\psi. \end{cases} \quad (1.16)$$

The field strength tensor for the abelian U(1) field is defined as  $F_{\mu\nu} = \partial_\mu A_\nu - \partial_\nu A_\mu$ . The locally invariant Lagrangian is then:

$$\mathcal{L}_{\text{local}} = \frac{1}{2}\partial^\mu\phi\partial_\mu\phi - V(\phi) + \bar{\psi}i\gamma_\mu\mathcal{D}^\mu\psi - m\bar{\psi}\psi + k_1\phi\bar{\psi}\psi - \frac{1}{4}F_{\mu\nu}F^{\mu\nu}. \quad (1.17)$$

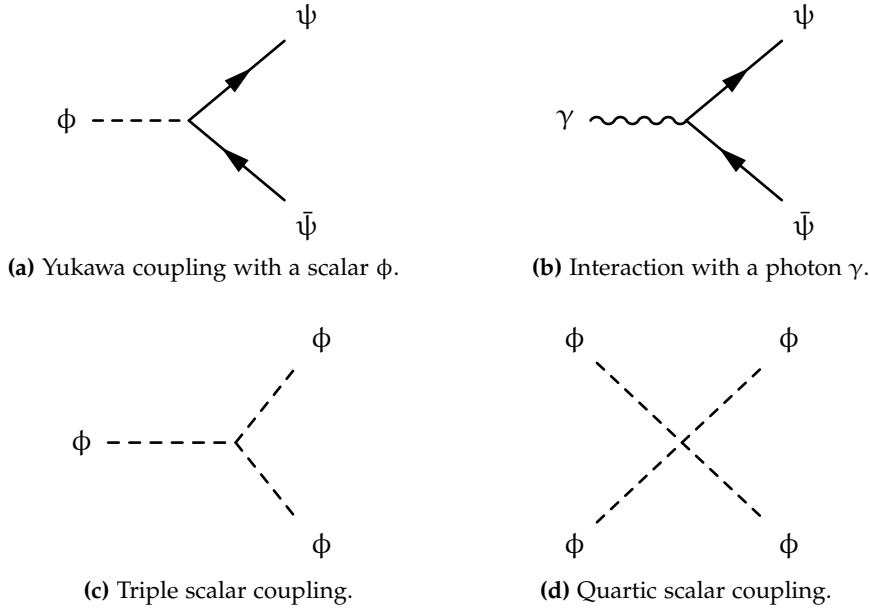


**Figure 1.2:** Feynman diagrams for Yukawa coupling, gauge boson coupling and quartic scalar coupling.

The interaction terms in this Lagrangian give rise to distinct vertices in Feynman diagrams. Figure 1.2a illustrates the Yukawa coupling  $k_1\phi\bar{\psi}\psi$ , which allows the scalar field to mediate fermion interactions. Figure 1.2b shows the gauge interaction arising from the covariant derivative term  $\bar{\psi}i\gamma_\mu\mathcal{D}^\mu\psi$ , where the photon couples to the charged fermion with strength

gq. Finally, Figures 1.2c and 1.2d depict the cubic ( $\alpha\phi^3$ ) and quartic ( $\lambda\phi^4$ ) scalar self-interactions from the potential  $V(\phi)$ , which are essential for the theory's renormalizability and vacuum stability.

With these ingredients and principles, we are now equipped to understand the structure of the SM Lagrangian, which will be discussed in the next section.

## 1.2 STANDARD MODEL

---

Fragment extracted and adapted from [20]

In 1965, Tomonaga, Feynman, and Schwinger were awarded the Nobel Prize for their independent formulation of Quantum Electrodynamics (QED) [21]. Their work established renormalization as a consistent method to separate infinities from finite, physically meaningful results in quantum field theory. QED provided predictions, such as the anomalous magnetic moment of the electron, that later experiments confirmed with remarkable precision [22, 23]. It became the prototypical example of a successful quantum field theory.

This success, however, did not extend to other fundamental interactions. The weak interaction was described by the chiral  $V - A$  model, in which processes such as the beta decay were represented by four-fermion contact terms. This framework was not renormalizable: divergences could not be absorbed into a finite set of parameters, restricting its validity to low energies. A fundamental description within the quantum field theory framework was still missing.

The issue was linked to the short-range character of the weak and strong forces. In quantum field theory, the range of an interaction depends on the mass of its mediating boson. A massless boson, such as the photon, generates a long-range force with an inverse-square dependence. A boson with mass  $m_A$ , in contrast, produces a Yukawa potential of the form  $\exp(-m_A r)/r$ , which falls off rapidly with distance. Therefore, a consistent theory for weak interactions required massive gauge bosons.

Here lay the apparent obstacle. A mass term for a gauge boson, such as  $m_A^2 A_\mu A^\mu$  in the Lagrangian, explicitly breaks gauge invariance, since it is not preserved under the transformation  $A_\mu \mapsto A_\mu + \partial_\mu \epsilon$ . This seemed to rule out gauge theories as candidates for describing short-range forces. The problem was recognized early on. For example, during a 1954 seminar by Chen Ning Yang on non-Abelian gauge theories, Wolfgang Pauli raised a fundamental objection: if the gauge bosons had mass, gauge invariance would be violated, yet without mass, the theory could not account for the short range of nuclear forces. This skepticism reflected a widely shared view: gauge symmetry appeared incompatible with short-range interactions.

The resolution of this problem came from two developments that allowed gauge bosons to behave as if they had mass, without explicitly breaking gauge symmetry:

1. The Higgs mechanism. In this framework, a scalar field permeates the vacuum. While the underlying Lagrangian remains gauge invariant, the vacuum state does not respect this symmetry. Gauge bosons interacting with this vacuum acquire mass in a renormalizable way. This mechanism explains the masses of the  $W$  and  $Z$  bosons.
2. Dynamical mass generation in non-Abelian gauge theories. In Quantum Chromodynamics (QCD), gluons and quarks (which are nearly massless at a fundamental level) are confined into hadrons that possess substantial masses. The appearance of this "mass gap" is a non-perturbative consequence of confinement. It is crucial to understand that most of the proton's mass, for example, does not come from the rest masses of its constituent quarks, but rather from the interaction energy of the confined gluon field via  $E = mc^2$ . This mass generation mechanism is conceptually distinct from the Higgs mechanism. Understanding it rigorously in the framework of gauge theories with non-Abelian symmetries (which allow for self-interactions among gauge bosons, like gluons) is the core of the Yang–Mills existence and mass gap Millennium Prize problem [24].

The SM incorporates both solutions. Electroweak theory relies on the Higgs mechanism (1), which provides a renormalizable description of the weak interaction. For the strong interaction, QCD employs dynamical mass generation (2), where most of the mass of hadrons arises from confinement rather than from the small quark masses introduced by the Higgs field.

### 1.2.1 PARTICLE CONTENT AND GAUGE GROUP

We begin by considering the chiral nature of elementary particles. While massive half-spin particles are fundamentally described by Dirac spinor fields (see Table 1.1), these do not transform under irreducible representations of the Lorentz group. Instead, Dirac spinors decompose into two Weyl spinors that do form irreducible representations. The left and right chiral projectors,  $P_L$  and  $P_R$ , extract these components from a Dirac spinor. For massless fermions, these chiral components decouple dynamically, becoming independent fields described by separate Lagrangian densities—for instance, the left-handed component obeys  $\mathcal{L} = -i\bar{\psi}\partial^\mu P_L \psi$  (see Appendix A in [25]).

The observed parity violation in weak interactions, first discovered in radioactive decays [26], reveals that these forces couple asymmetrically to the left and right chiral components of fermions. This fundamental asymmetry motivated the electroweak theory proposed by Glashow, Weinberg, and Salam [27–29], based on the gauge group  $SU(2)_L \times U(1)_Y$ . Within this framework, the  $SU(2)_L$  factor acts exclusively on left-chiral fermion components, while  $U(1)_Y$  (hypercharge) acts on both chiralities with component-specific charges.

The Standard Model further incorporates the strong interaction through the concept of color charge, fundamentally dividing fermions into two categories: color-charged particles (quarks), which transform as triplets under  $SU(3)_C$ , and color-neutral particles (leptons), which are singlets under  $SU(3)_C$ .

The complete gauge symmetry of the Standard Model is therefore:

$$G_{SM} = SU(3)_C \times SU(2)_L \times U(1)_Y, \quad (1.18)$$

where:

- $SU(3)_C$  governs the strong interaction (Quantum Chromodynamics),
- $SU(2)_L \times U(1)_Y$  describes the electroweak interaction.

This gauge structure organizes the fermionic content into doublets and singlets under  $SU(2)_L$ , while distinguishing between colored and colorless particles. We refer to the fermionic fields of the SM as the matter fields, distinguishing them into two categories: leptons and quarks.

- **Leptons:** As  $SU(3)_C$  singlets, leptons do not participate in strong interactions. Each generation consists of a left-handed  $SU(2)_L$  doublet containing a neutrino and a charged lepton, along with a right-handed singlet:

$$\ell_L = \begin{pmatrix} \nu_{eL} \\ e_L \end{pmatrix}, \quad e_R. \quad (1.19)$$

In the minimal model, the right-handed neutrino  $\nu_R$  is a complete gauge singlet, making it sterile.

- **Quarks:** As  $SU(3)_C$  triplets, quarks carry color charge and participate in all interactions. Each generation forms a left-handed  $SU(2)_L$  doublet together with right-handed singlets for both up-type and down-type quarks:

$$q_L = \begin{pmatrix} u_L \\ d_L \end{pmatrix}, \quad u_R, \quad d_R. \quad (1.20)$$

Remarkably, this entire pattern of gauge representations and hypercharge assignments is not unique to a single set of fermions. Instead, it repeats almost identically across **three generations**, each sharing the same gauge quantum numbers but differing in mass and flavor. This replication gives rise to the rich structure of flavor physics and underlies phenomena such as quark mixing and neutrino oscillations. The existence of three fermion families is one of the most intriguing empirical facts of the Standard Model, hinting at possible structures beyond it.

All fermions transform under  $U(1)_Y$  with generation-independent hypercharges. Left-handed components form  $SU(2)_L$  doublets, while right-handed components are singlets. Quarks transform as color triplets under  $SU(3)_C$ , whereas leptons are color singlets.

The chirality of the fermionic spectrum stands as one of the deepest properties of the Standard Model. The fact that left- and right-chirality components transform differently under the electroweak gauge group poses a fundamental challenge: such chiral asymmetry is compatible with gauge symmetry only if fermions are massless, since a direct Dirac mass term  $m\bar{f}_R f_L + h.c.$  would explicitly break the gauge invariance. Yet, fermions like the electron are unequivocally massive. This apparent contradiction finds its resolution in the Higgs mechanism, where masses emerge effectively from Yukawa couplings with the Higgs field.

This chiral gauge structure not only explains the parity-violating nature of weak interactions but also enables electroweak symmetry breaking, which generates masses for fermions and weak gauge bosons. The electroweak symmetry  $SU(2)_L \times U(1)_Y$  spontaneously breaks to the electromagnetic symmetry  $U(1)_{EM}$  via the Higgs mechanism, whose quantum excitation is the Higgs boson  $h$ . The hypercharge assignments in Table 1.2 relate to electric charges through the Gell-Mann–Nishijima relation [30]:

$$Q_{EM} = \frac{1}{2}Y + T_3, \quad (1.21)$$

where  $T_3 \equiv \text{diag}(\frac{1}{2}, -\frac{1}{2})$  is an  $SU(2)_L$  generator. This relation ensures charge quantization—for instance, the exact equality in magnitude of the proton and electron charges. Although these hypercharge assignments might appear arbitrary, they are uniquely determined by the requirement of quantum consistency.

Field	$SU(3)_C$	$SU(2)_L$	$U(1)_Y$	$U(1)_{EM}$
$q_L^i = (u^i, d^i)_L$	<b>3</b>	<b>2</b>	+1/3	(2/3, -1/3)
$u_R^i$	<b>̄3</b>	<b>1</b>	+4/3	+2/3
$d_R^i$	<b>̄3</b>	<b>1</b>	-2/3	-1/3
$\ell_L^i = (v^i, e^i)_L$	<b>1</b>	<b>2</b>	-1	(0, -1)
$e_R^i$	<b>1</b>	<b>1</b>	-2	-1
$H = (H^+, H^0)$	<b>1</b>	<b>2</b>	+1	(+1, 0)

**Table 1.2:** Gauge quantum numbers of Standard Model quarks, leptons, and the Higgs scalar.

### 1.2.2 GAUGE BOSONS

In the previous section, we have seen that the fundamental interactions of SM raise the gauge group

$$G_{SM} = SU(3)_C \times SU(2)_L \times U(1)_Y. \quad (1.22)$$

Each factor in this group corresponds to a fundamental interaction and requires the introduction of gauge fields that ensure the local symmetry of the theory.

The gauge bosons associated with each group are:

- From  $SU(3)_C$ : Eight massless gluons ( $G_\mu^a$ ) that mediate the strong force between color-charged particles.
- From  $SU(2)_L$ : Three isospin bosons ( $W_\mu^i$ ) responsible for weak interactions.
- From  $U(1)_Y$ : A single hypercharge boson ( $B_\mu$ ) associated with the abelian symmetry of hypercharge.

Before symmetry breaking, these are the gauge eigenstates of the theory. After electroweak symmetry breaking, the  $SU(2)_L$  and  $U(1)_Y$  fields mix to produce the physical gauge bosons: the massive  $W^\pm$  and  $Z$  bosons that mediate weak interactions, and the massless photon ( $\gamma$ ) responsible for electromagnetism.

The Lie algebra of the gauge group  $SU(3)_C \times SU(2)_L \times U(1)_Y$  follows

$$\begin{aligned} [t^a, t^b] &= if^{abc}t_c, \\ [T^i, T^j] &= i\epsilon^{ijk}T_k, \\ [T^i, Y] &= [t^a, T^j] = [t^a, Y] = 0, \end{aligned} \quad (1.23)$$

where  $f^{abc}$  and  $\epsilon^{ijk}$  are the structure constants of  $SU(3)$  and  $SU(2)$ .

Under gauge transformations, the gauge fields  $G_\mu$ ,  $W_\mu$ , and  $B_\mu$  transform as:

$$\begin{aligned} \delta B_\mu &= \partial_\mu \theta, \\ \delta W_\mu^i &= \partial_\mu \theta^i - g\epsilon^{ijk}\theta^j W_\mu^k, \\ \delta G_\mu^a &= \partial_\mu \theta^a - g_s f^{abc}\theta^b G_\mu^c. \end{aligned} \quad (1.24)$$

with  $g_s$ ,  $g$ , and  $g'$  being the coupling constants associated with  $SU(3)_C$ ,  $SU(2)_L$ , and  $U(1)_Y$ , respectively.

The corresponding field strength tensors are then defined as:

$$\begin{aligned} G_{\mu\nu}^a &= \partial_\mu G_\nu^a - \partial_\nu G_\mu^a + g_s f^{abc} G_\mu^b G_\nu^c \\ W_{\mu\nu}^i &= \partial_\mu W_\nu^i - \partial_\nu W_\mu^i + g\epsilon^{ijk} W_\mu^j W_\nu^k \\ B_{\mu\nu} &= \partial_\mu B_\nu - \partial_\nu B_\mu \end{aligned} \quad (1.25)$$

and the “kinetic” term for gauge fields in the Lagrangian is

$$\mathcal{L}_{\text{Gauge}} = -\frac{1}{4} G_{\mu\nu}^a G_a^{\mu\nu} - \frac{1}{4} W_{\mu\nu}^i W_i^{\mu\nu} - \frac{1}{4} B_{\mu\nu} B^{\mu\nu}. \quad (1.26)$$

These kinetic terms do not contain mass terms for the vector bosons. The masses of the  $W^\pm$  and  $Z$  bosons are generated via the Higgs mechanism, which induces mixing between the  $W^i$  and  $B$  gauge eigenstates. The field redefinitions leading to the physical mass eigenstates are

$$\left\{ \begin{array}{l} W_\mu^+ = \frac{1}{\sqrt{2}} (W_\mu^1 - iW_\mu^2) \\ W_\mu^- = \frac{1}{\sqrt{2}} (W_\mu^1 + iW_\mu^2) \\ Z_\mu = c_w W_\mu^3 - s_w B_\mu \\ A_\mu = s_w W_\mu^3 + c_w B_\mu \end{array} \right. \quad \text{where} \quad \left\{ \begin{array}{l} s_w = \sin \theta_w = \frac{g}{\sqrt{g^2 + g'^2}} \\ c_w = \cos \theta_w = \frac{g'}{\sqrt{g^2 + g'^2}} \end{array} \right. \quad (1.27)$$

Note that we denote the electromagnetic potential as  $A_\mu$  with  $\gamma$  being its quantum excitation.

In addition, due to the non-abelian nature of the  $SU(3)_C$  and  $SU(2)_L$  gauge groups, the kinetic terms in Eq. (1.26) give rise to three- and four-point self-interaction vertices for the corresponding gauge bosons (see Fig. 1.3), whose structure follows directly from the commutation relations of the Lie algebra.

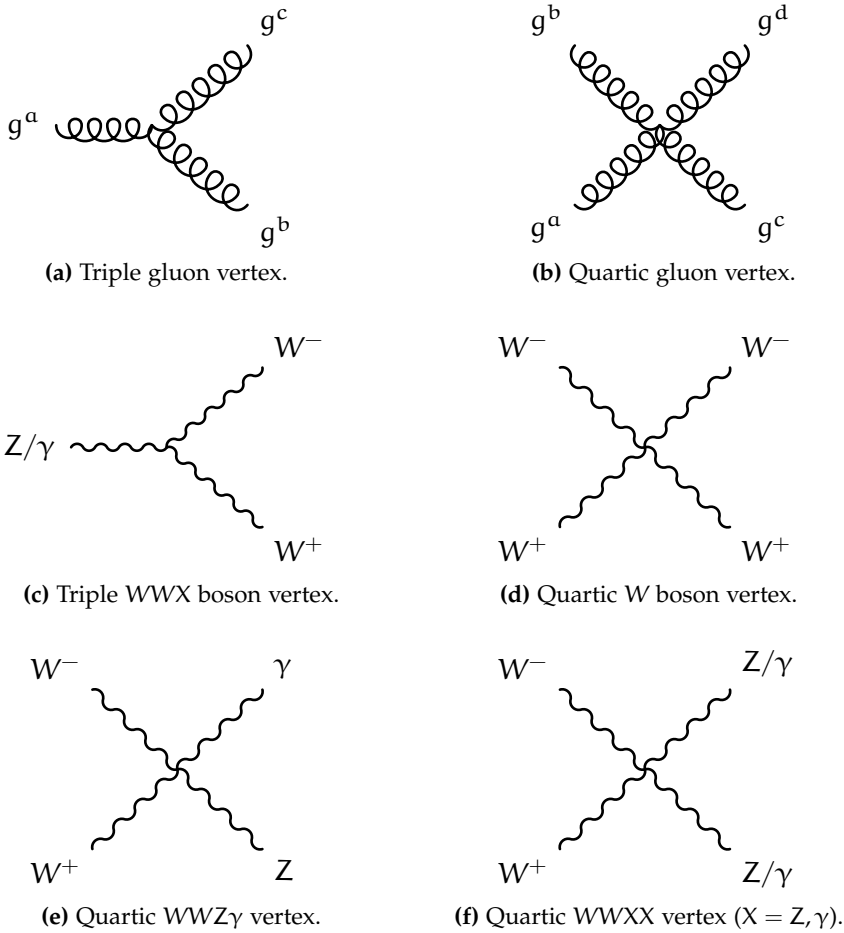


**Figure 1.3:** Feynman diagrams for gauge boson self-interactions (unitary gauge). We denote by  $X = Z, \gamma$  a neutral electroweak gauge boson.

### 1.2.3 MATTER FIELDS

In table 1.3, we can see that there are six leptons, three charged and three neutral: each charged lepton has an associated neutrino. Therefore, the electrically charged and the associated neutral leptons can be arranged as  $SU(2)_L$  doublets. In the case of quarks, we can divide these particles as up-and-down-type quarks, also arranged as  $SU(2)_L$  doublets, one per generation.

According to the SM, there are three generations (families) of fermions. Each generation contains a doublet of leptons and a doublet of quarks.

Fermion categories		Elementary particle generation		
Type	Subtype	First	Second	Third
Quarks (q)	up-type	(u) up	(c) charm	(t) top
	down-type	(d) down	(s) strange	(b) bottom
Leptons ( $\ell$ )	charged	(e) electron	( $\mu$ ) muon	( $\tau$ ) tauon
	neutrino	( $\nu_e$ )	( $\nu_\mu$ )	( $\nu_\tau$ )

**Table 1.3:** Three generations of fermions according to the SM of particle physics. Each generation containing two types of leptons and two types of quarks.

Among generations, particles differ by their flavour quantum number and mass, but their strong and electrical interactions are identical. Moreover, the flavour quantum number is a quantity conserved by all interactions except for the weak charged interaction. Each generation is more massive than the previous one. The second and third generations are unstable and they disintegrate into the first generation. This is why ordinary matter is composed of first generation fermions. All three generations are produced in colliders, nuclear reactors, and cosmic rays.

Under all the constraints on local gauge invariance and renormalizability of the theory, the fermionic Lagrangian for SM is given by

$$\mathcal{L}_{\text{Fer}} = i\bar{\ell}_L^j \not{\partial} \ell_L^j + i\bar{e}_R^j \not{\partial} e_R^j + i\bar{q}_L^j \not{\partial} q_L^j + i\bar{u}_R^j \not{\partial} u_R^j + i\bar{d}_R^j \not{\partial} d_R^j \quad (1.28)$$

where  $\not{\partial} \equiv \gamma^\mu \not{\partial}_\mu$ , for the covariant derivative

$$\not{\partial}_\mu = \partial_\mu - ig_s t_a G_\mu^a - ig T_i W_\mu^i - ig' \frac{Y}{2} B_\mu, \quad (1.29)$$

with the gauge fields  $G^a$ ,  $W^i$ , and  $B$  acting on each kind of fermion via

$$\begin{aligned} \not{\partial}_\mu \ell_L^i &= \left( \partial_\mu - ig T_j W_\mu^j + i \frac{g'}{2} B_\mu \right) \ell_L^i \\ \not{\partial}_\mu e_R^i &= \left( \partial_\mu - ig' B_\mu \right) e_R^i \\ \not{\partial}_\mu q_L^i &= \left( \partial_\mu - ig_s t_a G_\mu^a - ig T_j W_\mu^j - i \frac{g'}{6} B_\mu \right) q_L^i \\ \not{\partial}_\mu u_R^i &= \left( \partial_\mu - ig_s t_a G_\mu^a - i \frac{2g'}{3} B_\mu \right) u_R^i \\ \not{\partial}_\mu d_R^i &= \left( \partial_\mu - ig_s t_a G_\mu^a + i \frac{g'}{3} B_\mu \right) d_R^i, \end{aligned} \quad (1.30)$$

coupling the fermions to the gauge bosons. As we will show below, after electroweak symmetry breaking, these interactions give rise to the familiar electromagnetic, weak, and strong forces, where the physical  $\gamma$ ,  $Z$ , and  $W$  bosons are a superposition of the original  $B$  and  $W$  fields, as it was mentioned before. Representative tree-level gauge–fermion interaction vertices are displayed in Fig. 1.4.

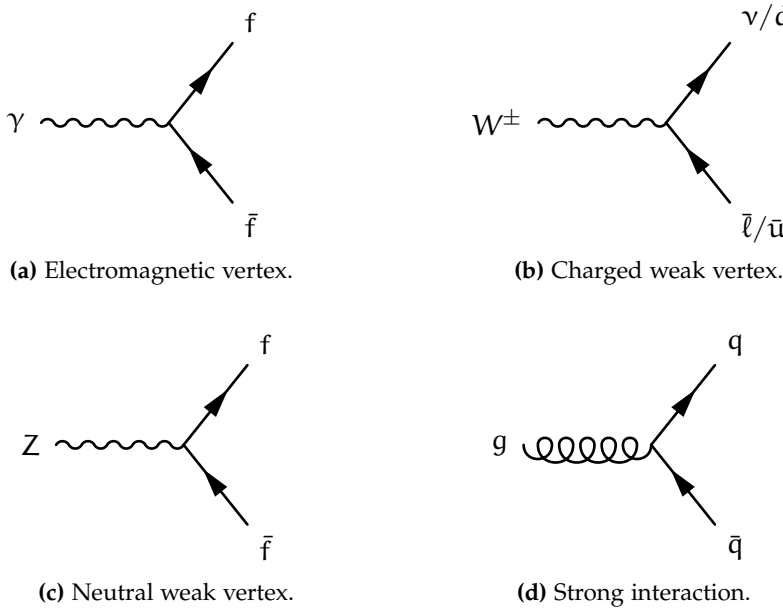


**Figure 1.4:** Feynman diagrams for gauge boson interactions in the Standard Model.

#### 1.2.4 ELECTROWEAK SYMMETRY BREAKING

As it was mentioned in Section 1.2.1, in the SM the EW symmetry,  $SU(2)_L \times U(1)_Y$ , is spontaneously broken down to the electromagnetic  $U(1)_{EM}$  group by a complex scalar Higgs field. This field transforms as an  $SU(2)_L$  doublet,  $H = (H^+, H^0)$ , with hypercharge +1. Its dynamics is governed by the potential

$$V(H) = -\mu^2|H|^2 + \lambda|H|^4, \quad \text{with } \mu^2, \lambda > 0. \quad (1.31)$$

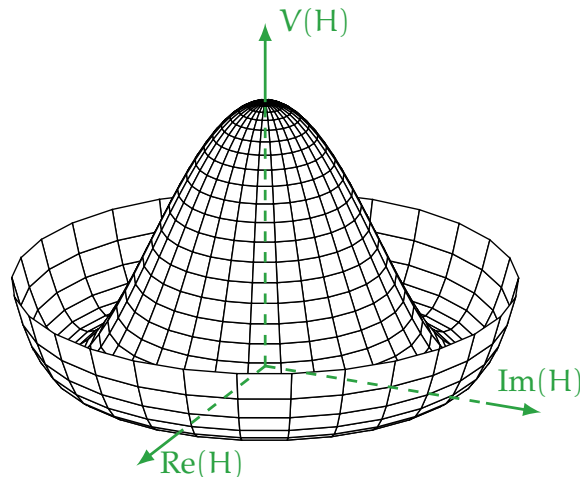


**Figure 1.5:** Schematic representation of the Higgs potential  $V(H) = -\mu^2|H|^2 + \lambda|H|^4$ . The potential exhibits a Mexican-hat shape with an unstable maximum at  $|H| = 0$  and a circle of degenerate minima at  $|H| = v$ .

The *negative* sign in front of the  $|H|^2$  term is crucial: it ensures that the potential minimum does not occur at  $|H| = 0$ , but instead at a nonzero field value. This gives rise to the characteristic Mexican-hat shape shown in Fig. 1.5, where the minimum forms a circle of degenerate vacua at

$$v^2 \equiv \langle H^\dagger H \rangle = \frac{\mu^2}{2\lambda}. \quad (1.32)$$

The vacuum expectation value (vev) aligns with the electrically neutral component,  $\langle H^0 \rangle = v/\sqrt{2} \simeq 174 \text{ GeV}$ , generating masses for the weak gauge bosons while preserving  $U(1)_{EM}$ .

We adopt the Kibble parametrization of the Higgs doublet in terms of one physical scalar  $h$  and three scalar fields  $G^\pm, G^0$ :

$$H = \begin{pmatrix} G^+ \\ \frac{1}{\sqrt{2}}(v + h + iG^0) \end{pmatrix}, \quad (1.33)$$

where  $G^\pm$  and  $G^0$  are the would-be Goldstone bosons associated with the broken generators of  $SU(2)_L \times U(1)_Y$ . In the unitary gauge, these unphysical degrees of freedom are “gauged away,” reducing the doublet to

$$H = \frac{1}{\sqrt{2}} \begin{pmatrix} 0 \\ v + h \end{pmatrix}. \quad (1.34)$$

Substituting this form into the Higgs potential yields the physical Higgs boson mass  $m_h = \sqrt{2\lambda}v \simeq 125 \text{ GeV}$ , and the scalar self-interactions shown in Fig. 1.6.

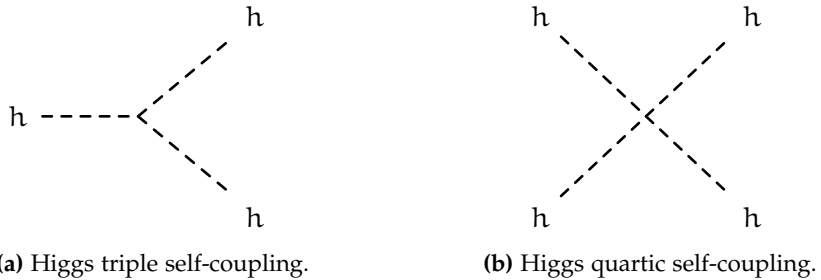


**Figure 1.6:** Feynman diagrams for Higgs self-interactions arising from the potential  $V(H^\dagger, H) = -\mu^2|H|^2 + \lambda|H|^4$  in the Higgs Lagrangian.

The Full Lagrangian of the scalar sector is

$$\mathcal{L}_H = \mathcal{D}_\mu H^\dagger \mathcal{D}^\mu H - V(H^\dagger, H), \quad (1.35)$$

with the covariant derivative defined as  $\mathcal{D}_\mu H = (\partial_\mu + igT_a W_\mu^a + ig'\frac{Y}{2}B_\mu) H$ . Substituting the Higgs vacuum expectation value, one obtains

$$\begin{aligned}\mathcal{L}_{\langle H \rangle} &= -\frac{1}{8} \begin{pmatrix} 0 & v \end{pmatrix} \begin{pmatrix} gW_\mu^3 - g'B_\mu & g(W_\mu^1 - iW_\mu^2) \\ g(W_\mu^1 + iW_\mu^2) & -gW_\mu^3 - g'B_\mu \end{pmatrix}^2 \begin{pmatrix} 0 \\ v \end{pmatrix} \\ &= -\frac{1}{8}v^2 V_\mu^T \begin{pmatrix} g^2 & 0 & 0 & 0 \\ 0 & g^2 & 0 & 0 \\ 0 & 0 & g^2 & -g'g \\ 0 & 0 & -g'g & g'^2 \end{pmatrix} V^\mu,\end{aligned}\quad (1.36)$$

where  $V_\mu^T = (W_\mu^1, W_\mu^2, W_\mu^3, B_\mu)$ . Diagonalizing this mass matrix yields the following eigenvalues

$$0, -\frac{1}{4}v^2g^2, -\frac{1}{4}v^2g^2, \text{ and } -\frac{1}{4}v^2(g^2 + g'^2).$$

These eigenvalues correspond to the physical masses

$$M_W = \frac{1}{2}gv \quad (\text{doubly degenerate}), \quad M_Z = \frac{1}{2}\sqrt{g^2 + g'^2}v. \quad (1.37)$$

while the massless state corresponds to the photon, which transforms under the representation of the unbroken generator  $Q_{EM}$ .

The origin of these masses can be understood in terms of the degrees of freedom of the Higgs field. Recall from Eq. (1.33) that the four real degrees of freedom of the complex Higgs doublet are parametrized as one physical scalar  $h$  (the Higgs boson) and three scalar fields  $G^\pm, G^0$ . If the electroweak symmetry were global rather than local, these three modes would become physical massless Goldstone bosons upon spontaneous breaking of  $SU(2)_L \times U(1)_Y \rightarrow U(1)_{EM}$ , as dictated by Goldstone's theorem. However, in a gauge theory, the situation is different. Through the Higgs mechanism, these would-be Goldstone modes are absorbed by the gauge bosons  $W^\pm$  and  $Z$ , providing them with the longitudinal polarization states necessary for massive vector bosons.

To see this transfer of degrees of freedom explicitly, consider the kinetic term of the Higgs field in the Kibble parametrization:

$$\mathcal{D}_\mu H = \partial_\mu H - ig\frac{\vec{\sigma}}{2} \cdot \vec{W}_\mu H - i\frac{g'}{2}B_\mu H. \quad (1.38)$$

Expanding around the vacuum with  $H = \frac{1}{\sqrt{2}}(G^+, v + h + iG^0)^T$  and keeping only the terms quadratic in gauge fields, we obtain

$$|\mathcal{D}_\mu H|^2 \supset \frac{1}{8}(v + h)^2 [g^2(W_\mu^1)^2 + g^2(W_\mu^2)^2 + (gW_\mu^3 - g'B_\mu)^2] + (\text{der. terms}). \quad (1.39)$$

The derivative terms contain kinetic mixing between the gauge fields and the Goldstone modes:

$$|\mathcal{D}_\mu H|^2 \supset \frac{1}{2} [(\partial_\mu G^+)(gW^{1\mu} + igW^{2\mu}) + (\partial_\mu G^0)(gW^{3\mu} - g'B^\mu)] + \text{h.c.} \quad (1.40)$$

These mixing terms are precisely what allow the Goldstone modes to be eliminated via a gauge transformation. Specifically, under an  $SU(2)_L \times U(1)_Y$  gauge transformation parametrized by  $\vec{\alpha}(x)$  and  $\beta(x)$ , the gauge fields transform as

$$\vec{W}_\mu \rightarrow \vec{W}_\mu + \frac{1}{g} \partial_\mu \vec{\alpha}, \quad B_\mu \rightarrow B_\mu + \frac{1}{g'} \partial_\mu \beta. \quad (1.41)$$

Choosing the gauge parameters appropriately, we can absorb the Goldstone fields into redefinitions of the gauge fields. For instance, setting  $\alpha^\pm = \mp G^\pm/v$  and  $\alpha^3 = -G^0/v$  eliminates  $G^\pm, G^0$  from the Lagrangian. This is the unitary gauge. In this gauge, the mass terms become

$$\mathcal{L}_{\text{mass}} = \frac{1}{2} M_W^2 W_\mu^+ W^{-\mu} + \frac{1}{2} M_Z^2 Z_\mu Z^\mu, \quad (1.42)$$

where  $M_W = \frac{1}{2} g v$  and  $M_Z = \frac{1}{2} \sqrt{g^2 + g'^2} v$ . The crucial point is that the three degrees of freedom originally residing in  $G^\pm, G^0$  have now been transferred to provide the longitudinal polarization states of  $W^\pm$  and  $Z$ . Before symmetry breaking, massless gauge bosons possess only two transverse polarization states; after symmetry breaking, the massive gauge bosons acquire a third (longitudinal) polarization state each, accounting for the three absorbed Goldstone modes.

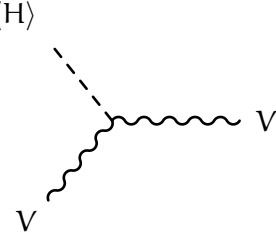


**Figure 1.7:** Vector boson mass insertion from the Higgs vacuum expectation value ( $V = W^\pm, Z$ ). This diagrammatic representation illustrates how the masses of the weak gauge bosons arise from their interaction with the non-zero vev of the Higgs field. The Higgs vev insertion effectively represents the absorption of the would-be Goldstone bosons ( $G^\pm, G^0$ ) into the gauge fields, providing the longitudinal degrees of freedom necessary for massive vector bosons.

This process is illustrated diagrammatically in Fig. 1.7, where the interaction of the gauge fields with the Higgs vev effectively incorporates the Goldstone degrees of freedom into the vector bosons. Meanwhile, the photon remains massless with only two transverse polarizations, corresponding to the unbroken  $U(1)_{\text{EM}}$  symmetry. The resulting Higgs–vector boson interaction structures are summarized in Fig. 1.8.

Having established how the Higgs mechanism generates masses for the weak gauge bosons through the absorption of Goldstone modes, we now turn to fermion masses, which arise through a different but equally important mechanism: Yukawa couplings. These represent the most general renormalizable interactions between the Higgs field and the fermion fields (see the diagrammatic decomposition in Fig. 1.9a–1.9d):

$$\mathcal{L}_{\text{Yuk}} = y_u^{ij} \bar{q}_L^i q_R^j \tilde{H} + y_d^{ij} \bar{q}_L^i d_R^j H + y_\ell^{ij} \bar{l}_L^i e_R^j H + \text{h.c.}, \quad (1.43)$$

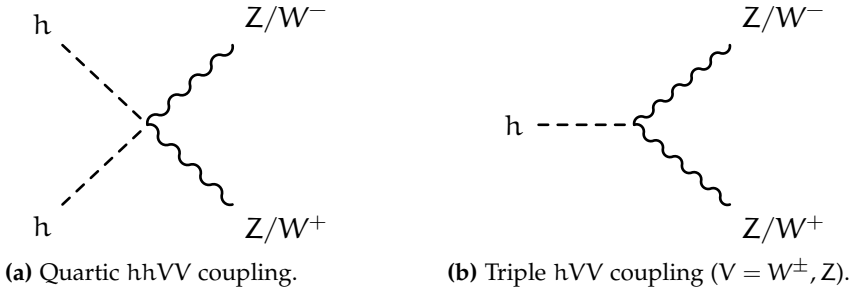


**Figure 1.8:** Feynman diagrams for Higgs–gauge boson interactions (unitary gauge) arising from  $\mathcal{D}_\mu H^\dagger \mathcal{D}^\mu H$ . Here  $V = W^\pm, Z$ .

where  $\tilde{H} = i\sigma_2 H^*$ , and  $y_u, y_d, y_\ell$  are arbitrary  $3 \times 3$  complex matrices in flavor space. When the Higgs acquires its vev,

$$\langle H \rangle = \begin{pmatrix} 0 \\ \frac{v}{\sqrt{2}} \end{pmatrix}, \quad (1.44)$$

these couplings generate Dirac mass terms for the fermions.

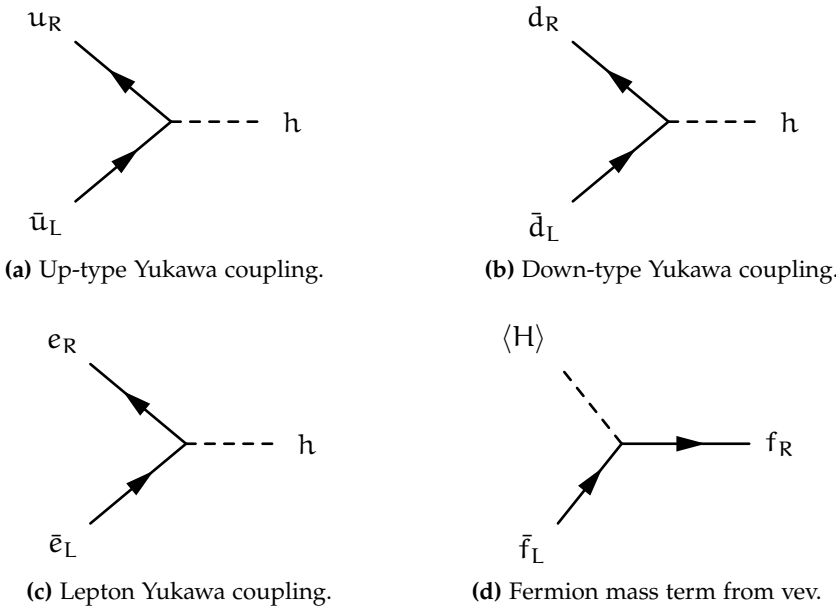


**Figure 1.9:** Feynman diagrams for Yukawa couplings.

The quark mass matrices are proportional to the Yukawa matrices:  $M_u = y_u v / \sqrt{2}$ ,  $M_d = y_d v / \sqrt{2}$ . Since  $y_u$  and  $y_d$  are general complex matrices, the mass matrices  $M_u$  and  $M_d$  cannot be simultaneously diagonalized. The reason for this is that the same left-handed quark doublet  $q_L$  appears in both the up-type and down-type Yukawa operators, so any unitary rotation of  $q_L$  that diagonalizes one mass matrix will generically affect the other. The physical quark masses and states are found by performing separate bi-unitary transformations on the left- and right-handed fields:

$$u_L \rightarrow V_L^u u_L, \quad u_R \rightarrow V_R^u u_R, \quad d_L \rightarrow V_L^d d_L, \quad d_R \rightarrow V_R^d d_R, \quad (1.45)$$

such that  $V_L^u M_u V_R^{u\dagger} = M_u^{\text{diag}}$  and  $V_L^d M_d V_R^{d\dagger} = M_d^{\text{diag}}$  are diagonal with real, positive entries.

This diagonalization procedure has a direct consequence for the charged-current interactions mediated by the  $W^\pm$  bosons. In the flavor basis the interaction reads

$$\mathcal{L}_W \supset -\frac{g}{\sqrt{2}}(\bar{u}_L, \bar{c}_L, \bar{t}_L)\gamma^\mu W_\mu^+(d_L, s_L, b_L)^T + \text{h.c.} \quad (1.46)$$

After moving to the mass basis, the left-handed up- and down-type quarks rotate differently ( $u_L \rightarrow V_L^u u_L$ ,  $d_L \rightarrow V_L^d d_L$ ), and the interaction becomes

$$\mathcal{L}_W \supset -\frac{g}{\sqrt{2}}(\bar{u}_L, \bar{c}_L, \bar{t}_L)\gamma^\mu W_\mu^+ V_{\text{CKM}}(d_L, s_L, b_L)^T + \text{h.c.}, \quad (1.47)$$

where the Cabibbo–Kobayashi–Maskawa (CKM) matrix appears as the mismatch between the two rotations:

$$V_{\text{CKM}} \equiv V_L^u V_L^{d\dagger} = \begin{pmatrix} V_{ud} & V_{us} & V_{ub} \\ V_{cd} & V_{cs} & V_{cb} \\ V_{td} & V_{ts} & V_{tb} \end{pmatrix}. \quad (1.48)$$

This unitary matrix encodes flavor mixing in charged-current weak interactions, and its non-diagonal structure allows the  $W$  boson to mediate flavor-changing transitions between quarks of different generations, such as  $s \rightarrow u$  or  $b \rightarrow c$ .

The situation is different for leptons in the minimal SM without right-handed neutrinos. The charged-lepton mass matrix  $M_\ell = y_\ell v / \sqrt{2}$  can be diagonalized by field redefinitions, but since neutrinos are massless in this framework, there is no additional rotation in the neutrino sector. This means that the same field redefinition that diagonalizes  $M_\ell$  can be applied to the neutrino fields without introducing any physical mixing. As a result, the charged-current interaction

$$\mathcal{L}_W \supset -\frac{g}{\sqrt{2}}\bar{\nu}_L \gamma^\mu W_\mu^+ \ell_L + \text{h.c.} \quad (1.49)$$

remains diagonal in the mass basis. In contrast to the quark sector, the  $W$  boson couples only to lepton pairs of the same generation, and flavor-changing transitions are absent.

A crucial feature of the SM gauge structure is that the electroweak interactions are *flavor-universal*: in the interaction basis, all fermion families couple to the gauge bosons with identical strength, determined solely by the gauge couplings  $g$  and  $g'$ . This universality persists in the mass basis. For quarks, although the CKM matrix introduces flavor mixing, the coupling strength remains universal—each element  $V_{ij}$  multiplies the same factor  $g/\sqrt{2}$ . For leptons with massless neutrinos, the absence of a leptonic mixing matrix means that the charged-current interactions are both diagonal and universal. The  $W$  boson couples to each  $\bar{\nu}_L \gamma^\mu \ell_L$  current with the same coefficient  $-g/\sqrt{2}$ , and the  $Z$  boson couplings to  $\ell_L$  and  $\ell_R$

are flavor-independent because the hypercharge assignments are identical for all families.

This property, often referred to as *Lepton Universality* (LU), implies that processes differing only by the lepton flavor, such as leptonic decays or semileptonic transitions, are predicted to occur with the same rates up to well-understood effects: differences in phase space, helicity suppression, lepton-mass dependence, and small radiative corrections. The assumption of LU is central in the extraction of CKM parameters, since experimental determinations from decays involving electrons, muons, and tau leptons can be consistently combined. Precision tests of LU focus on ratios of decay widths or branching fractions where theoretical and experimental uncertainties cancel to a large extent. Agreement with these tests confirms the gauge structure of the SM, while deviations would point to new physics. It is important to note that lepton universality does not forbid lepton flavor-violating processes such as  $\mu \rightarrow e\gamma$  at the level of effective operators; rather, it states that the fundamental gauge couplings are flavor-blind.

This suffices to illustrate how the SM, formulated as a relativistic quantum field theory, describes the interactions of matter fields through the fundamental forces, mediated by vector bosons. The Higgs boson, also part of the SM spectrum, plays the central role in generating masses for the weak bosons and the fermions, while indirectly distinguishing the photon as the only massless gauge boson of the EW sector.

Since its formulation, the SM has been tested extensively and has shown remarkable success, both in explaining existing data and in making accurate predictions. A well-known example is the agreement between its prediction and the experimental measurement of the electron magnetic dipole moment, consistent to twelve significant figures [31]. The discovery of the Higgs boson in 2012 was the culmination of almost fifty years of experimental efforts, confirming the mechanism incorporated into the SM in the late 1960s through the unification of the electromagnetic and weak interactions by Glashow, Weinberg, and Salam [27, 28]. With this discovery, the full particle spectrum predicted by the SM was finally observed.

### 1.3 DEFICIENCIES OF SM AND NEW PHYSICS

---

Despite its remarkable successes in describing the fundamental particles and interactions, with its parameters measured with increasing precision over several decades [22, 28], the SM cannot be the ultimate theory of fundamental particles and interactions. Although it provides the best current description of the subatomic world, it faces various shortcomings and leaves important questions unanswered [32, 33]. Some of these limitations are fundamentally incompatible with the SM framework and strongly motivate consistent extensions to address cosmological, phenomenological, and theoretical challenges.

In this thesis, we are particularly interested in *phenomenological* signatures and experimental anomalies that point toward physics beyond the

*Note: In the experimental literature, this property is commonly called Lepton Flavour Universality (LFU). We use the term Lepton Universality to emphasize the universal coupling strength, distinct from lepton flavor conservation.*

Standard Model [33, 34]. Therefore, we begin by highlighting the phenomenological problems most relevant to our work—direct experimental observations that the SM cannot accommodate or explain. We then briefly discuss cosmological and theoretical motivations for new physics to provide a broader context.

### 1.3.1 PHENOMENOLOGICAL PROBLEMS

**ANOMALIES IN  $b$ -HADRON DECAYS** Lepton-flavour universality (LFU) is a fundamental prediction of the SM, stating that the electroweak couplings of leptons are independent of their flavour. Measurements of ratios such as  $R_K = \mathcal{B}(B \rightarrow K\mu^+\mu^-)/\mathcal{B}(B \rightarrow Ke^+e^-)$  and  $R_{K^*}$  in  $b \rightarrow sll$  transitions showed persistent deviations from unity at the  $\sim 2\text{--}3\sigma$  level in earlier LHCb data, hinting at possible new physics coupling preferentially to muons. However, the 2022 LHCb analyses with the full Run 1+2 dataset report  $R_K$  and related ratios consistent with the SM within uncertainties [35], and the tension has largely subsided. Angular-observable tensions (e.g.  $P_5'$ ) persist at lower significance and are sensitive to hadronic uncertainties. In the charged-current sector, the ratios  $R_{D^{(*)}} = \mathcal{B}(B \rightarrow D^{(*)}\tau\nu)/\mathcal{B}(B \rightarrow D^{(*)}\ell\nu)$  showed earlier excesses above the SM prediction at the few- $\sigma$  level [36–39]; recent measurements and global averages (Belle/Belle II, LHCb, HFLAV) have trended closer to the SM, leaving a remaining combined significance of roughly  $2\text{--}3\sigma$  depending on inputs [40–42]. While current data are largely consistent with the SM, the pattern of earlier deviations motivates searches for flavour-violating interactions beyond the SM gauge structure.

**ANOMALOUS MAGNETIC DIPOLE MOMENT OF THE MUON** The Landé gyromagnetic ratio  $g_\mu$  of the muon is predicted to be exactly 2 by the Dirac equation, but quantum corrections shift it slightly. The anomalous magnetic moment  $a_\mu = (g_\mu - 2)/2$  provides a sensitive probe of virtual contributions from all SM particles and potential new physics. A long-standing discrepancy has existed between the SM prediction and the experimental value measured at Brookhaven (BNL). Fermilab’s 2023 update improved the experimental precision and confirmed the BNL result [43]. The significance of the discrepancy with the SM now depends critically on the hadronic vacuum polarization input: using the 2020 theory white paper gives a  $\sim 4\text{--}5\sigma$  deviation [44], whereas recent lattice-QCD evaluations (e.g. BMW) and new  $e^+e^- \rightarrow \pi^+\pi^-$  data from CMD-3 tend to reduce the tension [36, 45–48]. The persistent tension between experiment and theory-white-paper predictions suggests either missing SM contributions or new weakly-coupled particles contributing to the muon’s quantum corrections.

**NEUTRINO MASSES** Precision oscillation data require non-zero neutrino masses and mixing. Global fits prefer normal ordering, but the mass ordering and the Dirac CP phase remain unestablished; see the latest NuFIT summary [49]. Direct kinematic limits from KATRIN have pushed the effective electron-neutrino mass into the sub-eV regime (about 0.5 eV at 90% CL) [50, 51]. This evidence for neutrino oscillations suggests that the SM must be extended to accommodate neutrino masses [52].

**W-BOSON MASS** The precise CDF II determination,  $m_W = 80433.5 \pm 9.4$  MeV, remains in strong tension with the SM prediction and with other experimental measurements [53]. Recent measurements from ATLAS, CMS (2024), and earlier LEP/LHCb results are all compatible with the SM; see the PDG 2024 summary for a balanced overview [54]. The CDF II result stands as an outlier, and if confirmed by future measurements, would require modifications to electroweak radiative corrections or new particles contributing to the  $W$  mass; otherwise, it likely reflects unaccounted systematic effects in the CDF II analysis.

**CCA AND  $q\bar{q} \mapsto e^+e^-$**  First-row CKM unitarity tests show a mild ( $\sim 2$ – $3\sigma$ ) tension depending on treatment of radiative/nuclear corrections and kaon inputs [54–56]. High-mass Drell–Yan lepton universality measurements at the LHC with Run 2/3 data are generally consistent with the SM within uncertainties. Persistent CKM unitarity violations would signal either incomplete treatment of SM radiative corrections or new physics affecting weak decays.

### 1.3.2 THEORETICAL PROBLEMS

**HIERARCHY PROBLEM** The hierarchy problem concerns the enormous disparity between the electroweak scale ( $v \sim 246$  GeV) and the Planck scale ( $M_{Pl} \sim 10^{19}$  GeV), reflected in the ratio  $G_F/G_N \sim 10^{33}$  between Fermi’s constant (weak force) and Newton’s constant (gravity) [57]. In the SM, the Higgs mass receives quadratically divergent quantum corrections from loops of heavy particles, which would naturally drive it to the highest energy scale at which the theory is valid [58, 59]. Keeping the Higgs mass at its observed value requires an unnatural fine-tuning at the level of one part in  $10^{34}$  [60, 61], suggesting a fundamental problem on the understanding of the electroweak scale. New physics at the TeV scale is required to stabilize the Higgs mass and explain the hierarchy without extreme fine-tuning.

**STRONG CP PROBLEM** The QCD Lagrangian allows a CP-violating term proportional to a dimensionless parameter  $\theta$ . This term would induce a non-zero electric dipole moment (EDM) of the neutron proportional to  $\theta$ . However, experimental measurements constrain  $\theta < 10^{-10}$  [62], implying an unnatural fine-tuning of this parameter to nearly zero

without any known symmetry principle to explain it. Naively, one would expect  $\theta \sim \mathcal{O}(1)$ , yet nature requires it to be smaller than one part in  $10^{10}$ , suggesting the presence of unexplained physics. A dynamical mechanism or new symmetry principle beyond the SM is required to explain why  $\theta$  is so small.

**QUANTUM TRIVIALITY** The SM with an elementary scalar Higgs may not be a consistent quantum field theory at arbitrarily high energies. The Higgs self-coupling  $\lambda$  runs with energy scale according to its renormalization group equation, and for the observed Higgs mass ( $m_H \sim 125$  GeV),  $\lambda$  grows at high energies and eventually diverges at a finite energy scale known as the Landau pole, estimated to be around  $10^{17}\text{--}10^{18}$  GeV [63, 64]. This implies that the SM cannot be extrapolated to arbitrarily high scales as a fundamental theory and must be replaced by new physics or viewed as an effective theory valid only below the Landau pole. Alternatively, if  $\lambda$  is required to remain finite at all scales, it must asymptotically vanish, rendering the Higgs non-interacting (*i.e.*, trivial) at high energies [65]. The SM must either be replaced by a more fundamental theory at high scales or supplemented with new degrees of freedom to regulate the Higgs self-coupling.

**NUMBER OF PARAMETERS AND UNEXPLAINED RELATIONS** There are nineteen free parameters in the SM that must be determined experimentally: nine fermion masses, three gauge couplings, three CKM mixing angles, one CP-violating phase, two Higgs sector parameters, and the QCD  $\theta$  parameter. The theory provides no explanation for the observed values or patterns among these parameters. Intriguingly, several empirical relations suggest hidden structure. For example, the charged-lepton masses satisfy Yoshio Koide's formula [66]

$$\frac{m_e + m_\mu + m_\tau}{(\sqrt{m_e} + \sqrt{m_\mu} + \sqrt{m_\tau})^2} = 0.666661(7) \approx \frac{2}{3}, \quad (1.50)$$

accurate to better than 0.01%, suggesting that this particular choice of flavour structure in the leptons is not accidental. These patterns hint at an underlying flavor symmetry or dynamical mechanism beyond the SM that could reduce the number of free parameters and explain the observed mass spectrum and mixing structure. A more fundamental theory with fewer parameters and predictive power for fermion masses and mixings is needed to replace the SM's arbitrary Yukawa couplings.

### 1.3.3 COSMOLOGICAL PROBLEMS

**GRAVITY AND THE COSMOLOGICAL-CONSTANT PROBLEM** An ultraviolet (UV) complete quantum theory of gravity remains unknown. At low energies, general relativity can be treated as an effective field

theory, but it is non-renormalizable [67, 68]. Moreover, the observed vacuum energy (cosmological constant) driving cosmic acceleration is many orders of magnitude smaller than naive quantum-field-theory estimates, posing a severe naturalness problem [69]. A quantum theory of gravity and a resolution of the cosmological-constant problem require physics beyond the SM and classical general relativity.

**DARK MATTER** Cosmological and astrophysical data require a cold, non-baryonic, component with  $\Omega_c h^2 \simeq 0.12$  [70], consistent with the thermal weakly interacting massive particle (WIMP) production hypothesis [71]. The SM does not have a suitable dark matter particle candidate: active neutrinos are too light and hot, and baryons are limited by Big Bang Nucleosynthesis (BBN) and Cosmic Microwave Background (CMB) observations [54, 70, 72–74]. This points to new degrees of freedom BSM. Dark matter direct-detection experiments continue to improve sensitivity with null results. Recent LZ and XENONnT runs set the strongest spin-independent limits over a wide mass range [75–77]. The SM must be extended with at least one stable, electrically neutral, non-baryonic particle to account for the observed dark matter relic density.

**MATTER–ANTIMATTER ASYMMETRY (BARYON ASYMMETRY)** The Universe exhibits a nonzero baryon asymmetry,  $\eta_B \simeq 6 \times 10^{-10}$  from CMB/BBN [70]. The SM fails quantitatively: for  $m_H = 125$  GeV the electroweak transition is a crossover (no sufficient departure from equilibrium), and CKM CP violation is many orders of magnitude too small to generate the observed asymmetry. Therefore, additional CP violation and/or new dynamics are required, e.g. leptogenesis or electroweak baryogenesis [78–80]. New sources of CP violation and out-of-equilibrium dynamics beyond the SM are necessary to explain the matter–antimatter asymmetry of the Universe.

**DARK ENERGY** Observations of late-time cosmic acceleration require a dark energy component with equation-of-state parameter  $w = p/\rho \approx -1$  [81], consistent with a cosmological constant ( $w = -1$  exactly). This implies negative pressure driving accelerated expansion. The observed vacuum energy density is  $\rho_\Lambda \sim (10^{-3} \text{ eV})^4$ , yet naive quantum-field-theory estimates based on summing zero-point energies up to the Planck scale yield  $\rho_{\text{QFT}} \sim M_{\text{Pl}}^4$ , a discrepancy of approximately  $10^{120}$  orders of magnitude—the worst fine-tuning problem in physics [69]. Even using the electroweak scale as a cut-off still leaves a gap of  $\sim 10^{56}$ . The  $H_0$  tension persists and could reflect systematics or new physics. A fundamental understanding of vacuum energy and its contribution to cosmic acceleration demands new physics that can naturally suppress or cancel the cosmological constant.

Among the challenges outlined above, the anomalies observed in the lepton sector stand out as particularly compelling hints of BSM physics. These observations share a common thread: they suggest that the SM’s assumption of lepton universality may be an approximate symmetry rather than a fundamental one, potentially violated. Understanding whether these tensions represent genuine new physics or subtle theoretical/experimental effects requires a detailed examination of lepton universality tests and the theoretical frameworks that could accommodate violations of this fundamental SM principle.

In the following section, we examine in detail the concept of lepton flavour universality, its experimental tests across various processes, and the theoretical implications of potential violations. This analysis will establish the foundation for understanding how new particles with non-universal lepton couplings could simultaneously address multiple anomalies while remaining consistent with the wealth of precision measurements that confirm the SM.

#### 1.4 LEPTON UNIVERSALITY: TESTS AND ANOMALIES

---

As established previously, gauge interactions of charged leptons are flavour-universal [22, 27, 28] in the SM: the  $SU(2)_L \times U(1)_Y$  couplings are generation-independent [27, 28], meaning that after accounting for kinematic and mass effects, processes mediated by electroweak interactions predict identical couplings to electrons, muons, and tau leptons [22]. While small deviations can arise from well-understood mass-dependent, phase-space, and radiative corrections [22], genuine Lepton Universality Violation (LUV) would constitute evidence of new physics beyond the Standard Model [33, 34, 82].

Lepton Universality Violation (LUV) differs from Lepton Flavour Violation (LFV). LFV refers to processes where the initial-state lepton flavour quantum number does not match the final state—analogous to charge conservation but for lepton flavour. Neutrino oscillations already demonstrate LFV in the neutral sector [83, 84], constituting evidence of BSM physics. Charged-lepton flavour violation (cLFV), such as  $\mu \rightarrow e\gamma$  or  $\tau \rightarrow \mu\gamma$ , remains unobserved and is highly suppressed in the SM even with massive neutrinos [22]. In contrast, LUV concerns whether the gauge couplings themselves differ across lepton generations—a violation of the SM’s generation-independent coupling structure. One can have cLFV without LUV (e.g., through neutrino mixing alone), and conversely, LUV does not necessarily imply large cLFV rates. This section focuses specifically on LU tests and their current experimental status [22, 85].

Experimental programs probe LU across various processes [22]:

- **Rare B decays** ( $b \rightarrow sl^+l^-$ ): Ratios  $R_K$  and  $R_{K^*}$  comparing muon to electron modes [47, 48, 82, 86–89].
- **Charged-current B decays** ( $b \rightarrow cl\nu$ ): Ratios  $R_D$  and  $R_{D^*}$  comparing  $\tau$  to light leptons [36–39, 42, 90, 91].

- **Light-meson decays:** Leptonic ( $\pi, K \rightarrow \ell\nu$ ) and semileptonic ( $K_{\ell 3}$ ) universality tests [22, 92].
- **Electroweak boson decays:**  $W \rightarrow \ell\nu$  and  $Z \rightarrow \ell^+\ell^-$  universality [93, 94].
- **$\tau$  decays:** Tests of  $e/\mu/\tau$  universality in leptonic and semileptonic channels [22, 39].

Combinations of these measurements provide constraints on flavour dependent interactions beyond the SM [22].

Most LU tests involving light mesons,  $W/Z$  bosons, and  $\tau$  decays show agreement with SM predictions at the percent level [22]. Initially significant tensions emerged in semileptonic  $B$  decays [34, 82, 95–97], particularly in the neutral-current ratios  $R_K$  and  $R_{K^*}$  [47, 48, 86, 87, 98] and the charged-current ratios  $R_D$  and  $R_{D^*}$  [36–39, 42, 90, 91, 99–105] (discussed in detail in the following subsection). These measurements generated theoretical interest, with proposals for new physics scenarios that could explain potential deviations from SM predictions [33, 106–108]. Recent re-analyses have brought  $R_{K^{(*)}}$  measurements closer to SM predictions [85, 88, 89, 109], while the situation for  $R_{D^{(*)}}$  remains under investigation [39], with forthcoming data expected to provide insights [110]. These results motivate the study of scenarios where new particles might have preferential couplings to third-generation fermions [111–114].

Various theoretical frameworks can accommodate LUV, including extended gauge sectors with non-universal couplings and models where new particles couple to SM fermions through Yukawa-like interactions with generation-dependent hierarchies [111, 115, 116]. These models typically predict correlated signals across multiple precision observables [85, 109, 117]. Depending on their flavour structure—whether arising from non-universal gauge couplings or from fermion mixing patterns after spontaneous symmetry breaking—such models may also induce cLFV processes at potentially observable levels, subject to constraints from existing experimental limits [106, 118]. LUV and cLFV are distinct phenomena: models with universal gauge couplings before symmetry breaking can still exhibit effective non-universality and flavour violation in the mass basis through fermion mixing, analogous to how CKM mixing generates quark flavour violation despite universal  $SU(2)_L$  couplings in the SM.

These precision observables motivate direct searches for new physics at colliders [119, 120]. While deviations from LU in light-meson,  $\tau$ , and electroweak boson decays remain consistent with SM expectations [22, 94], the anomalies observed in  $B$  decays point to scenarios where new states may couple non-universally to leptons [34]. Other tensions in the leptonic sector, such as the muon ( $g - 2$ ) anomaly [3, 121, 122], provide motivation for exploring such scenarios, though their experimental status remains under investigation.

New particles may exhibit enhanced couplings to third-generation fermions [111, 123]. This scenario has several motivations. First, the pattern

of anomalies—particularly in  $b \rightarrow c\tau\nu$  transitions—directly involves the heaviest fermion generation. Second, such flavour structures are less constrained by precision measurements involving first- and second-generation fermions: processes like K and D meson decays, electroweak precision tests at LEP, and rare decays involving electrons and muons impose bounds on new physics that couples democratically to all generations [22, 94]. By concentrating new-physics effects in the third generation, these models can remain consistent with existing limits while providing signatures in B physics and processes involving top quarks, bottom quarks, and tau leptons [114, 116]. Third, generation-dependent couplings can arise in models with flavour symmetries or in scenarios where the Yukawa hierarchy of the SM is reflected in the couplings of new particles [111, 123].

Therefore, searches for new particles with preferential couplings to the third generation are a component of the BSM search strategy [119, 120]. However, the experimental signatures of such models are often complex and challenging to separate from SM backgrounds. Given the range of theoretical possibilities and the finite resources of experimental collaborations, it is useful to perform phenomenological feasibility studies before undertaking full experimental searches [124, 125]. These studies bridge the gap between theoretical model-building and experimental implementation: by simulating signal and background processes, evaluating detector effects, and optimizing analysis strategies, phenomenological studies can identify promising signatures, estimate discovery potential or exclusion reach with available data, and guide the experimental program [126]. Such studies also allow for exploration of model parameter space, identifying regions where experimental constraints are less stringent and where new searches could have sensitivity [33].

# 2

---

## PHENOMENOLOGICAL FRAMEWORK FOR LHC SEARCHES

---

Since its formulation, the SM has proven remarkably successful in describing the fundamental particles and interactions, and its parameters have been measured with increasing precision over several decades [22, 28]. However, as discussed in the previous chapter, various theoretical and experimental observations suggest that the SM is incomplete [32, 33]. As outlined previously, this is motivated by theoretical shortcomings such as the hierarchy problem [58, 59], the absence of a dark matter candidate [71], and non-zero neutrino masses [52], as well as by experimental anomalies [36, 47, 48]. These limitations motivate searches for physics beyond the SM [33, 34].

The search for BSM physics proceeds along two main axes: the construction of theoretical extensions to the SM [33, 34, 59], and the development of experimental methods to probe them [127–129]. A necessary condition for any viable BSM model is consistency with existing experimental data, which places strong constraints on its parameter space [22, 130, 131]. These constraints include lower limits on the masses of new particles from direct searches at high-energy colliders [130, 131], and upper bounds on couplings and mixing angles from precision measurements at both high and low energies [98, 132], which are sensitive to virtual corrections [85].

The area of particle physics phenomenology, connects theoretical models to experimental observables by calculating cross sections, decay rates, and other signatures for given model parameters [127, 133, 134]. A critical function of this field is to assess the experimental feasibility of BSM scenarios—evaluating whether predicted signals would be observable above background processes given the capabilities of current and future experiments [127–129]. This involves estimating production rates [127, 133, 135], modeling detector acceptance and efficiency [129, 136–138], and developing discrimination variables to maximize the likelihood of observing new signals above known SM backgrounds [139–142]. This feasibility assessment is essential for designing analysis strategies, particularly at LHC, where signals of new physics must be discriminated from large SM backgrounds [127, 129, 136, 137, 143].

The LHC has provided data at center-of-mass energies from 7 TeV to 13.6 TeV [131, 138]. During Run I (2010–2013), operations at 7–8 TeV led to the discovery of the Higgs boson using a dataset corresponding to an integrated luminosity of roughly  $30 \text{ fb}^{-1}$  [144, 145]. Run II (2015–2018)

significantly expanded this dataset, collecting approximately  $140 \text{ fb}^{-1}$  at 13 TeV [131, 138]. Run III (2022–2025) is currently underway at 13.6 TeV and its target is to collect over  $300 \text{ fb}^{-1}$  [138]. Future operations will be dominated by the High-Luminosity LHC (HL-LHC), starting around 2029, which is designed to accumulate an unprecedented integrated luminosity of  $3000 \text{ fb}^{-1}$  [146, 147]. This vast increase in data volume enables searches for exceedingly rare processes but also requires discriminating potential signals of new physics from correspondingly large and complex SM backgrounds, making sophisticated phenomenological tools increasingly important [127, 129].

This chapter establishes the phenomenological framework for LHC searches. Section 2.1 describes the detector architecture and particle reconstruction at multipurpose experiments, introducing the kinematic variables used in collider analyses. Section 2.2 covers jet reconstruction algorithms and specialized tagging techniques for  $\tau$ -jets and  $b$ -jets. Section 2.4 presents the Monte Carlo simulation pipeline connecting theoretical models to experimental observables. Section 2.5 develops the statistical framework for quantifying analysis sensitivity through likelihood-based hypothesis testing. Finally, Section 2.6 introduces machine learning methods for signal-background discrimination using multivariate classifiers.

## 2.1 DETECTORS AND SUBSYSTEMS

---

When two particle bunches from colliding beams cross each other, they generate individual interactions known as events [136, 137]. At the LHC, the beam intensity is so high that multiple interactions can take place in a single event; this phenomenon is referred to as in-time pile-up [147, 148]. In other words, the probability that several proton-proton interactions occur within the same bunch crossing is non-negligible, leading to multiple overlapping events in a single detector readout [134, 149]. In addition, particles from other bunch crossings with respect to the primary collision of interest can be detected. This latter experimental feature is known as out-of-time pile-up. The sum of these two effects, in-time and out-of-time pile-up, is commonly referred to as PU.

The particle collisions at the LHC, pp and heavy-ions, occur at four main interaction points, each hosting a large particle detector designed to record and analyze the outcomes [136, 137]. The two largest and most comprehensive experiments [136, 137] are the Compact Muon Solenoid (CMS) and A Toroidal LHC ApparatuS (ATLAS). Both are multipurpose detectors with broad physics programs, capable of exploring a wide range of phenomena [136, 137]. They perform precision measurements within the electroweak sector of the SM [22], probe the dynamics of quarks and gluons (including through heavy-ion collisions) [129], and conduct extensive searches for BSM physics using pp collision data [144, 145]. While CMS and ATLAS differ in their detector designs and reconstruction strategies,

their physics goals are largely overlapping, and their results are complementary [136, 137].

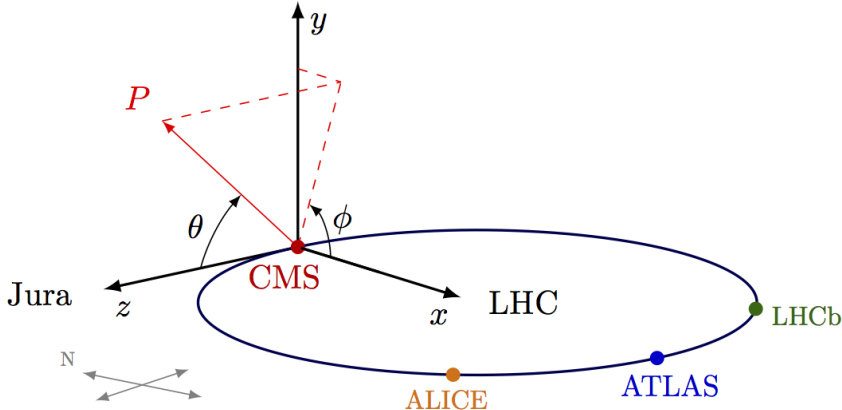


**Figure 2.1:** Coordinate system employed by the CMS experiment (retrieved from [150]).

Throughout this work, phenomenological studies and comparisons are primarily developed in the context of CMS, although several results from ATLAS are also referenced, given the close alignment in sensitivity and scope [136, 137]. Measurements performed at CMS adopt a right-handed coordinate system with its origin at the nominal collision point [137]. The z-axis is defined along the beam direction, the x-axis points radially inward toward the center of the LHC ring, and the y-axis points vertically upward [137]. The azimuthal angle  $\phi$  is measured in the transverse (xy) plane from the x-axis, while the polar angle  $\theta$  is measured from the z-axis, as shown in Fig. 2.1 [137]. Moreover, for kinematic analysis at hadron colliders, the Cartesian coordinate system is often reparameterized into quantities that are more physically meaningful and experimentally convenient as shown in Fig. 2.2 [151]:

**PSEUDO-RAPIDITY ( $\eta$ )** The polar angle is not a Lorentz invariant quantity. In addition, since the vast majority of particles are detected in the forward region of the detector, known as the endcap region, the distribution of the particle multiplicity as a function of  $\theta$  is not uniform. This non-uniformity makes it difficult to study the agreement between the observed data and the background prediction in the central part of the detector. Therefore, the CMS experiment uses a variable known as pseudo-rapidity [22, 137],  $\eta$ , defined in terms of the polar angle as:

$$\eta = -\ln \left( \tan \frac{\theta}{2} \right). \quad (2.1)$$

Therefore, the main advantages of using  $\eta$  instead of  $\theta$  are that it provides more uniform distributions than those over the polar angle [151]. And, furthermore, the difference in  $\eta$  is a Lorentz boosts invariant quantity, along the beam direction [22].

**TRANSVERSE MOMENTUM ( $p_T$ )** It refers to the component of momentum which is perpendicular to the beam line [151]. This quantity is preferred over the total momentum because the longitudinal momentum component (along the beam axis) is dominated by the remnants of the colliding protons, which carry unknown momentum fractions. In contrast, the transverse momentum is directly associated with the hard scattering process at the interaction vertex, making it a more robust observable for characterizing the collision dynamics [151].

**AZIMUTHAL ANGLE ( $\phi$ )** it measures the angle in the transverse plane relative to the  $x$ -axis, providing the directional component perpendicular to the beam line [137].

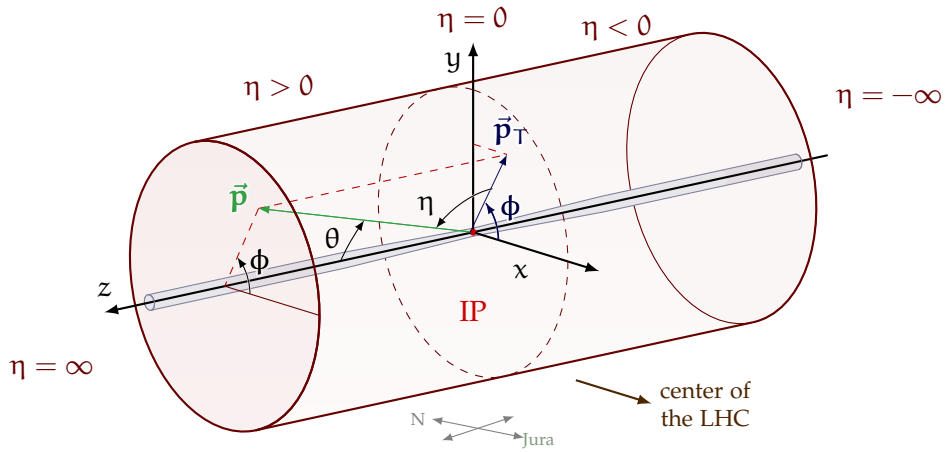


**Figure 2.2:** Detailed reparametrization of the coordinate system employed by the CMS experiment (retrieved from [150]).

Together, the triplet  $(p_T, \phi, \eta)$  forms a natural coordinate system that fully describes a particle's three-momentum vector at a hadron collider [22, 151]. The full four-momentum  $(E, p_x, p_y, p_z)$  can be reconstructed from these quantities, typically supplemented by either the particle's mass hypothesis (for identified particles like electrons or muons) or the energy deposited in the calorimeters (for neutral objects like photons or jets) [134, 152, 153]. This  $(p_T, \phi, \eta)$  system serves as the fundamental framework for defining physical objects, calculating event variables, and performing analyses at the LHC, providing both experimental convenience and physical insight into the collision dynamics [134, 151].

A key challenge is isolating the primary hard interaction from the additional concurrent PU interactions [147, 148]. This is accomplished by reconstructing distinct interaction vertices along the beam direction and associating charged particles to their point of origin using the CMS tracking and vertexing algorithms [151, 155]. The ultimate aim of the reconstruction chain is to identify all stable particles produced in the collision and measure their four-momenta, thereby enabling the identification of the underlying fundamental process [151].

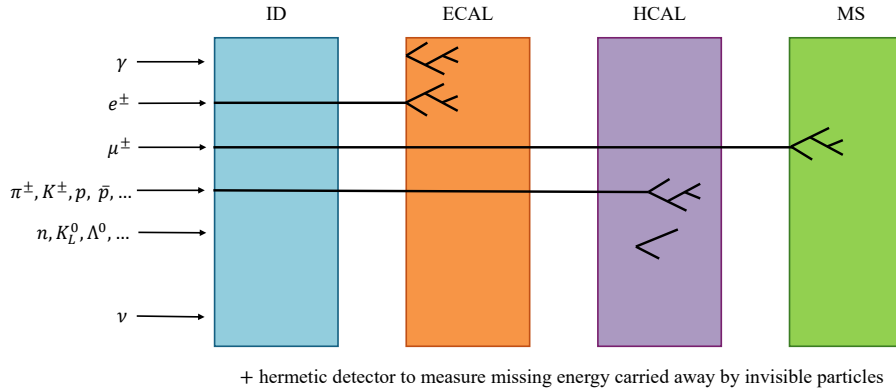


**Figure 2.3:** Illustration of high-energy particles being identified by consecutive types of subdetectors in a typical collider experiment. The curvature of the tracks in the magnetic field is not shown for simplicity. Representation of which particles and kinds of detectors are used in a multipurpose detector such as CMS or ATLAS. (retrieved from [154])

However, the reconstruction is complicated by several factors [137, 151]. The initial state of the colliding protons is not fully known, as they are composite particles made up of quarks and gluons (collectively referred to as partons) [135, 156]. The fraction of the proton's momentum carried by each parton is described by parton distribution functions (PDFs), which are determined experimentally. Among the available groups of PDFs, LHC analyses using Run II/III data have mainly implemented the PDF4LHC [135, 157] set. As a result, the longitudinal momentum is not constrained on an event-by-event basis, and it is not possible to reconstruct the four-momentum of the colliding protons [156]. Furthermore, not all particles are stable enough to reach the detector; some decay before being detected, and only their decay products are observed [22]. The design of a collider experiment, illustrated in Fig. 2.3, is optimized for the identification and energy measurement of the particles produced in high-energy collisions [129, 137]. Using the information from the different particle sub-detectors, it is possible to differentiate signatures from various particle types. This information is utilized by software algorithms, optimized for particle reconstruction and identification, to calculate the likelihood that a detector signature was created by a specific type of particle.

Finally, some hypothetical particles, such as those comprising dark matter, along with known neutrinos, interact very weakly with matter and escape direct detection [22, 71]. Therefore, a hermetic detector design is crucial to infer their presence by accurately measuring the imbalance of energy and momentum in the transverse plane, referred to as missing transverse momentum [151, 158].

In this way, a typical collider experiment comprises several main detector subsystems that are used jointly to detect and measure the properties of particles produced in the collision [129, 136, 137, 151]. A *schematic repre-*

sentation of such a generic multipurpose detector is shown in Fig. 2.4 [129, 137, 159]. The detector features an "onion-like" design of several concentric layers, each optimized to identify different types of particles and measure their properties [137, 151].

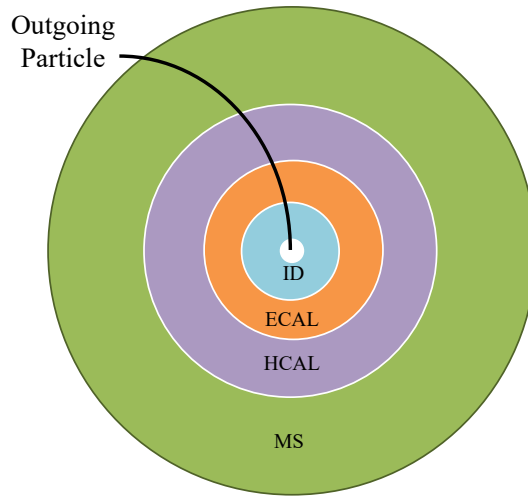


**Figure 2.4:** Schematic representation of a transverse section of a generic multipurpose detector. The innermost subsystem, the inner detector (ID) or tracker, is immersed in a strong axial magnetic field (typically 1–4 T) [137, 155]. It is designed to reconstruct the trajectories of charged particles, which are bent by the magnetic field [151, 155]. The direction and curvature of these trajectories, called **tracks**, allows to estimate the particle's momentum vector and electric charge [22, 155]. The most common long-lived charged particles from the SM are the so called light leptons (electrons  $e^-$  and muons  $\mu^-$ ) and hadrons (pions  $\pi^\pm$ , kaons  $K^\pm$ , and protons  $p^\pm$ ) [22]. In some detectors, the ID is complemented by a Cherenkov light detector (RICH) to measure particle velocity and aid particle identification [22, 160]. Combined with the momentum measurement, this velocity helps determine the particle mass, allowing for differentiation between pions, kaons, and protons [22, 159, 160].

The innermost subsystem, the inner detector (ID) or tracker, is immersed in a strong axial magnetic field (typically 1–4 T) [137, 155]. It is designed to reconstruct the trajectories of charged particles, which are bent by the magnetic field [151, 155]. The direction and curvature of these trajectories, called **tracks**, allows to estimate the particle's momentum vector and electric charge [22, 155]. The most common long-lived charged particles from the SM are the so called light leptons (electrons  $e^-$  and muons  $\mu^-$ ) and hadrons (pions  $\pi^\pm$ , kaons  $K^\pm$ , and protons  $p^\pm$ ) [22]. In some detectors, the ID is complemented by a Cherenkov light detector (RICH) to measure particle velocity and aid particle identification [22, 160]. Combined with the momentum measurement, this velocity helps determine the particle mass, allowing for differentiation between pions, kaons, and protons [22, 159, 160].

After the tracker, particles enter the electromagnetic calorimeter (ECAL), which is designed to fully absorb photons, electrons, and positrons [137, 152]. These particles deposit all their energy in the ECAL by initiating an electromagnetic shower via bremsstrahlung and  $e^+e^-$  pair production [152].

Electrons are identified as charged tracks that point to a compact, high-energy deposit in the ECAL [152, 159].

The hadronic calorimeter (HCAL) surrounds the ECAL and is built to absorb hadrons and measure their energy through hadronic interactions [129, 137]. High-energy quarks and gluons hadronize into collimated sprays of hadrons known as **jets**. The energy of jets is measured by combining calorimeter deposits with track momenta. The reconstruction of particles using the information of the different detector subsystems is formalized in particle-flow reconstruction [134, 149, 151, 159].

Muons are unique as they can penetrate the calorimeters; a dedicated muon system outside the calorimeters identifies and measures muons, and muon tracks in the ID are matched to tracks in the muon chambers [137, 153, 159].

Since the detector is nearly hermetic (covering almost the full solid angle), momentum conservation in the plane transverse to the beam line ( $x$ - $y$  plane) is a powerful tool. The vector sum of the momenta in the transverse plane ( $\vec{p}_T$ ) of all detected particles should be zero. Any significant imbalance indicates the presence of undetected neutral particles that did not interact with the detector, such as neutrinos or new hypothetical dark matter particles. This imbalance is referred to as missing transverse momentum ( $\vec{p}_T^{\text{miss}}$ ) and is formally defined as:

$$\vec{p}_T^{\text{miss}} \equiv - \sum_i \vec{p}_{T,i}, \quad (2.2)$$

where the sum runs over all reconstructed particles (e.g., leptons, photons, jets) or calorimeter deposits in the event.

The detector design, optimized for identifying and measuring SM particles, also makes it a powerful instrument to search for BSM physics.

### 2.1.1 COLLISION PARAMETERS

One of the main objectives of particle physics experiments is to quantify how frequently different processes occur and to characterize the properties of the particles involved. The expected rate of a given process, either from the SM or from new physics, is quantified using production **cross-sections**, a theoretical estimate, and the **luminosity**, a parameter that accounts for the amount of data delivered by the accelerator.

In essence, the cross-section ( $\sigma$ ) quantifies the probability for a specific process to occur. Formally, it represents the effective area of a target particle presented to an incoming beam particle for an interaction to happen. It has units of area, typically barn (b), where  $1 \text{ b} = 10^{-28} \text{ m}^2$ .

In the context of pp collisions at the LHC, the concept is generalized. Since both colliding particles are composite, the cross-section for a specific process is calculated by considering the interactions between their constituent partons (quarks and gluons). The total cross-section for a pro-

cess  $pp \rightarrow X$  is given by the convolution of the PDFs and the partonic cross-section  $\hat{\sigma}_{ij \rightarrow X}$  [154, Eq. 19.45]:

$$\sigma(pp \rightarrow X) = \sum_{i,j} \int_0^1 \int_0^1 dx_1 dx_2 f_i(x_1, \mu_F^2) f_j(x_2, \mu_F^2) \hat{\sigma}_{ij \rightarrow X}(\hat{s}, \mu_F^2, \mu_R^2), \quad (2.3)$$

The scales  $\mu_F$  and  $\mu_R$  are unphysical parameters introduced in perturbative calculations (typically QCD calculations). In an exact calculation to all orders, physical observables would be independent of these scales. However, at finite perturbative order (NLO, NNLO, etc.), a residual scale dependence remains, proportional to the next uncalculated order in  $g_s$ . This dependence is used to estimate theoretical uncertainties by varying  $\mu_R, \mu_F \in [Q/2, 2Q]$  with  $1/2 \leq \mu_R/\mu_F \leq 2$ , where  $Q$  is the characteristic hard scale of the process.

where:

- the sum runs over all possible parton types  $i, j$  (e.g.,  $u, d, g$ ) in the two protons.
- $f_i(x, \mu_F^2)$  is the PDF, representing the probability density to find a parton of type  $i$  carrying a fraction  $x$  of the proton's momentum at a factorization scale  $\mu_F$ .
- $\hat{s} = x_1 x_2 s$  is the square of the center-of-mass energy for the colliding partons, with  $s$  being the square of the  $pp$  center-of-mass energy (e.g., 13.6 TeV).
- $\hat{\sigma}_{ij \rightarrow X}$  is the partonic cross-section for the hard scattering process  $ij \rightarrow X$  at factorization scale  $\mu_F$  and renormalization scale  $\mu_R$ .

Then, on one side, the cross-section  $\sigma$  is a theoretical quantity that encapsulates the fundamental physics of the interaction, independent of the accelerator's performance. On the other side, the **luminosity** ( $\mathcal{L}$ ) is a property of the particle accelerator and beams. It measures the density of particles in the colliding beams and thus the rate at which interactions can occur. The instantaneous luminosity is defined by:

$$\mathcal{L} = \frac{\mathcal{F} n_1 n_2}{4\pi \sigma_x \sigma_y}, \quad (2.4)$$

where  $\mathcal{F}$  is the revolution frequency of the bunches,  $n_1$  and  $n_2$  are the numbers of particles in each bunch, and  $\sigma_x$  and  $\sigma_y$  are the transverse dimensions of the beams at the interaction point. The integrated luminosity is the integral of the instantaneous luminosity over time:

$$L = \int \mathcal{L} dt. \quad (2.5)$$

The primary unit of integrated luminosity is the inverse barn ( $b^{-1}$ ), commonly  $fb^{-1}$ .

Theoretically, the expected number of events of a SM or BSM process is estimated as

$$N_{\text{theory}} = \sigma \cdot L. \quad (2.6)$$

Under the context of a collider experiment one has to include the detector acceptance and efficiency of the particle identification and selection criteria used to discriminate the signal of interest among other processes. The variable  $\epsilon$  is defined as the product of the acceptance ( $\mathcal{A}$ ) and the

cumulative efficiency of all the selection criteria used to estimate the signal rate above the backgrounds:

$$\epsilon = \left( \prod_i \epsilon_i \right) \times \mathcal{A}. \quad (2.7)$$

Therefore, the expected number of events of a process of interest, for either a SM or BSM process, is estimated using the following equation [129, 151]:

$$N = \sigma \cdot L \cdot \epsilon. \quad (2.8)$$

Equation 2.8 allows one to estimate the expected number of observed events, accounting for reconstruction, particle identification, detector resolution, and acceptance effects, among other experimental considerations [151].

Note that the integrated luminosity  $L$  is a parameter that can be measured from the accelerator's performance [138], while  $\epsilon$  can be estimated using information from the detector calibration and simulation (including event generation, parton shower, and detector simulation) [127, 129, 133]. For a known process, if we know the expected number of events, we can use Equation 2.8 and solve for  $\sigma$  to extract a measurement of the production rate, through a statistical interpretation based on likelihood methods [126].

In the case of searches for BSM physics, we calculate the expected background  $N_{\text{bkg}}$  from known SM processes using Monte Carlo and data-driven techniques [127, 134]. Then, one studies the agreement in the event rates and shapes of various kinematic and topological distributions of interest, between the observed number of events in data ( $N_{\text{obs}}$ ) and the expected backgrounds from SM processes. Any significant deviation in a specific region in one of the relevant observables, for example in a reconstructed mass,  $N_{\text{obs}} - N_{\text{bkg}}$ , can be interpreted as a potential signal. Then, the significance of such difference—both local and global—can be determined using a profile-binned likelihood test, to determine the probability that a signal process of interest explains, within the associated statistical and systematic uncertainties, the discrepancy between data and the background [161–164].

## 2.2 JETS RECONSTRUCTION

---

Quarks and gluons are never observed as free particles because of colour confinement [165, 166]. Nevertheless, perturbative QCD treats them as the relevant short-distance degrees of freedom: factorization theorems and asymptotic freedom justify computing hard-scattering matrix elements for incoming and outgoing partons, even though QCD becomes non-perturbative at low scales [156]. The strong coupling  $\alpha_s$  grows large and effectively “blows up” around the confinement scale  $\Lambda_{\text{QCD}}$  [22]. Consequently, quarks and gluons cannot remain as free particles at low momentum scales and must hadronize [133]. In practice, gluons and quarks, except

for the top, hadronize producing cascades of baryons and mesons that themselves undergo further decays. Hadronization is modeled e.g. with the Lund string or cluster models [133, 165, 166]. At the LHC, these hadrons typically carry energies comparable to the electroweak scale, and relativistic boosts tend to collimate their decay products into narrow bunches [167]. Those collimated collections of hadrons are the jets we measure at hadron colliders and the objects we use to infer the partons produced in the hard interaction [149, 167].

Each high-energy parton produced in a collision, such as a quark from the process  $gg \rightarrow q\bar{q}$ , undergoes hadronization over a distance scale of  $\sim 10^{-15}$  m, producing a jet of hadrons [133, 165]. The energy composition of these jets is phenomenologically well established and is the basis of particle-flow (PF) reconstruction [151]: a technique that combines information from the tracker and calorimeters to identify and reconstruct individual particles (charged hadrons, photons, neutral hadrons, electrons, muons). On average roughly  $\sim 60\%$  of the jet energy is carried by charged particles (mostly  $\pi^\pm, K^\pm$ ),  $\sim 30\%$  by photons (from  $\pi^0 \rightarrow \gamma\gamma$ ) and  $\sim 10\%$  by neutral hadrons [151]. In high-energy jets, the particles can be too collimated to be resolved individually in coarse calorimeter segmentation. Nevertheless, the jet four-momentum is reconstructed from clustered particle-flow candidates (PF candidates) or calorimeter deposits and then corrected using jet energy corrections derived from simulation and in-situ data [129, 134, 151].

Phenomenologically one usually assumes that each high-energy parton yields a jet and that the measured jet four-momentum can, to useful accuracy, be related to the original parton four-momentum [168, 169]. Jets are therefore defined operationally using recombination (clustering) algorithms such as Cambridge–Aachen [170] or the (anti-)k<sub>T</sub> family [149]. Experimentally this means grouping a large number of energy depositions (or particle-flow candidates) observed in the calorimeters and tracker into a much smaller set of jets or sub-jets [151]. Nothing in the raw detector data, however, indicates a priori how many jets there should be: the clustering procedure and the choice of a resolution scale fix the outcome [167]. In practice one must either specify the desired number of final jets or choose a resolution/stop criterion (for example a distance parameter R, a clustering distance cut, or a jet-mass/sub-jet-resolution threshold) that determines the smallest substructure to be considered a separate parton-like object [171].

Modern reconstruction techniques at the LHC typically use PF candidates as input together with infrared- and collinear-safe clustering algorithms to define jet four-momenta [134, 151]. The anti-k<sub>T</sub> algorithm [149], implemented in FastJet [134], is widely used in ATLAS and CMS; it groups candidates by proximity in the rapidity–azimuth ( $y, \phi$ ) plane with a typical distance parameter  $R \sim 0.4\text{--}0.6$  and is relatively insensitive to soft radiation and pileup when combined with area-based subtraction techniques [172]. After clustering, jet energy corrections (JEC) derived from simulation and in-situ calibrations compensate for detector response, pileup, and underlying-event effects [173], while jet-substructure and tagging algo-

rithms help infer the flavour and origin of the initiating parton [171, 174, 175].

### 2.2.1 JET ALGORITHMS

Recombination (or sequential clustering) algorithms formalise the intuitive idea that parton showering produces collinear and soft splittings [167, 168, 170]: two nearby and kinematically compatible sub-jets are merged if they are more likely to have originated from a single parton [168, 170]. A practical implementation requires a measure of “distance” between objects [134, 168]; common choices combine an angular separation in the rapidity–azimuth plane,  $\Delta R_{ij}$ , with a transverse-momentum weighting [149, 168]. Typical distance measures are [149, 168, 170], where  $y_{ij}$  denotes the distance between two objects  $i$  and  $j$ , and  $y_{iB}$  denotes the distance between object  $i$  and the beam:

$$\begin{aligned} k_T : \quad y_{ij} &= \frac{\Delta R_{ij}}{R} \min(p_{T,i}, p_{T,j}), \quad y_{iB} = p_{T,i}, \\ C/A : \quad y_{ij} &= \frac{\Delta R_{ij}}{R}, \quad y_{iB} = 1, \\ \text{anti-}k_T : \quad y_{ij} &= \frac{\Delta R_{ij}}{R} \min(p_{T,i}^{-1}, p_{T,j}^{-1}), \quad y_{iB} = p_{T,i}^{-1}. \end{aligned} \quad (2.9)$$

The parameter  $R$  balances jet–jet and jet–beam criteria and sets the geometric size of jets. In LHC analyses, typical values are  $R \sim 0.4\text{--}0.7$  depending on the physics target [134].

Two operational modes are useful to distinguish. In an exclusive algorithm, one supplies a resolution scale  $y_{cut}$  and proceeds iteratively:

1. compute  $y^{\min} = \min_{i,j}\{y_{ij}, y_{iB}\}$ ;
2. if  $y^{\min} = y_{ij} < y_{cut}$  merge  $i$  and  $j$  and repeat;
3. if  $y^{\min} = y_{iB} < y_{cut}$  remove  $i$  as beam radiation and repeat;
4. stop when  $y^{\min} > y_{cut}$  and keep remaining sub-jets as jets.

An inclusive algorithm omits  $y_{cut}$  and instead declares a sub-jet a final-state jet when its jet–beam distance is the smallest quantity; iteration continues until no inputs remain. Inclusive algorithms therefore produce a variable number of jets, while exclusive algorithms deliver a scale-dependent fixed set.

A practical question is how to combine the kinematics of merged objects. The most common choice in modern experiments is the E-scheme: four-vectors are added, which preserves energy–momentum and yields a physical jet mass useful for substructure and boosted-object tagging. An alternative is to sum three-momenta and rescale the energy to enforce a massless jet. This might be appropriate when the analysis targets massless parton kinematics, but it discards potentially useful jet-mass information.

From a theoretical and experimental perspectives, the infrared and collinear safety considerations are important properties: a jet algorithm should yield stable results under the emission of soft particles or collinear splittings. The  $k_T$ , C/A, and anti- $k_T$  families are constructed to satisfy these requirements. For practical use, these algorithms have the following particular properties: the  $k_T$  technique naturally follows the physical shower history through soft-first clustering, while the C/A has a purely geometric approach, useful for declustering and substructure studies, and lastly the anti- $k_T$  approach produces regular cone-like jets that are experimentally robust and convenient.

Corrections for PU and underlying events are necessary at the LHC. These corrections depend on the jet area and are typically performed by estimating an event-wide transverse-momentum density and subtracting the corresponding contribution proportional to the jet area. Finally, because inclusive algorithms can produce jets arbitrarily close to the beam, a minimum jet  $p_T$  threshold, commonly ranging between 20–100 GeV, depending on the analysis, is imposed to ensure experimental observability and theoretical control.

### 2.2.2 $\tau$ TAGGING AT MULTIPURPOSE DETECTORS

The  $\tau$  lepton decays hadronically with a probability of  $\sim 65\%$ , producing a narrow “ $\tau$ -jet” that contains only a few charged and neutral hadrons [22, 176]. Hadronic  $\tau$  decays are dominated by one- and three-prong topologies and often include neutral pions that promptly decay to photon pairs, giving a sizable electromagnetic fraction in the calorimeters [22, 177]. When the  $\tau$  momentum is large compared to its mass, the decay products are highly collimated [142, 176]: for  $p_T > 50$  GeV roughly 90% of the visible energy is contained within a cone of radius  $R = \sqrt{(\Delta\eta)^2 + (\Delta\varphi)^2} = 0.2$  [176]. These properties motivate the use of small signal cones and narrow isolation annuli in reconstruction [142, 176].

Identification algorithms exploit three complementary classes of observables [142, 151, 176, 177]:

- Calorimetric isolation and shower-shape variables [176, 177]: hadronic  $\tau$  decays are characterized for localized energy deposits (showers) in the calorimetry system (in the ECAL+HCAL subdetectors) [176]. Experiments use isolation sums and shape ratios to quantify peripheral activity [176, 177]. Example variables are

$$\Delta E_T^{12} = \frac{\sum_{0.1 < \Delta R < 0.2} E_{T,j}}{\sum_{\Delta R < 0.4} E_{T,i}}, \quad P_{ISOL} = \sum_{\Delta R < 0.40} E_T - \sum_{\Delta R < 0.13} E_T, \quad (2.10)$$

In these examples, the lower  $\Delta R$  cut (e.g.  $\Delta R > 0.1$  or the subtraction of the  $\Delta R < 0.13$  cone) excludes the signal region containing the collimated  $\tau$  decay products themselves, ensuring that isolation variables measure only peripheral activity rather than the genuine

$\tau$  energy. This design maximizes discrimination against QCD jets, which exhibit broader energy distributions that extend into the isolation annulus [176].

- Charged-track isolation and prong topology [151, 176]: the few, collimated charged tracks of a  $\tau$  jet candidate allow powerful selections. A common procedure defines a matching cone of radius  $R_m$  around the calorimeter jet axis to select candidate tracks above a  $p_T^{\min}$  threshold. The leading track ( $tr_1$ ) defines a narrow signal cone  $R_S$  (1- or 3-prong hypotheses) and a larger isolation cone  $R_I$  is scanned for additional tracks [151, 176]. The scalar sum of the  $p_T$  of all tracks between the  $tr_1$  cone and the isolation cone, is expected to be small compared to the  $p_T$  of the leading track.
- Lifetime and vertexing observables [22, 155]: the finite  $\tau$  lifetime ( $c\tau \approx 87 \mu\text{m}$ ) produces displaced tracks and, for multi-prong decays, a reconstructible secondary vertex. Impact-parameter significances and secondary-vertex properties are exploited to separate genuine  $\tau_h$  from prompt jets or leptons [22, 155].

Additional discriminants include the invariant mass of the visible decay products computed from tracks and calorimeter clusters, electromagnetic energy fractions (sensitive to  $\pi^0 \rightarrow \gamma\gamma$ ), and dedicated shower-strip grouping for nearby photons. For example, invariant-mass reconstruction commonly uses a jet cone  $\Delta R_{\text{jet}} \lesssim 0.4$  while excluding calorimeter clusters matched to tracks by a minimum separation  $\Delta R_{\text{track}} \gtrsim 0.08$  to reduce double counting.

Reconstruction algorithms combine these inputs. CMS’s Hadron-Plus-Strips (HPS) algorithm explicitly builds decay-mode hypotheses and uses strip-clustering of photons, complemented by modern methods using multivariate or deep-learning discriminators (DeepTau) to reject jets, electrons, and muons [142, 178]. ATLAS employs analogous calorimeter+track based MVAs and BDTs [177]. Typical working points trade efficiency versus background: medium points often give  $\tau_h$  efficiencies of order 50–70% with light-jet misidentification rates in the per-mille to percent range, depending on kinematics and PU.

Practical implementations tune cone sizes, isolation thresholds, and MVA inputs to the kinematic region and analysis goals. The choice of working point is driven by the signal-to-background optimization for the search or measurement at hand.

### 2.2.3 B TAGGING AT MULTIPURPOSE DETECTORS

Jets originating from bottom quarks ( $b$ -jets) exhibit several distinctive properties that enable their identification. The relatively long lifetime of  $b$  hadrons (order 1.5 ps) produces displaced charged tracks and often reconstructible secondary vertices a few millimetres from the primary interaction point. The large  $b$ -hadron mass yields decay products with sizable

transverse momentum relative to the jet axis, and semileptonic branching fractions produce soft electrons or muons inside the jet. These features form the basis for b-tagging [179].

Practical algorithms exploit individual signatures or combine them:

- **Track-counting:** counts tracks with large impact-parameter significance to identify a b-like topology [179].
- **Jet-probability:** evaluates the compatibility of the jet’s track impact-parameter distribution with the primary vertex hypothesis [179].
- **Secondary-vertex:** explicitly reconstructs displaced vertices and uses their kinematic properties (decay length significance, vertex mass) [179].
- **Soft-lepton taggers:** identify low- $p_T$  leptons inside jets from semileptonic b decays [179].

Modern taggers combine many observables in multivariate or deep learning classifiers to maximize discrimination power. Contemporary approaches exploit rich, low-level inputs (track by track and PF candidate information, vertex features and kinematics) and advanced network architectures (DeepCSV/DeepJet, RNN/sequence, graph/set networks) [141, 179]. These developments yield measurable performance gains: modern deep classifiers typically improve b efficiency at fixed mistag rate relative to classical taggers and allow continuous discriminants with tunable operating points. Calibration with data-driven scale factors (from  $t\bar{t}$ , multijet or dilepton control samples) and propagation of associated systematic uncertainties remain essential for physics results [179].

- Deep feed-forward networks (e.g. DeepCSV/DeepJet) ingest a large set of high-level and per-track inputs to produce powerful binary or multi-class discriminants that separate b, c and light-flavour jets.
- Sequence models and recurrent networks (RNN-based taggers) process an arbitrary ordered list of track-level variables, improving sensitivity by directly exploiting per-track correlations and order-dependent information (impact-parameter sequences, track kinematics).
- Graph- and set-based architectures and combined particle+vertex networks (sometimes referred to as “DeepFlavour”-style models) aggregate heterogeneous inputs and return per-flavour probabilities, enabling natural multi-classification and calibrated operating points.

These developments yield measurable performance gains: modern deep classifiers typically improve b identification efficiencies at fixed mistag rates (or reduce mistag rates at fixed efficiency) relative to classical taggers. The continuous output of such networks permits analyses to choose operating points (loose/medium/tight) corresponding to desired efficiencies or mistag rate targets. Calibration remains essential: data-driven scale

factors derived from control samples (e.g.  $t\bar{t}$ , multijet, dilepton) are applied to correct simulation, and systematic uncertainties from the calibration, flavour composition, and kinematic extrapolation are propagated to physics results.

Examples in use are CMS DeepCSV / DeepJet and ATLAS MV2 / DL1 [142], which illustrate the transition from expert-designed high-level variables to large-scale machine learning leveraging low-level detector information. Typical medium working points yield b-tag efficiencies of order 60–80% with light-jet misidentification rates at or below the percent level. The precise choice of working point is tuned per analysis to optimize sensitivity while accounting for calibration and systematic uncertainties.

## 2.3 THE CMS DETECTOR

---

Fragment extracted and adapted from [180]

As previously mentioned, CMS is a general-purpose detector at the LHC. The detector has a length of 21.6 m, a diameter of 14.6 m, and a weight of 14,000 tonnes. Its cylindrical geometry is divided into a central barrel section and two endcaps. This design provides hermetic coverage to accurately measure momentum and energy balance, which is crucial for identifying non-interacting particles such as neutrinos, through missing transverse energy.

The detector is constructed from concentric layers of sub-detectors, as illustrated in Fig. 2.5. The innermost component is the silicon tracker, comprising a pixel detector and silicon strip tracker. It reconstructs the trajectories of charged particles and measures their  $p_T$  with a resolution of  $\approx 0.7\%$  for 10 GeV particles within a pseudorapidity range of  $|\eta| < 2.5$ .

Surrounding the tracker is the calorimeter system (ECAL and HCAL). The ECAL is made of dense lead-tungstate crystals. It is designed to measure electrons and photons with a high resolution of  $\approx 0.6\%$  for 50 GeV electrons. The HCAL detector, located outside the ECAL, is a brass-scintillator sampling calorimeter that measures hadrons (e.g., charged pions, kaons, protons) with an energy resolution of  $\approx 18\%$  for 50 GeV pions. Together, the ECAL and HCAL cover  $|\eta| < 3$ . The coverage is extended to  $|\eta| < 5$  with steel and quartz-fiber hadron calorimeters in the forward regions.

A key feature of CMS is its large superconducting solenoid, which encloses the tracker and calorimeters. The solenoid is constructed from a niobium-titanium alloy and cooled to 4.2 K with liquid helium. It generates a uniform magnetic field of 3.8 T throughout the tracking volume, enabling precise momentum measurement from the curvature of charged particle tracks.

The outermost system is dedicated to the identification of muon objects. Gas-based ionization detectors are embedded in the steel flux-return yoke that surrounds the solenoid. This system provides triggering and tracking capabilities for muons up to  $|\eta| < 2.4$ . The combination of the inner tracker

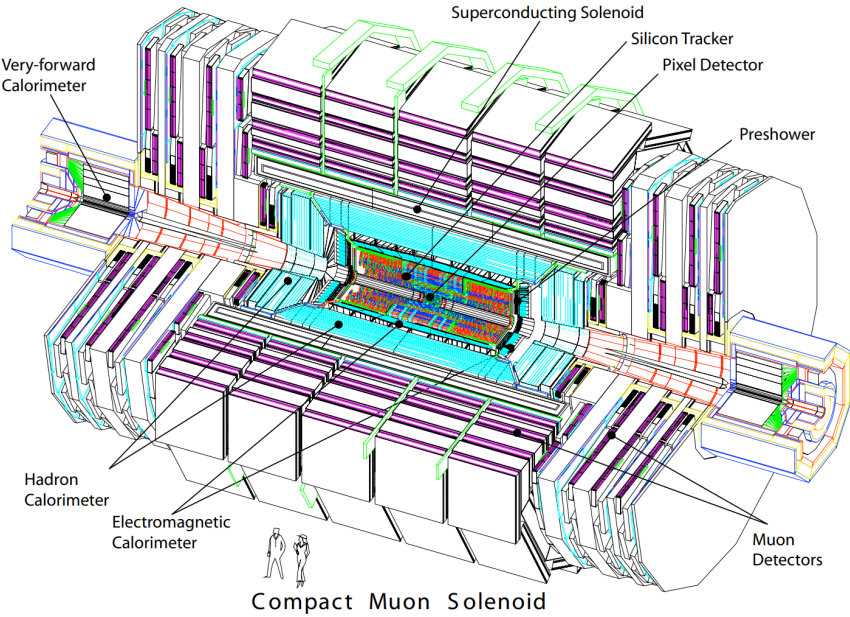


**Figure 2.5:** Layout of the CMS experiment at the CERN LHC. (retrieved from [180]).

and the muon system allows for a robust identification and momentum measurement of muons across a wide kinematic range.

The geometrical segmentation of the barrel and endcaps defines the detector’s acceptance in terms of pseudorapidity. The central barrel provides optimal coverage for  $|\eta| \lesssim 1.5$ , while the endcaps extend the acceptance to  $|\eta| \lesssim 2.5$  for the tracker and calorimeters, and to  $|\eta| \lesssim 2.4$  for the muon system.

This segmentation impacts the detection efficiency. The silicon trackers are highly efficient in the barrel, where particles cross the layers perpendicularly. In the endcaps, the reduced hit multiplicity from shallow-angle traversals leads to a slight decrease in tracking efficiency and resolution. The calorimeters are also optimized to maintain performance across  $\eta$ , though the material budget and granularity vary.

Muon reconstruction performance exhibits regional differences. In the barrel, drift tubes (DTs) provide high spatial resolution, while in the endcaps, cathode strip chambers (CSCs) and resistive plate chambers (RPCs) are used to handle higher background rates and non-uniform magnetic fields. The assumed identification efficiency for muons (electrons) is 95% (85%), with a mis-identification rate of 0.3% (0.6%) [146, 152, 153].

For the identification of heavy-flavor jets, CMS adopts the DeepCSV algorithm [179]. In our simulated data, we use the value corresponding to the “medium” working point, which provides a b-tagging efficiency of 70% with a light-flavor jet misidentification rate of approximately 1% across the entire  $p_T$  spectrum. The “loose” (85% efficiency, 10% mis-id) and “tight” (45% efficiency, 0.1% mis-id) working points were also explored during the analysis optimization.

For hadronically decaying  $\tau$  leptons ( $\tau_h$ ), CMS uses the DeepTau algorithm [142], which employs a deep neural network combining isolation and lifetime information to identify  $\tau_h$  decay modes, as explained in Section 2.2.2. The “medium” working point is chosen for this analysis, providing a  $\tau_h$  identification efficiency of 70% and a misidentification rate of 0.5% for jets originating from light quarks and gluons. This working point was selected through an optimization process that maximized the discovery reach of the analysis.

## 2.4 PHENOMENOLOGICAL PIPELINE

---

The estimation of signal and background event yields is performed through a comprehensive Monte Carlo (MC) simulation pipeline [127, 128, 181, 182]. This approach, a cornerstone of high-energy physics research, enables robust studies of BSM scenarios by emulating the entire data collection and processing chain of a collider experiment [129, 133]. The key advantages of this methodology include [127, 134]:

- The ability to perform automated calculations of theoretical quantities such as cross-sections and decay widths for complex processes.
- Rapid generation of large event samples with computational efficiency that enables extensive parameter space exploration and optimization studies.
- Conducting feasibility studies and optimizing analysis strategies prior to data acquisition.
- Estimating the efficiency of complex event selection criteria and the geometric acceptance of the detector.
- Predicting the rates and kinematical distributions of both irreducible and reducible background processes.
- Comparing and distinguishing between different theoretical hypotheses for a potential discovered signal.

The simulation workflow is modular, reflecting the logical progression from a theoretical Lagrangian to statistical significance estimates [127, 128, 181, 182]. As illustrated in Fig. 2.6, it can be organized into three main stages: (i) theoretical model implementation (green region), (ii) event generation and detector simulation (pink region), and (iii) statistical analysis and signal extraction (blue region). To delve further into this pipeline, each stage is described in detail below [127, 129]:

1. **Model Implementation:** The process begins with the implementation of the theoretical model in FeynRules (v2.3.43) [128, 181]. The Lagrangian of the new physics scenario, including all particle definitions, parameters, and interactions, is translated into a set of Feynman rules

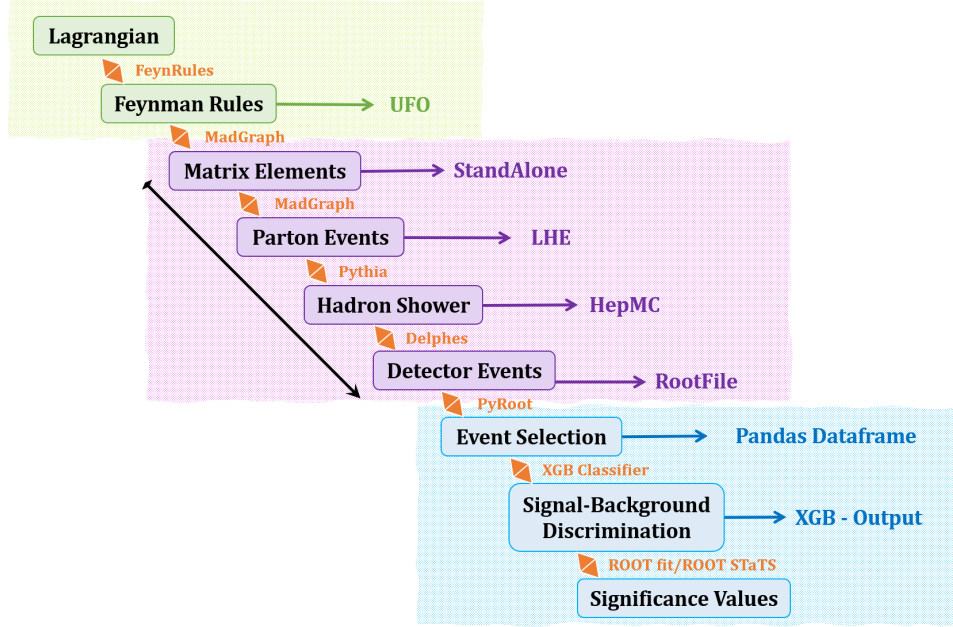


**Figure 2.6:** Schematic overview of the phenomenological MC pipeline. The workflow is divided into three stages: (green) model definition and UFO export using FeynRules; (pink) event generation from matrix elements through detector simulation using MadGraph, Pythia, Delphes, and PyRoot; (blue) statistical analysis including event selection, signal-background discrimination, and significance calculation using Pandas, XGBoost, and ROOT statistical tools.

and exported in the Universal FeynRules Output (UFO) format [182], interoperable with modern matrix-element generators [127].

Alternative tools exist for model implementation and phenomenological studies, such as SARAH [183] which can interface with spectrum generators like SPheno [184] to compute mass spectra, decay widths, flavor observables, and Wilson coefficients. These tools can also connect to specialized codes like HiggsBounds/HiggsSignals [185] for Higgs sector constraints, FlavorKit [186] for flavor physics observables, micrOMEGAs [187] for dark matter relic density and direct/indirect detection calculations, among many others. However, for the simplified models and collider-focused analyses considered in this work, the direct FeynRules-to-UFO workflow provides sufficient flexibility and computational efficiency.

2. **Matrix Element Generation:** This UFO module, accompanied by a parameter card defining numerical values for masses and couplings, serves as input to MadGraph5\_aMC@NLO (v3.5.7) [127, 188]. Within MadGraph, the hard process and corresponding matrix elements are generated and stored in Les Houches Event (LHE) files. The PDF choices (here NNPDF3.0 NLO [135]) and matching/merging settings (MLM/CKKW-type) are configured to control radiation and multi-jet overlap [189, 190].

To accurately model processes featuring significant interference effects between the new physics signal (e.g., a  $Z'$  boson) and the SM backgrounds, the full squared amplitude (often referred to as the Signal-Discriminated Events or SDE strategy) is employed for the phase-space integration. The MadEvent submodule generates unweighted parton-level events, stored in the LHE format, containing the four-momenta of all final-state particles. The generation is optimized through careful configuration of the `run_card`, setting appropriate kinematic cuts on final-state partons to avoid wasting computational resources on events that would subsequently be rejected by the detector simulation.

3. **Parton Shower and Hadronization:** Given the presence of additional jet radiation, the MLM matching scheme [189] is applied to mitigate the double-counting of jet emission between the matrix element calculation and the subsequent parton shower. The parton-level LHE events are then passed to PYTHIA (v8.2.44) [133] for the modeling of QCD and QED radiation (parton showering), hadronization, and particle decays. This step translates the colored partons into stable, color-singlet hadrons and resonances that form the observable final state. The resulting events, which include a full list of generator-level particles, are saved in the HepMC2 format.
4. **Detector Simulation:** Detector effects are simulated using DELPHES (v3.4.2) [129], a fast parametric detector simulation framework. The `delphes_card_CMS.tcl` configuration card is used to emulate the response of the CMS detector, including the geometric acceptance, tracking efficiency, calorimeter energy resolution and segmentation, and the inner and outer magnetic field. Key reconstruction algorithms are applied within DELPHES:
  - Jets are clustered from calorimeter towers using the anti- $k_t$  algorithm [149] with a distance parameter of  $R = 0.4$ , and b-tagging is simulated based on the efficiency and mis-tag rate of the CMS performance.
  - Muons and electrons are identified with efficiency maps that are functions of  $p_T$  and  $\eta$ .
  - The  $\vec{p}_T^{\text{miss}}$  is calculated from the negative vector sum of all reconstructed particle momenta, as it was defined in Equation 2.2.
  - Object calibrations (e.g., Jet Energy Corrections, lepton scale factors) are applied to align the simulation with the expected detector performance.

The final output, containing reconstructed physics objects (jets, leptons,  $|\vec{p}_T^{\text{miss}}|$ ), is stored in ROOT format [191].

At this stage, the analysis of the simulated samples converges with the methodology applied to real collider data. The subsequent steps,

corresponding to the blue region of the workflow in Fig. 2.6, involve the statistical analysis and signal extraction phase:

5. **Event Selection:** The ROOT ntuples containing reconstructed physics objects are converted into structured data formats (typically Pandas DataFrames [192]) for efficient manipulation and analysis using PyROOT [191]. Physics-motivated selection criteria are applied to enhance the signal-to-background ratio, including kinematic cuts on transverse momenta, pseudorapidity ranges, invariant masses, and topological variables.
6. **Signal-Background Discrimination:** The separation between signal and background events can be achieved through the careful selection of kinematic observables and the application of optimized selection cuts. Traditional cut-based analyses rely on sequential requirements on individual variables (e.g.,  $p_T$  thresholds, invariant mass windows) to enhance the signal-to-background ratio. However, this approach can be significantly improved by employing advanced multivariate analysis techniques, such as Boosted Decision Trees (BDT) or Gradient Boosting algorithms (e.g., XGBoost [193]). These machine learning classifiers are trained on high-level kinematic features and exploit correlations between observables that are not captured by simple cut-based selections. The output score predicted by these algorithms serves as an optimal discriminant observable for the final statistical test, effectively compressing the multidimensional feature space into a single powerful variable that maximizes signal-background separation.
7. **Significance Calculation:** Likelihood-based methods are used to extract signal yields, set exclusion limits, or estimate discovery significance, accounting for both statistical and systematic uncertainties through nuisance parameters. The results are typically expressed in terms of expected significance, confidence level exclusion limits (e.g., 95% CL), or posterior probability distributions in Bayesian frameworks. The expected sensitivity to the signal hypothesis is usually quantified using statistical hypothesis testing frameworks implemented in ROOT (e.g., RooFit, RooStats) [157, 194]. However, for this work, we preferred to use a custom implementation of the profile-binned likelihood test, as explained in Sec. 2.5.

The reliability of the simulation is validated by comparing the modeling of well-known SM processes (e.g., Drell-Yan,  $t\bar{t}$  production) against published results and data-driven control regions. Dominant theoretical systematic uncertainties, such as those arising from the choice of factorization and renormalization scales, PDF variations, and parton shower modeling, are evaluated and propagated through the analysis.

## 2.5 MEASUREMENT OF THE POWER OF AN ANALYSIS

---

In high energy physics experiments, data is often discretized into bins (e.g., histograms of collision events versus energy or momentum) to test competing hypotheses [195]. The fundamental framework compares two scenarios: the *null hypothesis* ( $H_0$ ), representing background-only processes (only a  $b_i$  number of events in each bin  $i$ ), and the *alternative hypothesis* ( $H_1$ ), including both signal ( $s_i$ ) and background events ( $s_i + b_i$ ) [196]. Event counts ( $n_i$ ) in a collider experiment follow a Poissonian distribution. Therefore, the likelihood for observing the data under each hypothesis is written as a binned-likelihood [126, 195]:

$$\mathcal{L}(n_i | \lambda_i) = \frac{e^{-\lambda_i} \lambda_i^{n_i}}{n_i!}, \quad \text{where } \lambda_i = \begin{cases} b_i & \text{for } H_0, \\ s_i + b_i & \text{for } H_1. \end{cases} \quad (2.11)$$

The Neyman-Pearson lemma [164, 196] provides a rigorous framework for hypothesis testing by establishing that the *likelihood ratio*  $Q = \mathcal{L}(\text{data} | H_1)/\mathcal{L}(\text{data} | H_0)$  is the most powerful test statistic for distinguishing between two simple hypotheses,  $H_0$  and  $H_1$  [126, 196]. This forms the basis for quantifying the evidence for new physics signals against known backgrounds [126, 161]. For binned analyses in particle physics, we define the likelihood ratio  $Q_i$  for each bin  $i$  as [126, 195],

$$Q_i = \frac{\mathcal{L}(n_i | s_i + b_i)}{\mathcal{L}(n_i | b_i)} = e^{-s_i} \left(1 + \frac{s_i}{b_i}\right)^{n_i}, \quad (2.12)$$

where  $n_i$  is the observed event count,  $s_i$  the expected signal, and  $b_i$  the expected background in bin  $i$ , as explained before [126, 195].

The test for the full analysis is constructed as the product of individual bin likelihood ratios [126, 195]:

$$Q = \prod_{i=1}^N Q_i, \quad (2.13)$$

where  $N$  is the total number of bins [195]. Under this formulation, each bin is treated as an independent experiment, allowing us to analyze the data in a modular way. This is convenient when combining results from multiple search channels or energy ranges [126, 161].

For convenience and to connect with asymptotic results, one commonly works with the log-likelihood ratio:

$$-2 \ln Q = 2 \sum_{i=1}^N \left[ s_i - n_i \ln \left(1 + \frac{s_i}{b_i}\right) \right], \quad (2.14)$$

and, by Wilks' theorem, its asymptotic distribution under the null hypothesis is chi-square distributed in regular cases [126, 197].

In practice, the Neyman-Pearson lemma motivates the use of a test statistic  $t$  that quantifies the evidence for a signal against the background-only hypothesis, which can be written as

$$t = -2 \ln Q = \sum_{i=1}^N [2s_i - 2n_i w_i], \quad (2.15)$$

with the optimal weight of each bin given by  $w_i = \ln\left(1 + \frac{s_i}{b_i}\right)$ .

The discovery significance  $\kappa$  quantifies the statistical separation of  $t$  if  $n$  is distributed according to the background-only hypothesis ( $H_0$ ) versus the signal-plus-background hypothesis ( $H_1$ ), normalized by the standard deviation of the  $H_1$  distribution ( $\sigma_{H_1}$ ),

$$\kappa = \frac{\langle t \rangle_{H_0} - \langle t \rangle_{H_1}}{\sigma_{H_1}}. \quad (2.16)$$

To evaluate  $\kappa$ , we need the expectation values and variances of  $t$  under both hypotheses. These expressions follow from the properties of Poisson-distributed random variables  $n_i$  and the linearity of expectation. For any hypothesis, the expectation value of  $t$  is given by

$$\langle t \rangle = \sum_i [2s_i - 2w_i \langle n_i \rangle], \quad (2.17)$$

where  $\langle n_i \rangle = \lambda_i$  depends on whether we assume the hypothesis in (2.11). The variance calculation relies on three key properties:

- In general, for any set of random variables  $X_i$ , the variance is

$$\sigma^2\left(\sum_i X_i\right) = \sum_i \sigma^2(X_i) + 2 \sum_{i < j} \sigma(X_i, X_j) \quad (2.18)$$

with  $\sigma(X_i, X_j)$  the covariance between  $X_i$  and  $X_j$ . Assuming that each bin is an independent experiment, the covariance term vanishes, and we get

$$\sigma^2\left(\sum_i X_i\right) = \sum_i \sigma^2(X_i). \quad (2.19)$$

- For constants  $a, c$ :  $\sigma^2(aX + c) = a^2 \sigma^2(X)$
- For Poisson  $n_i$ :  $\sigma^2(n_i) = \langle n_i \rangle = \lambda_i$

Applying these properties, the variance of each bin's contribution is given by

$$\sigma^2(2s_i - 2w_i n_i) = 4w_i^2 \sigma^2(n_i) = 4w_i^2 \lambda_i, \quad (2.20)$$

and summing over all bins yields the total variance under each hypothesis.

Thus, the expected behavior differs under the signal-plus-background ( $H_1$ ) and background-only ( $H_0$ ) hypotheses, as shown in the following expressions:

- Under  $H_1$  we expect that the  $n_i$  distribution follows  $\text{Pois}(s_i + b_i)$ :

$$\langle t \rangle_{s+b} = \sum_i [2s_i - 2(s_i + b_i)w_i] \implies \sigma_{s+b}^2(t) = 4 \sum_i (s_i + b_i)w_i^2. \quad (2.21)$$

- Under  $H_0$  we expect that the  $n_i$  distribution follows  $\text{Pois}(b_i)$ :

$$\langle t \rangle_b = \sum_i [2s_i - 2b_i w_i] \implies \sigma_b^2(t) = 4 \sum_i b_i w_i^2. \quad (2.22)$$

Substituting these results into  $\kappa$  gives a useful expression for the discovery significance,

$$\kappa = \frac{\sum_i s_i w_i}{\sqrt{\sum_i (s_i + b_i) w_i^2}}. \quad (2.23)$$

It quantifies the separation between the signal+background ( $s + b$ ) and the background-only hypotheses in units of standard deviations ( $\sigma$ ), where  $\kappa = 5$  corresponds to the traditional  $5\sigma$  discovery threshold,  $\kappa = 3$  to a  $3\sigma$  evidence to the traditional anomaly detection threshold, and  $\kappa = 1.64$  (1.96) to the 90% (95%) confidence level (CL) exclusion limit.

This figure of merit inherits optimality properties from the Neyman–Pearson construction: the logarithmic weights  $w_i = \ln(1 + s_i/b_i)$  arise from the log-likelihood ratio and therefore assign statistically efficient importance to each bin. In particular, for the single-bin case, the discovery sensitivity reduces to

$$\kappa_i = \frac{s_i w_i}{\sqrt{(s_i + b_i) w_i^2}} = \frac{s_i}{\sqrt{s_i + b_i}}. \quad (2.24)$$

The asymptotic behavior is transparent: in the signal-dominated regime ( $s_i \gg b_i$ ),  $\kappa_i \approx \sqrt{s_i}$ , while in the background-dominated regime ( $s_i \ll b_i$ ),  $\kappa_i \approx s_i/\sqrt{b_i}$ . Extending to multiple bins yields

$$\kappa \approx \sqrt{\sum_i \kappa_i^2} = \begin{cases} \sqrt{\sum_i s_i}, & s_i \gg b_i, \\ \sqrt{\sum_i s_i^2/b_i}, & s_i \ll b_i, \end{cases} \quad (2.25)$$

demonstrating that this measure automatically adapts to the underlying signal-to-background regime without manual reweighting. Thus,  $\kappa$  provides a unified and asymptotically efficient sensitivity metric across diverse analysis conditions.

In practice, we must take into account systematic effects by incorporating nuisance parameters into the likelihood and profiling over uncertainty ranges. The power calculation can be extended to include systematic uncertainties by modifying the denominator as,

$$\kappa_{\text{sys}} = \frac{\sum_i s_i w_i}{\sqrt{\sum_i [(s_i + b_i) + \delta_{\text{sys,signal},i}^2 + \delta_{\text{sys,bkg},i}^2] w_i^2}}, \quad (2.26)$$

where  $\delta_{\text{sys}}$  terms represent the systematic uncertainties on signal and background predictions.

This framework not only provides a figure of merit for an analysis but also serves as a roadmap for experimental optimization. The expected signal and background in each bin,  $s_i$  and  $b_i$ , are not fundamental inputs but are themselves products of the experimental setup and analysis choices. They can be expressed in terms of more fundamental experimental parameters (with acceptance absorbed into the selection efficiencies):

$$s_i = \sigma_{s,i} \cdot L \cdot \epsilon_{s,i}, \\ b_i = \sigma_{b,i} \cdot L \cdot \epsilon_{b,i},$$

where, following Equation 2.8,  $\sigma_{s,i}$  and  $\sigma_{b,i}$  are the fiducial cross-sections for signal and background processes in bin  $i$ ,  $L$  is the integrated luminosity, and  $\epsilon_{s,i}$  and  $\epsilon_{b,i}$  are the cumulative or total efficiencies (selection efficiency combined with detector acceptance and reconstruction effects).

Substituting these expressions into the significance  $\kappa$  reveals the multi-dimensional parameter space available for optimization:

$$\kappa = \frac{\sum_i \sigma_{s,i} \cdot \epsilon_{s,i} \cdot w_i}{\sqrt{\sum_i [(\sigma_{s,i} \epsilon_{s,i} + \sigma_{b,i} \epsilon_{b,i}) + \delta_{\text{sys}}^2] \cdot w_i^2}} \cdot \sqrt{L}.$$

This decomposition shows that the discovery significance can be enhanced through several distinct strategies. The primary handles are:

- **Increasing integrated luminosity ( $L$ ):** The  $\sqrt{L}$  scaling represents the fundamental statistical limit - doubling sensitivity requires quadrupling data collection time. This drives the construction of higher-luminosity colliders and longer data-taking campaigns.
- **Reducing systematic uncertainties:** The  $\delta_{\text{sys}}$  terms encompass uncertainties from theoretical predictions, detector calibration, background estimation methods, and luminosity measurement. Their reduction requires dedicated calibration measurements, improved Monte Carlo simulations, and sophisticated data-driven background estimation techniques.
- **Improving detector performance:** Effective efficiencies  $\epsilon_{s,i}$  and  $\epsilon_{b,i}$  can be improved through better detector design, increased coverage, and enhanced reconstruction and calibration algorithms that recover and correctly identify more signal events while controlling backgrounds.
- **Choosing optimal observables:** The weights  $w_i = \ln(1 + s_i/b_i)$  are maximized when the analysis uses variables that provide the best separation between signal and background. This motivates the development of advanced feature engineering and the use of multivariate methods that automatically learn the most discriminating variables.

- **Optimizing selection criteria:** Signal efficiency  $\epsilon_{s,i}$  can be maximized while background efficiency  $\epsilon_{b,i}$  is minimized through sophisticated trigger algorithms, multivariate analysis techniques, and machine learning classifiers that exploit subtle differences between signal and background event features.

Therefore, the power of an analysis, quantified by  $\kappa$ , is the result of a concerted effort across accelerator operation, detector performance, and analysis strategy.

The key limitation of the binned formulation in Eq. 2.26 is its treatment of bins as independent experiments, which discards valuable information from inter-bin correlations. This approximation becomes particularly evident in regions of high sensitivity, where the shape information of distributions becomes crucial. In such cases, multivariate methods that exploit the full correlation structure (such as matrix element methods, deep learning classifiers, or template fits) typically outperform simple binned significance estimates.

However, the formalism presented here provides theoretical insight and a useful approximation for quick sensitivity estimates. In the asymptotic limit and for counting experiments, this approach yields results consistent with statistical packages commonly used in high energy physics, such as `RooStats` and `RooFit`. These frameworks implement more rigorous statistical procedures that fully account for the likelihood structure, parameter correlations, and systematic uncertainties through nuisance parameters.

Despite this limitation, the  $\kappa$  metric remains invaluable for establishing *experimental sensitivity*, which is defined as the minimum signal strength required to achieve a certain significance level (e.g., 95% CL exclusion or  $5\sigma$  discovery potential). It provides a practical tool for guiding analysis design, optimizing selection criteria, and prioritizing experimental efforts.

For experimental final results and interpretation, full statistical treatments using profile likelihood methods within frameworks such as `RooStats` remain the gold standard, as they properly account for all correlations and systematic uncertainties. In this work, we are not interested in the final statistical interpretation of data, but rather in understanding and optimizing the experimental sensitivity to new physics signals. Therefore, the  $\kappa$  metric serves as a practical and insightful tool for guiding analysis design and experimental strategy.

## 2.6 ML ENHANCED SIGNAL-BACKGROUND DISCRIMINATION

---

As shown in Sec. 2.5, the sensitivity of a search depends on optimally separating signal and background processes [126, 198]. Traditional “cut-based” analyses, which apply sequential selection criteria to individual observables, cannot fully exploit the discriminatory information contained in the high-dimensional feature space of collision events [198, 199]. In this

approach, for an event described by a feature vector  $\mathbf{x} = (x_1, x_2, \dots, x_N)$ , selection criteria are applied in the form [200]

$$\text{Selection: } x_1 > c_1 \text{ AND } x_2 > c_2 \text{ AND } \dots \text{ AND } x_N > c_N, \quad (2.27)$$

where  $c_i$  represents a specific constraint (cut) imposed on the dataset.

This method has several limitations that become apparent when considering correlations among kinematic variables [198, 199]. A typical LHC event contains a large number of observables, and an optimal discriminator must consider these variables and their correlations simultaneously [139, 200]. Tight event selection criteria might severely limit the available phase space, discarding events that are signal-like in multivariate space but fall just outside univariate boundaries [198, 199]. The challenge of dimensionality also arises, as optimizing many cuts becomes unstable and is prone to statistical fluctuations [199, 201]. Finally, sequential cuts cannot capture non-linear relationships and complex decision boundaries that often provide the strongest discrimination [198, 199].

Supervised learning addresses these limitations directly [198, 199]. It learns a function  $f(\mathbf{x})$  that maps the high-dimensional input space to a continuous score, approximating the posterior probability [202, 203]:

$$f : \mathbb{R}^N \rightarrow [0, 1], \quad f(\mathbf{x}) \approx P(\text{signal} | \mathbf{x}). \quad (2.28)$$

It means that the task is to assign a label:

$$f(\mathbf{x}) = \begin{cases} 1 & \text{if the event originates from the signal process,} \\ 0 & \text{if the event originates from the background.} \end{cases} \quad (2.29)$$

This score incorporates correlations and nonlinearities present in the training data, providing a powerful and continuous discriminant [139, 198, 199, 202].

Logistic regression, SVMs [204], Random Forests [205], and boosted trees [193, 201] are common choices; see [199, 200] for comparisons and practical guidance.

In particular, logistic regression is often used as a baseline due to its simplicity and transparency. It assumes a linear decision boundary in the feature space, with the discriminant

$$f(\mathbf{x}) = \sigma(\mathbf{w} \cdot \mathbf{x} + b), \quad (2.30)$$

where  $\mathbf{w}$  are model parameters and  $b$  is a bias term. The model learns a linear combination  $z = \mathbf{w} \cdot \mathbf{x} + b$  that best separates the two classes. Then, it applies a sigmoid function to map this unbounded score to a probability-like output between  $[0, 1]$

$$\sigma(z) = \frac{1}{1 + e^{-z}}. \quad (2.31)$$

As illustrated in Fig. 2.7, a direct linear fit to the binary labels (orange line) is unbounded and can produce values outside the physically meaningful range  $[0, 1]$ . The sigmoid transformation (purple curve) constrains

the output while preserving the ordering of events and providing faster convergence to the asymptotic values: as  $z \rightarrow -\infty$ ,  $\sigma(z) \rightarrow 0$  (background region), and as  $z \rightarrow +\infty$ ,  $\sigma(z) \rightarrow 1$  (signal region).

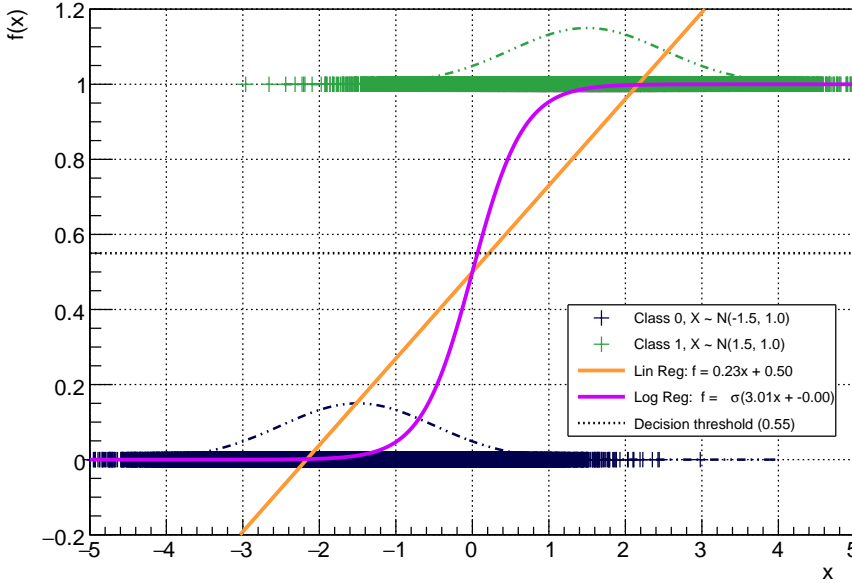


**Figure 2.7:** Illustration of logistic regression on a toy dataset with two classes drawn from Gaussian distributions. The orange line shows an ordinary linear regression fit  $f_{\text{lin}}(x) = \mathbf{w}_{\text{lin}} \cdot \mathbf{x} + b_{\text{lin}}$  to the binary labels, which is unbounded and can produce values outside  $[0, 1]$ . The purple curve shows the logistic regression output  $f(x) = \sigma(\mathbf{w} \cdot \mathbf{x} + b)$ , where the sigmoid function constrains the output to  $[0, 1]$ , while maintaining a smooth, monotonic response. The dashed Gaussian curves illustrate the underlying class distributions. A decision threshold (horizontal dashed line) at  $f(x) = 0.55$  would classify events above it as signal and below as background, though in practice the full continuous distribution is used for statistical inference.

While a hard decision threshold (e.g., classifying events with  $f(\mathbf{x}) > 0.55$  as signal) can be applied, modern analyses exploit the full continuous output distribution rather than collapsing it to a binary decision. Figure 2.8 shows the resulting distributions of  $f(\mathbf{x})$  for signal and background events after applying the trained logistic regression model. Signal events concentrate near  $f(\mathbf{x}) \approx 1$ , while background events peak near  $f(\mathbf{x}) \approx 0$ , with some overlap in intermediate regions reflecting the inherent classification uncertainty.

This approach—using the complete output distribution rather than a single cut—is central to the analysis strategy employed throughout this work. As detailed in Sec. 2.6.2, the classifier output is binned into a histogram, and each bin contributes to the final sensitivity calculation through the likelihood framework of Sec. 2.5. This maximizes the statistical power by preserving all discriminating information: events with intermediate

scores, which would be ambiguous under a hard threshold, still contribute meaningfully to the analysis through their likelihood contributions.

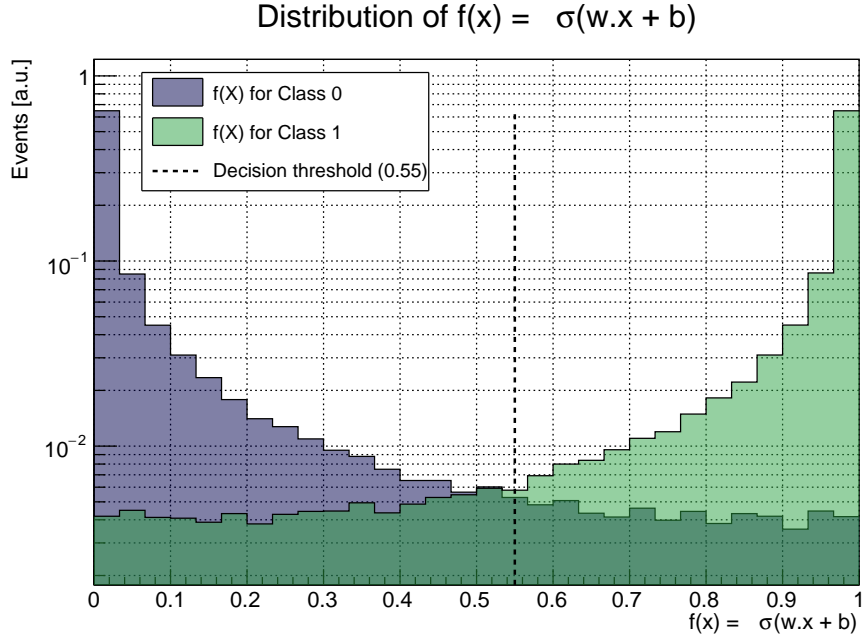


**Figure 2.8:** Distribution of the logistic regression output  $f(x) = \sigma(w \cdot x + b)$  for signal (green) and background (blue) events in the toy dataset. Rather than applying a single decision threshold, the analysis uses the full shape of these distributions as input to the statistical inference procedure described in Sec. 2.5, maximizing the sensitivity by exploiting all available discriminating information across the entire output range.

While logistic regression cannot capture complex non-linear relationships, it remains useful when signal and background are approximately linearly separable, and it provides a clear reference point to compare against more sophisticated methods.

Tree-based ensembles are among the most widely used methods. To understand how they work, we first consider the building block: a *decision tree*. This is a hierarchical model that recursively partitions the feature space through binary splits [199, 205]. Starting from the root node containing all training events, the algorithm selects the feature and threshold that best separates signal from background according to a splitting criterion. This process continues recursively, where each iteration is further split until a stopping condition is met (maximum depth, minimum events per node, or no further improvement). The terminal nodes, or *leaves*, assign weights based on the number of nodes classified correctly as signal or background. For example, a tree might first be split on events passing a  $p_T^{\text{leading jet}} > 150 \text{ GeV}$  threshold. Subsequently, a  $m_{jj} > 800 \text{ GeV}$  criterion is imposed on these events. This creates a sequence of increasingly refined regions in feature space. While conceptually transparent, individual trees are highly sensitive to training data fluctuations in the dataset. Small

changes might produce very different tree structures, making them a high-variance and low-bias learners [199].

To address the high variance conundrum, we can combine many trees, trained with different subsets of data. These ensemble methods have been proven to be effective to average out individual errors. The Random Forest algorithm approaches this through *bootstrap sampling* [205], a resampling technique that creates multiple training datasets from the original data.

Given a dataset of  $n$  events, each bootstrap sample is constructed by randomly drawing  $n$  events *with replacement*, meaning the same event can appear multiple times in a single sample. On average, each bootstrap sample contains approximately 63% of the unique original events, with the remaining 37% (called *out-of-bag* or OOB events) left out. By training a separate decision tree on each bootstrap sample and additionally introducing random feature selection at each split, Random Forests combine these diverse predictors through simple averaging:

$$F(x) = \frac{1}{B} \sum_{b=1}^B T_b(x), \quad (2.32)$$

where  $B$  is the number of trees and  $T_b(x)$  is the prediction of the  $b$ -th tree. For classification, this is typically the fraction of signal events in that leaf: if a leaf contains 80 signal and 20 background training events, then  $T_b(x) = 0.8$  for any test event reaching that leaf. The final Random Forest prediction  $F(x)$  is simply the arithmetic mean of these  $B$  individual tree predictions, effectively polling the entire ensemble to produce a robust, averaged probability estimate. This approach reduces variance and mitigates overfitting through averaging. Random Forests are robust, parallelizable, and provide natural feature importance measures, though they typically require more trees than boosted methods and may yield slightly lower performance on well-tuned tasks.

Boosted Decision Trees (BDTs) have become a standard tool in particle physics because they balance interpretability and performance. Unlike Random Forests, which build trees independently in parallel, BDTs employ a fundamentally different strategy: it constructs an ensemble *sequentially*, with each new tree specifically trained to correct the mistakes of the previous ensemble. This sequential, adaptive learning process is the defining characteristic of boosting methods.

The term *weak learner* refers to a simple model that performs only slightly better than random guessing—for binary classification, this means achieving accuracy modestly above 50%. In the context of BDTs, weak learners are typically shallow decision trees (depth 3–6), sometimes called *stumps* when limited to just a few splits. While such a tree alone provides minimal discriminating power, the boosting algorithm iteratively combines many of these weak learners into a *strong learner*—an ensemble that achieves high accuracy. This is the essence of boosting: transforming simple, individually weak classifiers into a powerful collective predictor through sequential refinement.

The boosting procedure works as follows. Initially, all training events are assigned equal weights. The first weak learner  $h_1(x)$  is trained on this dataset and makes predictions. Events that are misclassified—signal events predicted as background or vice versa—are then assigned higher weights, while correctly classified events receive lower weights. The second tree  $h_2(x)$  is trained on this reweighted dataset, forcing it to focus on the previously difficult cases. This process repeats: after each iteration  $m$ , events that remain misclassified have their weights increased, and the next tree  $h_{m+1}(x)$  is added to specifically target these problematic regions of feature space. The final ensemble combines all trees through a weighted sum:

$$F_M(x) = \sum_{m=1}^M \gamma_m h_m(x), \quad (2.33)$$

where  $M$  is the total number of trees,  $h_m(x)$  is the prediction of the  $m$ -th weak learner, and  $\gamma_m$  is its weight in the ensemble. The weight  $\gamma_m$  reflects the performance of tree  $m$ : more accurate trees receive larger weights and thus contribute more strongly to the final prediction. Each tree's prediction  $h_m(x)$  is obtained similarly to Random Forests—by passing the event through the tree's binary splits until reaching a leaf—but here the tree has been trained specifically to correct errors from  $F_{m-1}(x)$ , the ensemble of all previous trees.

This *sequential correction* or *residual learning* is what distinguishes boosting from bagging methods like Random Forests. Rather than averaging independent predictions, boosting builds a progression of specialists: each new tree learns from the failures of its predecessors, gradually refining the decision boundary in regions where the current ensemble performs poorly. The result is a powerful classifier that adaptively allocates modeling capacity to the most challenging parts of the feature space. BDTs are robust to outliers and non-Gaussian distributions, handle mixed variable types naturally, and perform implicit feature selection, often revealing which observables are most discriminating. These properties explain their widespread adoption in LHC analyses.

Finally, Deep Neural Networks (DNNs) represent the most expressive class of models, capable of learning highly complex, hierarchical representations of the input data. A deep network with multiple hidden layers can be written as

$$f(x) = \sigma^{(L)} \left( W^{(L)} \sigma^{(L-1)} \left( \dots \sigma^{(1)} (W^{(1)} x + b^{(1)}) \dots \right) + b^{(L)} \right), \quad (2.34)$$

where  $L$  is the number of layers. DNNs excel at capturing intricate patterns and correlations, but they require large training datasets, careful regularization, and extensive hyperparameter tuning. Their black-box nature also complicates interpretability and the assessment of systematic uncertainties.

In practice, Random Forests are often used as robust, low-maintenance alternatives, while SVMs have largely been superseded by tree-based methods and neural networks due to scalability issues. DNNs can outperform

other methods on very complex problems with sufficient data, but they demand significantly more computational resources. For most LHC searches, BDTs—particularly implementations such as XGBoost—provide the best balance between performance, interpretability, and computational efficiency. In Sec. 3.4, and in Tab. 3.3, we compare the performance of different methods and show that the gain in accuracy from DNNs is marginal compared to BDTs, while the training time is substantially larger.

### 2.6.1 XGBOOST: OPTIMIZED GRADIENT BOOSTING

XGBoost (eXtreme Gradient Boosting) is a widely used implementation of gradient boosting that has become standard in high energy physics due to its efficiency, predictive power, and robustness.

A single decision tree is a weak classifier: it partitions the feature space through binary splits but is highly sensitive to fluctuations in the training data. Boosting addresses this by constructing an ensemble of trees sequentially. At each step, a new tree is trained to predict the residual errors of the current ensemble. This iterative approach allows the classifier to improve gradually, with later trees focusing on events that were previously misclassified.

The algorithm minimizes a regularized objective function:

$$\mathcal{L} = \sum_{i=1}^n l(y_i, \hat{y}_i) + \sum_{m=1}^M \Omega(f_m), \quad (2.35)$$

where  $n$  is the number of training events,  $y_i \in \{0, 1\}$  is the true class label of event  $i$  (with  $y_i = 1$  for signal and  $y_i = 0$  for background), and  $\hat{y}_i$  is the model's current prediction for that event. The loss function  $l(y_i, \hat{y}_i)$  measures the prediction error—quantifying how far the predicted value  $\hat{y}_i$  deviates from the true label  $y_i$ —while  $\Omega(f_m)$  penalizes complex trees to prevent overfitting. Common choices for the loss function include logistic loss (also called log-loss or cross-entropy) for classification, which for a single event takes the form  $l(y, \hat{y}) = -[y \log(\hat{y}) + (1-y) \log(1-\hat{y})]$ , penalizing confident but incorrect predictions more heavily than uncertain ones. The regularization term is:

$$\Omega(f) = \gamma T + \frac{1}{2} \lambda \|\mathbf{w}\|^2 + \alpha \|\mathbf{w}\|_1, \quad (2.36)$$

where  $T$  is the number of leaves in the tree and  $\mathbf{w} = (w_1, w_2, \dots, w_T)$  is the vector of *leaf weights*—the prediction values assigned to each terminal node within a single tree, conceptually analogous to the leaf probabilities described for Random Forests. However, in XGBoost these leaf weights are treated as learnable parameters that are explicitly optimized during training, rather than being fixed as simple class frequency ratios. The distinction in notation is important:  $\mathbf{w}$  denotes weights *within* individual trees (at the leaf level), while  $\gamma_m$  in the ensemble expression  $F_M(x) = \sum_{m=1}^M \gamma_m h_m(x)$  denotes weights *between* trees in the full ensemble. The regularization

coefficients  $\gamma$ ,  $\lambda$ ,  $\alpha$  control tree complexity:  $\|\mathbf{w}\|^2$  is the  $L^2$  norm (Euclidean norm) squared, defined as  $\|\mathbf{w}\|^2 = \sum_{j=1}^T w_j^2$ , which penalizes large leaf weights and encourages smoother predictions;  $\|\mathbf{w}\|_1$  is the  $L^1$  norm (Manhattan norm), defined as  $\|\mathbf{w}\|_1 = \sum_{j=1}^T |w_j|$ , which promotes sparsity by driving some leaf weights toward exactly zero. Together, these regularization terms prevent the model from assigning extreme values to individual leaves, which would indicate overfitting to training data noise.

The model is built additively through sequential updates:

$$\hat{y}_i^{(t)} = \hat{y}_i^{(t-1)} + \eta f_t(x_i), \quad (2.37)$$

where  $t = 1, 2, \dots, M$  indexes the boosting iteration (tree number),  $\hat{y}_i^{(t)}$  is the ensemble prediction for event  $i$  after adding  $t$  trees, and  $\eta \in (0, 1]$  is the *learning rate* (or shrinkage parameter). The learning rate controls how much each new tree contributes to the ensemble: smaller values (e.g.,  $\eta = 0.01\text{--}0.1$ ) make the learning process more conservative, requiring more trees but typically improving generalization, while larger values (e.g.,  $\eta = 0.3\text{--}1.0$ ) lead to faster training but higher risk of overfitting. The dependence on  $t$  is implicit: at iteration  $t$ , the new tree  $f_t(x_i)$  is trained to correct the residual errors of the current ensemble  $\hat{y}_i^{(t-1)}$ , so the contribution of each successive tree adapts to the evolving state of the model. Starting from  $\hat{y}_i^{(0)} = 0$  (or a constant initial guess), each iteration adds a weighted correction:  $\hat{y}_i^{(1)} = \eta f_1(x_i)$ , then  $\hat{y}_i^{(2)} = \eta f_1(x_i) + \eta f_2(x_i)$ , and so on, with later trees focusing on increasingly difficult cases.

Each new tree is selected to minimize a second-order Taylor approximation of the loss:

$$f_t = \arg \min_f \sum_{i=1}^n \left[ g_i f(x_i) + \frac{1}{2} h_i f^{(2)}(x_i) \right] + \Omega(f), \quad (2.38)$$

where  $g_i$  and  $h_i$  are the first and second derivatives of the loss function  $l(y_i, \hat{y}_i)$  with respect to the current prediction  $\hat{y}_i^{(t-1)}$ , evaluated at event  $i$ :

$$g_i = \frac{\partial l(y_i, \hat{y}_i)}{\partial \hat{y}_i} \Big|_{\hat{y}_i=\hat{y}_i^{(t-1)}}, \quad (2.39)$$

$$h_i = \frac{\partial^2 l(y_i, \hat{y}_i)}{\partial \hat{y}_i^2} \Big|_{\hat{y}_i=\hat{y}_i^{(t-1)}}. \quad (2.40)$$

These gradient statistics  $g_i$  and  $h_i$  depend on three quantities: the true label  $y_i$  of event  $i$ , the current ensemble prediction  $\hat{y}_i^{(t-1)}$  before adding tree  $t$ , and the specific form of the loss function. For the default logistic loss (binary cross-entropy) used in classification,  $l(y, \hat{y}) = -[y \log(p) + (1 - y) \log(1 - p)]$  where  $p = \sigma(\hat{y}) = 1/(1 + e^{-\hat{y}})$  is the predicted probability obtained by applying the sigmoid function to the raw prediction  $\hat{y}$ . The derivatives are:

$$g_i = \frac{\partial l}{\partial \hat{y}_i} = p_i^{(t-1)} - y_i = \sigma(\hat{y}_i^{(t-1)}) - y_i, \quad (2.41)$$

$$h_i = \frac{\partial^2 l}{\partial \hat{y}_i^2} = p_i^{(t-1)}(1 - p_i^{(t-1)}), \quad (2.42)$$

where  $p_i^{(t-1)} = \sigma(\hat{y}_i^{(t-1)})$  is the current probability estimate. The first derivative  $g_i$  represents the residual error: for a correctly classified signal event ( $y_i = 1$ ) with high confidence ( $p_i \approx 1$ ),  $g_i \approx 0$  and the event receives little attention; for a misclassified signal event with low confidence ( $p_i \approx 0$ ),  $g_i \approx -1$  and the next tree focuses heavily on correcting this mistake. The second derivative  $h_i$  acts as an adaptive weight: it is largest ( $h_i = 0.25$ ) when the model is most uncertain ( $p_i = 0.5$ ) and smallest near the decision boundaries ( $p_i \rightarrow 0$  or  $p_i \rightarrow 1$ ), effectively allocating more optimization effort to ambiguous cases.

The performance of XGBoost depends on finding the right balance between underfitting and overfitting. Underfitting occurs when the model is too simple to capture the relevant patterns in the data, leading to poor performance on both training and test sets. In this case the model is characterized by high bias and low variance. Overfitting, on the other hand, arises when the model learns the training data too closely, including statistical fluctuations and noise. This yields very good performance on the training set but poor generalization to new data, with the model showing low bias and high variance.

Several hyperparameters play a central role in controlling this balance:

- **n\_estimators:** Number of boosting rounds. Too few trees lead to underfitting, while too many lead to overfitting. Early stopping is commonly used to determine the optimal number by monitoring validation performance.
- **Learning rate ( $\eta$ ):** Step size shrinkage applied at each boosting step. Small values (e.g. 0.01–0.1) improve generalization but require more trees; larger values speed up training but can overfit.
- **max\_depth:** Maximum depth of individual trees. Shallower trees (4–6) tend to be more stable, while deeper ones (7–10) can capture complex correlations but risk overfitting.
- **Regularization parameters:**
  - $\gamma$ : Minimum loss reduction required for a split. Larger values make the algorithm more conservative.
  - $\lambda$ : L<sub>2</sub> regularization on leaf weights, which limits large values and stabilizes the model.
  - $\alpha$ : L<sub>1</sub> regularization on leaf weights, which promotes sparsity and can serve as implicit feature selection.

Optimal hyperparameters are typically found through systematic search methods. The most common approach is *grid search with cross-validation* (GridSearchCV), which exhaustively tests all parameter combinations within predefined ranges. The core of this method is *k-fold cross-validation*, a robust technique for assessing model generalization.

The k-fold cross-validation procedure consists of the following steps: First, the available training data is randomly shuffled and partitioned into k equal-sized subsets called folds. This partitioning is typically stratified to preserve the class distribution in each fold. Then, the model is trained and evaluated k times in a round-robin fashion. For each iteration i (where i = 1 to k), the i-th fold is held out as validation data, while the remaining k-1 folds are used for training. The model's performance metric (typically negative log-loss, accuracy, or area under the ROC curve) is computed on the validation fold. After all k iterations are completed, the performance scores from each validation fold are averaged to produce a single estimation of the model's generalization error. This approach ensures that every data point is used exactly once for validation while being used k-1 times for training, providing an unbiased estimate of model performance that is robust to the specific partitioning of the data.

For XGBoost in HEP applications, we typically use k= 5 folds as it offers a good balance between computational cost and reliable error estimation. Each parameter combination is evaluated through this cross-validation process, ensuring that selected parameters generalize well beyond the training data and are not overly tuned to specific statistical fluctuations.

The grid search tests all combinations in the parameter space defined by ranges such as: `learning_rate`  $\eta \in [0.01, 0.3]$ , `max_depth`  $\in [3, 10]$ , `n_estimators`  $\in [100, 1000]$ , with regularization parameters  $\gamma$ ,  $\lambda$ , and  $\alpha$  typically explored in logarithmic scales.

While grid search is thorough, it becomes computationally expensive for high-dimensional parameter spaces. In such cases, more efficient methods like *randomized search* (which samples parameter combinations randomly) or *Bayesian optimization* (which uses probabilistic models to guide the search toward promising regions) can be employed.

The optimization process is iterative: initial broad searches identify promising parameter regions, followed by finer-grained searches around the best-performing configurations. Early stopping during training—monitoring validation performance and halting when no improvement is observed for a specified number of rounds—prevents overfitting and significantly reduces computational cost, making the hyperparameter optimization feasible for large-scale HEP analyses.

### 2.6.2 STANDARD ML ANALYSIS WORKFLOW

The XGBoost output score  $f(\mathbf{x})$  transforms high-dimensional data into a single optimal discriminant. When binned, the resulting histogram gives expected yields:

$$s_i = \int_{\text{bin } i} \sigma_s \cdot \mathcal{L} \cdot \epsilon_s \cdot p_s(f) df, \quad (2.43)$$

$$b_i = \int_{\text{bin } i} \sigma_b \cdot \mathcal{L} \cdot \epsilon_b \cdot p_b(f) df, \quad (2.44)$$

where  $p_s(f)$  and  $p_b(f)$  are the output distributions.

Integrating machine learning into high-energy physics analysis follows a standardized workflow designed to maximize sensitivity while ensuring robustness against overfitting and systematic biases:

1. **Dataset Preparation and Balancing:** Monte Carlo simulations generate signal and background samples. The signal sample corresponds to the hypothetical new physics process, while background samples include all known Standard Model processes that can produce similar experimental signatures. To prevent classifier bias toward the typically dominant background, datasets are balanced through undersampling (selecting a subset of the majority class) or, more commonly, event weighting using  $w_i = \sigma \cdot \mathcal{L} \cdot \epsilon / N_{\text{gen}}$ . Equal numbers of signal and background events are often used during training to ensure the algorithm learns both classes effectively, though the final evaluation uses proper physics weights.
2. **Feature Preprocessing:** Input variables (kinematic observables such as  $p_T$ ,  $\eta$ ,  $\phi$ , invariant masses, and angular separations) are standardized using techniques like StandardScaler (transforming to zero mean and unit variance) or MinMaxScaler (scaling to a fixed range, typically  $[0, 1]$ ). While tree-based methods like XGBoost are theoretically scale-insensitive, preprocessing improves numerical stability and convergence speed. Dimensionality reduction techniques like Principal Component Analysis (PCA) may be used for visualization or to address severe multicollinearity, though trees naturally handle correlated features.
3. **Model Training and Hyperparameter Optimization:** The classifier is trained on the preprocessed data using the procedures described in Sec. 2.6.1. Key hyperparameters—including learning rate, maximum tree depth, L1/L2 regularization strengths, and minimum child weight—are optimized via grid search, random search, or Bayesian optimization as detailed in the hyperparameter optimization strategy. Performance is evaluated using k-fold cross-validation to ensure generalizability and avoid overfitting, with the optimal configuration selected based on the best cross-validated performance.
4. **Output Score Generation:** Instead of binary class assignments, the trained model's continuous output is obtained using `predict_proba()`, which provides a per-event probability score  $f(\mathbf{x}) \in [0, 1]$  indicating the likelihood of belonging to the signal class. This score serves as a powerful discriminant variable that encapsulates the multidimensional separation power.
5. **Histogram Construction and Weighting:** Events are binned based on their classifier score to form a one-dimensional histogram. Each bin's content is calculated using the appropriate physics-level weights:

$$N_i^{\text{bin}} = \sum_{j \in \text{events in bin } i} w_j = \sum_{j \in \text{events in bin } i} (\sigma \cdot \mathcal{L} \cdot \epsilon / N_{\text{gen}})_j, \quad (2.45)$$

yielding the expected signal ( $s_i$ ) and background ( $b_i$ ) yields per bin. The binning is typically optimized to maximize the expected sensitivity, often with finer binning in regions of better signal-to-background ratio.

6. **Sensitivity Measurement:** The final histogram, incorporating all relevant systematic uncertainties as nuisance parameters, serves as input to the statistical model described in Sec. 2.5. The discovery significance  $\kappa$  (from Eq. 2.26) is computed, quantifying the analysis sensitivity and enabling comparison between different analysis strategies or machine learning approaches.

This end-to-end workflow seamlessly integrates machine learning into the established statistical framework of particle physics, transforming high-dimensional data into an optimized discriminant for sensitivity extraction.

# 3

---

## $U(1)_{T_R^3}$ GAUGE EXTENSION OF THE STANDARD MODEL

---

Extensions of the SM that introduce new  $U(1)$  gauge symmetries are among the most widely studied scenarios to address phenomenological hints while maintaining theoretical consistency. Some natural candidates to extend the SM gauge group via a  $U(1)$  factor arise from the fact that the SM exhibits several global symmetries that are not imposed by its gauge structure but emerge naturally from the renormalizable interactions allowed by the gauge group  $SU(3)_C \times SU(2)_L \times U(1)_Y$ . Among these, baryon number ( $B$ ) and lepton number ( $L$ ) conservation are particularly notable. In the SM Lagrangian, these quantum numbers are conserved at the perturbative level, making them *accidental symmetries*. However, they are not protected by any fundamental principle [206, 207].

The accidental nature of these symmetries motivates their promotion to local gauge symmetries, which would forbid dangerous operators that violate  $B$  and  $L$  at the renormalizable level, offer mechanisms for generating small neutrino masses, and address cosmological puzzles such as the matter-antimatter asymmetry [208–210]. However, not all combinations of  $B$  and  $L$  can be consistently gauged. A fundamental requirement for any gauge theory is the absence of gauge anomalies, which arise from triangle diagrams with chiral fermions and would render the quantum theory inconsistent [211–213].

Gauging  $B$  or  $L$  separately leads to gauge anomalies that cannot be canceled within the SM fermion content. In contrast, the  $U(1)_{B-L}$  combination is anomaly-free when right-handed neutrinos are included, as quarks carry  $B - L = 1/3$  while leptons carry  $B - L = -1$ , leading to natural cancellation generation by generation [208, 209]. This makes  $U(1)_{B-L}$  a particularly well-motivated extension that appears naturally in grand unified theories [214, 215] and in left-right symmetric models [216–218].

An interesting question in BSM model building concerns the possible connection between gauged  $B - L$  symmetry and the hypercharge  $U(1)_Y$  of the SM. In left-right symmetric models based on the gauge group  $SU(3)_C \times SU(2)_L \times SU(2)_R \times U(1)_{B-L}$  [216–218], the hypercharge emerges from the spontaneous breaking of the extended gauge symmetry. Specifically, the breaking pattern involves two  $U(1)$  factors:  $U(1)_{B-L}$  and an additional  $U(1)$  associated with the right-handed sector. This second factor, denoted  $U(1)_{T_R^3}$ , corresponds to the diagonal, electrically neutral generator of  $SU(2)_R$ —the

third component of the right-handed weak isospin. The name  $T_R^3$  reflects its role as the right-handed analog of the weak isospin component  $T_L^3$  in the SM's  $SU(2)_L$ . In that framework, the SM hypercharge emerges from the breaking pattern

$$U(1)_{B-L} \times U(1)_{T_R^3} \rightarrow U(1)_Y,$$

establishing a direct connection between  $B - L$  conservation and the electroweak structure. This relationship provides strong theoretical motivation for considering  $U(1)_{T_R^3}$  as a gauge extension of the SM [219–221]. Moreover, it suggests that phenomenological signatures associated with  $U(1)_{T_R^3}$  could provide indirect evidence for the underlying left-right symmetric structure and the role of  $B - L$  in electroweak symmetry breaking.

In this framework, right-handed SM fermions are charged under  $U(1)_{T_R^3}$ , leading to distinct phenomenological predictions. In the minimal realization, the  $SU(2)_L$  Higgs doublet is a singlet under  $U(1)_{B-L}$  and acquires its hypercharge from  $U(1)_{T_R^3}$ . Its vacuum expectation value (VEV) links the symmetry-breaking scales of  $U(1)_Y$  and  $U(1)_{T_R^3}$ . Alternatively, these scales can be decoupled by introducing an additional  $U(1)_G$  group, under which SM fermions are singlets but the Higgs is charged. The inclusion of this symmetry provides model-building freedom to explore a wider range of phenomenological scenarios. For that case, the hypercharge is given by the linear combination

$$Y = Q_{T_R^3} + \frac{1}{2}Q_{B-L} + Q_G. \quad (3.1)$$

More generally, scenarios can be constructed where the hypercharge is not directly related to  $U(1)_{T_R^3}$ .

In any case, recent theoretical and phenomenological work has focused on models where the low-energy gauge symmetry of the SM is extended by this Abelian group, with the crucial feature that the spontaneous breaking of  $U(1)_{T_R^3}$  is not tied to electroweak symmetry breaking. It has been shown to resolve tensions related to lepton flavor violation (LFV) and lepton universality violation (LUV) by explaining the anomalous magnetic moment of the muon ( $g - 2)_\mu$ , B meson anomalies [222], and providing viable dark matter candidates [223–225]. We are interested in exploring the collider phenomenology of this  $U(1)_{T_R^3}$  extension, assuming that the breaking of this symmetry occurs at a scale much higher than the electroweak scale.

The spontaneous breaking of  $U(1)_{T_R^3}$  requires the introduction of a complex scalar field  $\phi$ , which is a singlet under the SM gauge group. When  $\phi$  acquires a vacuum expectation value, the symmetry is spontaneously broken, and the associated electrically neutral gauge boson becomes massive by absorbing the CP-odd (pseudoscalar) component of  $\phi$  as its longitudinal degree of freedom. The CP-even component of  $\phi$  remains in the physical spectrum as a scalar particle, denoted  $\phi'$ , commonly referred to as the dark Higgs [226–229]. And, to ensure anomaly cancellation in the  $U(1)_{T_R^3}$  model, a right-handed neutrino  $\nu_R$  is required for each SM generation. In addition, a set of new vector-like fermions  $(\chi_u, \chi_d, \chi_\ell, \chi_\nu)$  is introduced to generate fermion masses in a UV-complete theory, following the universal see-saw

mechanism [230–235], see App. A. The universal see-saw mechanism introduces a non-trivial coupling between the top quark and the vector-like quark  $\chi_u$  through the dark Higgs  $\phi'$ , enabling the vertex  $\chi_u - t - \phi'$ . This coupling allows for the production of  $t\chi_u\phi'$  final states via  $\chi_u-t$  fusion. Since  $\chi_u$  couples to SM quarks and gluons, it can be copiously produced at hadron colliders. Its energetic decay products, together with a  $\phi'$  mediator carrying significant transverse momentum, can be efficiently detected, especially if  $\phi'$  decays to visible SM particles in the central detector region.

In this chapter, we present a phenomenological study of search strategies at the LHC for a light (GeV-scale) scalar  $\phi'$  produced in association with a heavy (TeV-scale) top-partner  $\chi_u$ . This work, that has been published as [2], focuses on the previously unexplored production channel  $pp \rightarrow t\chi_u\phi'$ . This contrasts with more commonly studied processes  $pp \rightarrow \chi_u\chi_u \rightarrow t\phi't\phi'$ , and the di-photon  $\phi'$  decay channels (see Sec. 3.2 and [236–240]).

To further maximize the sensitivity to this complex signal, a central component of our analysis is the use of ML. We employ an analysis based on Boosted Decision Trees (BDT) [201]. The BDT output is used in a profile-binned likelihood test to determine the signal significance for each model. The effectiveness of BDTs and other ML algorithms has been demonstrated in numerous experimental and phenomenological studies [241–250]. Our results show that the BDT approach significantly improves sensitivity.

The remainder of this chapter is organized as follows. Sec. 3.1 describes the minimal  $U(1)_{T_R^3}$  model. Sec. 3.2 reviews current relevant LHC results. Sec. 3.3 details the MC simulation samples used in this study. Sec. 3.4 discusses the motivation and implementation of the machine learning workflow, and Sec. 3.5 presents the main results.

### 3.1 THE MINIMAL $U(1)_{T_R^3}$ MODEL

---

The model extends the SM by an Abelian gauge symmetry  $U(1)_{T_R^3}$ , under which only the right-handed fermions are charged. The symmetry breaking is achieved via two independent Higgs mechanisms: one with the SM Higgs  $SU(2)_L$  doublet  $H$  for electroweak symmetry breaking, and another with a Higgs singlet  $\phi$  for  $U(1)_{T_R^3}$  breaking. These scalars acquire independent vacuum expectation values (VEVs),  $\langle H \rangle = v_h/\sqrt{2}$  and  $\langle \phi \rangle = v_\phi/\sqrt{2}$ . In the Kibble parametrization, the fields are written as:

$$H = \begin{pmatrix} G_+ \\ \frac{1}{\sqrt{2}}(v_h + \rho_0 + iG_0) \end{pmatrix}, \quad (3.2)$$

$$\phi = \frac{1}{\sqrt{2}}(v_\phi + \rho_\phi + iG_\phi). \quad (3.3)$$

In Eqs. (3.2) and (3.3),  $G_\pm$ ,  $G_0$ , and  $G_\phi$  are the Goldstone bosons absorbed by the SM  $W^\pm$  and  $Z$  bosons and the dark photon  $A'$  (associated with

$U(1)_{T_R^3}$ ) to acquire mass. The fields  $\rho_0$  and  $\rho_\phi$  mix to form the physical mass eigenstates, the SM-like Higgs boson  $h$  and a dark Higgs  $\phi'$ :

$$\begin{pmatrix} h \\ \phi' \end{pmatrix} = \begin{pmatrix} \cos \alpha & -\sin \alpha \\ \sin \alpha & \cos \alpha \end{pmatrix} \begin{pmatrix} \rho_0 \\ \rho_\phi \end{pmatrix}. \quad (3.4)$$

This mixing arises from diagonalizing the mass matrix derived from the gauge-invariant scalar potential:

$$\begin{aligned} V(H, \phi) = & \mu_H^2 H^\dagger H + \mu_\phi^2 \phi^* \phi \\ & + \lambda(H^\dagger H)(\phi^* \phi) + \lambda_H(H^\dagger H)^2 + \lambda_\phi(\phi^* \phi)^2. \end{aligned} \quad (3.5)$$

Minimizing the potential yields the tadpole equations:

$$\frac{\partial V}{\partial H} = \frac{v_h}{\sqrt{2}} \left( \mu_H^2 + \lambda_H v_h^2 + \frac{1}{2} \lambda v_\phi^2 \right) = 0, \quad (3.6)$$

$$\frac{\partial V}{\partial \phi} = \frac{v_\phi}{\sqrt{2}} \left( \mu_\phi^2 + \lambda_\phi v_\phi^2 + \frac{1}{2} \lambda v_h^2 \right) = 0. \quad (3.7)$$

These equations allow us to express the quadratic couplings  $\mu_H^2$  and  $\mu_\phi^2$  in terms of the VEVs and quartic couplings, ensuring that the VEVs  $v_h$  and  $v_\phi$  are true minima of the potential.

To determine the physical scalar masses, we expand the potential around the minimum. Substituting the Kibble parametrizations Eqs. (3.2) and (3.3) into the scalar potential and keeping only terms quadratic in the fluctuations  $\rho_0$  and  $\rho_\phi$ , we obtain:

$$V \supset \frac{1}{2} (\rho_0 \quad \rho_\phi) \begin{pmatrix} \frac{\partial^2 V}{\partial \rho_0^2} & \frac{\partial^2 V}{\partial \rho_0 \partial \rho_\phi} \\ \frac{\partial^2 V}{\partial \rho_\phi \partial \rho_0} & \frac{\partial^2 V}{\partial \rho_\phi^2} \end{pmatrix} \begin{pmatrix} \rho_0 \\ \rho_\phi \end{pmatrix}. \quad (3.8)$$

Computing the second derivatives at the minimum, we find the mass-squared matrix in the  $(\rho_0, \rho_\phi)$  basis to be:

$$\mathcal{M}^2 = \begin{pmatrix} 2\lambda_H v_h^2 & \lambda v_h v_\phi \\ \lambda v_h v_\phi & 2\lambda_\phi v_\phi^2 \end{pmatrix}, \quad (3.9)$$

where the diagonal elements  $\mathcal{M}_{11}^2 = 2\lambda_H v_h^2$  and  $\mathcal{M}_{22}^2 = 2\lambda_\phi v_\phi^2$  represent the squared masses of  $\rho_0$  and  $\rho_\phi$  in the absence of mixing, while the off-diagonal element  $\mathcal{M}_{12}^2 = \mathcal{M}_{21}^2 = \lambda v_h v_\phi$  quantifies the mixing between the two scalar fields induced by the portal coupling  $\lambda$ . This matrix is symmetric but not diagonal, indicating that  $\rho_0$  and  $\rho_\phi$  are not mass eigenstates. The physical scalar masses are obtained by diagonalizing  $\mathcal{M}^2$  via an orthogonal rotation parametrized by the mixing angle  $\alpha$ , as shown in Eq. (3.5). Explicitly, we perform the similarity transformation:

$$\mathcal{M}_{\text{diag}}^2 = R(\alpha)^\top \mathcal{M}^2 R(\alpha), \quad (3.10)$$

where  $R(\alpha)$  is the rotation matrix:

$$R(\alpha) = \begin{pmatrix} \cos \alpha & -\sin \alpha \\ \sin \alpha & \cos \alpha \end{pmatrix}. \quad (3.11)$$

Performing this matrix multiplication explicitly:

$$\begin{aligned}\mathcal{M}_{\text{diag}}^2 &= \begin{pmatrix} \cos \alpha & -\sin \alpha \\ \sin \alpha & \cos \alpha \end{pmatrix} \begin{pmatrix} 2\lambda_H v_h^2 & \lambda v_h v_\phi \\ \lambda v_h v_\phi & 2\lambda_\phi v_\phi^2 \end{pmatrix} \begin{pmatrix} \cos \alpha & \sin \alpha \\ -\sin \alpha & \cos \alpha \end{pmatrix} \\ &= \begin{pmatrix} m_h^2 & 0 \\ 0 & m_{\phi'}^2 \end{pmatrix},\end{aligned}\quad (3.12)$$

where the diagonal elements are the physical squared masses. The mixing angle  $\alpha$  is determined by requiring that the off-diagonal element of the rotated matrix vanishes. Computing this element explicitly:

$$(\mathcal{M}_{\text{diag}}^2)_{12} = (\lambda_\phi v_\phi^2 - \lambda_H v_h^2) \sin \alpha \cos \alpha + \lambda v_h v_\phi (\cos^2 \alpha - \sin^2 \alpha). \quad (3.13)$$

Setting this to zero and using the double-angle identities  $\sin 2\alpha = 2 \sin \alpha \cos \alpha$  and  $\cos 2\alpha = \cos^2 \alpha - \sin^2 \alpha$ , we obtain:

$$\frac{1}{2}(\lambda_\phi v_\phi^2 - \lambda_H v_h^2) \sin 2\alpha + \lambda v_h v_\phi \cos 2\alpha = 0, \quad (3.14)$$

from which we obtain:

$$\tan 2\alpha = \frac{-2\lambda v_h v_\phi}{\lambda_H v_h^2 - \lambda_\phi v_\phi^2}. \quad (3.15)$$

The physical scalar masses are then the eigenvalues of  $\mathcal{M}^2$ , given by:

$$m_{h,\phi'}^2 = \frac{1}{2} (\lambda_H v_h^2 + \lambda_\phi v_\phi^2) \pm \frac{1}{2} \sqrt{4\lambda^2 v_h^2 v_\phi^2 + (\lambda_H v_h^2 - \lambda_\phi v_\phi^2)^2}, \quad (3.16)$$

where the  $(+/-)$  sign corresponds to the heavier (lighter) mass eigenstate. The quartic couplings can be expressed in terms of the physical parameters:

$$\lambda_H = \frac{m_h^2 \cos^2 \alpha + m_{\phi'}^2 \sin^2 \alpha}{2v_h^2} = \frac{m_{\phi'}^2 + m_h^2 + (m_{\phi'}^2 - m_h^2) \cos 2\alpha}{4v_h^2}, \quad (3.17)$$

$$\lambda_\phi = \frac{m_h^2 \sin^2 \alpha + m_{\phi'}^2 \cos^2 \alpha}{2v_\phi^2} = \frac{m_{\phi'}^2 + m_h^2 - (m_{\phi'}^2 - m_h^2) \cos 2\alpha}{4v_\phi^2}, \quad (3.18)$$

$$\lambda = \frac{(m_{\phi'}^2 - m_h^2) \sin \alpha \cos \alpha}{v_h v_\phi} = \frac{m_{\phi'}^2 - m_h^2}{2v_h v_\phi} \sin 2\alpha. \quad (3.19)$$

Thus, the scalar sector has four free parameters: the masses  $m_h$  and  $m_{\phi'}$ , the mixing angle  $\alpha$ , and the dark Higgs VEV  $v_\phi$ . Similar to how  $v_h$  is fixed by the electroweak gauge boson masses,  $v_\phi$  is related to the dark photon mass by  $m_{A'}^2 = g_{T_R^3}^2 v_\phi^2$ , where  $g_{T_R^3}$  is the  $U(1)_{T_R^3}$  gauge coupling. Depending on the value of  $g_{T_R^3}$ , this gauge boson can behave as a heavy  $Z'$  or a light dark photon. In this chapter, we assume  $g_{T_R^3}$  is sufficiently small such that  $A'$  can be treated as a dark photon.

### 3.1.1 THE UNIVERSAL SEESAW MECHANISM

In this model, the masses of the SM fermions are generated through a universal seesaw mechanism by mixing with vector-like fermions  $\chi_f$ . The relevant mass terms in the Lagrangian are:

$$-\mathcal{L} \supset Y_{f_L} \bar{f}'_L \chi'_R H + Y_{f_R} \bar{\chi}'_{fL} f'_R \phi^* + m_{\chi'_f} \bar{\chi}'_{fL} \chi'_R + \text{h.c.} \quad (3.20)$$

This leads to the mass matrix:

$$M_f = \begin{pmatrix} 0 & Y_{f_L} v_h / \sqrt{2} \\ Y_{f_R} v_\phi / \sqrt{2} & m_{\chi'_f} \end{pmatrix}. \quad (3.21)$$

The mass eigenstates  $(f, \chi_f)$  are obtained by rotating the gauge eigenstates:

$$\begin{pmatrix} f_{L,R} \\ \chi_{f_{L,R}} \end{pmatrix} = \begin{pmatrix} \pm \cos \theta_{f_{L,R}} & \mp \sin \theta_{f_{L,R}} \\ \sin \theta_{f_{L,R}} & \cos \theta_{f_{L,R}} \end{pmatrix} \begin{pmatrix} f'_{L,R} \\ \chi'_{f_{L,R}} \end{pmatrix}, \quad (3.22)$$

such that  $\mathcal{R}(\theta_{f_L}) M_f \mathcal{R}^{-1}(\theta_{f_R}) = \text{diag}(m_f, m_{\chi_f})$ . For real parameters, the physical masses and mixing angles are given by:

$$m_f m_{\chi_f} = \frac{Y_{f_L} v_h Y_{f_R} v_\phi}{2}, \quad (3.23)$$

$$m_f^2 + m_{\chi_f}^2 = m_{\chi'_f}^2 + \frac{1}{2} (Y_{f_L}^2 v_h^2 + Y_{f_R}^2 v_\phi^2), \quad (3.24)$$

$$\tan \theta_{f_{L,R}} = \frac{\sqrt{2}}{m_{\chi'_f}} \left( \frac{Y_{f_{L,R}} v_{h,\phi}}{2} - \frac{m_f^2}{Y_{f_{L,R}} v_{h,\phi}} \right). \quad (3.25)$$

The Yukawa interactions of the physical fermions with the scalars  $h$  and  $\phi'$  are:

$$-\mathcal{L}_{\text{yuk}} = h \bar{\psi}_{f_L} \gamma_h \psi_{f_R} + \phi' \bar{\psi}_{f_L} \gamma_\phi \psi_{f_R}, \quad (3.26)$$

where  $\psi_f = \begin{pmatrix} f \\ \chi_f \end{pmatrix}$ . The Yukawa matrices are:

$$\gamma_h = \frac{1}{\sqrt{2}} \mathcal{R}(\theta_{f_L}) (Y_{f_L} \sigma_+ \cos \alpha - Y_{f_R} \sigma_- \sin \alpha) \mathcal{R}^{-1}(\theta_{f_R}), \quad (3.27)$$

$$\gamma_\phi = \frac{1}{\sqrt{2}} \mathcal{R}(\theta_{f_L}) (Y_{f_L} \sigma_+ \sin \alpha + Y_{f_R} \sigma_- \cos \alpha) \mathcal{R}^{-1}(\theta_{f_R}), \quad (3.28)$$

with  $\sigma_\pm = (\sigma_1 \pm i\sigma_2)/2$  being the ladder Pauli matrices.

The expressions above provide a simplified, one-generation view. The complete model involves a non-trivial flavor structure where the mass matrices are general  $3 \times 3$  matrices. The diagonalization of the full  $6 \times 6$  mass matrices, the procedure for absorbing unphysical unitary rotations, and the emergence of the CKM matrix are detailed in Appendix A. Furthermore, the appendix contains a rigorous treatment of the mass eigenvalue problem, deriving the exact relationship between the fundamental parameters  $(m_L, m_R, m_\chi)$  and the physical observables  $(m_f, m_F, \theta_L)$ , which leads to critical constraints on the model's parameter space to ensure perturbativity.

Field	$SU(3)_C$	$SU(2)_L$	$U(1)_Y$	$U(1)_{T_R^3}$
$q'_L$	<b>3</b>	<b>2</b>	$1/6$	0
$\ell'_L$	<b>1</b>	<b>2</b>	$-1/2$	0
$H$	<b>1</b>	<b>2</b>	$1/2$	0
$u'^c_R$	<b>3</b>	<b>1</b>	$-2/3$	-2
$d'^c_R$	<b>3</b>	<b>1</b>	$1/3$	2
$\ell'^c_R$	<b>1</b>	<b>1</b>	1	2
$\nu'^c_R$	<b>1</b>	<b>1</b>	0	-2
$\phi$	<b>1</b>	<b>1</b>	0	2
$\chi'_{u_L}$	<b>3</b>	<b>1</b>	$2/3$	0
$\chi'_{u_R}$	<b>3</b>	<b>1</b>	$-2/3$	0
$\chi'_{d_L}$	<b>3</b>	<b>1</b>	$-1/3$	0
$\chi'_{d_R}$	<b>3</b>	<b>1</b>	$1/3$	0
$\chi'_{\ell_L}$	<b>1</b>	<b>1</b>	-1	0
$\chi'_{\ell_R}$	<b>1</b>	<b>1</b>	1	0
$\chi'_{\nu_L}$	<b>1</b>	<b>1</b>	0	0
$\chi'_{\nu_R}$	<b>1</b>	<b>1</b>	0	0

**Table 3.1:** Minimal field content of the model and their representations under the SM and  $U(1)_{T_R^3}$  gauge groups.

### 3.1.2 MINIMAL UV-COMPLETE THEORY

To generate non-zero masses for all SM fermions and ensure gauge anomaly cancellation, the model must include at least one full generation of vector-like fermions  $\{\chi_u, \chi_d, \chi_\ell, \chi\}$  and the right-handed neutrinos  $\nu_R$  for each SM generation. Their quantum numbers are listed in Tab. 3.1. The Yukawa interactions in the UV-complete theory are:

$$\begin{aligned}
 -\mathcal{L} \supset & Y_{Lu}^{ij} \bar{q}_L^{i'} \chi_{uR}^{j'} \tilde{H} + Y_{Ru}^{ij} \bar{\chi}_{uL}^{i'} u_R^{j'} \phi^* + m_{\chi_u}^{ij} \bar{\chi}_{uL}^{i'} \chi_{uR}^{j'} \\
 & + Y_{Ld}^{ij} \bar{q}_L^{i'} \chi_{dR}^{j'} H + Y_{Rd}^{ij} \bar{\chi}_{dL}^{i'} d_R^{j'} \phi + m_{\chi_d}^{ij} \bar{\chi}_{dL}^{i'} \chi_{dR}^{j'} \\
 & + Y_{L\ell}^{ij} \bar{q}_L^{i'} \chi_{\ell R}^{j'} H + Y_{R\ell}^{ij} \bar{\chi}_{\ell L}^{i'} \ell_R^{j'} \phi + m_{\chi_\ell}^{ij} \bar{\chi}_{\ell L}^{i'} \chi_{\ell R}^{j'} \\
 & + Y_{L\nu}^{ij} \bar{q}_L^{i'} \chi_{\nu R}^{j'} \tilde{H} + Y_{R\nu}^{ij} \bar{\chi}_{\nu L}^{i'} \nu_R^{j'} \phi^* + m_{\chi_\nu}^{ij} \bar{\chi}_{\nu L}^{i'} \chi_{\nu R}^{j'} + \text{h.c.}
 \end{aligned} \tag{3.29}$$

Here,  $i, j = 1, 2, 3$  are generation indices. The diagonalization of the mass matrices for each fermion type follows the structure outlined in Eqs. (3.23) and (3.24), while the Yukawa matrices generalize the structure of Eqs. (3.27) and (3.28), now encoding the CKM and PMNS mixing matrices. The neutrino sector has a more complex structure due to the possibility of a Majorana mass term for the vector-like neutrinos  $\chi'_\nu$ .

## 3.2 CURRENT EXCLUSION LIMITS ON VECTOR-LIKE QUARKS

The ATLAS and CMS collaborations at CERN have conducted various searches for heavy vector-like quarks. These searches utilized pp collisions

at center-of-mass energies of  $\sqrt{s} = 8$  and 13 TeV. The studies primarily focused on  $\chi_u$  production through gluon-mediated QCD processes, either in pair production from quark-antiquark annihilation (Fig. 3.1) or in single- $\chi_u$  production from electroweak processes involving associated quarks (Fig. 3.2).

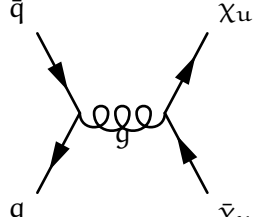


**Figure 3.1:** Representative Feynman diagram for  $\chi_u$  pair production via gluon-mediated QCD processes ( $q\bar{q} \rightarrow g \rightarrow \chi_u\bar{\chi}_u$ ).

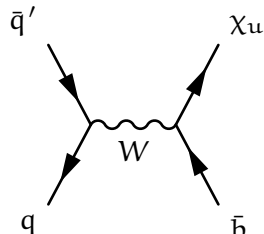


**Figure 3.2:** Representative Feynman diagram for single  $\chi_u$  production via electroweak processes ( $q\bar{q}' \rightarrow W \rightarrow \chi_u\bar{\chi}_u$ ).

In those studies,  $\chi_u$  decays into  $bW$ ,  $tZ$ , or  $tH$  have been considered. In the context of  $\chi_u$  pair production,  $\chi_u\bar{\chi}_u$ , via QCD processes, the cross sections are well-known and solely depend on the mass of the vector-like quark. Assuming a narrow  $\chi_u$  decay width ( $\Gamma/m(\chi_u) < 0.05$  or 0.1) and a 100% branching fraction to  $bW$ ,  $tZ$ , or  $tH$ , these searches have set stringent bounds on  $m(\chi_u)$ , excluding masses below almost 1.5 TeV at 95% confidence level [251–258]. The most recent analysis from the CMS collaboration probes  $\chi_u$ -quark production via  $pp \rightarrow \chi_u qb$ , in final states with  $\chi_u \rightarrow tZ$  or  $\chi_u \rightarrow tH$ , considering scenarios with preferential couplings to third-generation fermions. The analysis sets 95% confidence level upper limits of 68 – 1260 fb on the production cross section, for  $\chi_u$  masses ranging from 600–1200 GeV [252]. The latest studies from ATLAS probe vector-like quarks using the single- $\chi_u$  production mode with the  $\chi_u \rightarrow tH$  decay channel leading to a fully hadronic final state [253], the single- $\chi_u$  production mode with the  $\chi_u \rightarrow tZ$  decay channel leading to a multileptonic final state [254], the  $\chi_u\chi_u$  pair production mode with various  $\chi_u$  decay channels leading to multileptonic final states [255], and the  $\chi_u\chi_u$  pair production mode with various  $\chi_u$  decay channels leading to a single lepton plus missing momentum final state [256, 257]. The multilepton search offers the greatest sensitivity in most of the phase space, but the missing transverse energy based search has better sensitivity for low branching fraction  $\mathcal{B}(\chi_u \rightarrow Wb)$  and high  $\mathcal{B}(\chi_u \rightarrow Ht)$ . These searches have similar sensitivities for the singlet and doublet models, resulting in exclusion bounds for masses below about 1.25 TeV and 1.41 TeV, respectively.

A key consideration in the model interpretations summarized above is that the  $\chi_u$  branching fractions depend on the chosen model. The excluded mass range is less restrictive for specific branching fraction scenarios, such as  $\{\mathcal{B}(\chi_u \rightarrow tZ), \mathcal{B}(\chi_u \rightarrow bW), \mathcal{B}(\chi_u \rightarrow tH)\} = \{0.2, 0.6, 0.2\}$ , setting bounds on masses below about 0.95 TeV. Moreover, if the  $\chi_u \rightarrow \phi' t$  decay is allowed, or if the branching fractions  $\mathcal{B}(\chi_u \rightarrow tH/bW)$  are lower, the limits previously quoted must be re-evaluated. The authors of Ref. [259] emphasize that bounds on  $m(\chi_u)$  can be around 500 GeV when  $\chi_u \rightarrow t\phi'$  decays are permitted. Therefore, to facilitate a comprehensive study, benchmark scenarios in this paper are considered down to  $m(\chi_u) = 500$  GeV.

### 3.3 STRATEGY, SAMPLES AND SIMULATION

---

The universal see-saw mechanism introduces a non-trivial coupling between the top quark and the vector-like quark  $\chi_u$  through the dark Higgs  $\phi'$ , enabling the vertex  $\chi_u - t - \phi'$ . This coupling allows for the production of  $t\chi_u\phi'$  final states via  $\chi_u-t$  fusion, see Fig. 3.3. Since  $\chi_u$  couples to SM quarks and gluons, it can be copiously produced at hadron colliders. Its energetic decay products, together with a  $\phi'$  mediator carrying significant transverse momentum, can be efficiently detected, especially if  $\phi'$  decays to visible SM particles in the central detector region.

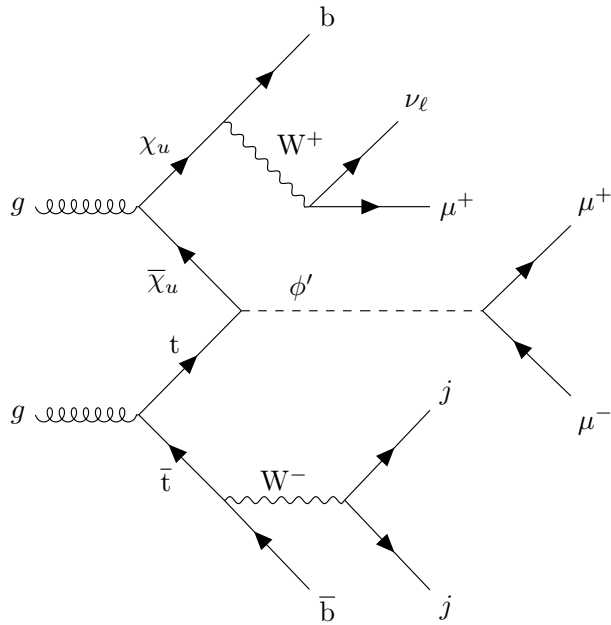


**Figure 3.3:** Representative Feynman diagram for the production of a  $\phi'$  boson in association with a  $\chi_u$  vector-like quark through the fusion of a top quark and  $\chi_u$  vector-like quark. Once again, the  $\phi'$  decays to a pair of muons, the top quark decays fully hadronically, and the  $\chi_u$  decays semi-leptonically to muons, neutrinos and  $b$ -jets.

This strategy is effective for reducing SM backgrounds and enhances the LHC discovery potential for heavy top partners and GeV-scale mediators, which are otherwise challenging to probe at hadron colliders. Moreover,  $t\chi_u\phi'$  final states can also arise from  $\chi_u\bar{\chi}_u$  production via QCD vertices, where one  $\chi_u$  decays to  $t\phi'$  (see Fig. 3.4). The presence of energetic decay products and a mediator with substantial transverse momentum provides greater sensitivity than searches considering  $\chi_u$  or  $\phi'$  alone.

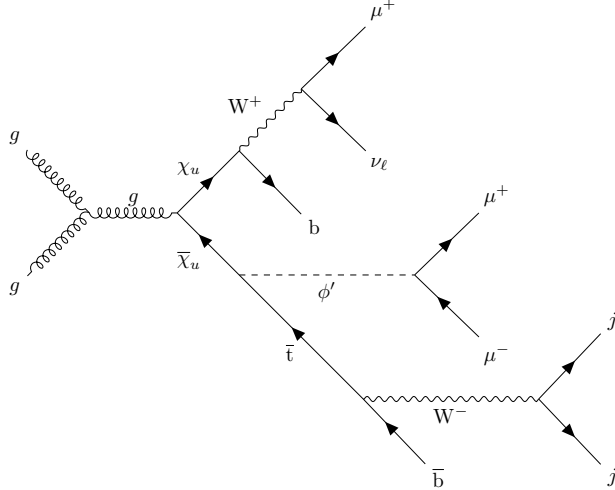


**Figure 3.4:** Representative Feynman diagram for the production of a  $\phi'$  boson in association with a  $\chi_u$  vector-like quark through the fusion of a gluon pair from incoming protons. The  $\phi'$  decays to a pair of muons, the top quark that decays fully hadronically, and the  $\chi_u$  decay semi-leptonically to muons, neutrinos and jets.

We consider the case where  $\phi'$  has family non-universal couplings to fermions, as proposed in [260]. Such couplings can address several open questions in the SM. Our analysis focuses on  $\phi' \rightarrow \mu^+\mu^-$  decays, as muons are efficiently reconstructed and identified. This allows for low  $p_T(\mu)$  triggers and provides a characteristically clean signature to suppress QCD multijet backgrounds.

The minimal  $U(1)_{T_R^3}$  model described in Sec. 3.1 is implemented *at tree level* into the FeynRules package [128], which generates the Feynman rules and exports them into a Universal FeynRules Output (UFO) [182]. The resulting UFO is utilized as input for a generator to produce the MC samples. We have used the implementation of the  $U(1)_{T_R^3}$  model in Ref. [261]. Both signal and background events are generated with the MadGraph5\_aMC@NLO v3.2.0 program [127, 188] at leading order (LO) in QCD, considering pp beams colliding with a center-of-mass energy of  $\sqrt{s} = 13.6$  TeV. Each signal and background sample is generated separately, with no interference effects between the signal and background considered. We use the NNPDF3.0 NLO [135] set for parton distribution functions (PDFs) for all event generation. Parton-level events are then interfaced with PYTHIA (v8.2.44) [133] to account for parton showering and hadronization processes. Finally, we use DELPHES (v3.4.2) [129] to simulate smearing and

other detector effects using the CMS detector geometric configurations and parameters for particle identification and reconstruction, using the CMS input card with 140 average pileup interactions.

All signal cross sections used in this analysis are obtained requiring the following kinematic criteria on leptons ( $\ell$ ), b quarks, and light-quark/gluon jets ( $j$ ) at parton level in MadGraph:  $p_T(\ell) > 35 \text{ GeV}$ ,  $|\eta(b)| < 2.5$ ,  $|\eta(\ell)| < 2.3$ ,  $p_T(j) > 20 \text{ GeV}$ , and  $|\eta(j)| < 5$ . These parton-level selections were applied exclusively to the signal processes to restrict event generation to the relevant phase space regions. For background processes, these default parton level requirements in MadGraph were imposed:  $p_T(\ell) > 10 \text{ GeV}$ ,  $|\eta(\ell)| < 2.5$ ,  $p_T(j) > 20 \text{ GeV}$ ,  $|\eta(j)| < 5$ , and  $|\eta(b)| < 5$ . This ensures that the phase space regions for the background near the analysis-level selection criteria are adequately described after parton showering since the pre-selections at the analysis level are more stringent than the parton-level requirements. Furthermore, we use the MLM algorithm for jet matching and jet merging. The parameters  $x_{\text{qcut}}$  and  $q_{\text{cut}}$  of the MLM algorithm are set to 30 and 45 respectively to ensure continuity of the differential jet rate as a function of jet multiplicity. Each simulated signal and background sample is produced separately at LO, with one million events at the generation level, neglecting potential interference effects between the signal and background due to the suppression caused by the different orders of magnitude in the coupling constants of the signal and background.

Signal samples are generated considering the production of a  $\phi'$  boson, an associated  $\chi_u$  vector-like quark, and a top quark ( $pp \rightarrow \chi_u t \phi'$ ) (see Figures 3.3-3.4). Signal samples were created considering coupling values of  $Y_{t_R} = Y_{t_L} = 2\sqrt{2}$  in the range of masses  $m_{\phi'} \in \{5, 10, 50, 100, 325\} \text{ GeV}$  for the dark higgs and  $m_{\chi_u} \in \{0.50, 0.75, 1.0, 1.5, 2.0, 2.5\} \text{ TeV}$  for the vector-like quark  $\chi_u$  [262]. The production cross section for  $pp \rightarrow \chi_u t \phi'$  is highly dependent on the choice of the Yukawa couplings in the Lagrangian. The  $\chi_u - t$  fusion process, shown in Fig. 3.3, is dominated by the  $Y_{t_R}$  coupling. However, the decay  $\chi_u \rightarrow t \phi'$  shown in Fig. 3.4 is inversely proportional to the  $Y_{t_L}$  coupling. This effect is shown in Fig. 3.5, which displays the total signal cross section, as a function of  $Y_{t_R}$  and  $Y_{t_L}$ , for a benchmark point with  $m_{\phi'} = 100 \text{ GeV}$  and  $m_{\chi_u} = 1.0 \text{ TeV}$ .

We target signal events where the top quark decays hadronically into a bottom quark and two jets ( $t \rightarrow bW \rightarrow bq\bar{q}'$ ), benefiting from its large branching ratio of  $\approx 67.2\%$ . In addition, the  $\chi_u$  decays semileptonically into a b quark, lepton, and neutrino (via  $\chi_u \rightarrow bW$  and  $W \rightarrow \mu\nu_\mu$ ), while the  $\phi'$  produces two muons. This final state provides clean signatures with relatively low trigger  $p_T$  thresholds. We emphasize again that the scalar  $\phi'$  particle could result from the mixture of the SM Higgs boson and additional scalar fields, and the Yukawas of the fermions could additionally arise from the mixing of the SM fermions with additional copies of the associated vector-like fermions. Therefore, the  $\phi'$  branching ratios are dependent on the chosen mechanism and model by which this mixture occurs, see for example, Refs. [118, 263–265]. For the purpose of this work,

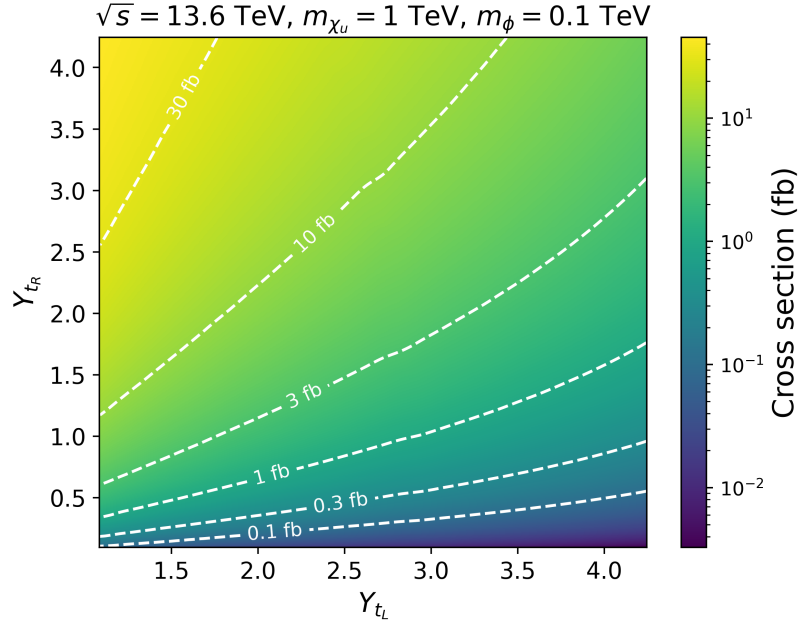


**Figure 3.5:** Signal production cross section,  $pp \rightarrow \chi_u t \phi'$ , in the  $Y_{t_R}$  versus  $Y_{t_L}$  plane, for a benchmark point with  $m_{\phi'} = 100$  GeV and  $m_{\chi_u} = 1.00$  TeV. The white-dashed contours show specific cross section values in the two dimensional plane.

and similar to Refs. [260, 261], the considered benchmark signal scenarios have  $\mathfrak{B}(\chi_u \rightarrow b W)$  of about 0.5 and  $\mathfrak{B}(\phi' \rightarrow \mu^+ \mu^-) = 1.00$ . Fig. 3.6 shows the production cross section in fb, as a function of  $m_{\phi'}$  and  $m_{\chi_u}$  masses, assuming the aforementioned decays, branching ratios, and couplings.

We note that for the parameter space of focus in this paper, the total mass of the  $t\chi_u$  system is larger than  $m_{\phi'}$ , thus the large rest energy of the  $t\chi_u$  system is converted into potentially large momentum values for the  $\phi'$ . Similarly, the  $t$ -quark produced through the  $\chi_u$ - $t$  fusion interaction can also have large momentum values, and thus in some cases the hadronic  $t$  decay products cannot be fully reconstructed independently of each other. This results in three possible  $t$  reconstruction scenarios: a fully merged scenario where the  $W \rightarrow jj$  system and the  $b$  quarks are very collimated and reconstructed as a single “fat jet” (henceforth referred to as a FatJet, FJ); a partially merged scenario, where the decay products of the  $W$  boson form a single FatJet but the  $b$  quark can still be separately identified; and an unmerged scenario where all decay products can be independently identified. Thus, jets are clustered using the anti- $k_t$  algorithm [266] as implemented in the FastJet (v3.4.2) [267] package, with a distance parameter of  $R = 0.4$  for standard jets and  $R = 0.8$  for fat jet objects. Each scenario has an associated identification efficiency and misidentification rate, which depends on the choice of the boosted  $t/W$  algorithm (our choice of efficiency and misidentification rates is described later).

Based on the details above, the final state of interest in this paper consists of three muons (two from the  $\phi'$  decay and one from the  $\chi_u$  decay),

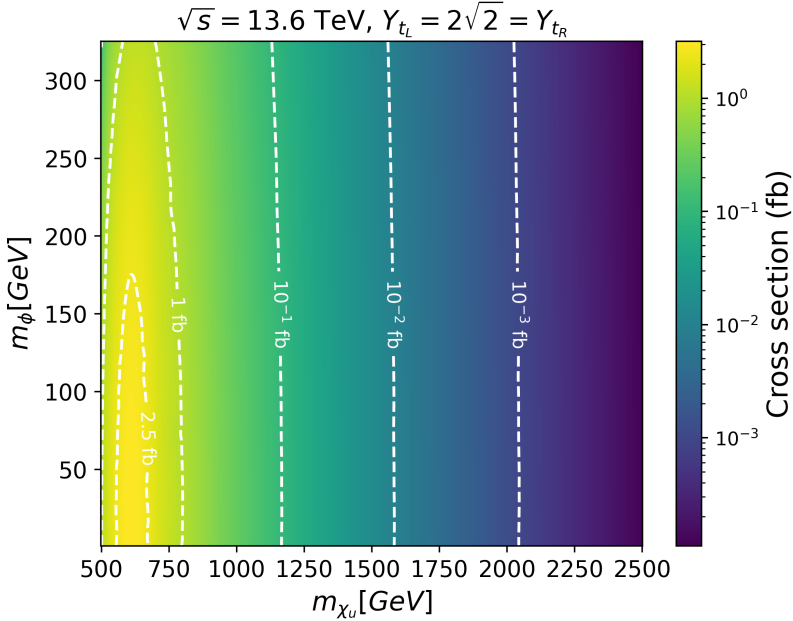


**Figure 3.6:** Projected cross section (fb) plot for  $\text{pp} \rightarrow t\chi_u\phi'$  and subsequent decay as a function of  $m_{\chi_u}$  and  $m_{\phi'}$ .

a (possibly boosted) top-tagged system, at least one b-tagged jet, and large  $\vec{p}_T^{\text{miss}}$ . For the partially merged and un-merged scenarios, there will be two b quarks present in the final state (one of which is part of the top tagged system).

We consider background sources from SM processes which can give similar objects in the final state as those expected for signal. Several background sources were considered and studied, such as QCD multijet events, production of vector boson pairs ( $VV$  :  $WW, ZZ, WZ$ ), vector boson triplets ( $VVV$  :  $WWZ, WZZ, ZZZ, WWW$ ), top-quark pairs in association with weak bosons ( $t\bar{t}X$ ), and  $t\bar{t}t\bar{t}$  processes. The dominant sources of SM background events are from the  $t\bar{t}X$ ,  $ZZW$ , and  $t\bar{t}t\bar{t}$  processes. The  $t\bar{t}X$  background is primarily associated production of a  $Z/\gamma^*$  from  $t\bar{t}$  fusion processes. The  $ZZW$  process becomes a background when one  $Z$  decays  $b\bar{b}$ , another  $Z$  decays to a pair of muons, and the  $W$  decays to a muon and a neutrino. Events from  $ZZW$  and  $t\bar{t}t\bar{t}$  have been combined, after being weighted by their corresponding production cross section. The combination is presented as the “ $b\bar{b}\mu\mu\mu\nu$ ” background in the remainder of this paper. The  $t\bar{t}X$  process is presented as part of the “ $t\bar{t}\mu^+\mu^-$ ” background. Fig. 3.7 shows a representative Feynman diagram for the  $t\bar{t}\mu^+\mu^-$  background process. Tab. 3.2 shows the production cross sections for the dominant background sources. The rest of the aforementioned background processes do not contribute meaningfully in our context, accounting for  $\ll 1\%$  of the total expected background yield.

The identification of leptons, boosted top quarks, and bottom quarks plays an important role in the ability to identify signal events, the ability to

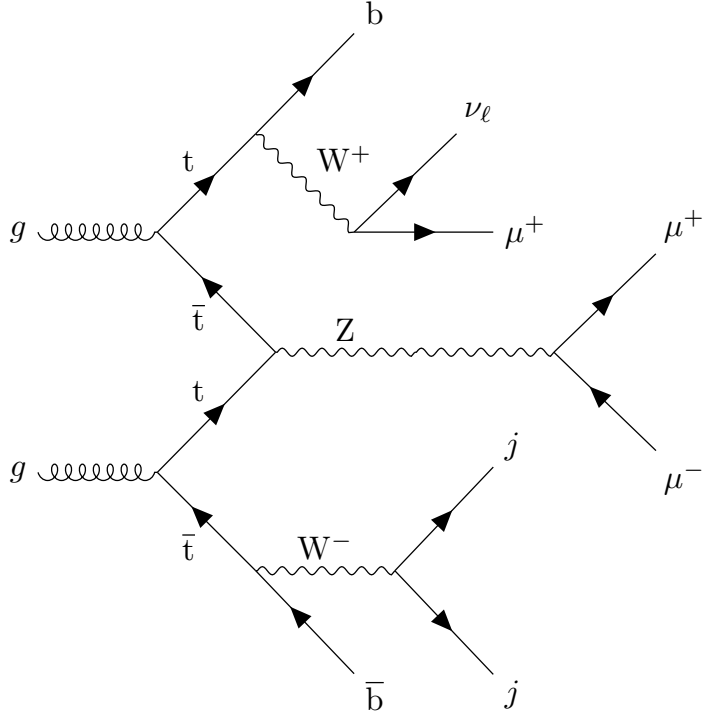


**Figure 3.7:** Representative Feynman diagram for a background event. A Z boson is produced in association with a top quark through the fusion of a top, anti top pair from incoming protons. The Z boson subsequently decays to a pair of muons and the two spectator top quarks decay semi-leptonically and purely hadronically to muons, neutrinos and jets, resulting in the same final states as the signal event.

minimize the rate of SM backgrounds, and thus also the discovery reach in the high-luminosity environment of the LHC. It is worth noting that the reconstruction and identification of leptons and the decay products of the top/bottom quarks may be non-trivial at the High-Luminosity LHC (HL-LHC) due to the presence of a potentially large number of in-time and out-of-time PU interactions. The impact of PU on the new physics discovery reach, and the importance of to mitigate its effects at CMS and ATLAS has been outlined in many articles, for example in Ref. [146]. We note the expected performance of the upgraded ATLAS and CMS detectors for the HL-LHC is beyond the scope of this work. However, the studies presented here do attempt to provide reasonable expectations by conservatively assuming some degradation in lepton and hadron identification efficiencies, using Ref. [146] as a benchmark, and considering the case of 140 average PU interactions in the DELPHES input cards, as described above.

For muons with  $|\eta| < 1.5$ , the assumed identification efficiency is 95% with a 0.3% misidentification rate [146, 153]. The performance degrades linearly with  $\eta$  for  $1.5 < |\eta| < 2.5$ , and we assume an identification efficiency of 65% with a 0.5% misidentification rate at  $|\eta| = 2.5$ . Similarly, the charged hadron tracking efficiency, which contributes to the jet clustering algorithm and  $\vec{p}_T^{\text{miss}}$  calculation, is 97% for  $1.5 < |\eta| < 2.5$ , and degrades to about 85% at  $|\eta| = 2.5$ . These potential inefficiencies due to the presence of secondary

pp interactions contribute to how well the lepton and top kinematics can be reconstructed. Following Refs. [268, 269], we consider the “Loose” working point for the identification of the fully merged (partially merged) t decays, which results in 80 – 85% top (W) identification efficiency and 11 – 25% misidentification rate, depending on the FatJet transverse momentum ( $p_T^{FJ}$ ). Following Ref. [270], we consider the “Loose” working point of the DeepCSV algorithm [141], which gives a 70 – 80% b-tagging efficiency and a 10% light quark mis-identification rate. The choice of boosted t/W and b-tagging working points is determined through an optimization process that maximizes discovery reach. It is noted that the contribution from SM backgrounds with a misidentified boosted t/W is negligible, and thus our discovery projections are not sensitive to uncertainties related to the boosted t/W misidentification rates.

Background Process	Cross-Section $\sigma$ [pb]
$pp \rightarrow t\bar{t} \mu^+ \mu^-$	$2.574 \times 10^{-3}$
$pp \rightarrow b\bar{b} \mu\mu\nu$	$4.692 \times 10^{-4}$

**Table 3.2:** A summary of dominant SM backgrounds produced by pp collisions and their cross sections in pb, as computed by MadGraph with  $n = 10^6$  events.

### 3.4 DATA ANALYSIS USING MACHINE LEARNING

The analysis of signal and background events is performed utilizing machine learning techniques. A machine learning-based approach offers sizeable advantages when compared to traditional event classification techniques. Unlike conventional methods, machine learning models have the capability to simultaneously consider all kinematic variables, allowing them to efficiently navigate the complex and high-dimensional space of event kinematics. Consequently, machine learning models can effectively enact sophisticated selection criteria that take into account the entirety of this high-dimensional space. This makes them ideal for high-energy physics applications.

The BDT method is a powerful machine learning technique that has proven its effectiveness in various applications, particularly in the field of collider physics. In this method, decision trees are trained greedily in a sequential manner, with each tree focusing on learning the discrepancies or residuals between its predictions and the expected values obtained from the previously trained tree. This iterative process aims to progressively minimize errors, making BDTs a particularly effective approach for enhancing model performance.

In the context of collider physics, BDTs have demonstrated their utility in addressing classification problems. In particular, BDTs can effectively discriminate between signal and background events, enabling accurate and efficient event classification. Their ability to handle subtle non-linear relationships within the data with high interpretability makes BDTs a

valuable tool to handle large amounts of data with a large number of parameters for each event.

The first step uses a specialized `MadAnalysis Expert Mode C++` script [271]. This script extracts essential kinematic and topological information from the simulated samples. The script will process the aforementioned variables contained within these files and transform them into a structured and informative CSV (Comma-Separated Values) format that can be used to train our machine learning models. These kinematic variables include crucial details about the events, such as particle momenta, energies, and topologies, providing the fundamental building blocks for our machine learning analysis.

To account for the differential significance of various events, we apply cross-section weighting. This ensures that the relative importance of signal and background events is appropriately balanced in the dataset. This weighting is crucial for addressing the varying likelihood of observing different types of events in high-energy physics experiments. The prepared and weighted datasets are then passed to our `MadAnalysis Expert Mode C++` script, where the simulated signal and background events are initially filtered, before being passed to the CSV file for use by the machine learning algorithm. The filtering process requires at least one well-reconstructed and identified b-jet candidate, at least one jet (regular or FJ) not tagged as a b jet, and exactly three identified muons. The filtering selections are motivated by experimental constraints, such as the geometric constraints of the CMS/ATLAS detectors, the typical kinematic thresholds for the reconstruction of particle objects, and the available lepton triggers which also drive the minimal kinematic thresholds. Selected jets must have  $p_T > 30 \text{ GeV}$  and  $|\eta(j)| < 5.0$ , while b-jet candidates with  $p_T > 20 \text{ GeV}$  and  $|\eta(b)| < 2.5$  are chosen. The  $\mu$  object must pass a  $p_T > 35 \text{ GeV}$  threshold and be within a  $|\eta(\ell)| < 2.3$ . We will refer to this filtering criteria as pre-selections. The efficiency of the pre-selections depends on  $m(\phi')$  and  $m(\chi_u)$ , but is typically about 25 – 30% for the signal samples. Events passing this pre-selection are used as input for the machine learning algorithm, which classifies them as signal or background, using a probability factor.

We explore the performance of a diverse set of machine learning models, specifically three neural networks of differing architectures and a BDT algorithm. To ensure robust model assessment, we employed a standard 90-10 train-test split of the dataset, partitioning it into a 90% portion for training and a 10% portion for testing. This division allows us to gauge the generalization capabilities of our models on unseen data.

The training and evaluation of the BDT were carried out in a high-performance computing environment. Specifically, an Nvidia A100 GPU was used. The canonical PyTorch [272] deep learning framework was employed for configuring, training, and evaluating the neural networks. PyTorch is well-regarded for its flexibility and performance in deep learning applications.

Model	Train/Test Acc.	Training Time
BDT	N.A./0.9993	6s
Neural Network 1	0.9999/0.9997	1h 58m
Neural Network 2	0.9999/0.9998	2h 12m
Neural Network 3	0.9999/0.9998	2h 32m

**Table 3.3:** Train/test results for the ML models.

For the BDT algorithm, we used hyperparameters  $\eta = 0.3$ ,  $\gamma = 0$ , and `max_depth = 6`. The XGBoost [193] library was used for the implementation of the Boosted Decision Tree algorithm. It offers high efficiency, optimization, and interpretability, making it a suitable choice for this particular task.

It is worth mentioning that we experimented with deep neural networks of various architectures. Although we found that they yield similar signal sensitivity to the BDT, the complex nature of the studies in this work (particle objects considered, experimental constraints in a high luminosity LHC, etc.) motivates the use of a BDT over a deep neural network because of its usefulness, efficiency, and simplicity in understanding the machine learning output in addition to significantly shorter training times. Therefore, we perform our proceeding analysis using the BDT. The outcomes of our model training and evaluation are presented in Table 3.

### 3.5 RESULTS

Figures 3.8, 3.9, and 3.10 show relevant kinematic distributions for two benchmark signal points and the dominant SM backgrounds, using the subset of events passing the pre-selections defined above. The signal benchmark points in these figures are  $m(\phi') = 325 \text{ GeV}$ ,  $m(\chi_u) = 2 \text{ TeV}$ , and  $m(\phi') = 1 \text{ GeV}$ ,  $m(\chi_u) = 500 \text{ GeV}$ . The distributions are normalized such that the area under the curve is unity. These distributions correspond to the reconstructed mass,  $m(\mu_1, \mu_2)$ , between the two muon candidates with the highest transverse momentum ( $\mu_1$  and  $\mu_2$ ), the transverse momentum of the b-jet candidate with the highest transverse momentum  $p_T$  ( $b_1$ ), and the muon candidate with the highest transverse momentum  $p_T$  ( $\mu_1$ ), respectively. Note that the signal distributions exhibit tails that are significantly the backgrounds. These distributions are among the variables identified by the BDT algorithm with the highest signal to background discrimination power.

As can be seen from Fig. 3.8, the  $\phi'$  mass can be reconstructed through its associated muon decay pair, which is observed as a peak in the  $m(\mu_1, \mu_2)$  distribution around the expected  $m(\phi')$  value, and has low- and high-mass tails which are a consequence of cases where the leading and/or subleading muon is not from the  $\phi'$  decay, but rather from the associated W boson from the  $\chi_u$  decay. For the backgrounds, muons come from Z (W) decays. Therefore, the  $m(\mu_1, \mu_2)$  background distributions show

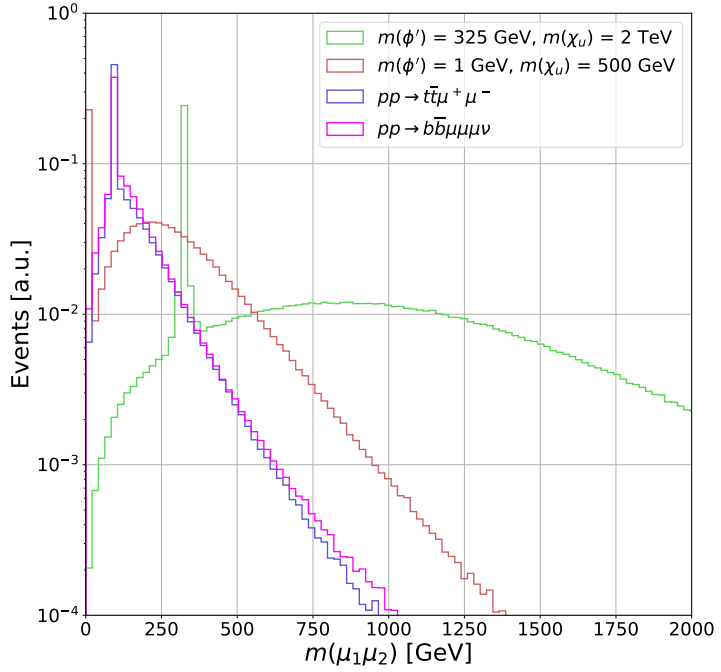


**Figure 3.8:** Invariant mass distribution of the muon pair with the highest and second highest transverse momentum. The distributions are shown for the two main SM background processes and two signal benchmark points.

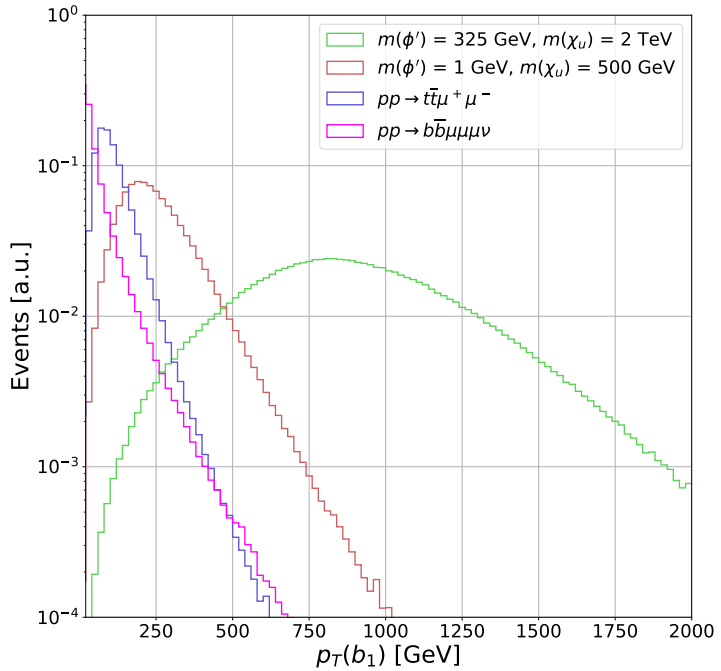


**Figure 3.9:** Transverse momentum distribution of the leading b-quark jet candidate. The distributions are shown for the two main SM background processes and two signal benchmark points.

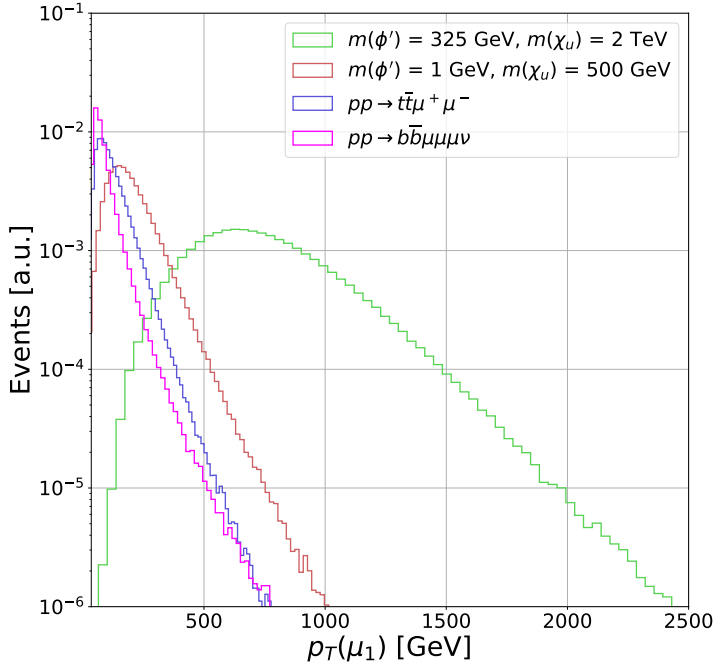


**Figure 3.10:** Transverse momentum distribution of the leading muon candidate. The distributions are shown for the two main SM background processes and two signal benchmark points.

a peak near  $m_{W/Z}$ , combined with a broad distribution indicative of the combination of two muon candidates from different decay vertices. We note that the  $\phi' \rightarrow \mu^+ \mu^-$  decay width depends on the square of the  $\phi' \rightarrow \mu^+ \mu^-$  coupling and  $\frac{m_\mu^2}{m_{\phi'}^2}$  and is thus suppressed by the relatively small muon mass. For the new physics phase space considered in this paper, the  $\phi'$  decay width is less than 1% of the  $\phi'$  resonant mass. Furthermore, as indicated previously, the signal/background interference effects are small and negligible compared to effects from experimental resolution. Therefore, the width of the  $m(\mu_1, \mu_2)$  signal distributions is driven by the experimental resolution in the reconstruction of the muon momenta, as well as the probability that the two leading muons are the correct pair from the  $\phi'$  decay. Since the probability that the two highest- $p_T$  muons are the correct pair from the  $\phi' \rightarrow \mu^+ \mu^-$  decay depends on  $m(\phi')$  and  $m(\chi_u)$ , it is important to include all possible combinations of dimuon pairs (i.e.,  $m(\mu_1, \mu_3)$  and  $m(\mu_2, \mu_3)$ ) in the training of the BDT.

Fig. 3.9 shows the distribution for the b-jet candidate with the highest  $p_T$ ,  $p_T(b_1)$ , for the same simulated samples shown in Fig. 3.8. Based on the signal topology and our choice of parameter space (i.e.,  $m_{\chi_u} > m_t$ ), it is expected that the leading b-jet candidate comes from the  $\chi_u$  decay, with an average  $p_T$  close to  $\frac{m_{\chi_u} - m_W}{2}$ , as observed in Fig. 3.9. For the  $t\bar{t}\mu^+\mu^-$  background, the b-jet candidates come from top-quark decays. Therefore, their average transverse momentum is expected to be  $\frac{m_t - m_W}{2} \approx 45$  GeV, as observed in Fig. 3.9. On the other hand, the b-jet candidates for the  $b\bar{b}\mu\mu\nu$

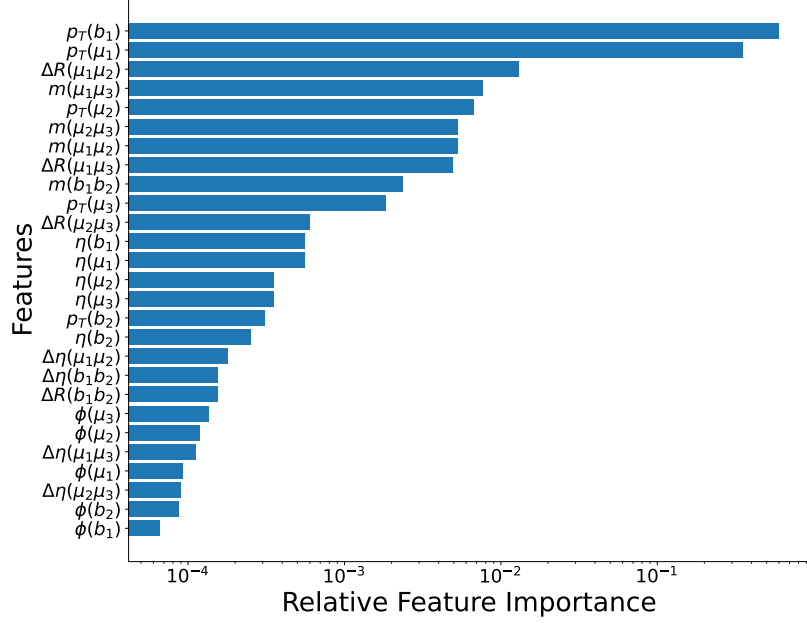


**Figure 3.11:** Relative importance of features in training for a benchmark signal scenario with  $m(\phi') = 325 \text{ GeV}$  and  $m(\chi_u) = 2000 \text{ GeV}$ .

background can come from off-mass-shell  $Z^*/\gamma^*$ , and thus typically have an even softer spectrum in comparison to the  $t\bar{t}\mu^+\mu^-$  background.

Fig. 3.10 shows the distribution for the muon candidate with the highest  $p_T$ ,  $p_T(\mu_1)$ . Similar to Fig. 3.9, when  $m(\chi_u) > m_t$  it is expected that the leading muon candidate comes from the  $\chi_u$  decay, with an average  $p_T$  of approximately  $\frac{m(\chi_u) - m_W}{4}$ , as observed in Fig. 3.10. For the major SM backgrounds, the muon candidates come from  $Z/W/\gamma^*$  decays. Therefore, their average transverse momentum is expected to be much lower,  $\frac{m_{Z/W}}{4} \approx 40 - 45 \text{ GeV}$ . This kinematic feature provides a nice handle to discriminate high  $m(\chi_u)$  signal events amongst the large SM backgrounds, which have lower average  $p_T(\mu)$  constrained by the SM weak boson masses.

In addition to these aforementioned variables in Figures 3.8-3.10, several other kinematic variables were included as inputs to the BDT algorithm. In particular, 27 such variables were used in total, and these included the momenta of b and muon candidates; invariant masses of pairs of muons; angular differences between b jets and between the muons. Fig. 3.11 shows the features that are used for training the machine learning models and their importance for a benchmark point.

As mentioned above, the variables  $m(\mu_i, \mu_j)$  for  $i, j \neq 1$  provide some additional discrimination between signal and background when the leading muons are not a  $\phi'$  decay candidate. The angular separation variables, such as  $\Delta R(\mu_i, \mu_j)$ , are designed to be sensitive to lower mass  $\phi'$ , since the low rest mass of those particles means they acquire more boost, and thus smaller angular separation  $\Delta R$  between the muon candidates. The trained BDT returns the discriminating power of each of its inputs, and the feature

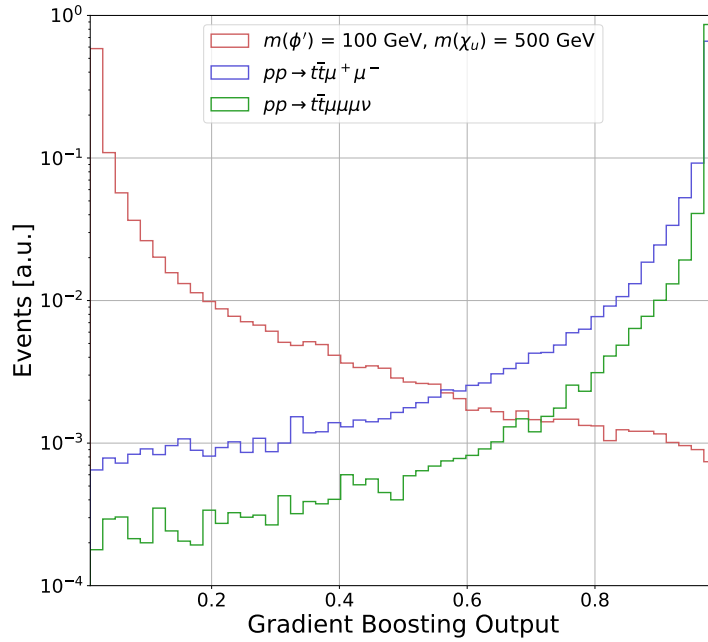


**Figure 3.12:** Output of the gradient boosting algorithm for a benchmark  $m(\phi') = 100$  GeV and  $m(\chi_u) = 500$  GeV signal, and dominant backgrounds. The distributions are normalized to unity.

importance for each variable is shown in Fig. 3.11 for a signal benchmark point with  $m(\phi') = 325$  GeV and  $m(\chi_u) = 2000$  GeV.

Fig. 3.12 shows the distributions for the output of the BDT algorithm, normalized to unity, for the representative signal benchmark point of  $m(\phi') = 1$  GeV,  $m(\chi_u) = 0.5$  TeV and the two dominant backgrounds. The output of the BDT algorithm is a value between 0 and 1, which quantifies the likelihood that an event is either background-like (BDT output near 1) or signal-like (BDT output near 0). Fig. 3.13 illustrates the true positive rate (TPR), defined as the probability of correctly selecting signal events using the BDT output, plotted against the false positive rate (FPR), defined as the probability of incorrectly selecting background events. For example, for  $m(\phi') = 100$  GeV and  $m(\chi_u) = 500$  GeV, when signal events are selected at 65% probability, the background is selected at about  $10^{-3}$  probability. We note that the primary discriminating feature between the signal and background is the boosted b-jet  $p_T$  coming from the  $\chi_u$  vector-like quark. The  $p_T$  of said b jet increases with  $m(\chi_u)$ , peaking at around  $[m(\chi_u) - m(W)]/2$ . This enhanced boost increases the separation between signal and background, improving the performance of the BDT algorithm as  $m(\chi_u)$  increases.

The outputs from the BDT machine learning algorithm are used to perform a profile-bin likelihood analysis to estimate the signal significance for a luminosity of  $3000 \text{ fb}^{-1}$ , corresponding to the expected amount of collected data by the end of the LHC era. For this purpose, the BDT distributions are normalized to cross section times pre-selection efficiency times luminosity for the different signal models. The significance is then calcu-

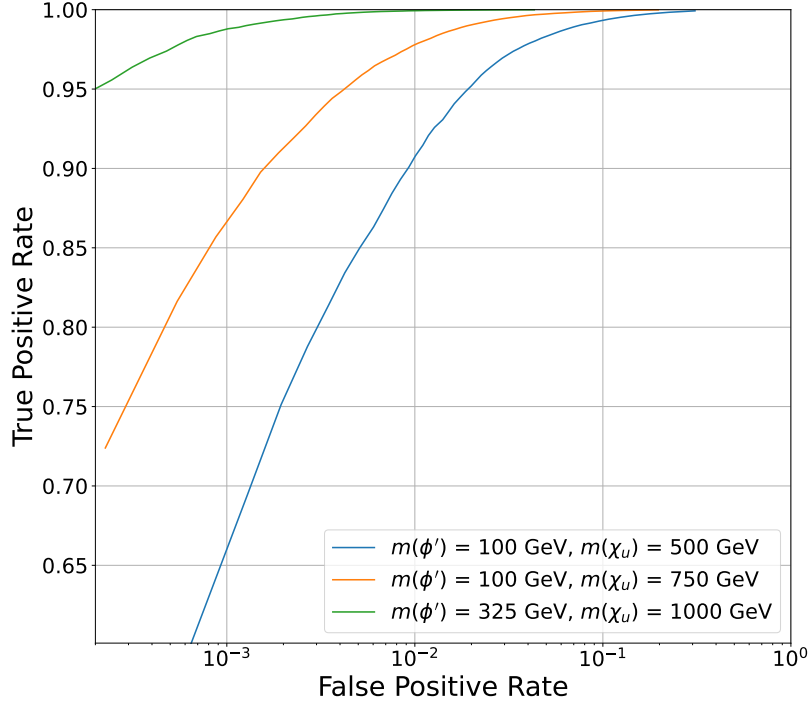


**Figure 3.13:** Receiver operating characteristic curve of the BDT algorithm for three different signal benchmark scenarios.

lated using the expected bin-by-bin yields of the BDT output distribution in a profile likelihood fit, using the ROOTFit [157] package developed by CERN. The expected signal significance  $Z_{\text{sig}}$  is estimated using the probability of obtaining the same test statistic for the signal plus background and the signal-null hypotheses, defined as the local p-value. Similar to Refs. [273–279], the significance corresponds to the point where the integral of a Gaussian distribution between  $Z_{\text{sig}}$  and  $\infty$  results in a value equal to the local p-value. The estimation of  $Z_{\text{sig}}$  incorporates systematic uncertainties. The uncertainty values have been included as nuisance parameters, considering lognormal priors for normalization and Gaussian priors for uncertainties associated with the modeling of the shapes similar to Refs. [280, 281].

The systematic uncertainties that have been included result from experimental and theoretical constraints. A 1-5% systematic uncertainty, depending on the simulated MC sample, has been included to account for the choice of Parton Distribution Function (PDF) set. The systematic uncertainty effect was incorporated following the PDF4LHC [157] recommendations. This systematic uncertainty has a small impact on the expected event yields for signal and background, but it does not affect the shape of the BDT output distribution. We additionally considered theoretical uncertainties related to the absence of higher-order contributions to the signal cross sections, which can change the pre-selection efficiencies and the shapes of kinematic variables used as inputs to the BDT algorithm. This uncertainty was calculated by varying the renormalization and factorization

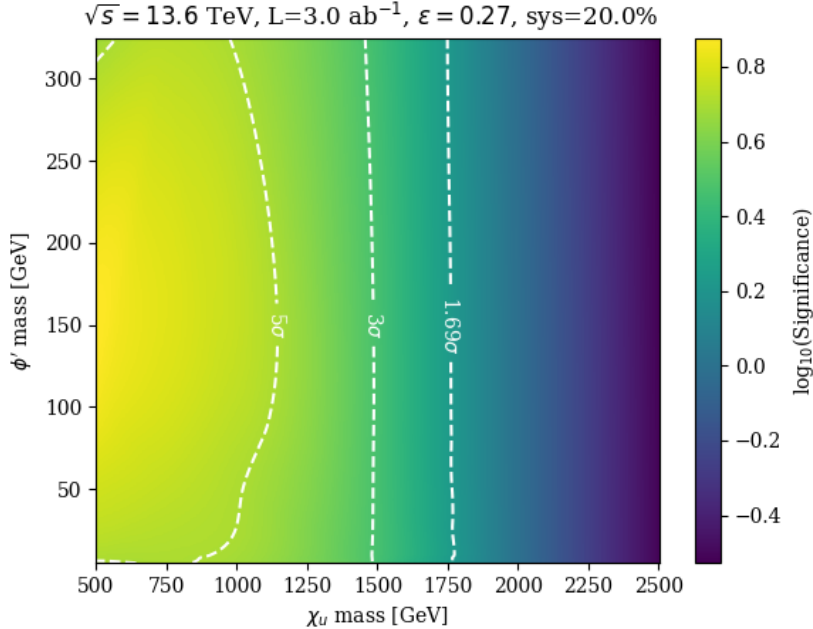


**Figure 3.14:** Signal significance for the high luminosity LHC era, considering with  $3000 \text{ fb}^{-1}$  of collected data.

scales by  $\times 2$ , and studying the resulting change in the bin-by-bin yields of the BDT distributions. They are found to be at most 2% in a given bin.

Regarding experimental uncertainties, following experimental measurements from CMS on the estimation of the integrated luminosity, a conservative 3% effect has been included [138]. A 5% systematic uncertainty associated with the reconstruction and identification of b-quark jets has been included, independent of  $p_T$  and  $\eta$  of the b-jet candidates. According to Ref. [270], this uncertainty is correlated between signal and background processes with genuine b-jets and is also correlated across BDT bins for each process. For muons, we include a 2% uncertainty associated with the reconstruction, identification, and isolation requirements, and a 3% systematic uncertainty to account for scale and resolution effects on the momentum and energy measurement. We consider jet energy scale uncertainties ranging from 2 – 5%, contingent on  $\eta$  and  $p_T$ , resulting in shape-based uncertainties on the BDT output distribution. Jet energy scale uncertainties were assumed to range from 1 – 5%, contingent on  $\eta$  and  $p_T$ . These assumptions lead to shape-based uncertainties on the BDT output distribution, varying from 1 – 2%. Additionally, we include a 10% systematic uncertainty to account for errors in the signal and background predictions. Considering all the various sources of systematic uncertainties, our conservative estimate yields a total effect of about 20%.

Fig. 3.14 shows the expected signal significance considering an integrated luminosity of  $3000 \text{ fb}^{-1}$ . The significance is shown as a heat map in a two-dimensional plane for different  $\phi'$  and  $\chi_u$  masses. The x-axis cor-

responds to  $m(\chi_u)$ , the y-axis to  $m(\phi')$ , and the heat map to  $\log_{10}(Z_{\text{sig}})$ . The white dashed lines are contours of constant signal significances of  $1.69\sigma$ ,  $3\sigma$  and  $5\sigma$  to represent regions of possible exclusion, evidence of new physics, and discovery, respectively. Under these conditions,  $\phi'$  ( $\chi_u$ ) masses ranging from 1 to 325 GeV (500 to 1800 GeV) can be probed. The range for a discovery with  $5\sigma$  signal significance varies from  $\chi_u$  masses from  $m(\chi_u) = 770$ -1100 GeV, depending  $m(\phi')$ . For large  $m(\chi_u)$ , the significance is almost independent of  $m(\phi')$  because the primary discriminating feature—the boosted b-quark originating from  $\phi'$ —is driven predominantly by the large  $m(\chi_u)$ , with the kinematic impact of  $m(\phi')$  being relatively negligible.

### 3.6 DISCUSSION

---

The LHC will continue to run with pp collisions at  $\sqrt{s} = 13.6$  TeV for the next decade. Given the increase in the integrated luminosity expected from the high-luminosity program, it is important to consider unexplored new physics phase space that diverges from the conventional assumptions made in many BSM theories, and which could have remained hidden in processes that have not yet been thoroughly examined. It is additionally crucial to explore advanced analysis techniques, in particular the use of artificial intelligence algorithms, to enhance the probability of detecting these rare corners where production cross sections are lower and discrimination from SM backgrounds is difficult.

In this work, we examine a model based on a  $U(1)_{T_R^3}$  extension of the SM, which can address various conceptual and experimental issues with the SM, including the mass hierarchy between generations of fermions, the thermal dark matter abundance, and the muon  $g - 2$ ,  $R_{(D)}$ , and  $R_{(D^*)}$  anomalies. This model contains a light scalar boson  $\phi'$ , with potential masses below the electroweak scale, and TeV-scale vector-like quarks  $\chi_u$ . We consider the scenario where the scalar  $\phi'$  has family non-universal fermion couplings and  $m(\phi') \geq 1$  GeV, as was suggested in Ref. [260], and thus the  $\phi'$  can primarily decay to a pair of muons. Previous works in Refs. [239, 261] considered scenarios motivating a search methodology with a merged diphoton system from  $\phi' \rightarrow \gamma\gamma$  decays. The authors of Ref [261], in which  $m(\phi') < 1$  GeV, indeed pointed out that if the  $\phi'$  is heavier than about 1 GeV, then decays to  $\mu^+\mu^-$  can become the preferable mode for discovery, which is the basis for the work presented in this paper. We further note that the final state topology studied in this paper would represent the most important mode for discovery at  $m(\phi') < 2m_t$  where the  $\phi' \rightarrow t\bar{t}$  decay is kinematically forbidden.

The main result of this paper is that we have shown that the LHC can probe the visible decays of new bosons with masses below the electroweak scale, down to the GeV-scale, by considering the simultaneous production of heavy QCD-coupled particles, which then decay to the SM particles that contain large momentum values and can be observed in the central regions

of the CMS and ATLAS detectors. The boosted system combined with innovative machine learning algorithms allows for the signal extraction above the lower-energy SM background. The LHC search strategy described here can be used to discover the prompt decay of new light particles. An important conclusion from this paper is that the detection prospects for low-mass particles are enhanced when it is kinematically possible to simultaneously access the heavy degrees of freedom which arise in the UV completion of the low-energy model. This specific scenario in which the couplings of the light scalars are generationally dependent, with important coupling values to the top quark, is an ideal example which would be difficult to directly probe at low energy beam experiments.

The proposed data analysis represents a competitive alternative to complement searches already being conducted at the LHC, allowing us to probe  $\phi'$  masses from 1 to 325 GeV, for  $m(\chi_u)$  values up to almost 2 TeV, at the HL-LHC. Therefore, we strongly encourage the ATLAS and CMS Collaborations to consider the proposed analysis strategy in future new physics searches.



# 4

---

## ON VECTORIAL LEPTOQUARKS SENSITIVITY AT THE LHC

---

As suggested in the introduction of Ch. 3, the patterns of LFV discussed in Sec. 1.4 motivate the construction of gauge-complete theoretical frameworks that can naturally accommodate non-universal couplings to fermions. Such frameworks could potentially link these anomalies to the resolution of other open questions in the SM, such as the B-meson anomalies. In particular, efforts have been made to embed  $U(1)_{T_R^3}$  in larger gauge groups, such as the Pati–Salam model [216], which unifies quarks and leptons in the same multiplet. This unification naturally leads to the presence of leptoquarks (LQs) in the particle spectrum, mediating quark–lepton transitions [116]. This was followed by intense theoretical development aiming to explain the anomalies via TeV-scale LQ exchange at tree level [34, 82, 96, 97, 107, 108, 113, 116, 282–289].

Leptoquarks are hypothetical bosons carrying both baryon and lepton number, enabling them to interact simultaneously with a lepton and a quark. They are a common feature of SM extensions where quarks and leptons belong to the same multiplet. Besides the Pati–Salam model [216], typical examples include SU(5) GUT scenarios [215]. They can also appear in theories with strong dynamics, such as compositeness [290]. LQs have exotic couplings that allow quark–lepton transitions, resulting in a rich and diverse phenomenology which naturally leads to multiple constraints. A particularly stringent one arises from proton decay, which pushes the LQ mass close to the Planck scale unless baryon and lepton numbers are conserved. Even in models where these numbers are preserved, LQs remain subject to a wide variety of experimental and phenomenological bounds [33, 291–295], including limits from meson mixing, electric and magnetic dipole moments, atomic parity violation tests, rare decays, and direct searches. The relative importance of these bounds is, however, highly model dependent.

Before the end of 2022, it was generally agreed that, within proposed single LQ solutions, the only candidate capable of addressing all B-meson anomalies simultaneously and surviving all other constraints was a vector LQ ( $U_1$ ), transforming as  $(\mathbf{3}, \mathbf{1}, 2/3)$ , and coupling mainly to third-generation fermions via  $b\tau$  and  $t\nu_\tau$  vertices [34, 116]. Despite a recent re-analysis of  $R_{K^{(*)}}$  data showing this ratio to be compatible with the SM prediction [85, 88, 89, 109], the solution to the  $R_{D^{(*)}}$  anomaly remains an

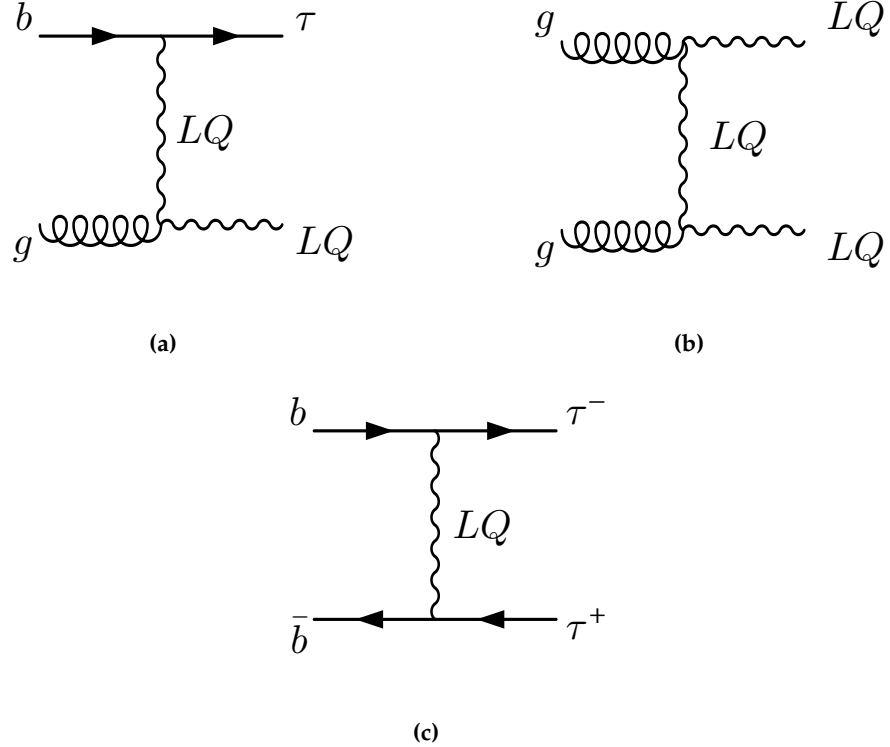


**Figure 4.1:** Representative Feynman diagrams of single (a), pair (b), and non-resonant (c) production leptoquarks in proton-proton collision experiments. In single and pair production, the diagrams shown involve t-channel LQ exchange, dominant for lower LQ mass. However, for larger mass there exist s-channel diagrams featuring a virtual bottom quark and gluon, respectively.

open question. This continues to be a valid motivation for the study of scenarios where new particles have preferential couplings to third-generation fermions. Thus, it is still of interest to continue exploring the possibility of observing the  $U_1$  LQ at the LHC [289].

As expected, the theoretical community has extensively participated in probing LQ models by scrutinizing search strategies, recasting LHC results, and predicting the reach in the parameter space via different searches involving third-generation fermions (see for instance [125, 243, 296–303]). In addition, several 13 TeV searches for LQs decaying into  $t/b$  and  $\tau/\nu$  final states have been performed by the CMS [119, 304–311] and ATLAS [120, 312–317] collaborations.

Of the searches above, we find [119] particularly interesting. Here, the CMS collaboration explores signals corresponding to  $t\nu b\tau$  and  $t\nu\tau$  final states, with  $137 \text{ fb}^{-1}$  of pp collision data. The former is motivated by LQ pair production, with one LQ decaying into  $t\nu$  and the other into  $b\tau$ , while the latter arises from a single LQ produced in association with a  $\tau$ , with a subsequent LQ decay into  $t\nu$  (see Fig. 4.1 for the corresponding diagrams). From the combination of both production channels, the search excludes  $U_1$

masses under  $1.3 - 1.7 \text{ TeV}$ , with this range depending on the  $U_1$  coupling to gluons and on its coupling  $g_U$  in the  $b_L \tau_L$  vertex.

What makes this search particularly attractive is that, for the first time, an LHC collaboration directly places (mass dependent) bounds on  $g_U$ . This is important, since having information on this parameter is crucial in order to understand if the  $U_1$  is really responsible for the  $R_D^{(*)}$  anomaly. The inclusion of the single-LQ production mode is important, since its cross-section is directly proportional to  $g_U^2$ . However, as can be seen in Figure 6 of [119], the current constraints are dominated by pair production, with single-LQ production playing a subleading role. While this is expected [299], it still leads us to ponder the possibility of improving the sensitivity of LHC searches to single-LQ production, and thus on achieving better constraints on  $g_U$ . Other complementary and similar searches to [119] were carried out by both ATLAS [316] and CMS [311].

It is also well known, though, that searches for an excess in the high- $p_T$  tails of  $\tau$  lepton distributions can strongly probe  $g_U$ , up to very large LQ masses. Indeed, as shown in [124, 289], the new physics effective operators contributing to  $R_D^{(*)}$  also contribute to an enhancement in the  $pp \rightarrow \tau\tau$  production rates. This has motivated a large number of recasts [106, 114, 116, 117, 125, 289, 299, 318, 319], as well as a CMS search explicitly providing constraints in terms of  $U_1$  [310]. Nevertheless, it is important to note that for these  $pp \rightarrow \tau\tau$  processes, the LQ participates non-resonantly, so contributions to the  $pp \rightarrow \tau\tau$  rates and kinematic distributions from non-LQ BSM diagrams containing possible virtual particles, such as a heavy neutral vector boson  $Z'$ , could spoil a straightforward interpretation of any possible excess [125]. Thus, it is also necessary to understand how the presence of other virtual particles can affect the sensitivity of an analysis probing  $g_U$ .

In this work we study the projected LQ sensitivity at the LHC, considering already available  $pp$  data as well as the expected amount of data to be acquired during the HL-LHC runs. We explore a proposed analysis strategy which utilizes a combination of single-, double-, and non-resonant-LQ production, targeting final states with varying  $\tau$ -lepton and  $b$ -jet multiplicities. The studies are performed considering various benchmark scenarios for different LQ masses and couplings, also taking into account distinct chiralities for the third-generation fermions in the LQ vertex. We also assess the impact of a companion  $Z'$ , which is typical of gauge models, in non-resonant LQ probes, and find that interference effects can have a significant effect on the discovery reach. We consider this effect to be of high interest, given that non-resonant LQ production can have the largest cross-section, and thus could be an important channel in terms of discovery potential.

An important aspect of this work is that the analysis strategy is developed using a ML algorithm based on BDTs[201]. The output of the event classifier is used to perform a profile-binned likelihood test to extract the overall signal significance for each model considered in the analysis. The

advantage of using BDTs and other ML algorithms has been demonstrated in several experimental and phenomenological studies [241–247]. In our studies, we find that the BDT algorithm gives sizeable improvement in signal significance.

#### 4.1 A SIMPLIFIED MODEL FOR THE $U_1$ LEPTOQUARK

---

Extending the SM with a massive  $U_1$  vector LQ is not straightforward, as one has to ensure the renormalizability of the model. Most of the theoretical community has focused on extensions of the Pati-Salam (PS) models which avoid proton decay, such as the scenario found in [219]. Other examples include PS models with vector-like fermions [320–322], the so-called 4321 models [111, 115, 123], the twin PS<sup>2</sup> model [112, 323], the three-site PS<sup>3</sup> model [324–326], as well as composite PS models [327–329].

In what follows, we shall restrict ourselves to a simplified non-renormalizable lagrangian, understood to be embedded into a more complete model. The SM is thus extended by adding the following terms featuring the  $U_1$  LQ:

$$\begin{aligned} \mathcal{L}_{U_1} = & -\frac{1}{2} U_{\mu\nu}^\dagger U^{\mu\nu} + M_U^2 U_{1\mu}^\dagger U_1^\mu \\ & -ig_s U_{1\mu}^\dagger T^a U_{1\nu} G^{a\mu\nu} - i\frac{2}{3}g' U_{1\mu}^\dagger U_{1\nu} B^{\mu\nu} \\ & + \frac{g_U}{\sqrt{2}} [U_{1\mu} (\bar{Q}_3 \gamma^\mu L_3 + \beta_L^{s\tau} \bar{Q}_2 \gamma^\mu L_3 \\ & + \beta_R \bar{b}_R \gamma^\mu \tau_R) + h.c.] \end{aligned} \quad (4.1)$$

where  $U_{\mu\nu} \equiv \mathcal{D}_\mu U_{1\nu} - \mathcal{D}_\nu U_{1\mu}$ , and  $\mathcal{D}_\mu \equiv \partial_\mu + ig_s T^a G_\mu^a + i\frac{2}{3}g' B_\mu$ . As evidenced by the second line above, we assume that the LQ has a gauge origin <sup>1</sup>.

The third and fourth lines in Eq. (4.1) shows the LQ interactions with SM fermions, with coupling  $g_U$ , which we have chosen as preferring the third generation <sup>2</sup>. These are particularly relevant for the LQ decay probabilities, as well as for the single-LQ production cross-section. The  $\beta_L^{s\tau}$  parameter, which is the  $LQ \rightarrow s\tau$  coupling in the  $\beta_L$  matrix (see footnote), is chosen to be equal to 0.2, following the fit done in [114], in order to simultaneously solve the  $R_{D^{(*)}}$  anomaly and satisfy the  $p p \rightarrow \tau^+ \tau^-$  constraints. Although  $\beta_L^{s\tau}$  technically alters the single-LQ production cross-section and LQ branching fractions, we have confirmed that a value of  $\beta_L^{s\tau} = 0.2$  results in negligible impact on our collider results, and thus is ignored in our subsequent studies.

The LQ right-handed coupling is modulated with respect to the left-handed one by the  $\beta_R$  parameter. The choice of  $\beta_R$  is important phe-

<sup>1</sup> The couplings in the second line of Eq. (4.1) can be found in the literature as  $g_s \rightarrow g_s(1 - \kappa_U)$  and  $g' \rightarrow g'(1 - \kappa_U)$ , in order to take into account the possibility of an underlying strong interaction.

<sup>2</sup> Before the demise of the  $R_{K^{(*)}}$  anomaly [85, 88, 89, 109], a  $3 \times 3$   $\beta_L$  matrix would be used instead, with values fitted to solve all B meson anomalies.

nomenologically, as it affects the LQ branching ratios <sup>3</sup>, as well as the single-LQ production cross-section. To illustrate the former, Fig. 4.2 (left) shows the  $LQ \rightarrow b\tau$  and  $LQ \rightarrow t\nu$  branching ratios as functions of the LQ mass, for two values of  $\beta_R$ . For large LQ masses, we confirm that with  $\beta_R = 0$  then  $BR(LQ \rightarrow b\tau) \approx BR(LQ \rightarrow t\nu) \approx \frac{1}{2}$ . However, for  $\beta_R = -1$ , as was chosen in [113], the additional coupling adds a new term to the total amplitude, leading to  $BR(LQ \rightarrow b\tau) \approx \frac{2}{3}$ . The increase in this branching ratio can thus weaken bounds from LQ searches targeting decays into  $t\nu$  final states, which motivates exploring the sensitivity in  $b\tau$  final states exclusively. Note that although a  $BR(LQ \rightarrow b\tau) \approx 1$  scenario is possible by having the LQ couple exclusively to right-handed currents (i.e.,  $g_U \rightarrow 0$ , but  $g_U \beta_R \neq 0$ ), it does not solve the observed anomalies in the  $R_{D^{(*)}}$  ratios. Therefore, although some LHC searches assume  $BR(LQ \rightarrow b\tau) = 1$ , we stress that in our studies we assume values of the model parameters and branching ratios that solve the  $R_{D^{(*)}}$  ratios.

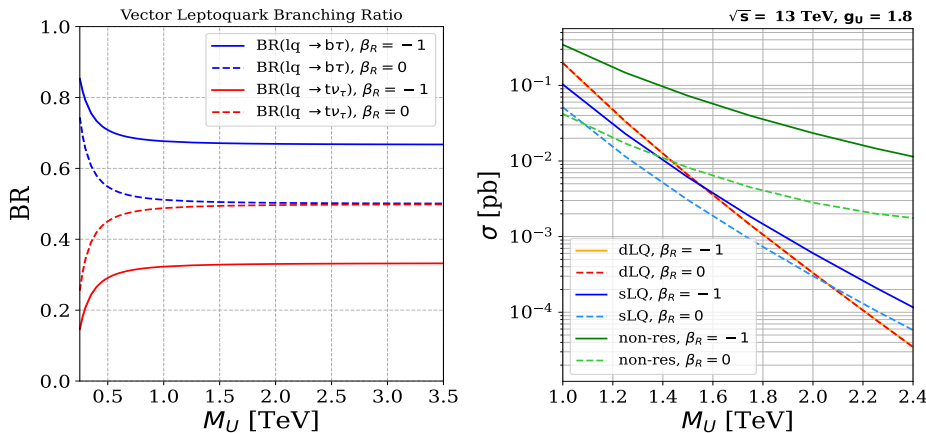


**Figure 4.2:** Left: The  $LQ \rightarrow b\tau$  and  $LQ \rightarrow t\nu$  branching ratios for  $\beta_R = 0$  (solid lines) and  $\beta_R = -1$  (dashed lines). Right: Signal cross-section as a function of the LQ mass, for  $\sqrt{s} = 13$  TeV, with  $g_U = 1.8$ . We show single, pair, and non-resonant production, for  $\beta_R = -1, 0$  in solid and dashed lines, respectively.

To further understand the role of  $\beta_R$  at colliders, Fig. 4.2 (right) shows the cross-section for single-LQ (sLQ), double-LQ (dLQ), and non-resonant (non-res) production, as a function of mass and for a fixed coupling  $g_U = 1.8$ , assuming  $p p$  collisions at  $\sqrt{s} = 13$  TeV. We note that this benchmark scenario with  $g_U = 1.8$  results in a  $LQ \rightarrow b\tau$  decay width that is  $< 5\%$  of the LQ mass, for mass values from 250 GeV to 2.5 TeV. In the Figure, we observe that, since dLQ production is mainly mediated by events from quantum chromodynamic processes, the choice of  $\beta_R$  does not affect the cross-section. However, for sLQ production, a non-zero value for  $\beta_R$  increases the cross-section by about a factor of 2 and by almost one order of magnitude in the case of non-res production. These results shown in Fig. 4.2 are easily understood by considering the diagrams shown in Fig. 4.1.

<sup>3</sup> Having  $\beta_L^{S\tau}$  different from zero also opens new decay channels. These, however, are either suppressed by  $\beta_L^{S\tau}$  and powers of  $\lambda_{CKM}$ . In any case, this effect would decrease  $BR(LQ \rightarrow b\tau)$  and  $BR(LQ \rightarrow t\nu)$  by less than 3%.

The LQ mass value where the sLQ production cross-section exceeds the dLQ cross-section depends on the choice of  $g_U$ .

We also note that to solve the  $R_{D^{(*)}}$  anomaly, the authors of [114] point out that the wilson coefficient  $C_U \equiv g_U^2 v_{SM}^2 / (4 M_U^2)$  is constrained to a specific range of values, and this range depends on the value of the  $\beta_R$  parameter. Therefore, the allowed values of the coupling  $g_U$  depend on  $M_U$  and  $\beta_R$ , and thus our studies are performed in this multi-dimensional phase space.

We study the role of a  $Z'$  boson in  $pp \rightarrow \tau\tau$  production. The presence of a  $Z'$  boson in LQ models has been justified in various papers, for example, in [125]. The argument is that minimal extensions of the SM which include a massive gauge  $U_1$  LQ, uses the gauge group  $SU(4) \times SU(3)' \times SU(2)_L \times U(1)_{T_R^3}$ . Such an extension implies the presence of an additional massive boson,  $Z'$ , and a color-octet vector,  $G'$ , arising from the spontaneous symmetry breaking into the SM, see for example App. B. The  $Z'$  in particular can play an important role in the projected LQ discovery reach, as it can participate in  $pp \rightarrow \tau\tau$  production by s-channel exchange, both resonantly and as a virtual mediator. To study the effect of a  $Z'$  on the  $pp \rightarrow \tau\tau$  production cross-sections and kinematics, we extend our benchmark Lagrangian in Eq. (4.1) with further non-renormalizable terms involving the  $Z'$ . Accordingly, we assume the  $Z'$  only couples to third-generation fermions. Our simplified model is thus extended by:

$$\begin{aligned} \mathcal{L}_{Z'} = & -\frac{1}{4} Z'_{\mu\nu} Z'^{\mu\nu} + \frac{1}{2} M_{Z'}^2 Z'_\mu Z'^\mu \\ & + \frac{9 g_{Z'}}{2\sqrt{6}} Z'^\mu (\zeta_q \bar{Q}_3 \gamma_\mu Q_3 + \zeta_t \bar{t}_R \gamma_\mu t_R \\ & + \zeta_b \bar{b}_R \gamma_\mu b_R - 3\zeta_\ell \bar{L}_3 \gamma_\mu L_3 - 3\zeta_\tau \bar{\tau}_R \gamma_\mu \tau_R) \end{aligned} \quad (4.2)$$

where the constants  $M_{Z'}$ ,  $g_{Z'}$ ,  $\zeta_q$ ,  $\zeta_t$ ,  $\zeta_b$ ,  $\zeta_\ell$ ,  $\zeta_\tau$ , are model dependent.

We study two extreme cases for the  $Z'$  mass, following [330], namely  $M_{Z'} = \sqrt{\frac{1}{2}} M_U < M_U$  and  $M_{Z'} = \sqrt{\frac{3}{2}} M_U > M_U$ . We also assume the LQ and  $Z'$  are uniquely coupled to left-handed currents, i.e.  $\zeta_q = \zeta_\ell = 1$  and  $\zeta_t = \zeta_b = \zeta_\tau = 0$ . With these definitions, Fig. 4.3 shows the effect of the  $Z'$  on the  $\tau\tau$  production cross-section, considering  $g_U = 1$ ,  $\beta_R = 0$ , and different  $g_{Z'}$  couplings. On the left, the cross-sections corresponding to the cases where  $M_{Z'} = \sqrt{\frac{1}{2}} M_U$  are shown. As expected, the  $\tau\tau$  production cross-section for the inclusive case (i.e.,  $g_{Z'} \neq 0$ ) is larger than that for the LQ-only non-res process ( $g_{Z'} = 0$ , depicted in blue). This effect increases with  $g_{Z'}$  and, within the evaluated values, can exceed the LQ-only cross-section by up to two orders of magnitude. In contrast, a more intricate behaviour can be seen on the right of Fig. 4.3, which corresponds to  $M_{Z'} = \sqrt{\frac{3}{2}} M_U$ . Here, for low values of  $M_U$ , a similar increase in the cross-section is observed. However, for higher values of  $M_U$ , the inclusive  $p p \rightarrow \tau\tau$  cross-section is smaller than the LQ-only  $\tau\tau$  cross-section. This behaviour suggests the presence of a dominant destructive interference at high masses, leaving its imprint on the results.

*Naively, the LQs are associated to the breaking of  $SU(4) \rightarrow SU(3)_{[4]} \times U(1)_{B-L}$ , the  $G'$  arises from  $SU(3)_{[4]} \times SU(3)' \rightarrow SU(3)_c$ , and the  $Z'$  comes from the breaking of  $U(1)_{B-L} \times U(1)_{T_R^3} \rightarrow U(1)_Y$ . Notice that the specific pattern of breaking, and the relations between the masses and couplings, are connected to the specific scalar potential used.*

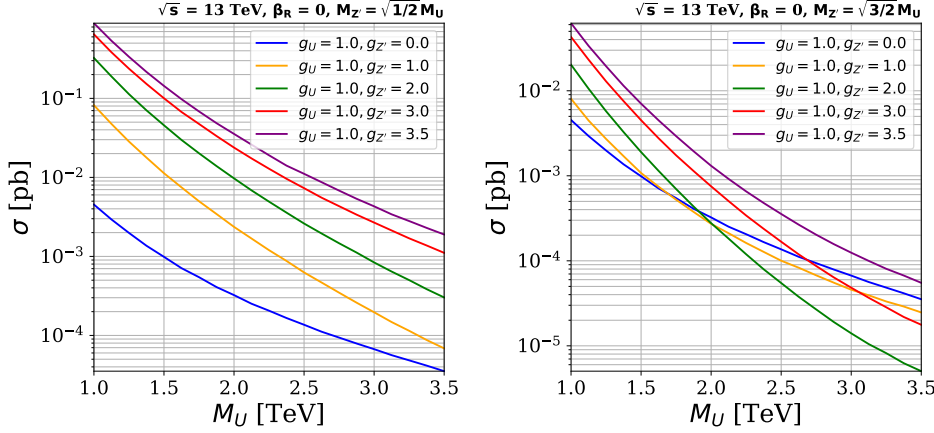


**Figure 4.3:**  $\tau\tau$  cross-section as a function of the LQ mass for different values of  $g_U$  and  $g_{Z'}$ . The estimates are performed at  $\sqrt{s} = 13$  TeV,  $\beta_R = 0$ ,  $M_{Z'} = \sqrt{1/2}M_U$  (left), and  $M_{Z'} = \sqrt{3/2}M_U$  (right).

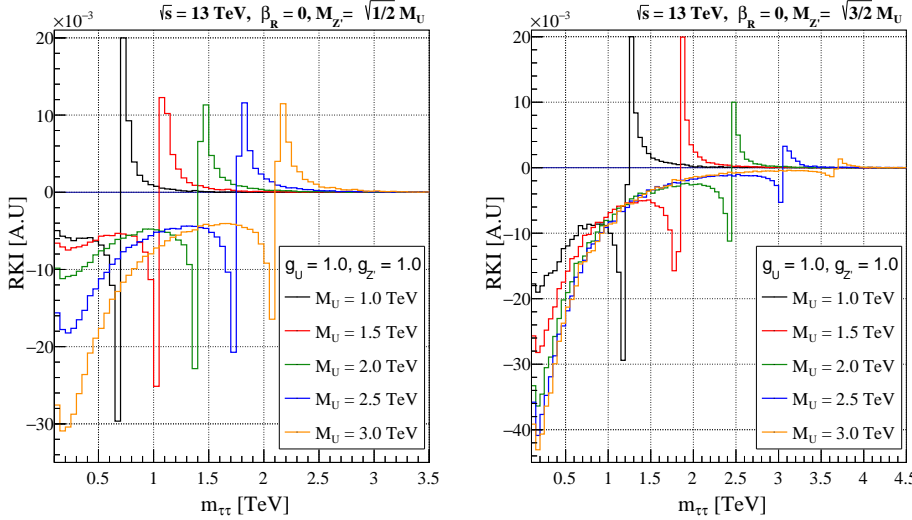


**Figure 4.4:** The relative kinematic interference (RKI), as a function of the reconstructed mass of two taus, for different LQ masses. The studies are performed assuming  $\sqrt{s} = 13$  TeV,  $\beta_R = 0$ ,  $g_U = 1.0$ ,  $g_{Z'} = 1.0$ ,  $M_{Z'} = \sqrt{1/2}M_U$  (left), and  $M_{Z'} = \sqrt{3/2}M_U$  (right).

In order to further illustrate the effect, Fig. 4.4 shows the relative kinematic interference (RKI) as a function of the reconstructed invariant mass  $m_{\tau\tau}$ , for  $g_{Z'} = 1$  and varying values of  $M_U$ . The RKI parameter is defined as

$$\text{RKI}(m_{\tau\tau}) = \frac{1}{\sigma_{\text{LQ}+Z'}} \left[ \frac{d\sigma_{\text{LQ}+Z'}}{dm_{\tau\tau}} - \left( \frac{d\sigma_{\text{LQ}}}{dm_{\tau\tau}} + \frac{d\sigma_{Z'}}{dm_{\tau\tau}} \right) \right], \quad (4.3)$$

where  $\sigma_X$  is the production cross-section arising due to contributions from  $X$  particles. For example,  $\sigma_{\text{LQ}+Z'}$  represents the inclusive cross-section where both virtual LQ and s-channel  $Z'$  exchange contribute. For both cases, we can observe the presence of deep valleys in the RKI curves when  $m_{\tau\tau} \rightarrow 0$ , indicating destructive interference between the LQ and the  $Z'$

contributions. This interference generates a suppression of the differential cross-section for lower values of  $m_{\tau\tau}$  and, therefore, in the integrated cross-section.

The observed interference effects are consistent with detailed studies on resonant and non-res  $p p \rightarrow t\bar{t}$  production, performed in reference [331].

## 4.2 SEARCH STRATEGY AND SIMULATION

---

Our proposed analysis strategy utilizes single-LQ (i.e.  $p p \rightarrow \tau LQ$ ), double-LQ (i.e.  $p p \rightarrow LQLQ$ ), and non-resonant LQ production (i.e.  $p p \rightarrow \tau\tau$ ) as shown in Fig. 4.1. At leading order in  $\alpha_s$ , since we focus on  $U_1 \rightarrow b\tau$  decays, the sLQ process results in the  $b\tau\tau$  mode, the dLQ process results in the  $bb\tau\tau$  mode, and the non-res process results in the  $\tau\tau$  mode. Therefore, in all cases we obtain two  $\tau$  leptons, with either 0, 1, or 2  $b$  jets. The  $\tau$  leptons decay to hadrons ( $\tau_h$ ) or semi-leptonically to electrons or muons ( $\tau_\ell$ ,  $\ell = e$  or  $\mu$ ). To this end, we study six final states:  $\tau_h\tau_{h/\ell}$ ,  $b\tau_h\tau_{h/\ell}$ , and  $bb\tau_h\tau_{h/\ell}$ , which can be naively associated to non-res, sLQ and dLQ production, respectively. Nevertheless, experimentally it is possible for  $b$  jets to not be properly identified or reconstructed, leading, for instance, to a fraction of dLQ signal events falling into the  $b\tau_h\tau_{h/\ell}$  and  $\tau_h\tau_{h/\ell}$  categories. Similarly, soft jets can fake  $b$  jets, such that non-res processes can contribute to the  $b\tau_h\tau_{h/\ell}$  and  $bb\tau_h\tau_{h/\ell}$  final states. This kind of signal loss and mixing is taken into account in our analysis<sup>4</sup>.

The contributions of signal and background events are estimated using Monte Carlo (MC) simulations. We implemented the  $U_1$  model from [125], adjusted to describe the lagrangian in Equations (4.1) and (4.2), using FeynRules (v2.3.43) [128, 181]. The branching ratios and cross-sections have been calculated using MadGraph5\_aMC (v3.1.0) [127, 188], the latter at leading order in  $\alpha_s$ . The corresponding samples are generated considering  $p p$  collisions at  $\sqrt{s} = 13$  TeV and  $\sqrt{s} = 13.6$  TeV. All samples are generated using the NNPDF3.0 NLO [135] set for parton distribution functions (PDFs) and using the full amplitude square SDE strategy for the phase-space optimization due to strong interference effects with the  $Z'$  boson. Parton level events are then interfaced with the PYTHIA (v8.2.44) [133] package to include parton fragmentation and hadronization processes, while DELPHES (v3.4.2) [129] is used to simulate detector effects, using the input card for the CMS detector geometric configurations, and for the performance of particle reconstruction and identification.

At parton level, jets and leptons are required to have a minimum transverse momentum ( $p_T$ ) of 20 GeV, while  $b$  jets are required to have a minimum  $p_T$  of 30 GeV. Additionally, we constrain the pseudorapidity ( $\eta$ )

---

<sup>4</sup> Note that further signal mixing can also occur at the event generation level by including terms at larger order in  $\alpha_s$ . For example, in the non-res diagram in Fig. 4.1, one of the initial  $b$  could come from a  $g \rightarrow b\bar{b}$  splitting, leading to non resonant production of  $b\tau_h\tau_{h/\ell}$ . Simulating and studying the role of such NLO contributions is outside the scope of this work.

Variable	Threshold							
	$\tau_h \tau_h$	$b\tau_h \tau_h$	$bb\tau_h \tau_h$	$\tau_h \tau_\ell$	$b\tau_h \tau_\ell$	$bb\tau_h \tau_\ell$		
$N(b)$	= 0	= 1	$\geq 2$	= 0	= 1	$\geq 2$		
$p_T(b)$	-		$\geq 30 \text{ GeV}$	-		$\geq 30 \text{ GeV}$		
$ \eta(b) $	-		$\leq 2.4$	-		$\leq 2.4$		
$N(\ell)$		$= 0$			$= 1$			
$p_T(e)$		-			$\geq 35 \text{ GeV}$			
$p_T(\mu)$		-			$\geq 30 \text{ GeV}$			
$ \eta(\ell) $		-			$\leq 2.4$			
$N(\tau_h)$		$= 2$			$= 1$			
$p_T(\tau_h)$		$\geq 50 \text{ GeV}$						
$ \eta(\tau_h) $		$\leq 2.3$						
$\Delta R(p_i, p_j)$		$\geq 0.3$						

**Table 4.1:** Preliminary event selection criteria used to filter events before feeding them to the BDT algorithm. A  $\Delta R(p_i, p_j) > 0.3$  requirement is imposed between all pairs of reconstructed particle candidates  $p_i, p_j$ .

to  $|\eta| < 2.5$  for b jets and leptons, and  $|\eta| < 5.0$  for jets. The production cross-sections shown in the bottom panel of Figures 4.2 and 4.3 are obtained with the aforementioned selection criteria.

Tab. 4.1 shows the preliminary event selection criteria for each channel at analysis level. The channels are divided based on the multiplicity of b jets,  $N(b)$ , number of light leptons,  $N(\ell)$ , number of hadronic tau leptons,  $N(\tau_h)$ , and kinematic criteria based on  $\eta$ ,  $p_T$  and spatial separation of particles in the detector volume ( $\Delta R = \sqrt{(\Delta\eta)^2 + (\Delta\phi)^2}$ ). The minimum  $p_T$  thresholds for leptons are chosen following references [119, 310, 313], based on experimental constraints associated to trigger performance. Following reference [179], we use a flat identification efficiency for b jets of 70% across the entire  $p_T$  spectrum with misidentification rate of 1%. These values correspond with the “medium working point” of the CMS algorithm to identify b jets, known as DeepCSV. We also explored the “Loose” (“Tight”) working point using an efficiency of 85% (45%) and mis-identification rate of 10% (0.1%). The “medium working point” was selected as it gives the best signal significance for the analysis.

For the performance of  $\tau_h$  identification in DELPHES, we consider the latest technique described in [142], which is based on a deep neural network (i.e. DeepTau) that combines variables related to isolation and  $\tau$ -lepton lifetime as input to identify different  $\tau_h$  decay modes. Following [142], we consider three possible DeepTau “working points”: (i) the “Medium” working point of the algorithm, which gives a 70%  $\tau_h$ -tagging efficiency and 0.5% light-quark and gluon jet mis-identification rate; (ii) the “Tight”

Sample	t̄t	single t	VV	V+jets	signals
$N_{\text{events}} \times 10^{-6}$	24.31	11.50	32.35	39.45	0.60

**Table 4.2:** The number of simulated events for the signal and background samples.

working point, which gives a 60%  $\tau_h$ -tagging efficiency and 0.2% light-quark and gluon jet mis-identification rate; and (iii) the “VTight” working point, which gives a 50%  $\tau_h$ -tagging efficiency and 0.1% light-quark and gluon jet mis-identification rate. Similar to the choice of b-tagging working point, the choice of  $\tau_h$ -tagging working point is determined through an optimization process which maximizes discovery reach. The “Medium” working point was ultimately shown to provide the best sensitivity and therefore chosen for this study. For muons (electrons), the assumed identification efficiency is 95% (85%), with a 0.3% (0.6%) mis-identification rate [146, 152, 153].

After applying the preliminary selection criteria, the primary sources of background are production of top quark pairs ( $t\bar{t}$ ), and single-top quark processes (single t), followed by production of vector bosons with associated jets from initial or final state radiation (V+jets), and pair production of vector bosons (VV). The number of simulated MC events used for each sample is shown in Tab. 4.2.

We use two different sets of signal samples. The first set includes various  $\{M_U, g_U\}$  scenarios, for two different values of  $\beta_R \in \{0, -1\}$ . We generate signal samples for  $M_U$  values between 250 GeV and 5000 GeV, in steps of 250 GeV. The considered  $g_U$  coupling values are between 0.25 and 3.5, in steps of 0.25. Although the signal cross-sections depend on both  $M_U$  and  $g_U$ , the efficiencies of our selections only depend on  $M_U$  (for all practical purposes) since the decay widths are relatively small compared to the mass of  $M_U$  ( $\frac{\Gamma_U}{M_U} < 5\%$ ), and thus more sensitive to experimental resolution. In total there are 280  $\{M_U, g_U, \beta_R\}$  scenarios simulated for this first set of signal samples, and for each of these scenarios two subsets of samples are generated, which are used separately for the training and testing of the machine learning algorithm. The second set of signal samples is used to evaluate interference effects between LQs and the  $Z'$  bosons in non-res production. Using benchmark values  $g_U = 1.8$  and  $\beta_R = 0$ , we consider various  $\{M_U, g_{Z'}\}$  scenarios for two different  $Z'$  mass hypotheses,  $(M_{Z'}/M_U)^2 \in \{\frac{1}{2}, \frac{3}{2}\}$ . The  $M_U$  values vary between 500 GeV and 5000 GeV, in steps of 250 GeV. The  $g_{Z'}$  coupling values are between 0.25 and 3.5, in steps of 0.25. Therefore, in total there are 280  $\{M_U, g_{Z'}, (M_{Z'}/M_U)^2\}$  scenarios simulated for this second set of signal samples, and for each of these scenarios a total of  $6.0 \times 10^5$  MC events are generated.

As noted previously, the simulated signal and background events are initially filtered using selections which are motivated by experimental constraints, such as the geometric constraints of the CMS detector, the typical kinematic thresholds for reconstruction of particle objects, and the available triggers. The remaining events after the preliminary event selection criteria are used to train and execute a BDT algorithm for each signal point in

the  $\{M_U, g_U\}$  space, in order to maximize the probability to detect signal amongst background events. The BDT algorithm is implemented using the `scikit-learn` [139] and `xgboost` (XGB) [193] python libraries. We use the `XGBClassifier` class from the `xgboost` library, a 10-fold cross validation using the `scikit-learn` method (`GridCV`<sup>5</sup>) for a grid in a hyperparameter space with 75, 125, 250, and 500 estimators, maximum depth in 3, 5, 7, 9, as well as learning rates of 0.01, 0.1, 1, and 10. For the cost function, we utilize the default mean square error (MSE). Additionally, we use the tree method based on the approximate greedy algorithm (histogram-optimized), referred to as `hist`, with a uniform sample method. These choices allow us to maximize the detection capability of the BDT algorithm by carefully tuning the hyperparameters, selecting an appropriate cost function, and utilizing an optimized tree construction method.

For each of the six analysis channels and  $\{M_U, g_U\}$  signal point, the binary XGB classifier was trained (tested) with 20% (80%) of the simulated events, for each signal and background MC sample. Over forty kinematic and topological variables were studied as input for the XGB. These included the momenta of b jets and  $\tau_{h,\ell}$  candidates; both invariant and transverse masses of pairs of  $\tau$  objects and of b $\tau$  combinations; angular differences between b jets, between  $\tau$  objects, and between the  $\tau_{h,\ell}$  and b jets; and additional variables derived from the missing momentum in the events. After studying correlations between variables and their impact on the performance of the BDT, we found that only eight variables were necessary and responsible for the majority of the sensitivity of the analysis. The variable that provides the best signal to background separation is the scalar sum of the  $p_T$  of the final state objects ( $\tau_h$ ,  $\tau_{h/\ell}$ , and b jets) and the missing transverse momentum, referred to as  $S_T^{\text{MET}}$ :

$$S_T^{\text{MET}} = |\vec{p}_T^{\text{miss}}| + \sum_{\tau_h, \tau_{h/\ell}, b} |\vec{p}_T| \quad (4.4)$$

The  $S_T^{\text{MET}}$  variable has been successfully used in LQ searches at the LHC, since it probes the mass scale of resonant particles involved in the production processes. Other relevant variables include the magnitude of the vectorial difference in  $p_T$  between the two lepton candidates ( $|\Delta\vec{p}_T|_{\tau_h \tau_{h/\ell}}$ ), the  $\Delta R_{\tau_h \tau_{h/\ell}}$  separation between them, the reconstructed dilepton mass  $m_{\tau_h \tau_{h/\ell}}$ , and the product of their electric charges ( $Q_{\tau_h} \times Q_{\tau_{h/\ell}}$ ). We also use the  $|\Delta\vec{p}_T|$  between the  $\tau_h$  candidate and  $\vec{p}_T^{\text{miss}}$ , and (if applicable) the  $|\Delta\vec{p}_T|$  between the  $\tau_h$  candidate and the leading b jet. For the final states including two  $\tau_h$  candidates, the one with the highest  $p_T$  is used.

---

<sup>5</sup> GridCV is a method that allows to find the best combination of hyperparameter values for the model, as this choice is crucial to achieve an optimal performance.

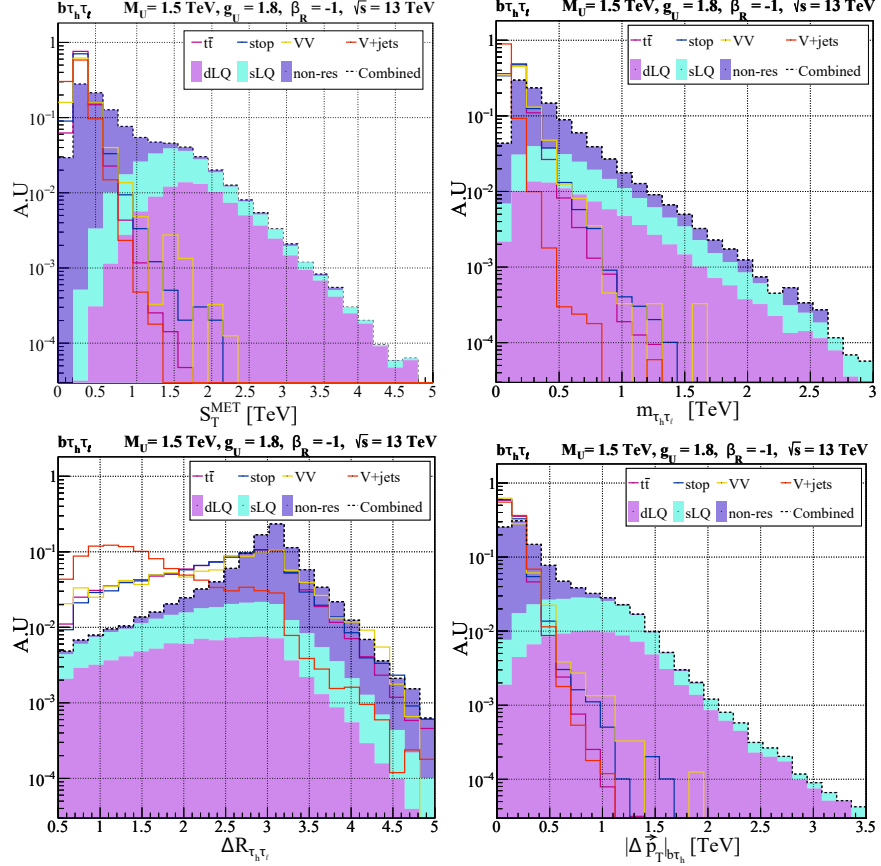


**Figure 4.5:**  $S_T^{MET}$ ,  $m_{\tau_h \tau_\ell}$ ,  $\Delta R_{\tau_h \tau_\ell}$ ,  $|\Delta \vec{p}_T|_{b\tau_h}$  signal and background distributions for the  $b\tau_h \tau_\ell$  channel. The signal distributions are generated for a benchmark sample with LQ mass of 1.5 TeV maximally coupled to right-handed currents. The combined distribution (shown as a stacked histogram) is the sum of the distributions, correctly weighted according to their respective cross-sections, assuming a coupling  $g_U = 1.8$ .

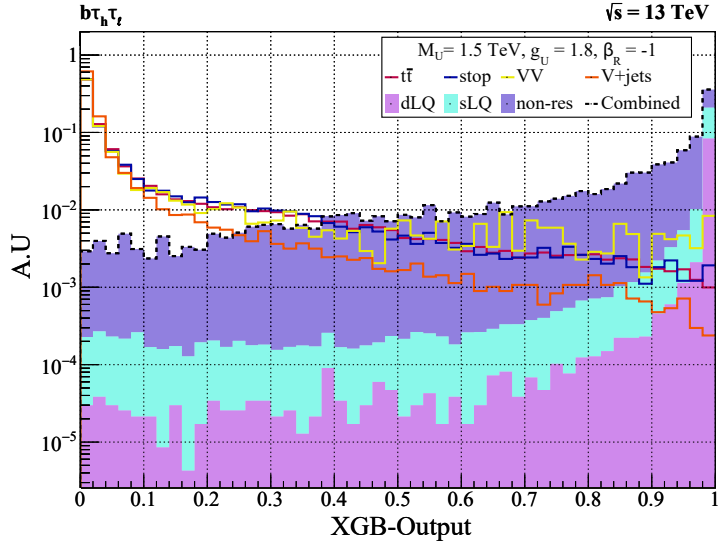
Fig. 4.5 shows some relevant topological distributions, including  $S_T^{MET}$  on the top, for the  $b\tau_h \tau_\ell$  category. In the Figure we include all signal production modes to this channel, with each component weighted with respect to their total contribution to the combined signal. The combined signal distribution is normalised to unity. We also show all background processes contributing to this channel, each of them individually normalised to unity. We find that the combined signal is dominated by sLQ production for large values of  $S_T^{MET}$ , while non-res production dominates for small  $S_T^{MET}$ . Interestingly, the backgrounds also sit at low  $S_T^{MET}$  values, since  $S_T^{MET}$  is driven by the mass scale of the SM particles being produced, in this case top quarks and Z/W bosons. This suggest that the sLQ and dLQ signals can indeed be separated from the SM background. As expected, the  $S_T^{MET}$  sLQ and dLQ signal distributions have a mean near  $M_U$ , representative of resonant production, and a broad width as expected for large mass  $M_U$  hypotheses when information about the z-components of the momenta of objects is not utilised in the  $S_T^{MET}$  calculation.

Fig. 4.5 (second from the top) shows the reconstructed mass of the ditau system, for the  $b\tau_h\tau_\ell$  search channel. Since the two  $\tau$  candidates in signal events arise from different production vertices (e.g., each  $\tau$  candidate in dLQ production comes from a different LQ decay chain), the ditau mass distribution for signal scales as  $m_{\tau_h\tau_\ell} \sim p_T(\tau_h) + p_T(\tau_\ell)$ , and thus has a tail which depends on  $M_U$  and sits above the expected SM spectrum. On the other hand, the SM  $m_{\tau_h\tau_\ell}$  distributions sit near  $m_{Z/W}$  since the  $\tau$  candidates in SM events arise from  $Z/W$  decays.

Fig. 4.5 (third from the top) shows the  $\Delta R_{\tau_h\tau_\ell}$  distribution for the  $b\tau_h\tau_\ell$  channel. In the case of the  $p p \rightarrow \tau\tau$  non-res signal distribution, the two  $\tau$  leptons must be back-to-back to preserve conservation of momentum. Therefore, the visible  $\tau$  candidates,  $\tau_h$  and  $\tau_\ell$ , give rise to a  $\Delta R_{\tau_h\tau_\ell}$  distribution that peaks near  $\pi$  radians. In the case of sLQ production, although the LQ and associated  $\tau$  candidate must be back-to-back, the second  $\tau$  candidate arising directly from the decay of the LQ does not necessarily move along the direction of the LQ (since the LQ also decays to a b quark). As a result, the  $\Delta R_{\tau_h\tau_\ell}$  distribution for the sLQ signal process is smeared out, is broader, and has a mean below  $\pi$  radians. On the other hand, the  $\tau_h$  candidate in  $t\bar{t}$  events is often a jet being misidentified as a genuine  $\tau_h$ . When this occurs, the fake  $\tau_h$  candidate can arise from the same top quark decay chain as the  $\tau_\ell$  candidate, thus giving rise to small  $\Delta R_{\tau_h\tau_\ell}$  values. This difference in the signal and background distributions provides a nice way for the ML algorithm to help decipher signal and background processes.

As noted above, the  $|\Delta\vec{p}_T|$  distribution between the visible  $\tau$  candidates and the b-quark jets is an important variable to help the BDT distinguish between signal and background processes. The discriminating power can be seen in Fig. 4.5 (bottom), which shows the  $|\Delta\vec{p}_T|$  between the  $\tau_h$  and b-jet candidate of the  $b\tau_h\tau_\ell$  channel. In the case of dLQ production, the b quarks and  $\tau$  leptons from the  $LQ \rightarrow b\tau$  decay acquire transverse momentum of  $p_T \sim M_U/2$ . However, when the  $\tau$  lepton decays hadronically (i.e.  $\tau \rightarrow \tau_h\nu$ ), a large fraction of the momentum is lost to the neutrino. Therefore, the  $|\Delta\vec{p}_T|_{b\tau_h}$  distribution for the dLQ (and sLQ) process peaks below  $M_U/2$ . On the other hand, for a background process such as V+jets, the b jet arises due to initial state radiation, and thus must balance the momentum of the associated vector boson (i.e.  $p_T(b) \sim p_T(V) \sim m_V$ ). Since the visible  $\tau$  candidate is typically produced from the V boson decay chain, its momentum (on average) is approximately  $p_T(\tau_h) \sim p_T(V)/4 \sim m_V/4$ . Therefore, to first order, the  $|\Delta\vec{p}_T|$  distribution for the V+jets background is expected to peak below the  $m_V$  mass.

Lets us turn to the results of the  $b\tau_h\tau_\ell$  BDT classifier, which is shown in Fig. 4.6 for the different signal production modes and backgrounds. Similar to Fig. 4.5, the distribution for each individual signal production mode is weighted with respect to their total contribution to the combined signal. The background distributions and combined signal distribution are normalized to an area under the curve of unity. Fig. 4.6 shows the XGB



**Figure 4.6:** Postfit XGB-output normalised distribution in the  $b\tau_h\tau_l$  channel, for LQ mass of 1.5 TeV, constant coupling  $g_U = 1.8$ , and maximally coupled to right-handed currents.

distributions for a signal benchmark point with  $M_U = 1.5 \text{ TeV}$ ,  $g_U = 1.8$ , and  $\beta_R = -1$ . The XGB output is a value between 0 and 1, which quantifies the likelihood that an event is either signal-like (XGB output near 1) or background-like (XGB output near 0). We see that the presence of the sLQ and dLQ production modes is observed as an enhancement near a XGB output of unity, while the backgrounds dominate over the low end of the XGB output spectrum, especially near zero. In fact, over eighty percent of the sLQ and dLQ distributions reside in the last two bins, XGB output greater than 0.96, while more than sixty percent of the backgrounds fall in the first two bins, XGB output less than 0.04. It is also interesting to note that in comparison to the sLQ and dLQ distributions in Fig. 4.6, non-res is broader and not as narrowly peaked near XGB output of 1, which is expected due to the differences in kinematics described above. Overall, if we focus on the last bin in this distribution, we find approximately 0.2% of the background, in contrast to 22% of the non-res, 78% of the sLQ, and 91% of the dLQ signal distributions. These numbers highlight the effectiveness of the XGB output in reducing the background in the region where the signal is expected.

The output signal and background distributions of the XGB classifier, normalised to their cross section times pre-selection efficiency times luminosity, are used to perform a profile binned likelihood statistical test in order to determine the expected signal significance. The estimation is performed using the RooFit [332] package, following the same methodology as in Refs. [273–278, 333–342]. The value of the significance ( $Z_{\text{sig}}$ ) is measured using the probability to obtain the same outcome from the test statistic in the background-only hypothesis, with respect to the signal plus

background hypothesis. This allows for the determination of the local p-value and thus the calculation of the signal significance, which corresponds to the point where the integral of a Gaussian distribution between  $Z_{\text{sig}}$  and  $\infty$  results in a value equal to the local p-value.

Systematic uncertainties are incorporated as nuisance parameters, considering log-priors for normalization and Gaussian priors for shape uncertainties. Our consideration of systematic uncertainties includes both experimental and theoretical effects, focusing on the dominant sources of uncertainty. Following [138], we consider a 3% systematic uncertainty on the measurement of the integrated luminosity at the LHC. A 5% uncertainty arises due to the choice of the parton distribution function used for the MC production, following the PDF4LHC prescription [157]. The chosen PDF set only has an effect on the overall expected signal and background yields, but the effect on the shape of the XGB output distribution is negligible. Reference [142] reports a systematic uncertainty of 2-5%, depending on the  $p_T$  and  $\eta$  of the  $\tau_h$  candidate. Therefore, we utilize a conservative 5% uncertainty per  $\tau_h$  candidate, independent of  $p_T$  and  $\eta$ , which is correlated between signal and background processes with genuine  $\tau_h$  candidates, and correlated across XGB bins for each process. We assumed a 5%  $\tau_h$  energy scale uncertainty, independent of  $p_T$  and  $\eta$ , following the CMS measurements described in [142]. Finally, we assume a conservative 3% uncertainty per b-jet candidate, following reference [270], and an additional 10% uncertainty in all the background predictions to account for possible mismodeling by the simulated samples. The uncertainties on the background estimates are typically derived from collision data using dedicated control samples that have negligible signal contamination and are enriched with events from the specific targeted background. The systematic uncertainties on the background estimates are treated as uncorrelated between background processes.

### 4.3 RESULTS

---

The expected signal significance for sLQ, dLQ and non-res production, and their combination, is presented in Fig. 4.7. Here, the significance is shown as a heat map in a two dimensional plane of  $g_U$  versus  $M_U$ , considering exclusive couplings to left-handed currents, *i.e.*  $\text{BR}(\text{LQ} \rightarrow b\tau) = \frac{1}{2}$ . The dashed lines show the contours of constant signal significance. The  $1.69\sigma$  contour represents exclusion at 95% confidence level, and the  $3-5\sigma$  contours represent potential discovery. The grey band defines the set of  $\{M_U, g_U\}$  values that can explain the B-meson anomalies,  $C_U \sim 0.01$  for this scenario. The estimates are performed under the conditions for the second run, RUN-II, of the LHC ( $\sqrt{s} = 13 \text{ TeV}$  and  $L = 137 \text{ fb}^{-1}$ ). We find that the dLQ interpretation plot (Figure 4.7 second from the top) does not depend on  $g_U$ , which is expected due to dLQ production arising exclusively from interactions with gluons. For this reason, the dLQ production process provides the best mode for discovery when  $g_U$  is small. On the other

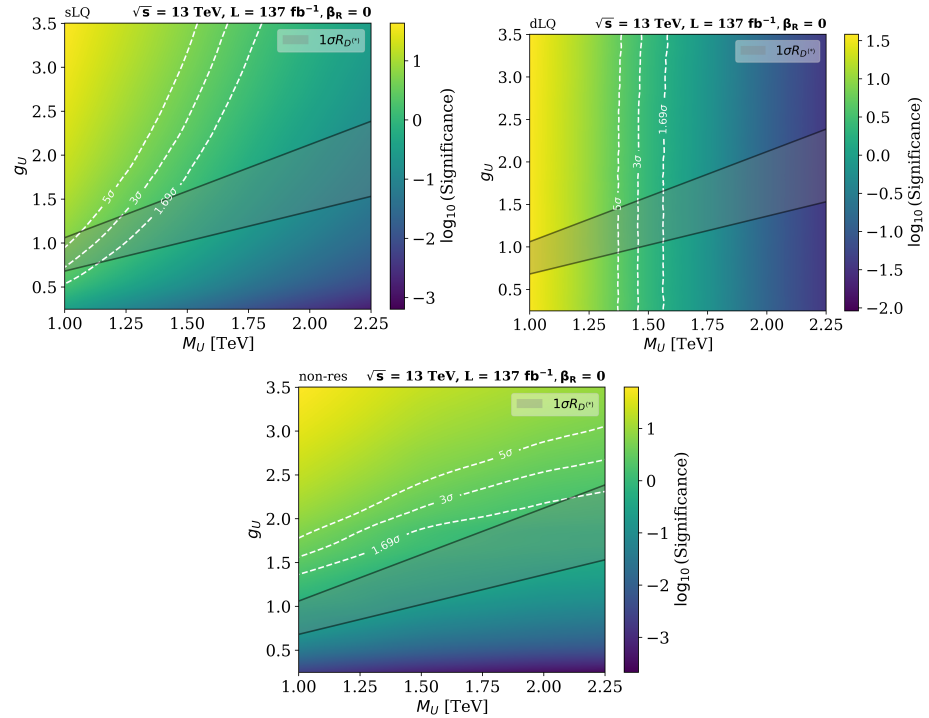


**Figure 4.7:** Signal significance for different coupling scenarios and LQ masses, without right-handed currents, using the combination of all search channels. The results pertaining to sLQ, dLQ and non-res production are displayed respectively from the top. These results are for  $\sqrt{s} = 13 \text{ TeV}$  and  $137 \text{ fb}^{-1}$ .

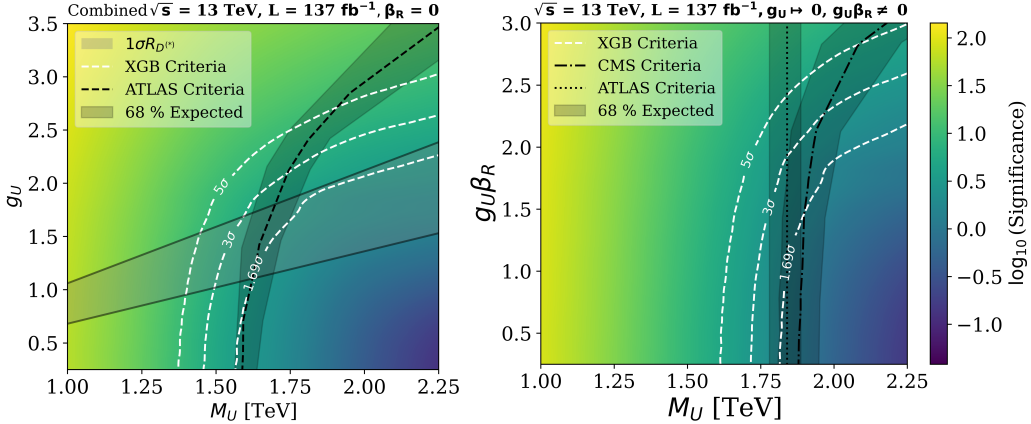


**Figure 4.8:** The top (bottom) panel shows signal significance comparison with ATLAS [316] (CMS and ATLAS [311, 317]) background only hypothesis, for the combination of all channels, with uniquely coupling to left-handed (right-handed) currents. The estimates are performed at  $\sqrt{s} = 13 \text{ TeV}$  and  $137 \text{ fb}^{-1}$ .

hand, the non-res channel is more sensitive to changes in the coupling parameter  $g_U$ , as its production cross-section depends on  $g_U^4$ . Therefore, the non-res production process provides the best mode for discovery when  $g_U$  is large. These results confirm the expectations from previous analyses (see for instance [299]), in the sense that the dLQ and non-res processes complement each other nicely at low and high  $g_U$  scenarios. The sLQ channel combines features from both the dLQ and non-res channels, in principle making it an interesting option to explore different scenarios and gain a better understanding of LQ properties, but the evolution of the signal significance in the full phase space is more complicated as it involves resonant LQ production with a cross-section that depends non-trivially on  $M_U$ ,  $g_U$ , and the LQ coupling to gluons. However, Fig. 4.7 shows that the sLQ production process can provide complementary and competitive sensitivity to the non-res and dLQ processes, in certain parts of the phase space.

The top panel of Fig. 4.8 presents the sensitivity of all signal production processes combined, and compares our expected exclusion region with the latest one from the ATLAS Collaboration [316]. The comparison suggests that our proposed analysis strategy provides better sensitivity than current methods being carried out at ATLAS, especially at large values of  $g_U$ . In particular, we find that with the pp data already available from RUN-II, our expected exclusion curves begin to probe solutions to the B-anomalies for LQ masses up to 2.25 TeV.

Fig. 4.8 shows the expected signal significance considering  $\text{BR}(\text{LQ} \rightarrow b\tau) = 1$ , in order to compare our analysis with the corresponding results from the CMS [311] and ATLAS [317] Collaborations. Let us emphasize again that  $\text{BR}(\text{LQ} \rightarrow b\tau)$  depends on  $\beta_R$ , as illustrated on the top panel of Fig. 4.2. Thus, although the  $\text{BR}(\text{LQ} \rightarrow b\tau) = 1$  scenario is a possible physical case, it does not solve the observed anomalies in the  $R_{D^{(*)}}$  ratios,

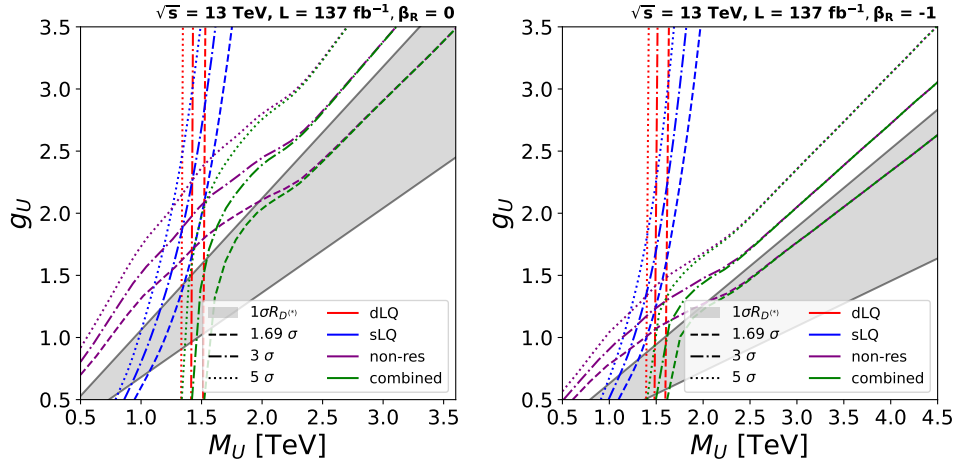


**Figure 4.9:** Signal significance for different coupling scenarios and LQ masses for all channels. This plot summarizes our results with  $\beta_R = 0$  (without right-handed currents) and  $\beta_R = -1$  (maximally coupled to right-handed currents). The estimates are performed at  $\sqrt{s} = 13 \text{ TeV}$  and  $137 \text{ fb}^{-1}$ .

as it corresponds to the case where LQs couple exclusively to right-handed currents.

With this in mind, the scenario studied by CMS in [311] considers couplings only to left-handed currents, setting artificially the condition  $\text{BR}(\text{LQ} \rightarrow b\tau) = 1$ . In order to compare, we scale the efficiency  $\times$  acceptance of our selection criteria for  $\beta_R = 0$ , by a factor of 2.0 for sLQ and 4.0 for dLQ. According to Fig. 4.8, the ML approach that we have followed again suggests an optimisation of the signal and background separation, having the potential of improving the regions of exclusion ( $1.69\sigma$ ) with respect to that of CMS. In the bottom panel of the Figure we have also included a similar exclusion by ATLAS [317]. However, since ATLAS only considers dLQ production in the analysis, the results are not entirely comparable, so are included only as a reference.

We now turn to the role of  $\beta_R$ , and our capacity of probing the regions solving the B-meson anomalies. Fig. 4.9 shows the maximum significant contours, under LHC RUN-II conditions, for the different LQ production mechanisms and their combination, considering scenarios with only left-handed currents ( $\beta_R = 0$ , top) and with maximal right-handed currents ( $\beta_R = -1$ , bottom). We find a noticeable improvement in signal significance in all channels when taking  $\beta_R = -1$ , as is expected from the increase in  $\text{BR}(\text{LQ} \rightarrow b\tau)$  branching ratio and production cross-sections (see Fig. 4.2). However, the region solving the B-meson anomalies also changes, preferring lower values of  $g_U$ , such that in both cases we find ourselves just starting to probe this region at large  $M_U$ .

The combined significance contours for the different BR scenarios that have been considered is presented in Fig. 4.10. These contours illustrate the regions of exclusion for the three cases of interest, namely exclusive left-handed currents ( $\text{BR}(\text{LQ} \rightarrow b\tau) = \frac{1}{2}$ ,  $\beta_R = 0$ ), maximal left and right

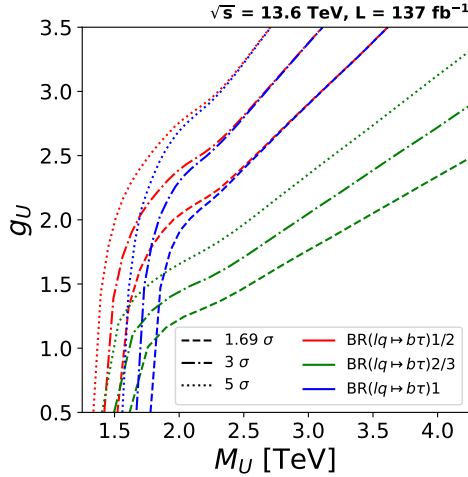


**Figure 4.10:** Signal significance for different coupling scenarios and LQ masses, considering the case without coupling to right-handed currents  $\text{BR}(\text{LQ} \rightarrow b\tau) = \frac{1}{2}$ , the case maximally coupled to right- and left-handed currents  $\text{BR}(\text{LQ} \rightarrow b\tau) = \frac{2}{3}$ , and the case uniquely coupled to right-handed currents  $\text{BR}(\text{LQ} \rightarrow b\tau) = 1$ . The estimates are performed at  $\sqrt{s} = 13 \text{ TeV}$  and  $137 \text{ fb}^{-1}$ .

couplings ( $\text{BR}(\text{LQ} \rightarrow b\tau) = \frac{2}{3}, \beta_R = -1$ ), and exclusive right-handed currents ( $\text{BR}(\text{LQ} \rightarrow b\tau) = 1, g_U \rightarrow 0, g_U \beta_R = 1$ ). For small  $g_U$ , we find that the exclusive right-handed scenario is most sensitive, while the exclusive left-handed case is the worst. The reason for this is that this region is excluded principally by dLQ production, such that having the largest branching ratio is crucial in order to have a large number of events. For larger couplings, both exclusive scenarios end up having similar exclusion regions, with the  $\beta_R = -1$  case being significantly more sensitive. The reason in this case is that the exclusion is dominated by non-res, which has a much larger production cross-section if both currents are turned on.

In order to finalise our analysis of the LQ-only model, we show in Fig. 4.11 the expected combined significance in the relatively near future. For this, considering  $\sqrt{s} = 13.6 \text{ TeV}$ , we show contours for the sensitivity corresponding to integrated luminosities of  $137 \text{ fb}^{-1}$ ,  $300 \text{ fb}^{-1}$ , and  $3000 \text{ fb}^{-1}$ , for scenarios with only left-handed currents (top) and with maximal coupling to right-handed currents (bottom). Note that for  $\beta_R = 0$  ( $\beta_R = -1$ ), couplings  $g_U$  close to 3.18 (1.85) and  $M_U = 5.0 \text{ TeV}$  can be excluded with  $1.69\sigma$  significance for the high luminosity LHC era, allowing us to probe the practically the entirety of the B-meson anomaly favored region. Note that the background yields for the high luminosity LHC might be larger due to pileup effects. Nevertheless, as it was mentioned in Sec. 4.2, we have included a conservative 10% systematic uncertainty associated with possible fluctuations on the background estimations. Although effects from larger pileup might be significant, they can be mitigated by improvements in the algorithms for particle reconstruction and identification, and also on the data-analysis techniques.

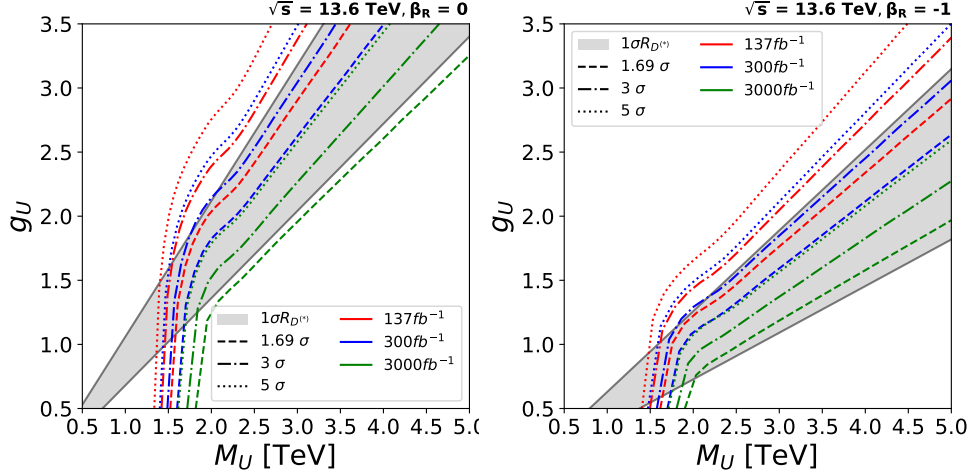


**Figure 4.11:** Projected signal significance for different coupling scenarios and LQ masses maximally coupled to right-handed currents. The estimates are performed at  $\sqrt{s} = 13.6 \text{ TeV}$ ,  $137 \text{ fb}^{-1}$ ,  $300 \text{ fb}^{-1}$  and  $3000 \text{ fb}^{-1}$ .

As commented on the Introduction, non-res production can be significantly affected by the presence of a companion  $Z'$ , which provides additional s-channel diagrams that add to the total cross-section and can interfere destructively with the LQ t-channel process (see Figures 4.3 and 4.4). From our previous results, we see that non-res always is of high importance in determining the exclusion region, particularly at large  $M_U$  and  $g_U$ , meaning it is crucial to understand how this role is affected in front of a  $Z'$  with similar mass.

The change in sensitivity on the non-res signal significance due this interference effect with the  $Z'$  boson is shown in Fig. 4.12. We consider two opposite cases for the  $Z'$  mass:  $M_{Z'}^2 = M_U^2/2$  (top) and  $M_{Z'}^2 = 3M_U^2/2$  (bottom). Our results are shown on the  $g_{Z'} - M_U$  plane, for a fixed  $g_U = 1.8$  and  $\beta_R = 0$ . For the  $M_{Z'}^2 = M_U^2/2$  scenario, there is an overall increase in the total cross-section, with a larger  $g_{Z'}$  implying a larger sensitivity. This means that our ability to probe smaller values of  $g_U$  could be enhanced, as a given observation would be reproduced with both a specific  $g_U$  and vanishing  $g_{Z'}$ , or a smaller  $g_U$  with large  $g_{Z'}$ . Thus, for a large enough  $g_{Z'}$ , it could be possible to enhance non-res to the point that the entire region favoured by B-anomalies could be ruled out. In contrast, for  $M_{Z'}^2 = 3M_U^2/2$  the cross-section is strongly affected by the large destructive interference, such that a larger  $g_{Z'}$  does not necessarily imply an increase in sensitivity. In fact, as can be seen in the bottom panel, for large  $M_U$  the significance is reduced as  $g_{Z'}$  increases, leading to the opposite conclusion than above, namely, that a large  $g_{Z'}$  could reduce the effectiveness of non-res.

The impact of the above can be seen in Fig. 4.13, which shows our previous sensitivity curves on the  $M_U - g_U$  plane, but this time with a  $Z'$  contribution to non-res. We use the same values of  $M_{Z'}$  as before, but fix  $g_{Z'} = 3.5$ . For smaller  $M_{Z'}$  (top), the non-res contribution is enhanced so much, that both sLQ and dLQ play no role whatsoever in determining the

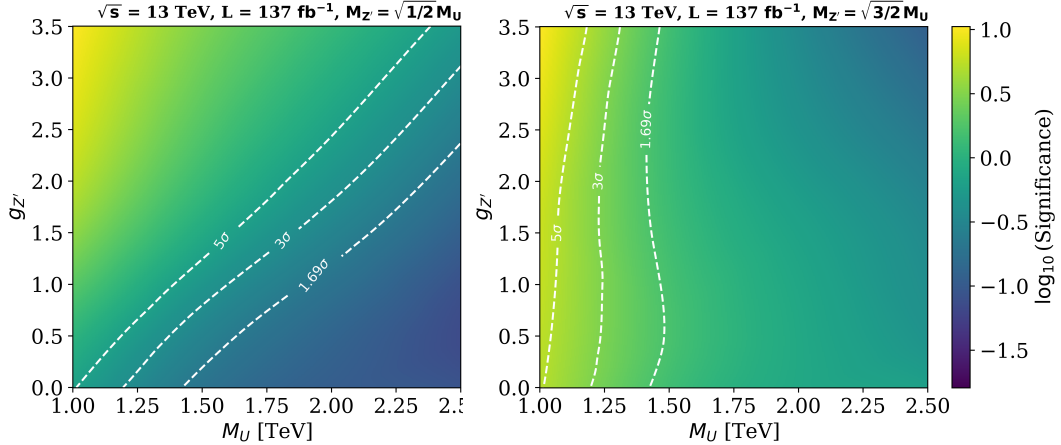


**Figure 4.12:** Change on the non-res signal significance for different  $Z'$  coupling scenarios and LQ masses. The estimates are performed at  $\sqrt{s} = 13.0$  TeV,  $\beta_R = 0$ ,  $g_U = 1.8$ ,  $M_{Z'} = \sqrt{1/2} M_U$  (top), and  $M_{Z'} = \sqrt{3/2} M_U$  (bottom).

exclusion region. We find that, for small  $g_U$ , the sensitivity is dominated by  $Z'$  production such that, since  $M_U$  is related to  $M_{Z'}$ , LQ masses up to  $\sim 3$  TeV are excluded. This bound is slightly relaxed for larger values of  $g_U$ , which is attributed to destructive interference effects due to an increased LQ contribution.

The bottom panel of Fig. 4.13 shows that case where  $M_{Z'}$  is larger than  $M_U$ . As expected from our previous discussion, the behaviour and impact of non-res is modified. For small  $g_U$ , we again have the pure  $Z'$  production dominating the non-res cross-section, leading to a null sensitivity on  $g_U$ , similar to what happens in dLQ. In contrast, for very large  $g_U$ , we find that the pure LQ non-res production is the one that dominates, and we recover sensitivity regions with a slope similar to those shown in Figures 4.7–4.11, shifted towards larger values of  $g_U$ . For intermediate values of this coupling, the destructive interference have an important effect again, twisting the exclusion region slightly towards the left. Still, even in this case, we find that sLQ plays a marginal role in defining the combined exclusion region, and that the final result again depends primarily on dLQ and non-res production.

#### 4.4 DISCUSSION AND CONCLUSIONS

Experimental searches for LQs with preferential couplings to third generation fermions are currently of great interest due to their potential to explain observed tensions in the  $R_D$  and  $R_{D^*}$  decay ratios of B mesons with respect to the SM predictions. Although the LHC has a broad physics program on searches for LQs, it is very important to consider the impact of each search within wide range of different theoretical assumptions within a specific model. In addition, in order to improve the sensitivity to detect possible signs of physics beyond the SM, it is also important to strongly consider

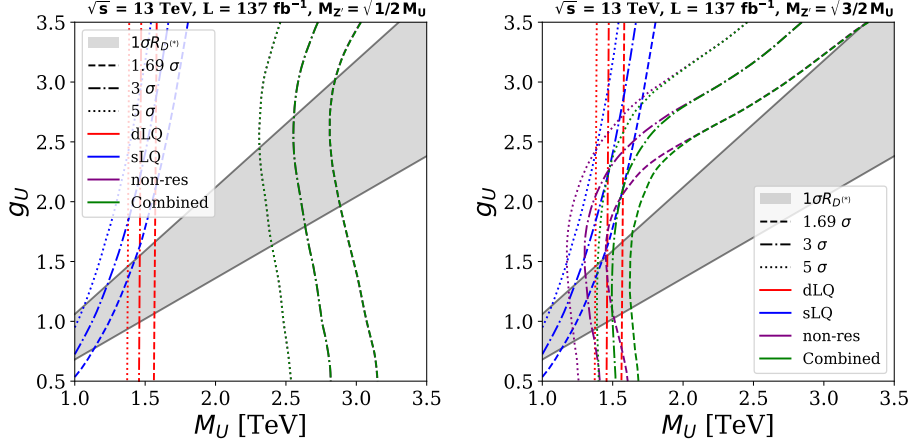


**Figure 4.13:** Signal significance for different coupling scenarios and LQ masses, for all channels, with an additional  $Z'$  contribution to non-res production. We set  $\beta_R = 0$  and  $g_{Z'} = 3.5$ , taking  $M_{Z'}^2$  equal to  $M_U^2/2$  ( $3M_U^2/2$ ) on the top (bottom) panel.

new computational techniques based on machine learning (ML). Therefore, we have studied the production of  $U_1$  LQs with preferential couplings to third generation fermions, considering different couplings, masses and chiral currents. These studies have been performed considering  $p p$  collisions at  $\sqrt{s} = 13$  TeV and 13.6 TeV and different luminosity scenarios, including projections for the high luminosity LHC. A ML algorithm based on boosted decision trees is used to maximize the signal significance. The signal to background discrimination output of the algorithm is taken as input to perform a profile binned-likelihood test statistic to extract the expected signal significance.

The expected signal significance for sLQ, dLQ and non-res production, and their combination, is presented as contours on a two dimensional plane of  $g_U$  versus  $M_U$ . We present results for the case of exclusive couplings to left-handed, mixed, and exclusive right-handed currents. For the first two, the region of the phase space that could explain the B meson anomalies is also presented. We confirm the findings of previous works that the largest production cross-section and best overall significance comes from the combination of dLQ and non-res production channels. We also find that the sensitivity to probe the parameter space of the model is highly dependent on the chirality of the couplings. Nevertheless, the region solving the B-meson anomalies also changes with each choice, such that in all evaluated cases we find ourselves just starting to probe this region at large  $M_U$ .

Our studies compare our exclusion regions with respect to the latest reported results from the ATLAS and CMS Collaborations. The comparison suggests that our ML approach has a better sensitivity than the standard cut-based analyses, especially at large values of  $g_U$ . In addition, our projections for the HL-LHC cover the whole region solving the B-anomalies, for masses up to 5.00 TeV.

Finally, we consider the effects of a companion  $Z'$  boson on non-res production. We find that such a contribution can have a considerable impact on the LQ sensitivity regions, depending on the specific masses and couplings. In spite of this, we still consider non-res production as an essential channel for probing LQs in the future.



# 5

---

## CONCLUSIONS AND OUTLOOK

---

The SM of particle physics describes elementary particles and their interactions through the gauge group  $SU(3)_C \times SU(2)_L \times U(1)_Y$  with remarkable precision. However, persistent experimental tensions combined with theoretical challenges provide compelling motivation for BSM physics. These anomalies share a common feature: they suggest new particles with preferential couplings to second and third-generation fermions.

This thesis has presented two phenomenological studies exploring search strategies at the LHC to probe BSM models addressing these anomalies. The first investigates light scalar production in the  $U(1)_{T_R^3}$  model through the channel  $pp \rightarrow t\chi_u\phi'$ , demonstrating sensitivity to  $\phi'$  masses from 5 to 325 GeV and  $\chi_u$  masses up to 2 TeV at the HL-LHC. The second examines  $U_1$  vector leptoquark phenomenology through single, pair, and non-resonant production, showing complete coverage of the  $R_{D^{(*)}}$ -motivated parameter space for masses up to 5 TeV. Both analyses employ BDT-based machine learning to maximize signal-background discrimination and profile-binned-likelihood methods to quantify discovery potential, demonstrating that carefully designed strategies can significantly extend the reach of LHC experiments into previously inaccessible regions of BSM parameter space.

### 5.1 SUMMARY

---

Chapter 1 established the theoretical foundation by presenting the SM as a quantum field theory based on the gauge group  $SU(3)_C \times SU(2)_L \times U(1)_Y$ , and systematically examined its deficiencies. Among the phenomenological challenges, particular emphasis was placed on the anomalies in B-meson decays, which suggest violations of lepton flavor universality. The ratios  $R_{D^{(*)}} = \mathcal{B}(B \rightarrow D^{(*)}\tau\nu_\tau)/\mathcal{B}(B \rightarrow D^{(*)}\ell\nu_\ell)$  have been measured by BaBar, Belle, and LHCb to consistently exceed SM predictions. While recent measurements of the  $R_{K^{(*)}}$  ratio have shown consistency with SM predictions, the persistent tension in the  $R_{D^{(*)}}$  ratio provides strong motivation for considering BSM scenarios with non-universal lepton couplings. These experimental hints share a common feature: they point towards new physics that breaks lepton universality, potentially involving enhanced couplings to heavier fermion generations.

Chapter 2 established the methodological framework employed throughout this thesis, describing the LHC accelerator complex and the associated multipurpose detectors, explaining particle reconstruction and identification, and introducing the kinematic variables used in collider analyses. The chapter presented the Monte Carlo simulation pipeline that connects theoretical models to experimental observables, consisting of hard-process generation using matrix-element calculations, parton showering and hadronization, and detector simulation. The statistical framework for quantifying analysis sensitivity was developed through likelihood-based hypothesis testing, with the profile likelihood ratio test statistic as the standard method for discriminating between signal-plus-background and background-only hypotheses. Machine learning methods for signal-background discrimination were introduced, with BDTs presented as multivariate classifiers that can learn complex, non-linear correlations between kinematic variables. This ML-enhanced approach represents a significant advancement over traditional “cut and count” based analyses, particularly in scenarios with low signal-to-background ratios and overlapping kinematic distributions.

In Chapter 3, we investigated the phenomenology of a minimal  $U(1)_{T_R^3}$  gauge extension of the SM. This model, motivated by left-right symmetric theories and the embedding of a  $U(1)_{B-L}$  gauge symmetry, predicts a light scalar boson  $\phi'$ , with masses potentially below the electroweak scale, and TeV-scale vector-like quarks  $\chi_u$  with QCD couplings. We proposed a search strategy focusing on the previously unexplored production channel  $pp \rightarrow t\chi_u\phi'$ , where the light scalar is produced in association with a heavy top-partner and a SM top quark. The key insight is that the simultaneous production of heavy QCD-coupled particles naturally provides the large momentum required for the decay products of the light  $\phi'$  to be efficiently detected in the central regions of the CMS and ATLAS detectors. This “boosted light particle” strategy represents a paradigm shift: rather than searching for light scalars through direct low-energy production, we exploit the UV completion of the model by accessing the heavy degrees of freedom that produce the light scalar with substantial transverse momentum.

Our analysis considered the scenario where  $\phi'$  has family non-universal couplings and decays primarily to muon pairs ( $\phi' \rightarrow \mu^+\mu^-$ ) for  $m(\phi') \geq 1$  GeV. The final state signature comprises three muons, a boosted top-quark system, at least one b-tagged jet, and large missing transverse momentum. To discriminate this complex signature from SM backgrounds (primarily  $t\bar{t}\mu^+\mu^-$  and  $b\bar{b}\mu\mu\nu$ ), we developed a BDT-based machine learning classifier trained on a broad set of kinematic variables. We also compared the performance of DNNs against BDTs and found that while DNNs achieved marginally better discrimination, the improvement was modest compared to the significantly increased computational cost and training time, making BDTs the more practical choice for this analysis. The classifier output was used in a profile binned-likelihood framework to extract signal significance. The main results demonstrate that with  $3000 \text{ fb}^{-1}$  of HL-LHC data,  $\phi'$  ( $\chi_u$ ) masses from 5 to 325 GeV (up to 1.8 TeV) can be probed. This result

provides a significant extension of the accessible parameter space compared to previous searches. The analysis shows that detection prospects for low-mass particles are substantially enhanced when it is kinematically possible to simultaneously access the heavy degrees of freedom in the UV completion.

Chapter 4 focused on the  $U_1$  vector LQ phenomenology, which transforms as  $(\mathbf{3}, \mathbf{1}, 2/3)$  under the SM gauge group. This hypothetical particle is interesting as it represents one of the few viable single-mediator solutions capable of explaining the anomalies in the  $R_{D^{(*)}}$  ratios in charged-current B-meson decays, with accessible signatures feasible for detection at the LHC. The key feature of this model is that the LQ couples preferentially to third-generation fermions through  $b\tau$  and  $t\bar{\nu}_\tau$  vertices. We developed an analysis strategy combining three complementary production channels: single LQ production (sLQ), pair production (dLQ), and non-resonant production (non-res), where the LQ mediates  $pp \rightarrow \tau^+\tau^-$  processes at the amplitude level. Each channel has distinct sensitivity to probe different ranges of LQ masses ( $M_{U_1}$ ) and its coupling to fermions,  $g_{U_1}$ . The sLQ production cross section scales as  $g_{U_1}^2$ , making it particularly sensitive to the coupling strength, while dLQ production depends primarily on the QCD couplings and provides model-independent constraints on the mass.

An important aspect of this work was the systematic study of how the chiral structure of the LQ couplings affects the phenomenology. We considered three scenarios: exclusive couplings to left-handed currents, mixed chirality, and exclusive right-handed currents. Each scenario predicts different kinematic distributions and different regions of parameter space capable of explaining the B-meson anomalies. We found that while the sensitivity is highly dependent on chirality, in all cases the combination of production channels allows for complete coverage of the parameter space. The analysis employed a BDT-based machine learning approach to maximize signal-background discrimination, considering final states with varying  $\tau$ -lepton and  $b$ -jet multiplicities. Our results show that the ML approach significantly improves sensitivity compared to traditional “cut-based” analyses, particularly at large values of  $g_{U_1}$ . The HL-LHC projections indicate complete coverage of the parameter space solving the B-anomalies for LQ masses up to 5.0 TeV. An important finding concerns the impact of additional particles predicted by complete gauge theories. We evaluated the effects of a companion  $Z'$  boson on non-resonant production and found that interference effects can have considerable impact on the sensitivity regions, depending on the specific masses and couplings.

## 5.2 METHODOLOGICAL INSIGHTS

---

Both studies in this thesis exemplify several key principles in modern collider phenomenology that have applicability beyond the specific models investigated:

*Machine Learning as a Useful Tool.* Traditional “cut-based” analyses, while transparent and robust, often fail to fully exploit the information contained in the high-dimensional phase space of LHC events. Both studies demonstrate that machine learning algorithms, particularly BDTs, can learn complex, non-linear correlations between kinematic variables to construct powerful discriminators that significantly enhance sensitivity. The improvements are most pronounced in scenarios with low signal-to-background ratios and overlapping kinematic distributions—precisely the challenging cases where new physics is most likely to remain hidden. The BDT approach allows for optimal use of all available kinematic information simultaneously, rather than imposing sequential cuts that may discard events containing valuable discriminating information in other variables.

*Importance of UV Completions.* Both studies in this thesis illustrate a crucial principle: low-energy phenomena and collider signatures are often best understood by considering the full particle spectrum that arises in the UV completion of the theory. The  $U(1)_{T_R^3}$  study demonstrates that light particles can be efficiently probed by accessing the heavy degrees of freedom with which they are produced, rather than relying solely on direct low-energy production. The conventional approach of searching for light scalars through direct production may miss important regions of parameter space, while associated production with heavy vector-like quarks naturally provides the boosted kinematics needed for detection. Similarly, the LQ study shows that UV completeness introduces additional particles—such as the companion  $Z'$  boson in gauge theories—whose presence significantly affects the phenomenology through interference effects in key production channels. In the non-resonant production process, the  $Z'$  contributions modify the  $pp \rightarrow \tau^+\tau^-$  cross section in regions of parameter space that would otherwise appear most promising for discovery. These interference effects, which depend sensitively on the relative masses and couplings of the LQ and the  $Z'$ , can enhance or suppress the signal depending on the specific UV completion.

*Complementarity of Search Channels.* Both studies demonstrate that different production mechanisms provide complementary sensitivity to different regions of parameter space. In the  $U(1)_{T_R^3}$  case,  $\chi_u\bar{\chi}_u t$  fusion and  $\chi_u\bar{\chi}_u$  production probe different couplings and provide sensitivity across different mass ranges. In the LQ case, single, pair, and non-resonant production have different dependencies on  $M_U$  and  $g_U$ , with pair production dominating at low coupling, single production becoming important at intermediate coupling, and non-resonant production providing the strongest constraints at high coupling. Optimal search strategies must consider all relevant channels and their combination, as focusing on a single channel may miss significant portions of the viable parameter space.

### 5.3 OUTLOOK AND FUTURE DIRECTIONS

---

The work presented in this thesis opens several avenues for future research, both in extending the current analyses and in exploring related phenomenological questions.

#### 5.3.1 EXTENDED PHENOMENOLOGY OF THE $U(1)_{T_R^3}$ MODEL

*Dark Matter in the Neutrino Sector.* The  $U(1)_{T_R^3}$  model predicts right-handed neutrinos  $\nu_R$  that are required for anomaly cancellation. In certain parameter regimes, the lightest right-handed neutrino could serve as a viable dark matter candidate. A comprehensive study of this scenario would naturally connect collider phenomenology with cosmological observations and dark matter searches. The dark matter properties would be determined by the interplay between the  $U(1)_{T_R^3}$  breaking scale, the neutrino mass scale, and the couplings to the new  $Z'$  gauge boson and the  $\phi'$  scalar. Constraints would come from multiple fronts: relic abundance calculations requiring the correct thermal freeze-out density, direct detection experiments probing neutrino-nucleon scattering, indirect detection searching for annihilation products in cosmic rays, and collider searches for dark matter production in association with visible particles. The correlations between these different observables could provide a rich phenomenological landscape for testing the model, connecting the LHC signatures studied in this thesis with dark matter experiments and precision cosmology.

*Electroweak Precision Tests and  $Z'$  Phenomenology.* The  $Z'$  gauge boson arising from the spontaneously broken  $U(1)_{T_R^3}$  symmetry has not been the primary focus of this thesis but warrants detailed study. The  $Z'$  couples to right-handed SM fermions and could contribute to precision electroweak observables through loop corrections, as well as to rare flavor-changing processes. A comprehensive phenomenological program would explore: precision measurements of  $Z$ -pole observables constrained by LEP data, contributions to rare processes such as  $B_s$ - $\bar{B}_s$  mixing and  $\mu \rightarrow e$  conversion, and direct production at the LHC through Drell-Yan processes  $pp \rightarrow Z' \rightarrow \ell^+ \ell^-$ . Current LHC searches exclude  $Z'$  masses below  $\sim 4\text{-}5$  TeV for SM-like couplings, but weaker constraints apply for non-universal couplings characteristic of the  $U(1)_{T_R^3}$  model. The interplay between high-energy collider searches and low-energy precision measurements would provide complementary constraints on the  $Z'$  mass and coupling strength, with different observables dominating the sensitivity in different regions of parameter space.

*$\phi'$  Production in Rare Decays.* While the study in Chapter 3 focused on  $\phi'$  production in association with vector-like quarks, the dark Higgs could also be produced in rare decays of SM particles if the model allows for appropriate flavor-violating couplings. Two particularly interesting possibilities

emerge from the flavor structure of the model. First, if  $\phi'$  couples to quarks through mixing with the SM Higgs or through direct Yukawa couplings to vector-like quarks, it could appear in rare B meson decays such as  $B \rightarrow K\phi'$ . When the  $\phi'$  subsequently decays to muon pairs, this would produce a distinctive signature with the di-muon invariant mass peaked at  $m_{\phi'}$ , distinguishing it from the SM process  $B \rightarrow K\mu^+\mu^-$ . Second, flavor-changing neutral current decays of the top quark mediated by  $\phi'$ , such as  $t \rightarrow c\phi'$ , could occur at observable rates if the  $\phi'$  has flavor-violating couplings. These rare decay processes not only probe the scalar couplings directly but also provide indirect sensitivity to the vector-like fermion sector.

### 5.3.2 LEPTOQUARK PHENOMENOLOGY BEYOND THE LHC

*Complementarity with Low-Energy Experiments.* While the LHC provides direct sensitivity to LQ masses up to several TeVs, low-energy precision experiments offer complementary constraints on the coupling strength. Future B-factory experiments such as Belle II will measure  $R_{D^{(*)}}$  with improved precision, potentially confirming or resolving the current  $\sim 3\sigma$  tension with SM predictions. Additionally, next-generation experiments searching for charged lepton flavor violation processes such as  $\mu \rightarrow e\gamma$  and  $\mu \rightarrow e$  conversion in nuclei will probe parameter regions where LQ models typically predict observable effects.

*Future Colliders.* Future colliders would provide complementary sensitivity to LQ phenomenology beyond the reach of the HL-LHC. A High-Energy LHC upgrade to 27 TeV would extend the mass reach to  $\sim 3\text{--}4$  TeV for pair production and potentially above 6 TeV for single production. A Future Circular Collider at 100 TeV would probe LQ masses up to  $\sim 10\text{--}15$  TeV, entering the boosted regime where specialized reconstruction techniques become necessary. A high-energy muon collider would offer a particularly clean environment for LQs coupling to muons, enabling precision measurements of their properties through both pair and single production channels.

### 5.3.3 ADVANCED ANALYSIS TECHNIQUES

*Tau Polarization Measurements.* In both studies,  $\tau$  leptons play important roles in the final states. The polarization of  $\tau$  leptons carries information about the chiral structure of the new physics couplings. In the LQ study, left-handed and right-handed couplings produce  $\tau$  leptons with different polarization states, which in turn affect the kinematics of the visible decay products. Developing machine learning algorithms specifically designed to extract  $\tau$  polarization information from the kinematics of hadronic  $\tau$  decays could provide an additional discriminating variable to enhance signal sensitivity and to distinguish between different theoretical scenarios.

The  $\tau$  polarization can be inferred from the energy fractions carried by the visible decay products in hadronic decays. For example, in the decay  $\tau^- \rightarrow \pi^- \nu_\tau$ , the pion carries a larger fraction of the  $\tau$  energy when the  $\tau$  is right-handed polarized. More complex decay modes such as  $\tau^- \rightarrow \rho^- \nu_\tau \rightarrow \pi^- \pi^0 \nu_\tau$  provide additional information through the invariant mass and angular distributions of the decay products. Machine learning algorithms, particularly deep neural networks, could be trained to learn the complex correlations between the visible decay products and the initial  $\tau$  polarization state, providing a probabilistic polarization measurement for each event.

Such polarization-sensitive analyses would require sophisticated reconstruction of the  $\tau$  decay products and careful treatment of the missing neutrino momentum. Recent developments in neural network architectures for particle physics, including attention mechanisms and graph neural networks, could be particularly well-suited for this task.

*Attention Mechanisms and Graph Neural Networks.* While BDTs have proven highly effective in both studies presented in this thesis, recent developments in deep learning offer promising alternatives that could provide further improvements. Graph Neural Networks (GNNs) can naturally handle the variable-multiplicity jet and lepton content of LHC events by representing each event as a graph where particles are nodes and their relationships are encoded in edges. This representation is particularly natural for collider events, where the relevant information includes not only the properties of individual particles but also their relationships (e.g., angular separations, invariant masses of pairs).

Attention mechanisms allow the network to dynamically focus on the most relevant features for each event. For example, in the  $U(1)_{T_R^3}$  analysis, the network could learn to identify which of the three muons likely originated from the  $\phi'$  decay, and which kinematic variables are most discriminating for that particular event topology. This dynamic feature selection could be more powerful than the fixed decision tree structure of BDTs.

These architectures have shown impressive performance in jet tagging tasks, such as distinguishing quark-initiated jets from gluon-initiated jets, and identifying jets from boosted heavy particles. Recent work has also demonstrated their effectiveness in full event classification tasks. Applying these techniques to the searches presented in this thesis could provide incremental improvements in sensitivity, particularly in the most challenging regions of parameter space where signal and background distributions are most similar.

*Unbinned Likelihood Methods.* The statistical analyses in this thesis employed binned likelihood approaches, which are standard in high-energy physics but inevitably lose some information through binning. The choice of binning—how many bins to use and where to place the bin boundaries—

can affect the final sensitivity. Recent work on unbinned likelihood methods using neural density estimation could provide more powerful hypothesis tests.

These methods use neural networks to learn the full probability density of events in the multidimensional feature space, allowing for optimal statistical inference without binning losses. The network is trained to estimate the likelihood ratio directly, which is the optimal test statistic according to the Neyman-Pearson lemma. This approach could be particularly beneficial in the leptoquark analysis, where the BDT output is binned before performing the likelihood fit. An unbinned approach could extract additional information from the detailed shape of the BDT distribution, potentially improving sensitivity by 10–20% in some regions of parameter space.

#### 5.4 CLOSING REMARKS

---

The LHC has entered a new era with Run 3 and will continue to accumulate data for at least another decade through the High-Luminosity program. The HL-LHC will deliver an unprecedented dataset of  $3000 \text{ fb}^{-1}$ , representing a twenty-fold increase compared to the data collected during Run 1 and Run 2. This enormous dataset offers remarkable opportunities to search for physics beyond the SM, but also presents significant challenges in extracting weak signals from enormous backgrounds.

This thesis has demonstrated that carefully designed phenomenological studies, leveraging modern computational tools including machine learning, are essential for maximizing the discovery potential of the LHC. By identifying optimal search strategies, quantifying sensitivity to specific BSM scenarios, and understanding the interplay between different observables, phenomenological work provides crucial guidance for the experimental program.

The two studies presented here—searching for light scalars in the  $U(1)_{T_R^3}$  model and probing vector LQs—represent concrete examples of this approach. Both analyses explore BSM scenarios motivated by persistent experimental anomalies and develop search strategies that could significantly extend the reach of the ATLAS and CMS experiments:

- The  $U(1)_{T_R^3}$  study demonstrates that the LHC can probe light scalars with masses from 5 to 325 GeV by exploiting the UV completion of the theory and producing the scalar in association with heavy vector-like quarks. This strategy provides sensitivity to a mass range that is difficult to access through other means and illustrates the power of considering the full particle spectrum of BSM models.
- The LQ study shows that combining multiple production channels (single, pair, and non-resonant) with machine learning techniques provides comprehensive coverage of the parameter space relevant for explaining the B-anomalies. The HL-LHC will be able to probe LQ

masses up to 5 TeV for couplings that can address the  $R_{D^{(*)}}$  tensions, providing a definitive test of this class of explanations.

The methodologies developed in these studies—particularly the application of machine learning for signal-background discrimination, the framework for statistical interpretation, and the systematic exploration of model parameter space—are broadly applicable to other BSM searches. The BDT-based approach has proven effective in both studies, providing significant improvements over traditional cut-based analyses. The extension to more advanced architectures such as graph neural networks and attention mechanisms represents a promising direction for future work.

Beyond the specific results for the  $U(1)_{T_R^3}$  and LQ models, this thesis contributes to the effort of developing and validating phenomenological tools for the LHC era. The Monte Carlo simulation pipeline, the machine learning workflow, and the statistical analysis framework established here can be applied to a wide range of BSM scenarios. The emphasis on considering UV-complete models, exploring the full parameter space, and combining complementary search channels provides a template for future phenomenological studies.

The next decade of LHC operations will be decisive. With the HL-LHC dataset, we will either discover new particles that explain the observed anomalies, or we will constrain BSM scenarios to the point where new experimental approaches or higher-energy colliders become necessary. The phenomenological studies presented in this thesis demonstrate that the LHC has the potential to make transformative discoveries if we employ optimal search strategies and leverage the full power of modern computational techniques. The future of particle physics depends on this combination of theoretical insight, phenomenological innovation, and experimental precision.



# A

---

## ON THE UNIVERSAL SEESAW MECHANISM

---

In models with a universal seesaw mechanism, such as the  $U(1)_{T_3^R}$  extension studied here, the Standard Model fermion masses are not generated through direct Yukawa couplings to the Higgs doublet. Instead, they arise from mixing with new vector-like fermions  $\chi_f$  via an extended scalar sector that includes an additional scalar field  $\phi$  coupled to the right-handed SM fermions.

### A.1 SINGLE CHIRAL FERMION: THE CORE MECHANISM

---

#### A.1.1 MASS MATRIX SETUP AND DIAGONALIZATION

To illustrate the universal seesaw mechanism, consider a simplified scenario with a single chiral fermion  $f$  (representing a SM fermion) and its corresponding vector-like partner  $\chi_f$ . The relevant Lagrangian terms involving these fields and the scalar fields  $H$  (the SM Higgs doublet) and  $\phi$  (the new scalar field) can be written as:

$$-\mathcal{L} \supset Y_{f_L} \bar{f}_L \chi_{fR} H + Y_{f_R} \bar{\chi}_{fL} f_R \phi^* + m_{\chi_f} \bar{\chi}_{fL} \chi_{fR} + \text{h.c.} \quad (\text{A.1})$$

After electroweak symmetry breaking ( $\langle H \rangle = v_h/\sqrt{2}$ ) and  $U(1)_{T_3^R}$  breaking ( $\langle \phi \rangle = v_\phi/\sqrt{2}$ ), the Yukawa interactions generate mass terms for the fermions. Specifically,

$$-\mathcal{L} \supset (f_L \quad \bar{\chi}_{fL}) \begin{pmatrix} 0 & Y_{f_L} v_h/\sqrt{2} \\ Y_{f_R} v_\phi/\sqrt{2} & m_{\chi_f} \end{pmatrix} \begin{pmatrix} f_R \\ \chi_{fR} \end{pmatrix} + \text{h.c.} \quad (\text{A.2})$$

this leads to the mass matrix:

$$\mathcal{M}_f = \begin{pmatrix} 0 & Y_{f_L} v_h/\sqrt{2} \\ Y_{f_R} v_\phi/\sqrt{2} & m_{\chi_f} \end{pmatrix}. \quad (\text{A.3})$$

Defining the Dirac masses:

$$m_L = \frac{Y_{f_L} v_h}{\sqrt{2}}, \quad m_R = \frac{Y_{f_R} v_\phi}{\sqrt{2}}, \quad (\text{A.4})$$

the mass matrix becomes:

$$\mathcal{M}_f = \begin{pmatrix} 0 & m_L \\ m_R & m_{\chi_f} \end{pmatrix}, \quad (\text{A.5})$$

where we denote  $m_\chi \equiv m_{\chi_f}$  for simplicity.

As this matrix is not symmetric, we perform a bi-unitary transformation to diagonalize it:

$$\mathcal{M}_f^{\text{diag}} = U_L \mathcal{M}_f U_R^\dagger, \quad (\text{A.6})$$

where  $U_L$  and  $U_R$  are unitary matrices that rotate the left- and right-handed fields, respectively.

The physical squared masses are found from the eigenvalues of the Hermitian matrices:

$$H_L = \mathcal{M}_f \mathcal{M}_f^\dagger, \quad \text{diagonalized by } U_L, \quad (\text{A.7})$$

$$H_R = \mathcal{M}_f^\dagger \mathcal{M}_f, \quad \text{diagonalized by } U_R. \quad (\text{A.8})$$

This follows from:

$$\mathcal{M}_f^{\text{diag}} \mathcal{M}_f^{\text{diag}\dagger} = U_L \mathcal{M}_f U_R^\dagger U_R \mathcal{M}_f^\dagger U_L^\dagger = U_L \mathcal{M}_f \mathcal{M}_f^\dagger U_L^\dagger = U_L H_L U_L^\dagger \equiv \tilde{H}_L, \quad (\text{A.9})$$

and similarly:

$$\mathcal{M}_f^{\text{diag}\dagger} \mathcal{M}_f^{\text{diag}} = U_R \mathcal{M}_f^\dagger U_L^\dagger U_L \mathcal{M}_f U_R^\dagger = U_R \mathcal{M}_f^\dagger \mathcal{M}_f U_R^\dagger = U_R H_R U_R^\dagger \equiv \tilde{H}_R. \quad (\text{A.10})$$

Explicitly, we have:

$$H_L = \mathcal{M}_f \mathcal{M}_f^\dagger = \begin{pmatrix} |m_L|^2 & m_L m_\chi^* \\ m_\chi m_L^* & |m_R|^2 + |m_\chi|^2 \end{pmatrix}, \quad (\text{A.11})$$

$$H_R = \mathcal{M}_f^\dagger \mathcal{M}_f = \begin{pmatrix} |m_R|^2 & m_R m_\chi^* \\ m_\chi m_R^* & |m_L|^2 + |m_\chi|^2 \end{pmatrix}. \quad (\text{A.12})$$

By construction  $H_R$  and  $H_L$  have the same eigenvalues. Assuming all parameters are real for clarity, the solutions are the squared masses of the two mass eigenstates:

$$m_f^2 = \frac{1}{2} \left( m_\chi^2 + m_L^2 + m_R^2 - \sqrt{(m_\chi^2 + m_L^2 + m_R^2)^2 - 4m_L^2 m_R^2} \right), \quad (\text{A.13})$$

$$m_F^2 = \frac{1}{2} \left( m_\chi^2 + m_L^2 + m_R^2 + \sqrt{(m_\chi^2 + m_L^2 + m_R^2)^2 - 4m_L^2 m_R^2} \right), \quad (\text{A.14})$$

where  $m_f$  is the light SM-like fermion mass, and  $m_F$  is the heavy vector-like partner mass.

### A.1.2 MIXING ANGLES AND EXPLICIT PARAMETER RELATIONS

The bi-unitary transformation can be performed by matrices parameterized by mixing angles. For one generation, the left-handed mixing matrix is:

$$U_L = \begin{pmatrix} \cos \theta_L & -\sin \theta_L \\ \sin \theta_L & \cos \theta_L \end{pmatrix}. \quad (\text{A.15})$$

The angle  $\theta_L$  quantifies the mixing between the SM fermion and its vector-like partner. The exact expressions for the fundamental parameters  $m_L, m_R, m_\chi$  in terms of the physical masses  $m_f, m_F$  and the mixing angle  $\theta_L$  can be found by equating  $\tilde{H}_L = \text{diag}(m_f^2, m_F^2)$ .

Starting from the Hermitian matrix:

$$H_L = M_f M_f^\dagger = \begin{pmatrix} |m_L|^2 & m_L m_\chi^* \\ m_\chi m_L^* & |m_R|^2 + |m_\chi|^2 \end{pmatrix}, \quad (\text{A.16})$$

and assuming real parameters for clarity, we consider its diagonalization:

$$\begin{aligned} \tilde{H}_L &= \begin{pmatrix} \cos \theta_L & -\sin \theta_L \\ \sin \theta_L & \cos \theta_L \end{pmatrix} \begin{pmatrix} m_L^2 & m_L m_\chi \\ m_\chi m_L & m_R^2 + m_\chi^2 \end{pmatrix} \begin{pmatrix} \cos \theta_L & \sin \theta_L \\ -\sin \theta_L & \cos \theta_L \end{pmatrix} \\ &= \begin{pmatrix} m_f^2 & 0 \\ 0 & m_F^2 \end{pmatrix}. \end{aligned}$$

A more direct approach to obtain the simplified system is to apply the inverse rotations. Starting from the diagonal form:

$$\begin{pmatrix} m_f^2 & 0 \\ 0 & m_F^2 \end{pmatrix} = \begin{pmatrix} \cos \theta_L & -\sin \theta_L \\ \sin \theta_L & \cos \theta_L \end{pmatrix} \begin{pmatrix} m_L^2 & m_L m_\chi \\ m_\chi m_L & m_R^2 + m_\chi^2 \end{pmatrix} \begin{pmatrix} \cos \theta_L & \sin \theta_L \\ -\sin \theta_L & \cos \theta_L \end{pmatrix},$$

we multiply both sides on the left by  $U_L^\dagger$  and on the right by  $U_L$ :

$$\begin{pmatrix} \cos \theta_L & \sin \theta_L \\ -\sin \theta_L & \cos \theta_L \end{pmatrix} \begin{pmatrix} m_f^2 & 0 \\ 0 & m_F^2 \end{pmatrix} \begin{pmatrix} \cos \theta_L & -\sin \theta_L \\ \sin \theta_L & \cos \theta_L \end{pmatrix} = \begin{pmatrix} m_L^2 & m_L m_\chi \\ m_\chi m_L & m_R^2 + m_\chi^2 \end{pmatrix}.$$

Proceeding with the explicit computation of the left-hand side, we first evaluate the middle product:

$$\begin{pmatrix} m_f^2 & 0 \\ 0 & m_F^2 \end{pmatrix} \begin{pmatrix} \cos \theta_L & -\sin \theta_L \\ \sin \theta_L & \cos \theta_L \end{pmatrix} = \begin{pmatrix} m_f^2 \cos \theta_L & -m_f^2 \sin \theta_L \\ m_F^2 \sin \theta_L & m_F^2 \cos \theta_L \end{pmatrix}.$$

The full left-hand side then becomes:

$$\begin{pmatrix} m_L^2 & m_L m_\chi \\ m_\chi m_L & m_R^2 + m_\chi^2 \end{pmatrix} = \begin{pmatrix} m_f^2 \cos^2 \theta_L + m_F^2 \sin^2 \theta_L & (m_F^2 - m_f^2) \sin \theta_L \cos \theta_L \\ (m_F^2 - m_f^2) \sin \theta_L \cos \theta_L & m_f^2 \sin^2 \theta_L + m_F^2 \cos^2 \theta_L \end{pmatrix}. \quad (\text{A.17})$$

By reading off the matrix elements, we obtain the simplified system:

$$m_L^2 = m_f^2 \cos^2 \theta_L + m_F^2 \sin^2 \theta_L, \quad (\text{A.18})$$

$$m_R^2 + m_\chi^2 = m_f^2 \sin^2 \theta_L + m_F^2 \cos^2 \theta_L, \quad (\text{A.19})$$

$$m_L m_\chi = (m_F^2 - m_f^2) \sin \theta_L \cos \theta_L. \quad (\text{A.20})$$

To further simplify, we employ the double-angle trigonometric identities:

$$\begin{aligned}\cos^2 \theta_L &= \frac{1 + \cos 2\theta_L}{2}, \\ \sin^2 \theta_L &= \frac{1 - \cos 2\theta_L}{2}, \\ \sin \theta_L \cos \theta_L &= \frac{\sin 2\theta_L}{2},\end{aligned}$$

which transform the system into:

$$m_L^2 = \frac{1}{2} (m_f^2 + m_F^2 + (m_f^2 - m_F^2) \cos 2\theta_L), \quad (\text{A.21})$$

$$m_R^2 + m_\chi^2 = \frac{1}{2} (m_f^2 + m_F^2 - (m_f^2 - m_F^2) \cos 2\theta_L), \quad (\text{A.22})$$

$$m_L m_\chi = \frac{1}{2} (m_F^2 - m_f^2) \sin 2\theta_L. \quad (\text{A.23})$$

We now proceed to solve explicitly for  $m_L^2$ ,  $m_R^2$ , and  $m_\chi^2$ . Equation (A.21) directly provides:

$$m_L^2 = \frac{1}{2} [m_f^2 + m_F^2 + (m_f^2 - m_F^2) \cos 2\theta_L]. \quad (\text{A.24})$$

From equation (A.23), we find:

$$m_\chi = \frac{m_F^2 - m_f^2}{2m_L} \sin 2\theta_L, \quad (\text{A.25})$$

and consequently:

$$m_\chi^2 = \frac{(m_F^2 - m_f^2)^2 \sin^2 2\theta_L}{4m_L^2}. \quad (\text{A.26})$$

Turning to equation (A.22), we express  $m_R^2$  as:

$$m_R^2 = \frac{1}{2} [m_f^2 + m_F^2 - (m_f^2 - m_F^2) \cos 2\theta_L] - m_\chi^2. \quad (\text{A.27})$$

Substituting (A.26) yields:

$$m_R^2 = \frac{\Sigma + \Delta \cos 2\theta_L}{2} - \frac{\Delta^2 \sin^2 2\theta_L}{4m_L^2}, \quad (\text{A.28})$$

where  $\Sigma = m_f^2 + m_F^2$  and  $\Delta = m_f^2 - m_F^2$ . Using the expression for  $m_L^2$  from (A.24), namely  $m_L^2 = (\Sigma - \Delta \cos 2\theta_L)/2$ , we simplify:

$$\begin{aligned}m_R^2 &= \frac{\Sigma + \Delta \cos 2\theta_L}{2} - \frac{\Delta^2 \sin^2 2\theta_L}{2(\Sigma - \Delta \cos 2\theta_L)} \\ &= \frac{(\Sigma + \Delta \cos 2\theta_L)(\Sigma - \Delta \cos 2\theta_L) - \Delta^2 \sin^2 2\theta_L}{2(\Sigma - \Delta \cos 2\theta_L)} \\ &= \frac{\Sigma^2 - \Delta^2 \cos^2 2\theta_L - \Delta^2 \sin^2 2\theta_L}{2(\Sigma - \Delta \cos 2\theta_L)}.\end{aligned} \quad (\text{A.29})$$

The numerator simplifies further:

$$\Sigma^2 - \Delta^2(\cos^2 2\theta_L + \sin^2 2\theta_L) = \Sigma^2 - \Delta^2. \quad (\text{A.30})$$

Noting that  $\Sigma^2 - \Delta^2 = (m_f^2 + m_F^2)^2 - (m_f^2 - m_F^2)^2 = 4m_f^2 m_F^2$ , we obtain:

$$\begin{aligned} m_R^2 &= \frac{4m_f^2 m_F^2}{2(\Sigma - \Delta \cos 2\theta_L)} = \frac{2m_f^2 m_F^2}{\Sigma - \Delta \cos 2\theta_L} \\ &= \frac{m_f^2 m_F^2}{m_L^2}. \end{aligned} \quad (\text{A.31})$$

Collecting our results, we have the complete solution:

$$m_L^2 = \frac{1}{2} [m_f^2 + m_F^2 + (m_f^2 - m_F^2) \cos 2\theta_L], \quad (\text{A.32})$$

$$m_R^2 = \frac{m_f^2 m_F^2}{m_L^2}, \quad (\text{A.33})$$

$$m_\chi^2 = \frac{(m_F^2 - m_f^2)^2 \sin^2 2\theta_L}{4m_L^2}. \quad (\text{A.34})$$

And, replacing  $\Delta$  and  $\Sigma$  back, the final explicit expressions are:

$$m_L^2 = \frac{1}{2} (m_f^2 + m_F^2 - (m_F^2 - m_f^2) \cos 2\theta_L), \quad (\text{A.35})$$

$$m_R^2 = \frac{m_f^2 m_F^2}{m_L^2} = \frac{2m_f^2 m_F^2}{m_f^2 + m_F^2 - (m_F^2 - m_f^2) \cos 2\theta_L}, \quad (\text{A.36})$$

$$m_\chi^2 = \frac{(m_F^2 - m_f^2)^2 \sin^2 2\theta_L}{2(m_f^2 + m_F^2 - (m_F^2 - m_f^2) \cos 2\theta_L)}. \quad (\text{A.37})$$

### A.1.3 PERTURBATIVITY CONSTRAINTS FOR THE TOP QUARK

Equation (A.13) is fundamental. It shows that the light mass  $m_f$  is not simply proportional to  $m_L$  (the SM Higgs VEV). We can solve Eq. (A.13) for  $m_L^2$ :

$$\begin{aligned} m_f^2(m_\chi^2 + m_L^2 + m_R^2 - m_f^2) &= m_L^2 m_R^2 \quad (\text{from the exact seesaw relation}) \\ m_L^2(m_R^2 - m_f^2) &= m_f^2(m_\chi^2 + m_R^2 - m_f^2) \\ m_L^2 &= m_f^2 \left( \frac{m_\chi^2 + m_R^2 - m_f^2}{m_R^2 - m_f^2} \right) = m_f^2 \left( 1 + \frac{m_\chi^2}{m_R^2 - m_f^2} \right). \end{aligned}$$

Expressing this in terms of the original Yukawa couplings, where  $m_L = \frac{v_h}{\sqrt{2}} Y_{f_L}$  and the SM Yukawa is defined by  $m_f = \frac{v_h}{\sqrt{2}} Y_f^{\text{SM}}$ , we find:

$$Y_{f_L}^2 = (Y_f^{\text{SM}})^2 \left( 1 + \frac{m_\chi^2}{m_R^2 - m_f^2} \right). \quad (\text{A.38})$$

This relation reveals the core of the universal seesaw mechanism: the Yukawa coupling  $Y_{f_L}$  that couples the SM fermions to the Higgs is *enhanced*

compared to the standard model value  $Y_f^{\text{SM}}$ . The enhancement factor is  $\sqrt{1 + m_\chi^2/(m_R^2 - m_f^2)}$ .

This has profound implications: On one hand, for light fermions  $Y_f^{\text{SM}} \ll 1$ , a large hierarchy  $m_\chi^2 \gg m_R^2 \gg m_f^2$  can generate this tiny mass from a more “natural”  $Y_{f_L} \sim \mathcal{O}(0.1 - 1)$ . On the other hand, for the top quark,  $Y_t^{\text{SM}} \approx 1$  is already large. An enhancement could easily push  $Y_{t_L}$  into the non-perturbative regime ( $Y_{t_L}^2/4\pi > 1$ ). To avoid this, we must require the enhancement factor to be  $\mathcal{O}(1)$ , which implies  $m_\chi^2 \lesssim m_R^2 - m_t^2$ . Since  $m_R = \frac{v_\phi}{\sqrt{2}} Y_{f_R}$ , this suggests  $v_\phi > m_\chi$  is a natural condition.

The critical constraint to keep the top Yukawa perturbative is  $m_\chi^2 < m_R^2$ . Using Eqs. (A.36) and (A.37), the ratio is:

$$\frac{m_\chi^2}{m_R^2} = \frac{(m_F^2 - m_f^2)^2 \sin^2 2\theta_L}{4m_f^2 m_F^2} < 1. \quad (\text{A.39})$$

For the top quark with  $m_f = m_t \approx 173$  GeV and assuming a heavy partner  $m_F \gg m_t$ , this simplifies to:

$$\frac{m_F^4 \sin^2 2\theta_L}{4m_t^2 m_F^2} \approx \frac{m_F^2}{4m_t^2} \sin^2 2\theta_L < 1 \quad \Rightarrow \quad \sin^2 2\theta_L < \frac{4m_t^2}{m_F^2}. \quad (\text{A.40})$$

This is a very strong constraint. For example, if  $m_F = 1$  TeV, then  $\sin^2 2\theta_L < 0.12$ , meaning  $\theta_L < 10^\circ$ . In the small  $\theta_L$  limit,  $\cos 2\theta_L \approx 1 - 2\theta_L^2$  and  $\sin^2 2\theta_L \approx 4\theta_L^2$ . Substituting this into Eq. (A.35):

$$\begin{aligned} m_L^2 &\approx \frac{1}{2} (m_t^2 + m_F^2 - (m_F^2 - m_t^2)(1 - 2\theta_L^2)) \\ &= \frac{1}{2} (m_t^2 + m_F^2 - m_F^2 + m_t^2 + 2(m_F^2 - m_t^2)\theta_L^2) \\ &= m_t^2 + (m_F^2 - m_t^2)\theta_L^2. \end{aligned}$$

From the constraint (A.40),  $\theta_L^2 < m_t^2/m_F^2$ . Therefore:

$$m_L^2 < m_t^2 + (m_F^2 - m_t^2) \frac{m_t^2}{m_F^2} = 2m_t^2 - \frac{m_t^4}{m_F^2}. \quad (\text{A.41})$$

Converting back to Yukawa couplings:

$$Y_{t_L}^2 \lesssim (Y_t^{\text{SM}})^2 \left( 2 - \frac{m_t^2}{m_F^2} \right). \quad (\text{A.42})$$

This shows that the maximum enhancement for the top Yukawa is less than a factor of  $\sqrt{2}$ , which is perfectly perturbative.

## A.2 EXTENSION TO QUARKS, LEPTONS, AND NEUTRINOS

---

The single-generation analysis presented above captures the essential physics of the universal seesaw mechanism. However, the realistic case involves three generations of quarks and leptons, with additional complications arising from flavor mixing and the special role of neutrinos.

### A.2.1 QUARK SECTOR: FULL FLAVOR STRUCTURE

The most general gauge-invariant and renormalizable Lagrangian for the quark sector in the  $U(1)_{T_3^R}$  model is given by:

$$\begin{aligned} \mathcal{L}_{\text{mass}}^{\text{quark}} \supset & \bar{Q}_L^i (Y_{uL})_{ij} \chi_{uR}^j \tilde{H} + \bar{Q}_L^i (Y_{dL})_{ij} \chi_{dR}^j H \\ & + \bar{\chi}_{uL}^i (Y_{uR})_{ij} u_R^j \phi^* + \bar{\chi}_{dL}^i (Y_{dR})_{ij} d_R^j \phi \\ & + \bar{\chi}_{uL}^i (m_{\chi u})_{ij} \chi_{uR}^j + \bar{\chi}_{dL}^i (m_{\chi d})_{ij} \chi_{dR}^j + \text{h.c.}, \end{aligned} \quad (\text{A.43})$$

where  $i, j = 1, 2, 3$  are flavor indices,  $H$  is the SM Higgs doublet with  $\tilde{H} = i\sigma_2 H^*$ , and  $\phi$  is the additional scalar field that acquires a vacuum expectation value  $v_\phi$ . An entirely analogous set of terms exists for the lepton sector. The Yukawa matrices  $Y_{uL}, Y_{dL}, Y_{uR}, Y_{dR}$  and the vector-like mass matrices  $m_{\chi u}, m_{\chi d}$  are general complex  $3 \times 3$  matrices, making the flavor structure highly non-trivial.

To make physical predictions, we must diagonalize these matrices. We express them in terms of their singular value decompositions (i.e., their diagonal forms) and the associated unitary mixing matrices:

$$\begin{aligned} Y_{uL} &= U_{LL}^\dagger Y_{uL}^d U_{LR}, & Y_{uR} &= U_{RL}^\dagger Y_{uR}^d U_{RR}, \\ Y_{dL} &= V_{LL}^\dagger Y_{dL}^d V_{LR}, & Y_{dR} &= V_{RL}^\dagger Y_{dR}^d V_{RR}, \\ m_{\chi u} &= W_{uL}^\dagger m_{\chi u}^d W_{uR}, & m_{\chi d} &= W_{dL}^\dagger m_{\chi d}^d W_{dR}. \end{aligned} \quad (\text{A.44})$$

Here, the matrices  $Y^d$  and  $m^d$  are real, diagonal, and non-negative. The unitary matrices  $U, V, W$  are not physical by themselves but encode the mixing between flavor states.

We now perform a series of field redefinitions to absorb the maximal number of these unitary matrices into the definitions of the fermion fields. The goal is to make as many mass parameters diagonal as possible. The redefinitions are:

$$\begin{aligned} Q_L &\rightarrow U_{LL} Q_L, & \chi_{uR} &\rightarrow W_{uR} \chi_{uR}, & \chi_{uL} &\rightarrow W_{uL} \chi_{uL}, & u_R &\rightarrow U_{RR} u_R, \\ \chi_{dR} &\rightarrow W_{dR} \chi_{dR}, & \chi_{dL} &\rightarrow W_{dL} \chi_{dL}, & d_R &\rightarrow V_{RR} d_R. \end{aligned} \quad (\text{A.45})$$

Applying these transformations to the Lagrangian (A.43) and using the definitions above, we obtain the simplified form:

$$\begin{aligned} \mathcal{L}_{\text{Yuk}} = & \bar{Q}_L Y_{uL}^d (U_{LR} W_{uR}^\dagger) \chi_{uR} \tilde{H} + \bar{Q}_L (U_{LL} V_{LL}^\dagger) Y_{dL}^d (V_{LR} W_{dR}^\dagger) \chi_{dR} H \\ & + \bar{\chi}_{uL} (W_{uL} U_{RL}^\dagger) Y_{uR}^d u_R \phi^* + \bar{\chi}_{dL} (W_{dL} V_{RL}^\dagger) Y_{dR}^d d_R \phi \\ & + \bar{\chi}_{uL} m_{\chi u}^d \chi_{uR} + \bar{\chi}_{dL} m_{\chi d}^d \chi_{dR} + \text{h.c.} \end{aligned} \quad (\text{A.46})$$

The matrix  $\tilde{V}_{\text{CKM}} \equiv U_{LL} V_{LL}^\dagger$  is identified as the unitary matrix that will yield the observed Cabibbo-Kobayashi-Maskawa (CKM) quark mixing. For simplicity, and to focus on the essential mass generation mechanism, we adopt a *flavor-aligned* scenario. This assumes that all unitary matrices except those forming the CKM matrix are equal to the identity:

$$U_{LR} = W_{uR} = W_{uL} = U_{RL} = V_{LR} = W_{dR} = W_{dL} = V_{RL} = U_{RR} = V_{RR} = I. \quad (\text{A.47})$$

This is a strong assumption that minimizes new sources of flavor violation beyond the SM. Under this assumption, the Lagrangian simplifies dramatically to:

$$\begin{aligned}\mathcal{L}_{\text{Yuk}} = & \bar{Q}_L Y_{uL}^d \chi_{uR} \tilde{H} + \bar{Q}_L \tilde{V}_{\text{CKM}} Y_{dL}^d \chi_{dR} H \\ & + \bar{\chi}_{uL} Y_{uR}^d u_R \phi^* + \bar{\chi}_{dL} Y_{dR}^d d_R \phi \\ & + \bar{\chi}_{uL} m_{\chi u}^d \chi_{uR} + \bar{\chi}_{dL} m_{\chi d}^d \chi_{dR} + \text{h.c.}\end{aligned}\quad (\text{A.48})$$

All matrices  $Y^d$  and  $m^d$  are now diagonal. The only remaining off-diagonal flavor structure is in  $\tilde{V}_{\text{CKM}}$ , which can be identified with the physical CKM matrix after diagonalizing the fermion mass matrices.

### A.2.2 THREE GENERATIONS AND THE CKM MATRIX

The generalization to three generations involves the diagonalization of the full  $6 \times 6$  mass matrices for both up-type and down-type quarks. For a single generation, we found the mass matrix in Eq. (A.5). For three generations, this extends to:

$$\mathcal{M}_u = \begin{pmatrix} 0_{3 \times 3} & m_L^u \\ m_R^u & m_X^u \end{pmatrix}, \quad \mathcal{M}_d = \begin{pmatrix} 0_{3 \times 3} & m_L^d \\ m_R^d & m_X^d \end{pmatrix}, \quad (\text{A.49})$$

where each entry is now a  $3 \times 3$  matrix. In the flavor-aligned scenario,  $m_L^{u,d} = \frac{v_h}{\sqrt{2}} Y_{u,dL}^d$ ,  $m_R^{u,d} = \frac{v_\phi}{\sqrt{2}} Y_{u,dR}^d$ , and  $m_X^{u,d} = m_{\chi u,d}^d$  are all diagonal matrices.

The diagonalization proceeds via bi-unitary transformations for each sector:

$$U_L^u \mathcal{M}_u (U_R^u)^\dagger = \text{diag}(m_{u_1}, m_c, m_t, m_{u_1}, m_{u_2}, m_{u_3}), \quad (\text{A.50})$$

$$U_L^d \mathcal{M}_d (U_R^d)^\dagger = \text{diag}(m_{d_1}, m_s, m_b, m_{d_1}, m_{d_2}, m_{d_3}), \quad (\text{A.51})$$

where  $U_L^{u,d}$  and  $U_R^{u,d}$  are  $6 \times 6$  unitary matrices. Each matrix can be partitioned into  $3 \times 3$  blocks:

$$U_L^{u,d} = \begin{pmatrix} (U_L^{u,d})_{11} & (U_L^{u,d})_{12} \\ (U_L^{u,d})_{21} & (U_L^{u,d})_{22} \end{pmatrix}. \quad (\text{A.52})$$

The physical CKM matrix emerges in the charged-current weak interactions. After diagonalization, the  $W$  boson couples the mass eigenstates with a mixing matrix:

$$V_{\text{CKM}} = [(U_L^u)_{11}]^\dagger \tilde{V}_{\text{CKM}} (U_L^d)_{11}. \quad (\text{A.53})$$

In the limit where the mixing angles between SM quarks and their vector-like partners are small (i.e.,  $(U_L^{u,d})_{11} \approx I_{3 \times 3}$ ), we recover  $V_{\text{CKM}} \approx \tilde{V}_{\text{CKM}}$ , and the observed CKM matrix is reproduced.

The matrix  $\tilde{V}_{\text{CKM}}$  introduced during field redefinition will manifest in the charged current weak interactions of the mass eigenstates. After

diagonalization, the SM  $W$  boson will couple not only to the three light quarks but also to the heavy vector-like quarks, with couplings suppressed by the mixing angles. The observed  $3 \times 3$  CKM matrix emerges as the effective mixing matrix among the three light quarks when the heavy states are integrated out.

### A.2.3 LEPTON AND NEUTRINO SECTORS

The charged lepton sector follows an identical procedure to the quark sector. The Lagrangian contains terms:

$$\mathcal{L}_{\text{mass}}^{\text{lepton}} \supset \bar{L}_L^i (Y_{\ell L})_{ij} \chi_{\ell R}^j H + \bar{\chi}_{\ell L}^i (Y_{\ell R})_{ij} \ell_R^j \phi + \bar{\chi}_{\ell L}^i (m_{\chi \ell})_{ij} \chi_{\ell R}^j + \text{h.c.}, \quad (\text{A.54})$$

where  $L_L$  are the SM lepton doublets,  $\ell_R$  are the SM charged lepton singlets, and  $\chi_\ell$  are the vector-like charged leptons. The diagonalization proceeds analogously to the quark case, generating the charged lepton masses  $m_e, m_\mu, m_\tau$  and three heavy vector-like partners.

The neutrino sector, however, offers further richness. The right-handed neutrinos  $\nu_R$  can possess both Dirac masses ( $m_R$ ) from coupling to  $\phi$  and Majorana mass terms  $M_R \bar{\nu}_R^c \nu_R$ , which are allowed by the gauge symmetry once  $U(1)_{T_3}$  is broken. The vector-like neutrinos  $\chi_\nu$  can also have Majorana masses. The most general neutrino mass Lagrangian is:

$$\begin{aligned} \mathcal{L}_{\text{mass}}^\nu &\supset \bar{L}_L Y_{\nu L} \chi_{\nu R} \tilde{H} + \bar{\chi}_{\nu L} Y_{\nu R} \nu_R \phi^* + \bar{\chi}_{\nu L} m_{\chi \nu} \chi_{\nu R} \\ &+ \frac{1}{2} \bar{\nu}_R^c M_R \nu_R + \frac{1}{2} \bar{\chi}_\nu^c M_\chi \chi_\nu + \text{h.c.}, \end{aligned} \quad (\text{A.55})$$

where  $M_R$  and  $M_\chi$  are Majorana mass matrices. This combination of Dirac and Majorana masses for both  $\nu_R$  and  $\chi_\nu$  can generate a double or triple seesaw mechanism, providing a natural explanation for the tiny masses of the observed light neutrinos.

In the basis  $(\nu_L, \chi_{\nu L}, \nu_R^c, \chi_{\nu R}^c)$ , the neutrino mass matrix becomes a  $12 \times 12$  complex symmetric matrix:

$$\mathcal{M}_\nu = \begin{pmatrix} 0 & m_L^\nu & 0 & 0 \\ m_L^{\nu T} & 0 & m_R^\nu & m_{\chi \nu} \\ 0 & m_R^{\nu T} & M_R & 0 \\ 0 & m_{\chi \nu}^T & 0 & M_\chi \end{pmatrix}, \quad (\text{A.56})$$

where  $m_L^\nu = \frac{v_h}{\sqrt{2}} Y_{\nu L}$  and  $m_R^\nu = \frac{v_\phi}{\sqrt{2}} Y_{\nu R}$ . This matrix is diagonalized by a single unitary transformation (since it is symmetric). The eigenvalues yield six light neutrino masses (three of which correspond to the observed active neutrinos  $\nu_e, \nu_\mu, \nu_\tau$  with masses  $\lesssim 1$  eV) and six heavy states.

The diagonalization of this extended neutrino mass matrix also generates the Pontecorvo-Maki-Nakagawa-Sakata (PMNS) mixing matrix, analogous to the CKM matrix in the quark sector. The hierarchy of neutrino masses and the large mixing angles observed in neutrino oscillations can be naturally accommodated by appropriate choices of the parameters  $M_R, M_\chi, m_L^\nu, m_R^\nu$ , and  $m_{\chi \nu}$ .



# B

---

## THE 4321 MODEL

---

This appendix summarises the main features of the 4321 model presented in [115], based on the construction showed in [226]. The model is built upon the extended gauge group

$$\mathcal{G}_{4321} \equiv \mathrm{SU}(4) \times \mathrm{SU}(3)' \times \mathrm{SU}(2)_L \times \mathrm{U}(1)'.$$

The Standard Model (SM) gauge group,  $\mathcal{G}_{321} \equiv \mathrm{SU}(3)_c \times \mathrm{SU}(2)_L \times \mathrm{U}(1)_Y$ , is embedded into  $\mathcal{G}_{4321}$  through two key identifications.

First, the SM strong force is identified with the diagonal subgroup of the two  $\mathrm{SU}(3)$  factors:

$$\mathrm{SU}(3)_c = (\mathrm{SU}(3)_{[4]} \times \mathrm{SU}(3)')_{\text{diag}}, \quad (\text{B.1})$$

where  $\mathrm{SU}(3)_{[4]} \subset \mathrm{SU}(4)$ . Second, and more crucially, the SM hypercharge is a linear combination of charges from the  $\mathrm{SU}(4)$  and  $\mathrm{U}(1)'$  sectors:

$$Y = Q_{B-L} + Y'. \quad (\text{B.2})$$

Here, the baryon minus lepton number ( $Q_{B-L}$ ) is generated by a diagonal  $\mathrm{SU}(4)$  generator,  $Q_{B-L} = 2\sqrt{6}T^{15}/3$ ,

The spontaneous breaking of the full  $\mathcal{G}_{4321}$  symmetry down to the SM  $\mathcal{G}_{321}$  gives mass to the gauge bosons associated with the broken generators. The spectrum of these new massive vectors and their quantum numbers under the SM group are:

- A vector leptoquark,  $U \sim (\mathbf{3}, \mathbf{1}, 2/3)$ ,
- A coloron,  $g' \sim (\mathbf{8}, \mathbf{1}, 0)$ ,
- A massive neutral boson,  $Z' \sim (\mathbf{1}, \mathbf{1}, 0)$ .

Heuristically, each of these bosons originates from a distinct part of the symmetry breaking pattern: the leptoquark ( $U$ ) emerges from the breaking  $\mathrm{SU}(4) \rightarrow \mathrm{SU}(3)_{[4]} \times \mathrm{U}(1)_{B-L}$ , the coloron ( $g'$ ) from  $\mathrm{SU}(3)_{[4]} \times \mathrm{SU}(3)' \rightarrow \mathrm{SU}(3)_c$ , and the  $Z'$  from  $\mathrm{U}(1)_{B-L} \times \mathrm{U}(1)_{T_R^3} \rightarrow \mathrm{U}(1)_Y$ .

The spontaneous breaking of the  $\mathcal{G}_{4321}$  symmetry down to the Standard Model  $\mathcal{G}_{321}$  and subsequently to electromagnetism is achieved through a scalar sector comprising four multiplets. The primary breaking  $\mathcal{G}_{4321} \rightarrow \mathcal{G}_{321}$  is induced by the vacuum expectation values (vevs) of three scalar fields:

*As we see in chapter 3, the  $\mathrm{U}(1)'$  charge could be identified with twice the third component of right-handed isospin,  $Y' \equiv 2Q_{T_R^3}$ . This specific embedding reveals the model's left-right symmetric foundation; the SM electric charge operator can now be expressed in the manifestly left-right symmetric form:*

$$Q = Q_{T_L^3} + Q_{T_R^3} + \frac{1}{2}Q_{B-L}.$$

- $\Omega_1 \sim (\bar{\mathbf{4}}, \mathbf{1}, \mathbf{1}, -1/2)$ ,
- $\Omega_3 \sim (\bar{\mathbf{4}}, \mathbf{3}, \mathbf{1}, 1/6)$ ,
- $\Omega_{15} \sim (\mathbf{15}, \mathbf{1}, \mathbf{1}, 0)$  (taken to be a real field).

The final electroweak symmetry breaking,  $\mathcal{G}_{321} \rightarrow U(1)_{EM}$ , is triggered by the Higgs doublet  $H \sim (\mathbf{1}, \mathbf{1}, \mathbf{2}, 1/2)$ .

A suitable scalar potential (analyzed in detail in above) allows for a vev configuration that ensures this breaking pattern. Phenomenological constraints suggest a clear hierarchy between these scales:

$$\langle \Omega_3 \rangle > \langle \Omega_1 \rangle \gg \langle \Omega_{15} \rangle \gg \langle H \rangle. \quad (\text{B.3})$$

Given this hierarchy, we simplify the analysis by first considering the  $\Omega_3$  and  $\Omega_1$  system in isolation to understand the primary TeV-scale breaking. The effects of incorporating the smaller vevs of  $\Omega_{15}$  and  $H$  will be discussed subsequently.

To analyze the  $\Omega_3$ - $\Omega_1$  subsystem, we represent these fields as a  $4 \times 3$  matrix and a 4-vector, transforming as  $\Omega_3 \rightarrow U_4^* \Omega_3 U_3^\top$ , and  $\Omega_1 \rightarrow U_4^* \Omega_1$  under  $SU(4) \times SU(3)'$ , respectively. The desired vacuum configuration that breaks  $\mathcal{G}_{4321}$  to  $\mathcal{G}_{321}$  is:

$$\langle \Omega_3 \rangle = \frac{1}{\sqrt{2}} \begin{pmatrix} v_3 & 0 & 0 \\ 0 & v_3 & 0 \\ 0 & 0 & v_3 \\ 0 & 0 & 0 \end{pmatrix}, \quad \langle \Omega_1 \rangle = \frac{1}{\sqrt{2}} \begin{pmatrix} 0 \\ 0 \\ 0 \\ v_1 \end{pmatrix}. \quad (\text{B.4})$$

The most general renormalizable scalar potential that admits this vacuum as a stationary point, and in the limit where the bare masses vanish ( $\mu_3 = \mu_1 = 0$ ) and the cubic coupling is absent ( $\lambda_6 = 0$ ), can be written as:

$$\begin{aligned} V_{\Omega_3, \Omega_1} = & \mu_1^2 |\Omega_1|^2 + \mu_3^2 \text{Tr}(\Omega_3^\dagger \Omega_3) \\ & + \lambda_1 \left( \text{Tr}(\Omega_3^\dagger \Omega_3) - \frac{3}{2} v_3^2 \right)^2 + \lambda_2 \text{Tr} \left( \Omega_3^\dagger \Omega_3 - \frac{1}{2} v_3^2 \mathbb{1}_3 \right)^2 \\ & + \lambda_3 \left( |\Omega_1|^2 - \frac{1}{2} v_1^2 \right)^2 + \lambda_4 \left( \text{Tr}(\Omega_3^\dagger \Omega_3) - \frac{3}{2} v_3^2 \right) \left( |\Omega_1|^2 - \frac{1}{2} v_1^2 \right) \\ & + \lambda_5 \Omega_1^\dagger \Omega_3 \Omega_3^\dagger \Omega_1 + \lambda_6 ([\Omega_3 \Omega_3 \Omega_3 \Omega_1]_1 + \text{h.c.}). \end{aligned} \quad (\text{B.5})$$

Here,  $\mathbb{1}_3$  denotes the  $3 \times 3$  identity matrix. We have used a relative rephasing between the fields  $\Omega_1$  and  $\Omega_3$  to remove the phase of  $\lambda_6$ . The unique quartic term,

$$[\Omega_3 \Omega_3 \Omega_3 \Omega_1]_1 \equiv \epsilon_{\alpha \beta \gamma \delta} \epsilon^{\alpha \beta \gamma} (\Omega_3)_a^\alpha (\Omega_3)_b^\beta (\Omega_3)_c^\gamma (\Omega_1)^\delta, \quad (\text{B.6})$$

is required to avoid accidental global symmetries in the scalar potential that would lead to unwanted massless Goldstone bosons.

The inclusion of the other two representations,  $\Omega_{15}$  and  $H$ , in the scalar potential can be safely considered as a perturbation. They are assumed to take the vevs  $\langle \Omega_{15} \rangle = T_{15} v_{15}$  and  $\langle H \rangle = \frac{1}{\sqrt{2}} (0, v)^\top$ , with  $v = 246$  GeV. This

treatment is justified because their vevs are subleading for phenomenological reasons and they do not alter the pattern of global symmetries of the  $\Omega_3 - \Omega_1$  potential. Finally, the decomposition of  $\Omega_{15}$  under  $\mathcal{G}_{321}$  is  $\Omega_{15} \rightarrow (\mathbf{1}, \mathbf{1}, 0) \oplus (\mathbf{3}, \mathbf{1}, 2/3) \oplus (\bar{\mathbf{3}}, \mathbf{1}, -2/3) \oplus (\mathbf{8}, \mathbf{1}, 0)$ . The mixing of these states with those contained in  $\Omega_{3,1}$  is parametrically suppressed by the ratio  $v_{15}^2/v_{3,1}^2$ , hence they play a subleading role in phenomenology.

Given the extended gauge group  $\mathcal{G}_{4321}$ , we denote the gauge fields by  $H_\mu^\alpha, G_\mu'^a, W_\mu^i, B_\mu'$ ; the gauge couplings by  $g_4, g_3, g_2, g_1$ ; and the generators by  $T^\alpha, T^a, T^i, Y'$  (with indices  $\alpha = 1, \dots, 15$ ,  $a = 1, \dots, 8$ ,  $i = 1, 2, 3$ ).

To determine the gauge boson spectrum, we start from the covariant derivatives acting on the scalar fields  $\Omega_{3,1,15}$ :

$$\begin{aligned} D_\mu \Omega_1 &= (\partial_\mu + ig_4 H_\mu^\alpha T^{\alpha*} - \frac{1}{2}ig_1 B'_\mu) \Omega_1, \\ D_\mu \Omega_3 &= (\partial_\mu + ig_4 H_\mu^\alpha T^{\alpha*} - ig_3 G_\mu'^a T^a + \frac{1}{6}ig_1 B'_\mu) \Omega_3, \\ D_\mu \Omega_{15} &= \partial_\mu \Omega_{15} - ig_4 [T^\alpha, \Omega_{15}] H_\mu^\alpha. \end{aligned}$$

We define the index  $A = 9, \dots, 14$  to span the  $SU(4)/(SU(3)_4 \times U(1)_4)$  coset. Neglecting electroweak symmetry breaking effects, the gauge boson masses are extracted from the canonically normalized kinetic terms of the scalar fields:

$$\begin{aligned} \mathcal{L} \supset &+ \frac{1}{2} \left( g_4^2 v_1^2 + g_4^2 v_3^2 + \frac{4}{3} g_4^2 v_{15}^2 \right) H_\mu^A H^{\mu A} \\ &+ \frac{v_3^2}{4} (H_\mu^a \quad G_\mu'^a) \begin{pmatrix} g_4^2 & -g_4 g_3 \\ -g_4 g_3 & g_3^2 \end{pmatrix} \begin{pmatrix} H^{b\mu} \\ G'^{b\mu} \end{pmatrix} \\ &+ \frac{3v_1^2 + v_3^2}{4} (H_\mu^{15} \quad B'_\mu) \begin{pmatrix} \frac{g_4^2}{4} & -\frac{g_4 g_1}{2\sqrt{6}} \\ -\frac{g_4 g_1}{2\sqrt{6}} & \frac{g_1^2}{6} \end{pmatrix} \begin{pmatrix} H^{15\mu} \\ B'^{\mu} \end{pmatrix}. \end{aligned} \tag{B.7}$$

Diagonalizing these mass matrices, we obtain the massive gauge boson spectrum:

$$U_\mu^{1,2,3} = \frac{1}{\sqrt{2}} (H_\mu^{9,11,13} - i H_\mu^{10,12,14}), \quad M_U^2 = \frac{1}{4} g_4^2 \left( v_1^2 + v_3^2 + \frac{4}{3} v_{15}^2 \right), \tag{B.8}$$

$$g_\mu'^a = \frac{g_4 H_\mu^a - g_3 G_\mu'^a}{\sqrt{g_4^2 + g_3^2}}, \quad M_{g'}^2 = \frac{1}{2} (g_4^2 + g_3^2) v_3^2, \tag{B.9}$$

$$Z'_\mu = \frac{g_4 H_\mu^{15} - \sqrt{\frac{2}{3}} g_1 B'_\mu}{\sqrt{g_4^2 + \frac{2}{3} g_1^2}}, \quad M_Z^2 = \frac{1}{4} \left( g_4^2 + \frac{2}{3} g_1^2 \right) \left( v_1^2 + \frac{1}{3} v_3^2 \right). \tag{B.10}$$

The combinations orthogonal to (B.9) and (B.10) correspond to the massless  $SU(3)_c \times U(1)_Y$  gauge bosons of  $\mathcal{G}_{321}$  prior to electroweak symmetry breaking:

$$g_\mu^a = \frac{g_3 H_\mu^a + g_4 G'_\mu^a}{\sqrt{g_4^2 + g_3^2}}, \quad (B.11)$$

$$B_\mu = \frac{\sqrt{\frac{2}{3}} g_1 H_\mu^{15} + g_4 B'_\mu}{\sqrt{g_4^2 + \frac{2}{3} g_1^2}}. \quad (B.12)$$

The matching between the fundamental couplings  $g_4, g_3, g_1$  and the SM couplings  $g_s, g_Y$  is readily obtained by acting with the covariant derivative on a field which transforms trivially under  $SU(4)$ . This yields:

$$g_s = \frac{g_4 g_3}{\sqrt{g_4^2 + g_3^2}}, \quad (B.13)$$

$$g_Y = \frac{g_4 g_1}{\sqrt{g_4^2 + \frac{2}{3} g_1^2}}. \quad (B.14)$$

Evolving the SM gauge couplings up to  $\mu = 2$  TeV, we obtain  $g_s = 1.02$  and  $g_Y = 0.363$ . Since  $g_s \leq g_{4,3}$  and  $g_Y \leq \sqrt{\frac{3}{2}} g_4, g_1$ , the hierarchy  $g_s \gg g_Y$  also implies  $g_{4,3} \gg g_Y \simeq g_1$ . In the limit  $v_3 \gg v_1 \gg v_{15}$ , the mass spectrum simplifies. For example, if the gauge couplings also satisfy  $g_4 \sim g_3$ , one finds  $M_{g'} \simeq \sqrt{2} M_U$  and  $M_{Z'} \simeq \frac{1}{\sqrt{2}} M_U$ .

In the 4321 model, the observed SM fermion masses and mixings arise from the mixing between elementary chiral fermions—charged under  $SU(3)' \times SU(2)_L \times U(1)'$  with SM-like quantum numbers—and three generations of vector-like fermions transforming as fundamentals of  $SU(4)$ . This mixing is triggered once the scalars  $\Omega_1$  and  $\Omega_3$  acquire VEVs (see Fig. B.1). The full matter content of the model is summarized in Tab. B.1.

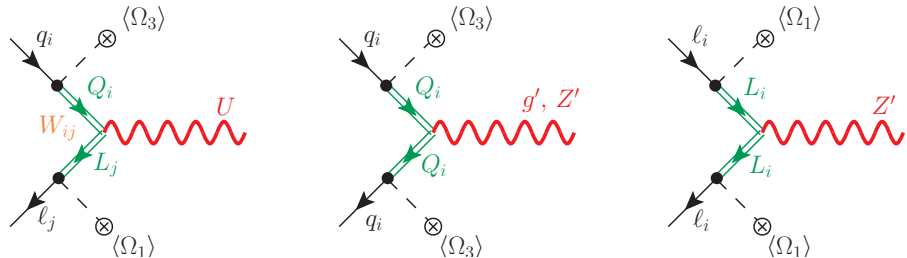


**Figure B.1:** Diagrammatic representation of the interactions between the SM fermions and the heavy vector-like fermions  $\Psi$ , induced by the Yukawa couplings to  $\Omega_1$  and  $\Omega_3$  after symmetry breaking.

Field	SU(4)	SU(3)'	SU(2) <sub>L</sub>	U(1)'
q_L <sup>i</sup>	<b>1</b>	<b>3</b>	<b>2</b>	1/6
u_R <sup>i</sup>	<b>1</b>	<b>3</b>	<b>1</b>	2/3
d_R <sup>i</sup>	<b>1</b>	<b>3</b>	<b>1</b>	-1/3
l_L <sup>i</sup>	<b>1</b>	<b>1</b>	<b>2</b>	-1/2
e_R <sup>i</sup>	<b>1</b>	<b>1</b>	<b>1</b>	-1
Ψ_L <sup>i</sup>	<b>4</b>	<b>1</b>	<b>2</b>	0
Ψ_R <sup>i</sup>	<b>4</b>	<b>1</b>	<b>2</b>	0
H	<b>1</b>	<b>1</b>	<b>2</b>	1/2
Ω <sub>1</sub>	<b>4</b>	<b>1</b>	<b>1</b>	-1/2
Ω <sub>3</sub>	<b>4</b>	<b>3</b>	<b>1</b>	1/6
Ω <sub>15</sub>	<b>15</b>	<b>1</b>	<b>1</b>	0

**Table B.1:** Field content of the 4321 model. The index  $i = 1, 2, 3$  runs over generations.

The mixing between the elementary fermions and the vector-like fermions is described by the Yukawa Lagrangian  $\mathcal{L}_Y = \mathcal{L}_{\text{SM-like}} + \mathcal{L}_{\text{mix}}$ , where

$$\mathcal{L}_{\text{SM-like}} = -\bar{q}'_L Y_d H d'_R - \bar{q}'_L Y_u \tilde{H} u'_R - \bar{l}'_L Y_e H e'_R + \text{h.c.}, \quad (\text{B.15})$$

$$\mathcal{L}_{\text{mix}} = -\bar{q}'_L \lambda_q \Omega_3^T \Psi_R - \bar{l}'_L \lambda_\ell \Omega_1^T \Psi_R - \bar{\Psi}_L (M + \lambda_{15} \Omega_{15}) \Psi_R + \text{h.c..} \quad (\text{B.16})$$

Here,  $\tilde{H} = i\sigma_2 H^*$ , and  $Y_{u,d,e}, \lambda_{q,\ell,15}, M$  are  $3 \times 3$  matrices in flavour space.

The vector-like fermions transform under  $\mathcal{G}_{4321}$  as

$$\Psi_{L,R} = \begin{pmatrix} Q'_{L,R} \\ L'_{L,R} \end{pmatrix} \sim (\mathbf{4}, \mathbf{1}, \mathbf{2}, 0). \quad (\text{B.17})$$

Under the breaking  $\text{SU}(4) \rightarrow \text{SU}(3)_{[4]} \times \text{U}(1)_{B-L}$ , they decompose as  $Q'_{L,R} \sim (\mathbf{3}, \mathbf{2}, 1/6)$  and  $L'_{L,R} \sim (\mathbf{1}, \mathbf{2}, -1/2)$ . Their vector-like masses are generated by the  $M$  term and are split by the VEV of  $\Omega_{15}$ :

$$M_Q = M + \frac{\lambda_{15} v_{15}}{2\sqrt{6}}, \quad M_L = M - \frac{3\lambda_{15} v_{15}}{2\sqrt{6}}. \quad (\text{B.18})$$

To comply with flavour constraints, the authors on [226] employ the following Yukawa textures as a starting point

$$\lambda_q = \hat{\lambda}_q \equiv \text{diag}(\lambda_{12}^q, \lambda_{12}^q, \lambda_3^q),$$

$$\lambda_\ell = \hat{\lambda}_\ell W^\dagger \equiv \text{diag}(\lambda_1^\ell, \lambda_2^\ell, \lambda_3^\ell) \begin{pmatrix} 1 & 0 & 0 \\ 0 & \cos \theta_{LQ} & -\sin \theta_{LQ} \\ 0 & \sin \theta_{LQ} & \cos \theta_{LQ} \end{pmatrix}, \quad (\text{B.19})$$

$$\lambda_{15} \propto \hat{M} \propto \mathbb{1}.$$

After the  $\text{SU}(3)_{[4]} \times \text{SU}(3)' \rightarrow \text{SU}(3)_c$  symmetry breaking, the  $6 \times 6$  fermion mass matrices for the quarks read:

$$\mathcal{M}_u = \begin{pmatrix} V^\dagger \hat{Y}_u \frac{v}{\sqrt{2}} & \hat{\lambda}_q \frac{v_3}{\sqrt{2}} \\ 0 & \hat{M}_Q \end{pmatrix}, \quad \mathcal{M}_d = \begin{pmatrix} \hat{Y}_d \frac{v}{\sqrt{2}} & \hat{\lambda}_q \frac{v_3}{\sqrt{2}} \\ 0 & \hat{M}_Q \end{pmatrix}. \quad (\text{B.20})$$

Similarly, after the  $U(1)_{B-L} \times U(1)_{T_R^3} \rightarrow U(1)_Y$  symmetry breaking, the  $6 \times 6$  fermion mass matrices for the leptons read:

$$\mathcal{M}_N = \begin{pmatrix} 0 & \hat{\lambda}_\ell \frac{v_1}{\sqrt{2}} \\ 0 & \hat{M}_L \end{pmatrix}, \quad \mathcal{M}_e = \begin{pmatrix} \hat{Y}_e \frac{v}{\sqrt{2}} & \hat{\lambda}_\ell W^\dagger \frac{v_1}{\sqrt{2}} \\ 0 & \hat{M}_L \end{pmatrix}. \quad (\text{B.21})$$

Here,  $\hat{Y}_{u,d,e}$  and  $\hat{\lambda}_{q,\ell}$  are diagonal matrices,  $V$  and  $W$  are unitary Cabibbo-like mixing matrices, and  $M_Q, M_L$  are proportional to the identity matrix.

The structure of the mass matrices in Eqs. (B.21) allows them to be diagonalized by unitary transformations of the form  $\psi'_x = U_x \psi_x$ , where  $\psi_x$  ( $x = q, u, d, \ell, e, N$ ) denotes a 6-dimensional vector containing both the chiral and vector-like fermions, and the unprimed fields represent the mass eigenstates.

The chosen flavour structure in Eq. (B.19) ensures that in the limit  $W \rightarrow \mathbb{1}$ , the mixing is family-specific: each vector-like fermion generation mixes predominantly with only one generation of chiral fermions (up to CKM rotations). At leading order, the unitary mixing matrices are given by:

$$\begin{aligned} U_q &\approx \mathcal{R}_{14}(\theta_{q_1}) \mathcal{R}_{25}(\theta_{q_2}) \mathcal{R}_{36}(\theta_{q_3}), & U_\ell &\approx \mathcal{R}_{14}(\theta_{\ell_1}) \mathcal{R}_{25}(\theta_{\ell_2}) \mathcal{R}_{36}(\theta_{\ell_3}), \\ U_u &\approx \mathcal{R}_{14}(\theta_{u_R}) \mathcal{R}_{25}(\theta_{c_R}) \mathcal{R}_{36}(\theta_{t_R}), & U_e &\approx \begin{pmatrix} 1 & 0 \\ 0 & W \end{pmatrix} \mathcal{R}_{14}(\theta_{e_R}) \mathcal{R}_{25}(\theta_{\mu_R}) \mathcal{R}_{36}(\theta_{\tau_R}), \\ U_d &\approx \mathcal{R}_{14}(\theta_{d_R}) \mathcal{R}_{25}(\theta_{s_R}) \mathcal{R}_{36}(\theta_{b_R}), & U_N &\approx \begin{pmatrix} 0 & 0 \\ 0 & W \end{pmatrix}. \end{aligned}$$

Here, we have adopted a flavour basis for the SM  $SU(2)_L$  fermion multiplets defined by:

$$q^i = \begin{pmatrix} V_{ji}^* u_L^j \\ d_L^i \end{pmatrix}, \quad \ell^\alpha = \begin{pmatrix} v_L^\alpha \\ e_L^\alpha \end{pmatrix}, \quad (\text{B.22})$$

where  $V$  is the CKM matrix. The mixing angles are related to the Lagrangian parameters by:

$$\begin{aligned} \sin \theta_{q_i} &= \frac{\lambda_i^q v_3}{\sqrt{|\lambda_i^q|^2 v_3^2 + 2\hat{M}_Q^2}}, & \cos \theta_{q_i} &= \frac{\sqrt{2} \hat{M}_Q}{\sqrt{|\lambda_i^q|^2 v_3^2 + 2\hat{M}_Q^2}}, \\ \sin \theta_{\ell_i} &= \frac{\lambda_i^\ell v_1}{\sqrt{|\lambda_i^\ell|^2 v_1^2 + 2\hat{M}_L^2}}, & \cos \theta_{\ell_i} &= \frac{\sqrt{2} \hat{M}_L}{\sqrt{|\lambda_i^\ell|^2 v_1^2 + 2\hat{M}_L^2}}, \\ \sin \theta_{u_R^i} &= \frac{m_{u_i}}{M_{Q_i}} \tan \theta_{q_i}, & \sin \theta_{d_R^i} &= \frac{m_{d_i}}{M_{Q_i}} \tan \theta_{q_i}, \\ \sin \theta_{e_R^i} &= \frac{m_{e_i}}{M_{L_i}} \tan \theta_{\ell_i}, & \cos \theta_{f_R^i} &= 1 \quad (f = u, d, e). \end{aligned} \quad (\text{B.23})$$

In these expressions,  $m_i$  and  $M_i$  denote the physical fermion masses. Up to corrections of  $\mathcal{O}(m_i^2/M_i^2)$ , these are given by:

$$\begin{aligned} M_{L_i} &= \sqrt{\frac{|\lambda_i^\ell|^2 v_1^2}{2} + \hat{M}_L^2}, & M_{Q_i} &= \sqrt{\frac{|\lambda_i^q|^2 v_3^2}{2} + \hat{M}_Q^2}, \\ m_{f_i} &\approx |\hat{Y}_f| \cos \theta_{f_i} \frac{v}{\sqrt{2}} \quad (f = u, d, e). \end{aligned} \quad (\text{B.24})$$

The interaction terms of the massive gauge bosons with the fermions in the interaction basis are derived from the covariant derivative. For the left-handed fields, we find:

$$\begin{aligned} \mathcal{L}_L &= \frac{g_4}{\sqrt{2}} \bar{Q}'_L \gamma^\mu L'_L U_\mu + \text{h.c.} \\ &+ g_s \left( \frac{g_4}{g_3} \bar{Q}'_L \gamma^\mu T^a Q'_L - \frac{g_3}{g_4} \bar{q}'_L \gamma^\mu T^a q'_L \right) g'_\mu^a \\ &+ g_Y \left( \sqrt{\frac{3}{2}} \frac{g_4}{g_1} Y(Q'_L) \bar{Q}'_L \gamma^\mu Q'_L - \sqrt{\frac{2}{3}} \frac{g_1}{g_4} Y(q'_L) \bar{q}'_L \gamma^\mu q'_L \right) Z'_\mu \\ &+ g_Y \left( \sqrt{\frac{3}{2}} \frac{g_4}{g_1} Y(L'_L) \bar{L}'_L \gamma^\mu L'_L - \sqrt{\frac{2}{3}} \frac{g_1}{g_4} Y(\ell'_L) \bar{\ell}'_L \gamma^\mu \ell'_L \right) Z'_\mu, \end{aligned} \quad (\text{B.25})$$

and for the right-handed fields:

$$\begin{aligned} \mathcal{L}_R &= \frac{g_4}{\sqrt{2}} \bar{Q}'_R \gamma^\mu L'_R U_\mu + \text{h.c.} \\ &+ g_s \left( \frac{g_4}{g_3} \bar{Q}'_R \gamma^\mu T^a Q'_R - \frac{g_3}{g_4} \bar{u}'_R \gamma^\mu T^a u'_R - \frac{g_3}{g_4} \bar{d}'_R \gamma^\mu T^a d'_R \right) g'_\mu^a \\ &+ g_Y \left( \sqrt{\frac{3}{2}} \frac{g_4}{g_1} Y(Q'_R) \bar{Q}'_R \gamma^\mu Q'_R - \sqrt{\frac{2}{3}} \frac{g_1}{g_4} Y(u'_R) \bar{u}'_R \gamma^\mu u'_R - \sqrt{\frac{2}{3}} \frac{g_1}{g_4} Y(d'_R) \bar{d}'_R \gamma^\mu d'_R \right) Z'_\mu \\ &+ g_Y \left( \sqrt{\frac{3}{2}} \frac{g_4}{g_1} Y(L'_R) \bar{L}'_R \gamma^\mu L'_R - \sqrt{\frac{2}{3}} \frac{g_1}{g_4} Y(\ell'_R) \bar{\ell}'_R \gamma^\mu \ell'_R \right) Z'_\mu. \end{aligned} \quad (\text{B.26})$$

The SM hypercharges are:  $Y(Q'_L) = Y(Q'_R) = Y(q'_L) = \frac{1}{6}$ ,  $Y(u'_R) = \frac{2}{3}$ ,  $Y(d'_R) = -\frac{1}{3}$ ,  $Y(L'_L) = Y(L'_R) = Y(\ell'_L) = -\frac{1}{2}$ , and  $Y(e'_R) = -1$ .

To express the interactions in Eqs. (B.25) and (B.26) in the fermion mass basis, we collect the fields into 6-dimensional multiplets,  $\psi_x$  ( $x = q, u, d, \ell, e$ ), and apply the corresponding unitary transformations  $U_x$ . Neglecting the right-handed rotations—which are suppressed by the small masses of the SM fermions—we obtain:

$$\begin{aligned} \mathcal{L}_U &= \frac{g_4}{\sqrt{2}} U_\mu [\beta \bar{\Psi}_q \gamma^\mu \psi_\ell + W \bar{Q}_R \gamma^\mu L_R] + \text{h.c.}, \\ \mathcal{L}_{g'} &= g_s \frac{g_4}{g_3} g'_\mu^a [\kappa_q \bar{\Psi}_q \gamma^\mu T^a \psi_q + \kappa_u \bar{\Psi}_u \gamma^\mu T^a \psi_u + \kappa_d \bar{\Psi}_d \gamma^\mu T^a \psi_d], \\ \mathcal{L}_{Z'} &= \frac{g_Y}{2\sqrt{6}} \frac{g_4}{g_1} Z'_\mu [\zeta_q \bar{\Psi}_q \gamma^\mu \psi_q + \zeta_u \bar{\Psi}_u \gamma^\mu \psi_u \\ &\quad + \zeta_d \bar{\Psi}_d \gamma^\mu \psi_d - 3\zeta_\ell \bar{\Psi}_\ell \gamma^\mu \psi_\ell - 3\zeta_e \bar{\Psi}_e \gamma^\mu \psi_e]. \end{aligned} \quad (\text{B.27})$$

The coupling matrices are defined as follows (with indices  $A, B = 4, 5, 6$  spanning the heavy vector-like states, and  $\alpha, \beta = 1, \dots, 6$  spanning the full 6-dimensional space):

$$\begin{aligned}\beta^{\alpha\beta} &= [U_q]_{A\alpha}^* [W]_{AB} [U_\ell]_{B\beta}, \\ \kappa_q^{\alpha\beta} &= [U_q]_{A\alpha}^* [U_q]_{A\beta} - \frac{g_3^2}{g_4^2} \delta_{\alpha\beta}, \quad \kappa_u \approx \kappa_d \approx \begin{pmatrix} 0 & 0 \\ 0 & \mathbb{1}_{3\times 3} \end{pmatrix} - \frac{g_3^2}{g_4^2} \mathbb{1}_{6\times 6}, \\ \zeta_q^{\alpha\beta} &= [U_q]_{A\alpha}^* [U_q]_{A\beta} - \frac{2g_1^2}{3g_4^2} \delta_{\alpha\beta}, \quad \zeta_u \approx \zeta_d \approx \begin{pmatrix} 0 & 0 \\ 0 & \mathbb{1}_{3\times 3} \end{pmatrix} - \frac{2g_1^2}{3g_4^2} \mathbb{1}_{6\times 6}, \\ \zeta_\ell^{\alpha\beta} &= [U_\ell]_{A\alpha}^* [U_\ell]_{A\beta} - \frac{2g_1^2}{3g_4^2} \delta_{\alpha\beta}, \quad \zeta_e \approx \begin{pmatrix} 0 & 0 \\ 0 & \mathbb{1}_{3\times 3} \end{pmatrix} - \frac{2g_1^2}{3g_4^2} \mathbb{1}_{6\times 6}. \end{aligned} \tag{B.28}$$

A key result of the assumed flavour structure is that the matrix  $W$  cancels due to unitarity in the  $Z'$  and  $g'$  interactions. This cancellation is crucial for suppressing unwanted flavour-changing neutral currents (FCNCs) in these sectors.

Assuming  $W = \mathcal{R}_{56}(\theta_{LQ})$  and no CP violation in the mixing angles, the left-handed coupling matrices can be explicitly written as:

$$\beta \approx \begin{pmatrix} \text{diag}(s_{q_1}s_{\ell_1}, s_{q_2}s_{\ell_2}, s_{q_3}s_{\ell_3})W & -\text{diag}(s_{q_1}c_{\ell_1}, s_{q_2}c_{\ell_2}, s_{q_3}c_{\ell_3})W \\ \text{diag}(c_{q_1}s_{\ell_1}, c_{q_2}s_{\ell_2}, c_{q_3}s_{\ell_3})W & -\text{diag}(c_{q_1}c_{\ell_1}, c_{q_2}c_{\ell_2}, c_{q_3}c_{\ell_3})W \end{pmatrix}, \tag{B.29}$$

$$\kappa_q \approx \begin{pmatrix} \text{diag}(s_{q_1}^2, s_{q_2}^2, s_{q_3}^2) & -\frac{1}{2}\text{diag}(s_{2q_1}, s_{2q_2}, s_{2q_3}) \\ -\frac{1}{2}\text{diag}(s_{2q_1}, s_{2q_2}, s_{2q_3}) & \text{diag}(c_{q_1}^2, c_{q_2}^2, c_{q_3}^2) \end{pmatrix} - \frac{g_3^2}{g_4^2} \mathbb{1}_{6\times 6}, \tag{B.30}$$

$$\zeta_q \approx \begin{pmatrix} \text{diag}(s_{q_1}^2, s_{q_2}^2, s_{q_3}^2) & -\frac{1}{2}\text{diag}(s_{2q_1}, s_{2q_2}, s_{2q_3}) \\ -\frac{1}{2}\text{diag}(s_{2q_1}, s_{2q_2}, s_{2q_3}) & \text{diag}(c_{q_1}^2, c_{q_2}^2, c_{q_3}^2) \end{pmatrix} - \frac{2g_1^2}{3g_4^2} \mathbb{1}_{6\times 6}, \tag{B.31}$$

$$\zeta_\ell \approx \begin{pmatrix} \text{diag}(s_{\ell_1}^2, s_{\ell_2}^2, s_{\ell_3}^2) & -\frac{1}{2}\text{diag}(s_{2\ell_1}, s_{2\ell_2}, s_{2\ell_3}) \\ -\frac{1}{2}\text{diag}(s_{2\ell_1}, s_{2\ell_2}, s_{2\ell_3}) & \text{diag}(c_{\ell_1}^2, c_{\ell_2}^2, c_{\ell_3}^2) \end{pmatrix} - \frac{2g_1^2}{3g_4^2} \mathbb{1}_{6\times 6}. \tag{B.32}$$

Following the flavour structure in [34], the assumption of a single  $U(2)_q$  breaking spurion in both the leptoquark and SM Yukawa couplings implies the relation  $\beta_L^{13} = V_{td}^*/V_{ts}^* \beta_L^{23}$ . More generally, from  $U(2)$  symmetries acting on both quark and lepton sectors, we expect the hierarchy:

$$|\beta_L^{31}| \ll |\beta_L^{23}|, |\beta_L^{32}| \ll |\beta_R^{33}|, |\beta_L^{33}| = \mathcal{O}(1),$$

and analogously for the  $\zeta_{\ell,e,Q}^{ij}$  and  $\kappa_Q^{ij}$  couplings.

This structure can be achieved with a specific choice of the  $\lambda$  parameters in the potential, leading to particular values for the mixing angles  $\theta_{q_i}$  and  $\theta_{\ell_i}$ . To explain the B-physics anomalies, a large mixing angle  $\theta_{\ell_3}$  is required, while the other two angles  $\theta_{\ell_{1,2}}$  must be small to avoid large contributions to muon and electron observables. The quark mixing angles

$\theta_{q_i}$  should be small for the first two generations to avoid large contributions to meson mixing observables, while a moderate value of  $\theta_{q_3}$  is needed to explain the B-physics anomalies.



---

## BIBLIOGRAPHY

---

- [1] A. Flórez et al. "On the sensitivity reach of LQ production with preferential couplings to third generation fermions at the LHC". In: *The European Physical Journal C* 83.11 (Nov. 2023), p. 1023. ISSN: 1434-6052. DOI: [10.1140/epjc/s10052-023-12177-4](https://doi.org/10.1140/epjc/s10052-023-12177-4).
- [2] Umar Sohail Qureshi et al. "Probing light scalars and vector-like quarks at the high-luminosity LHC". In: *Eur. Phys. J. C* 85.4 (2025), p. 379. DOI: [10.1140/epjc/s10052-025-14085-1](https://doi.org/10.1140/epjc/s10052-025-14085-1). arXiv: [2410.17854 \[hep-ph\]](https://arxiv.org/abs/2410.17854).
- [3] R. Aliberti et al. "The anomalous magnetic moment of the muon in the Standard Model: an update". In: *Physics Reports* 1143 (2025). The anomalous magnetic moment of the muon in the Standard Model: An update, pp. 1–158. ISSN: 0370-1573. DOI: <https://doi.org/10.1016/j.physrep.2025.08.002>.
- [4] W Greiner. *Relativistic Quantum Mechanics. Wave Equations*. Springer, 2000. ISBN: 9783540674573.
- [5] Stefan Pokorski. *Gauge field theories*. Cambridge Monographs on Mathematical Physics. Cambridge University Press, 2000. ISBN: 9780521478168.
- [6] David Tong. *Quantum Field Theory University of Cambridge Part III Mathematical Tripos*. Vol. 45. 12. 1995.
- [7] Herbert Goldstein, Charles P Poole, and John L Safko. *Classical mechanics*. 3rd ed. Addison Wesley, 2001. ISBN: 9780201657029,0201657023.
- [8] J V José and E J Saletan. *Classical Dynamics: A Contemporary Approach*. Cambridge University Press, 1998. ISBN: 9780521636360.
- [9] Roberto Martínez. *Teoría cuántica de campos*. Colección Textos. Universidad Nacional de Colombia, Facultad de Ciencias, Departamento de Física, 2002. ISBN: 9789587011203.
- [10] Steven Weinberg. *The Quantum Theory of Fields, Volume 3: Supersymmetry*. Cambridge University Press, 2005. ISBN: 0521670551,9780521670555.
- [11] D.A. Bromley Walter Greiner Joachim Reinhardt. *Field quantization*. 1st ed. Springer, 1996. ISBN: 3540591796,9783540591795.
- [12] Dan V. Schroeder Michael E. Peskin. *An Introduction To Quantum Field Theory*. Frontiers in Physics. Westview Press, 1995. ISBN: 9780201503975.
- [13] P C W Davies N. D. Birrell. *Quantum fields in curved space*. CUP. Cambridge Monographs on Mathematical Physics. Cambridge University Press, 1984. ISBN: 9780521278584,0521278589.

- [14] Amitabha Lahiri and Palash B Pal. *A First Book of Quantum Field Theory*. Alpha Science International, 2006, p. 380. ISBN: 1842652494.
- [15] Reinhold A. Bertlmann. *Anomalies in Quantum Field Theory*. Oxford University Press, 1996. ISBN: 9780198520476.
- [16] Daniel Z. Freedman and Antoine Van Proeyen. *Supergravity*. Cambridge University Press, 2012. ISBN: 9780521194013.
- [17] Diego Gallego. *Estudio de uplifts efectivos en compactificaciones de supercuerdas tipo-IIB*. Tech. rep. Tunja: Universidad Pedagógica y Tecnológica de Colombia, 2016, p. 96.
- [18] Antoine Van Proeyen. “Tools for Supersymmetry”. In: *Physics AUC* 9.I (1999), pp. 1–49. arXiv: 9910030 [hep-th].
- [19] Stephen P. Martin. “TASI 2011 lectures notes: two-component fermion notation and supersymmetry”. In: *arXiv* (2012). arXiv: 1205.4076.
- [20] M Robinson. *Symmetry and the Standard Model: Mathematics and Particle Physics*. 1st ed. SpringerLink : Bucher. New York: Springer-Verlag, 2011. ISBN: 9781441982674. DOI: 10.1007/978-1-4419-8267-4.
- [21] “Physics: 1963–1970”. In: Nobel lectures, including presentation speeches and laureates’ biographies. Elsevier Publishing Company, 1972.
- [22] P.A. Zyla et al. “Review of Particle Physics”. In: *PTEP* 2020.8 (2020), p. 083C01. DOI: 10.1093/ptep/ptaa104.
- [23] F. J. Dyson. “The Radiation Theories of Tomonaga, Schwinger, and Feynman”. In: *Phys. Rev.* 75 (3 1949), pp. 486–502. DOI: 10.1103/PhysRev.75.486.
- [24] Clay Mathematics Institute. *Yang–Mills Existence and Mass Gap*. Accepted: 2025-10-24. 2000. URL: <https://www.claymath.org/millennium/yang-mills-the-maths-gap/>.
- [25] Cristian Rodriguez. “Evaluacion del Lagrangiano de Supergravedad  $\mathcal{N} = 1$  utilizando el formalismo Superconforme.” BA thesis. UPTC, 2018.
- [26] C. S. Wu et al. “Experimental Test of Parity Conservation in Beta Decay”. In: *Phys. Rev.* 105 (4 1957), pp. 1413–1415. DOI: 10.1103/PhysRev.105.1413.
- [27] Sheldon L. Glashow. “Partial-symmetries of weak interactions”. In: *Nuclear Physics* 22.4 (1961), pp. 579–588. ISSN: 0029-5582. DOI: [https://doi.org/10.1016/0029-5582\(61\)90469-2](https://doi.org/10.1016/0029-5582(61)90469-2).
- [28] Steven Weinberg. “A Model of Leptons”. In: *Phys. Rev. Lett.* 19 (21 1967), pp. 1264–1266. DOI: 10.1103/PhysRevLett.19.1264.
- [29] Abdus Salam. “Weak and Electromagnetic Interactions”. In: *Elementary particle theory: Relativistic groups and analyticity*. Ed. by N. Svartholm. Stockholm: Almqvist & Wiksell, 1968, pp. 367–377.

- [30] Tadao Nakano and Kazuhiko Nishijima. "Charge Independence for V-particles". In: *Progress of Theoretical Physics* 10.5 (Nov. 1953), pp. 581–582. ISSN: 0033-068X. DOI: [10.1143/PTP.10.581](https://doi.org/10.1143/PTP.10.581).
- [31] B. Odom et al. "New Measurement of the Electron Magnetic Moment Using a One-Electron Quantum Cyclotron". In: *Phys. Rev. Lett.* 97 (3 2006), p. 030801. DOI: [10.1103/PhysRevLett.97.030801](https://doi.org/10.1103/PhysRevLett.97.030801).
- [32] H.P. P Nilles. "Supersymmetry, supergravity and particle physics". In: *Physics Reports* 110.1-2 (1984), pp. 1–162. ISSN: 03701573. DOI: [10.1016/0370-1573\(84\)90008-5](https://doi.org/10.1016/0370-1573(84)90008-5).
- [33] I. Doršner et al. "Physics of leptoquarks in precision experiments and at particle colliders". In: *Phys. Rept.* 641 (2016), pp. 1–68. DOI: [10.1016/j.physrep.2016.06.001](https://doi.org/10.1016/j.physrep.2016.06.001). arXiv: [1603.04993 \[hep-ph\]](https://arxiv.org/abs/1603.04993).
- [34] D. Buttazzo et al. "B-physics anomalies: a guide to combined explanations". In: *JHEP* 11 (2017), p. 044. DOI: [10.1007/JHEP11\(2017\)044](https://doi.org/10.1007/JHEP11(2017)044). arXiv: [1706.07808 \[hep-ph\]](https://arxiv.org/abs/1706.07808).
- [35] LHCb Collaboration. "Test of lepton universality in  $b \rightarrow s\ell^+\ell^-$  decays". In: *Physical Review Letters* 131 (2023), p. 051803. DOI: [10.1103/PhysRevLett.131.051803](https://doi.org/10.1103/PhysRevLett.131.051803). arXiv: [2212.09152 \[hep-ex\]](https://arxiv.org/abs/2212.09152).
- [36] BaBar Collaboration. "Evidence for an excess of  $\bar{B} \rightarrow D^{(*)}\tau^-\bar{\nu}_\tau$  decays". In: *Phys. Rev. Lett.* 109 (2012), p. 101802. DOI: [10.1103/PhysRevLett.109.101802](https://doi.org/10.1103/PhysRevLett.109.101802). arXiv: [1205.5442 \[hep-ex\]](https://arxiv.org/abs/1205.5442).
- [37] Belle Collaboration. "Measurement of the branching ratio of  $\bar{B} \rightarrow D^{(*)}\tau^-\bar{\nu}_\tau$  relative to  $\bar{B} \rightarrow D^{(*)}\ell^-\bar{\nu}_\ell$  decays with hadronic tagging at Belle". In: *Phys. Rev. D* 92.7 (2015), p. 072014. DOI: [10.1103/PhysRevD.92.072014](https://doi.org/10.1103/PhysRevD.92.072014). arXiv: [1507.03233 \[hep-ex\]](https://arxiv.org/abs/1507.03233).
- [38] LHCb Collaboration. "Measurement of the ratio of branching fractions  $\mathcal{B}(\bar{B}^0 \rightarrow D^{*+}\tau^-\bar{\nu}_\tau)/\mathcal{B}(\bar{B}^0 \rightarrow D^{*+}\mu^-\bar{\nu}_\mu)$ ". In: *Phys. Rev. Lett.* 115.11 (2015). [Erratum: *Phys. Rev. Lett.* 115, 159901 (2015)], p. 111803. DOI: [10.1103/PhysRevLett.115.111803](https://doi.org/10.1103/PhysRevLett.115.111803). arXiv: [1506.08614 \[hep-ex\]](https://arxiv.org/abs/1506.08614).
- [39] Y. Amhis et al. "Averages of b-hadron, c-hadron, and  $\tau$ -lepton properties as of 2018". In: *The European Physical Journal C* 81.3 (2021). DOI: [10.1140/epjc/s10052-020-8156-7](https://doi.org/10.1140/epjc/s10052-020-8156-7).
- [40] HFLAV Collaboration. *Averages of b-hadron, c-hadron, and  $\tau$ -lepton properties as of 2021*. Updated results and plots available at <https://hflav.web.cern.ch>. 2023. arXiv: [2206.07501 \[hep-ex\]](https://arxiv.org/abs/2206.07501).
- [41] Belle II Collaboration. "Measurement of  $\mathcal{R}(D)$  and  $\mathcal{R}(D^*)$  with a semileptonic tagging method". In: *Physical Review Letters* 131 (2023), p. 171804. DOI: [10.1103/PhysRevLett.131.171804](https://doi.org/10.1103/PhysRevLett.131.171804). arXiv: [2301.08266 \[hep-ex\]](https://arxiv.org/abs/2301.08266).
- [42] LHCb Collaboration. "Measurement of the ratios of branching fractions  $\mathcal{R}(D^*)$  and  $\mathcal{R}(D^0)$ ". In: (2023). DOI: [10.48550/arXiv.2302.02886](https://doi.org/10.48550/arXiv.2302.02886). arXiv: [2302.02886 \[hep-ex\]](https://arxiv.org/abs/2302.02886).

- [43] Muon g2 Collaboration. "Measurement of the positive muon anomalous magnetic moment to 0.20 ppm". In: *Physical Review Letters* 131 (2023), p. 161802. doi: 10.1103/PhysRevLett.131.161802. arXiv: 2308.06230 [hep-ex].
- [44] Tatsumi Aoyama et al. "The anomalous magnetic moment of the muon in the Standard Model". In: *Physics Reports* 887 (2020), pp. 1–166. doi: 10.1016/j.physrep.2020.07.006. arXiv: 2006.04822 [hep-ph].
- [45] Sz. Borsanyi et al. "Leading hadronic contribution to the muon magnetic moment from lattice QCD". In: *Nature* 593 (2021), pp. 51–55. doi: 10.1038/s41586-021-03418-1. arXiv: 2002.12347 [hep-lat].
- [46] CMD-3 Collaboration. "Measurement of the  $e^+e^- \rightarrow \pi^+\pi^-$  cross section from threshold to 1.2 GeV with the CMD-3 detector". In: *Physical Review D* 109 (2024), p. 112002. doi: 10.1103/PhysRevD.109.112002. arXiv: 2302.08834 [hep-ex].
- [47] LHCb Collaboration. "Test of lepton universality using  $B^+ \rightarrow K^+\ell^+\ell^-$  decays". In: *Phys. Rev. Lett.* 113 (2014), p. 151601. doi: 10.1103/PhysRevLett.113.151601. arXiv: 1406.6482 [hep-ex].
- [48] LHCb Collaboration. "Test of lepton universality with  $B^0 \rightarrow K^{*0}\ell^+\ell^-$  decays". In: *JHEP* 08 (2017), p. 055. doi: 10.1007/JHEP08(2017)055. arXiv: 1705.05802 [hep-ex].
- [49] Ivan Esteban et al. *The fate of hints: updated global analysis of three-flavor neutrino oscillations*. Updated results available at <http://www.nufit.org>. 2020. arXiv: 2007.14792 [hep-ph].
- [50] KATRIN Collaboration. "Direct neutrino-mass measurement with sub-electronvolt sensitivity". In: *Nature Physics* 18 (2022), pp. 160–166. doi: 10.1038/s41567-021-01463-1. arXiv: 2105.08533 [hep-ex].
- [51] KATRIN Collaboration. "Direct neutrino mass measurement with KATRIN: Improved sensitivity from the first two measurement campaigns". In: (2024). arXiv: 2406.13516 [hep-ex].
- [52] P. K. Mohapatra, R. N. Mohapatra, and P. B. Pal. "Implications of E6 Grand Unification". In: *Phys. Rev. D* 33 (1986), p. 2010. doi: 10.1103/PhysRevD.33.2010.
- [53] CDF Collaboration. "High-precision measurement of the W boson mass with the CDF II detector". In: *Science* 376 (2022), pp. 170–176. doi: 10.1126/science.abk1781.
- [54] Particle Data Group. *Review of Particle Physics*. 2024. doi: 10.1103/PhysRevD.110.030001.
- [55] Chien-Yeah Seng et al. "Reduced hadronic uncertainty in the determination of  $V_{ud}$ ". In: *Physical Review Letters* 121 (2018), p. 241804. doi: 10.1103/PhysRevLett.121.241804. arXiv: 1807.10197 [hep-ph].

- [56] J. C. Hardy and I. S. Towner. “Superallowed  $0^+ \rightarrow 0^+$  nuclear  $\beta$  decays: 2020 critical survey, with implications for  $V_{ud}$  and CKM unitarity”. In: *Physical Review C* 102 (2020), p. 045501. doi: [10.1103/PhysRevC.102.045501](https://doi.org/10.1103/PhysRevC.102.045501).
- [57] Martinus J. G. Veltman. “The infrared-ultraviolet connection”. In: *Acta Physica Polonica B* 12 (1981), p. 437.
- [58] Lisa Randall and Raman Sundrum. “A Large mass hierarchy from a small extra dimension”. In: *Phys. Rev. Lett.* 83 (1999), pp. 3370–3373. doi: [10.1103/PhysRevLett.83.3370](https://doi.org/10.1103/PhysRevLett.83.3370). arXiv: [hep-ph/9905221](https://arxiv.org/abs/hep-ph/9905221).
- [59] G. F. Giudice. “Naturalness after LHC”. In: *arXiv e-prints* (2013). arXiv: [1307.7879 \[hep-ph\]](https://arxiv.org/abs/1307.7879).
- [60] Leonard Susskind. “Dynamics of spontaneous symmetry breaking in the Weinberg-Salam theory”. In: *Physical Review D* 20 (1979), pp. 2619–2625. doi: [10.1103/PhysRevD.20.2619](https://doi.org/10.1103/PhysRevD.20.2619).
- [61] Riccardo Barbieri and G. F. Giudice. “Upper bounds on supersymmetric particle masses”. In: *Nuclear Physics B* 306 (1988), pp. 63–76. doi: [10.1016/0550-3213\(88\)90171-X](https://doi.org/10.1016/0550-3213(88)90171-X).
- [62] C. Abel et al. “Measurement of the permanent electric dipole moment of the neutron”. In: *Physical Review Letters* 124 (2020), p. 081803. doi: [10.1103/PhysRevLett.124.081803](https://doi.org/10.1103/PhysRevLett.124.081803). arXiv: [2001.11966 \[hep-ex\]](https://arxiv.org/abs/2001.11966).
- [63] David J. E. Callaway. “Triviality pursuit: Can elementary scalar particles exist?” In: *Physics Reports* 167 (1988), pp. 241–320. doi: [10.1016/0370-1573\(88\)90008-7](https://doi.org/10.1016/0370-1573(88)90008-7).
- [64] Thomas Hambye and Kurt Riesselmann. “Matching conditions and Higgs mass upper bounds revisited”. In: *Physical Review D* 55 (1997), pp. 7255–7262. doi: [10.1103/PhysRevD.55.7255](https://doi.org/10.1103/PhysRevD.55.7255). arXiv: [hep-ph/9610272 \[hep-ph\]](https://arxiv.org/abs/hep-ph/9610272).
- [65] Martin Lüscher and Peter Weisz. “Scaling laws and triviality bounds in the lattice  $\phi^4$  theory: (III). n-component model”. In: *Nuclear Physics B* 318 (1989), pp. 705–741. doi: [10.1016/0550-3213\(89\)90637-8](https://doi.org/10.1016/0550-3213(89)90637-8).
- [66] Alejandro Rivero and Andre Gsponer. *The strange formula of Dr. Koide*. 2005. doi: [10.48550/ARXIV.HEP-PH/0505220](https://doi.org/10.48550/ARXIV.HEP-PH/0505220).
- [67] John F. Donoghue. “General relativity as an effective field theory: The leading quantum corrections”. In: *Phys. Rev. D* 50 (1994), pp. 3874–3888. doi: [10.1103/PhysRevD.50.3874](https://doi.org/10.1103/PhysRevD.50.3874). arXiv: [gr-qc/9405057](https://arxiv.org/abs/gr-qc/9405057).
- [68] C. P. Burgess. “Quantum gravity in everyday life: General relativity as an effective field theory”. In: *Living Rev. Rel.* 7 (2004), pp. 5–56. doi: [10.12942/lrr-2004-5](https://doi.org/10.12942/lrr-2004-5). arXiv: [gr-qc/0311082](https://arxiv.org/abs/gr-qc/0311082).
- [69] Steven Weinberg. “The Cosmological Constant Problem”. In: *Rev. Mod. Phys.* 61 (1989). Ed. by Jong-Ping Hsu and D. Fine, pp. 1–23. doi: [10.1103/RevModPhys.61.1](https://doi.org/10.1103/RevModPhys.61.1).

- [70] Planck Collaboration. “Planck 2018 results. VI. Cosmological parameters”. In: *Astronomy & Astrophysics* 641 (2020), A6. doi: [10.1051/0004-6361/201833910](https://doi.org/10.1051/0004-6361/201833910). arXiv: [1807.06209 \[astro-ph.CO\]](https://arxiv.org/abs/1807.06209).
- [71] Gianfranco Bertone, Dan Hooper, and Joseph Silk. “Particle dark matter: evidence, candidates and constraints”. In: *Physics Reports* 405 (2005), pp. 279–390. doi: [10.1016/j.physrep.2004.08.031](https://doi.org/10.1016/j.physrep.2004.08.031). arXiv: [hep-ph/0404175 \[hep-ph\]](https://arxiv.org/abs/hep-ph/0404175).
- [72] Richard H. Cyburt et al. “Big Bang Nucleosynthesis: 2015”. In: *Reviews of Modern Physics* 88 (2016), p. 015004. doi: [10.1103/RevModPhys.88.015004](https://doi.org/10.1103/RevModPhys.88.015004). arXiv: [1505.01076 \[astro-ph.CO\]](https://arxiv.org/abs/1505.01076).
- [73] Cyril Pitrou et al. “Precision Big Bang Nucleosynthesis with improved Helium-4 predictions”. In: *Physics Reports* 754 (2018), pp. 1–66. doi: [10.1016/j.physrep.2018.04.005](https://doi.org/10.1016/j.physrep.2018.04.005). arXiv: [1801.08023 \[astro-ph.CO\]](https://arxiv.org/abs/1801.08023).
- [74] Brian D. Fields et al. “Big-Bang Nucleosynthesis after Planck”. In: *Journal of Cosmology and Astroparticle Physics* 2020.03 (2020), p. 010. doi: [10.1088/1475-7516/2020/03/010](https://doi.org/10.1088/1475-7516/2020/03/010). arXiv: [1912.01132 \[astro-ph.CO\]](https://arxiv.org/abs/1912.01132).
- [75] LZ Collaboration. “First Dark Matter Search Results from the LZ Experiment”. In: (2022). arXiv: [2207.03764 \[hep-ex\]](https://arxiv.org/abs/2207.03764).
- [76] J. Aalbers et al. “First constraints on WIMP-nucleon effective field theory couplings in an extended energy region from LUX-ZEPLIN”. In: *Phys. Rev. D* 109.9 (2024), p. 092003. doi: [10.1103/PhysRevD.109.092003](https://doi.org/10.1103/PhysRevD.109.092003). arXiv: [2312.02030 \[hep-ex\]](https://arxiv.org/abs/2312.02030).
- [77] XENON Collaboration. “First Dark Matter Search with Nuclear Recoils from the XENONnT Experiment”. In: (2023). arXiv: [2303.14729 \[hep-ex\]](https://arxiv.org/abs/2303.14729).
- [78] A. D. Sakharov. “Violation of CP Invariance, C asymmetry, and baryon asymmetry of the universe”. In: *Pisma Zh. Eksp. Teor. Fiz.* 5 (1967), pp. 32–35. doi: [10.1070/PU1991v034n05ABEH002497](https://doi.org/10.1070/PU1991v034n05ABEH002497).
- [79] Sacha Davidson, Enrico Nardi, and Yosef Nir. “Leptogenesis”. In: *Physics Reports* 466 (2008), pp. 105–177. doi: [10.1016/j.physrep.2008.06.002](https://doi.org/10.1016/j.physrep.2008.06.002). arXiv: [0802.2962 \[hep-ph\]](https://arxiv.org/abs/0802.2962).
- [80] David E. Morrissey and Michael J. Ramsey-Musolf. “Electroweak baryogenesis”. In: *New Journal of Physics* 14 (2012), p. 125003. doi: [10.1088/1367-2630/14/12/125003](https://doi.org/10.1088/1367-2630/14/12/125003). arXiv: [1206.2942 \[hep-ph\]](https://arxiv.org/abs/1206.2942).
- [81] DESI Collaboration. “DESI 2024 VI: Cosmological constraints from the measurements of baryon acoustic oscillations”. In: (2024). arXiv: [2404.03002 \[astro-ph.CO\]](https://arxiv.org/abs/2404.03002).
- [82] G. Hiller and M. Schmaltz. “ $R_K$  and future  $b \rightarrow s\ell\ell$  physics beyond the standard model opportunities”. In: *Phys. Rev. D* 90 (2014), p. 054014. doi: [10.1103/PhysRevD.90.054014](https://doi.org/10.1103/PhysRevD.90.054014). arXiv: [1408.1627 \[hep-ph\]](https://arxiv.org/abs/1408.1627).

- [83] Y. Fukuda et al. "Evidence for oscillation of atmospheric neutrinos". In: *Phys. Rev. Lett.* 81 (1998), pp. 1562–1567. doi: [10.1103/PhysRevLett.81.1562](https://doi.org/10.1103/PhysRevLett.81.1562). arXiv: [hep-ex/9807003](https://arxiv.org/abs/hep-ex/9807003).
- [84] Q. R. Ahmad et al. "Direct evidence for neutrino flavor transformation from neutral current interactions in the Sudbury Neutrino Observatory". In: *Phys. Rev. Lett.* 89 (2002), p. 011301. doi: [10.1103/PhysRevLett.89.011301](https://doi.org/10.1103/PhysRevLett.89.011301). arXiv: [nucl-ex/0204008](https://arxiv.org/abs/nucl-ex/0204008).
- [85] M. Ciuchini et al. "Constraints on lepton universality violation from rare B decays". In: *Phys. Rev. D* 107 (5 2023), p. 055036. doi: [10.1103/PhysRevD.107.055036](https://doi.org/10.1103/PhysRevD.107.055036).
- [86] LHCb Collaboration. "Search for lepton-universality violation in  $B^+ \rightarrow K^+ \ell^+ \ell^-$  decays". In: *Phys. Rev. Lett.* 122.19 (2019), p. 191801. doi: [10.1103/PhysRevLett.122.191801](https://doi.org/10.1103/PhysRevLett.122.191801). arXiv: [1903.09252 \[hep-ex\]](https://arxiv.org/abs/1903.09252).
- [87] LHCb Collaboration. "Test of lepton universality in beauty-quark decays". In: *Nature Phys.* 18.3 (2022), pp. 277–282. doi: [10.1038/s41567-021-01478-8](https://doi.org/10.1038/s41567-021-01478-8). arXiv: [2103.11769 \[hep-ex\]](https://arxiv.org/abs/2103.11769).
- [88] LHCb Collaboration. "Test of lepton universality in  $b \rightarrow \ell^+ \ell^-$  decays". In: (2022). doi: [10.48550/arXiv.1705.05802](https://doi.org/10.48550/arXiv.1705.05802). arXiv: [2212.09152 \[hep-ex\]](https://arxiv.org/abs/2212.09152).
- [89] LHCb Collaboration. "Measurement of lepton universality parameters in  $B^+ \rightarrow K^+ \ell^+ \ell^-$  and  $B^0 \rightarrow K^0 \ell^+ \ell^-$  decays". In: (2022). doi: [10.48550/arXiv.2212.09153](https://doi.org/10.48550/arXiv.2212.09153). arXiv: [2212.09153 \[hep-ex\]](https://arxiv.org/abs/2212.09153).
- [90] BaBar Collaboration. "Measurement of an excess of  $\bar{B} \rightarrow D^{(*)} \tau^- \bar{\nu}_\tau$  decays and implications for charged Higgs bosons". In: *Phys. Rev. D* 88.7 (2013), p. 072012. doi: [10.1103/PhysRevD.88.072012](https://doi.org/10.1103/PhysRevD.88.072012). arXiv: [1303.0571 \[hep-ex\]](https://arxiv.org/abs/1303.0571).
- [91] LHCb Collaboration. "Test of lepton flavor universality by the measurement of the  $B^0 \rightarrow D^{*-} \tau^+ \nu_\tau$  branching fraction using three-prong  $\tau$  decays". In: *Phys. Rev. D* 97.7 (2018), p. 072013. doi: [10.1103/PhysRevD.97.072013](https://doi.org/10.1103/PhysRevD.97.072013). arXiv: [1711.02505 \[hep-ex\]](https://arxiv.org/abs/1711.02505).
- [92] M. Antonelli et al. "An Evaluation of  $|V_{us}|$  and precise tests of the Standard Model from world data on leptonic and semileptonic kaon decays". In: *Eur. Phys. J. C* 69 (2010), pp. 399–424. doi: [10.1140/epjc/s10052-010-1406-3](https://doi.org/10.1140/epjc/s10052-010-1406-3). arXiv: [1005.2323 \[hep-ph\]](https://arxiv.org/abs/1005.2323).
- [93] ATLAS Collaboration et al. "Test of the universality of  $\tau$  and  $\mu$  lepton couplings in  $W$ -boson decays from  $t\bar{t}$  events with the ATLAS detector". In: *arXiv preprint arXiv:2007.14040* (2020).
- [94] S. Schael et al. "Precision electroweak measurements on the Z resonance". In: *Phys. Rept.* 427 (2006), pp. 257–454. doi: [10.1016/j.physrep.2005.12.006](https://doi.org/10.1016/j.physrep.2005.12.006). arXiv: [hep-ex/0509008](https://arxiv.org/abs/hep-ex/0509008).
- [95] Bernat Capdevila et al. "Patterns of New Physics in  $b \rightarrow s \ell^+ \ell^-$  transitions in the light of recent data". In: *Journal of High Energy Physics* 2018.1 (2018). doi: [10.1007/jhep01\(2018\)093](https://doi.org/10.1007/jhep01(2018)093).

- [96] R. Alonso, B. Grinstein, and J. M. Camalich. “Lepton universality violation and lepton flavor conservation in B-meson decays”. In: *JHEP* 10 (2015), p. 184. doi: [10.1007/JHEP10\(2015\)184](https://doi.org/10.1007/JHEP10(2015)184). arXiv: [1505.05164 \[hep-ph\]](https://arxiv.org/abs/1505.05164).
- [97] L. Calibbi, A. Crivellin, and T. Ota. “Effective field theory approach to  $b \rightarrow s\ell\ell^{(\prime)}$ ,  $B \rightarrow K^{(*)}\nu\bar{\nu}$  and  $B \rightarrow D^{(*)}\tau\nu$  with third generation couplings”. In: *Phys. Rev. Lett.* 115 (2015), p. 181801. doi: [10.1103/PhysRevLett.115.181801](https://doi.org/10.1103/PhysRevLett.115.181801). arXiv: [1506.02661 \[hep-ph\]](https://arxiv.org/abs/1506.02661).
- [98] Wolfgang Altmannshofer and David M. Straub. “New physics in  $b \rightarrow s$  transitions after LHC run 1”. In: *The European Physical Journal C* 75.8 (2015). doi: [10.1140/epjc/s10052-015-3602-7](https://doi.org/10.1140/epjc/s10052-015-3602-7).
- [99] Belle Collaboration. “Measurement of  $\mathcal{R}(D)$  and  $\mathcal{R}(D^*)$  with a semileptonic tagging method”. In: (2019). doi: [10.48550/arXiv.1904.08794](https://doi.org/10.48550/arXiv.1904.08794). arXiv: [1904.08794 \[hep-ex\]](https://arxiv.org/abs/1904.08794).
- [100] Belle Collaboration. “Measurement of the  $\tau$  lepton polarization and  $R(D^*)$  in the decay  $\bar{B} \rightarrow D^*\tau^-\bar{\nu}_\tau$  with one-prong hadronic  $\tau$  decays at Belle”. In: *Phys. Rev. D* 97 (2018), p. 012004. doi: [10.1103/PhysRevD.97.012004](https://doi.org/10.1103/PhysRevD.97.012004). arXiv: [1709.00129 \[hep-ex\]](https://arxiv.org/abs/1709.00129).
- [101] Belle Collaboration. “Measurement of the branching ratio of  $\bar{B}^0 \rightarrow D^{*+}\tau^-\bar{\nu}_\tau$  relative to  $\bar{B}^0 \rightarrow D^{*+}\ell^-\bar{\nu}_\ell$  decays with a semileptonic tagging method”. In: *Phys. Rev. D* 94 (2016), p. 072007. doi: [10.1103/PhysRevD.94.072007](https://doi.org/10.1103/PhysRevD.94.072007). arXiv: [1607.07923 \[hep-ex\]](https://arxiv.org/abs/1607.07923).
- [102] Belle Collaboration. “Measurement of the  $\tau$  lepton polarization and  $R(D^*)$  in the decay  $\bar{B} \rightarrow D^*\tau^-\bar{\nu}_\tau$ ”. In: *Phys. Rev. Lett.* 118 (2017), p. 211801. doi: [10.1103/PhysRevLett.118.211801](https://doi.org/10.1103/PhysRevLett.118.211801). arXiv: [1612.00529 \[hep-ex\]](https://arxiv.org/abs/1612.00529).
- [103] Belle Collaboration. “Measurement of the branching ratio of  $\bar{B} \rightarrow D^{(*)}\tau^-\bar{\nu}_\tau$  relative to  $\bar{B} \rightarrow D^{(*)}\ell^-\bar{\nu}_\ell$  decays with hadronic tagging at Belle”. In: *Phys. Rev. D* 92 (2015), p. 072014. doi: [10.1103/PhysRevD.92.072014](https://doi.org/10.1103/PhysRevD.92.072014). arXiv: [1507.03233 \[hep-ex\]](https://arxiv.org/abs/1507.03233).
- [104] LHCb Collaboration. “Measurement of the ratio of branching fractions  $\mathcal{B}(\bar{B}^0 \rightarrow D^{*+}\tau^-\bar{\nu}_\tau)/\mathcal{B}(\bar{B}^0 \rightarrow D^{*+}\mu^-\bar{\nu}_\mu)$ ”. In: *Phys. Rev. Lett.* 115 (2015). [Erratum: *Phys. Rev. Lett.* 115, 159901 (2015)], p. 111803. doi: [10.1103/PhysRevLett.115.111803](https://doi.org/10.1103/PhysRevLett.115.111803). arXiv: [1506.08614 \[hep-ex\]](https://arxiv.org/abs/1506.08614).
- [105] LHCb Collaboration. “Measurement of the ratio of the  $B^0 \rightarrow D^{*-}\tau^+\nu_\tau$  and  $B^0 \rightarrow D^{*-}\mu^+\nu_\mu$  branching fractions using three-prong  $\tau$ -lepton decays”. In: *Phys. Rev. Lett.* 120 (2018), p. 171802. doi: [10.1103/PhysRevLett.120.171802](https://doi.org/10.1103/PhysRevLett.120.171802). arXiv: [1708.08856 \[hep-ex\]](https://arxiv.org/abs/1708.08856).
- [106] A. Angelescu et al. “Closing the window on single leptoquark solutions to the B-physics anomalies”. In: *JHEP* 10 (2018), p. 183. doi: [10.1007/JHEP10\(2018\)183](https://doi.org/10.1007/JHEP10(2018)183). arXiv: [1808.08179 \[hep-ph\]](https://arxiv.org/abs/1808.08179).

- [107] M. Bauer and M. Neubert. “Minimal leptoquark explanation for the  $R_{D^{(*)}}$ ,  $R_K$ , and  $(g-2)_\mu$  anomalies”. In: *Phys. Rev. Lett.* 116.14 (2016), p. 141802. doi: [10.1103/PhysRevLett.116.141802](https://doi.org/10.1103/PhysRevLett.116.141802). arXiv: [1511.01900 \[hep-ph\]](https://arxiv.org/abs/1511.01900).
- [108] A. Crivellin, D. Muller, and T. Ota. “Simultaneous explanation of  $R(D^*)$  and  $b \rightarrow \mu^+ \mu^-$ :the last scalar leptoquark standing”. In: *JHEP* 09 (2017), p. 040. doi: [10.1007/JHEP09\(2017\)040](https://doi.org/10.1007/JHEP09(2017)040). arXiv: [1703.09226 \[hep-ph\]](https://arxiv.org/abs/1703.09226).
- [109] A. Greljo et al. “Rare b decays meet high-mass Drell-Yan”. In: *JHEP* 2023.5 (2023). doi: [10.1007/jhep05\(2023\)087](https://doi.org/10.1007/jhep05(2023)087).
- [110] W. Altmannshofer et al. “The Belle II Physics Book”. In: *PTEP* 2019.12 (2019). Ed. by E. Kou and P. Urquijo. [Erratum: *PTEP* 2020, 029201 (2020)], p. 123C01. doi: [10.1093/ptep/ptz106](https://doi.org/10.1093/ptep/ptz106). arXiv: [1808.10567 \[hep-ex\]](https://arxiv.org/abs/1808.10567).
- [111] Admir Greljo and Ben A. Stefanek. “Third family quark-lepton unification at the TeV scale”. In: *Phys. Lett. B* 782 (2018), pp. 131–138. doi: [10.1016/j.physletb.2018.05.033](https://doi.org/10.1016/j.physletb.2018.05.033). arXiv: [1802.04274 \[hep-ph\]](https://arxiv.org/abs/1802.04274).
- [112] S. F. King. “Twin Pati-Salam theory of flavour with a TeV scale vector leptoquark”. In: *JHEP* 11 (2021), p. 161. doi: [10.1007/JHEP11\(2021\)161](https://doi.org/10.1007/JHEP11(2021)161). arXiv: [2106.03876 \[hep-ph\]](https://arxiv.org/abs/2106.03876).
- [113] C. Cornellà, J. Fuentes-Martín, and G. Isidori. “Revisiting the vector leptoquark explanation of the B-physics anomalies”. In: *JHEP* 07 (2019), p. 168. doi: [10.1007/JHEP07\(2019\)168](https://doi.org/10.1007/JHEP07(2019)168). arXiv: [1903.11517 \[hep-ph\]](https://arxiv.org/abs/1903.11517).
- [114] C. Cornellà et al. “Reading the footprints of the B-meson flavor anomalies”. In: *JHEP* 08 (2021), p. 050. doi: [10.1007/JHEP08\(2021\)050](https://doi.org/10.1007/JHEP08(2021)050). arXiv: [2103.16558 \[hep-ph\]](https://arxiv.org/abs/2103.16558).
- [115] L. Di Luzio, A. Greljo, and M. Nardecchia. “Gauge leptoquark as the origin of B-physics anomalies”. In: *Phys. Rev. D* 96.11 (2017), p. 115011. doi: [10.1103/PhysRevD.96.115011](https://doi.org/10.1103/PhysRevD.96.115011). arXiv: [1708.08450 \[hep-ph\]](https://arxiv.org/abs/1708.08450).
- [116] A. Angelescu et al. “Single leptoquark solutions to the B-physics anomalies”. In: *Phys. Rev. D* 104.5 (2021), p. 055017. doi: [10.1103/PhysRevD.104.055017](https://doi.org/10.1103/PhysRevD.104.055017). arXiv: [2103.12504 \[hep-ph\]](https://arxiv.org/abs/2103.12504).
- [117] L. Allwicher et al. “Drell-Yan tails beyond the standard model”. In: *JHEP* 2023.3 (2023). doi: [10.1007/jhep03\(2023\)064](https://doi.org/10.1007/jhep03(2023)064).
- [118] Gianluca Blankenburg, Gino Isidori, and Joel Jones-Perez. “Neutrino Masses and LFV from Minimal Breaking of  $U(3)^5$  and  $U(2)^5$  flavor Symmetries”. In: *Eur. Phys. J. C* 72 (2012), p. 2126. doi: [10.1140/epjc/s10052-012-2126-7](https://doi.org/10.1140/epjc/s10052-012-2126-7). arXiv: [1204.0688 \[hep-ph\]](https://arxiv.org/abs/1204.0688).

- [119] CMS Collaboration. "Search for singly and pair-produced leptoquarks coupling to third-generation fermions in proton-proton collisions at  $s=13$  TeV". In: *Phys. Lett. B* 819 (2021), p. 136446. doi: [10.1016/j.physletb.2021.136446](https://doi.org/10.1016/j.physletb.2021.136446). arXiv: [2012.04178 \[hep-ex\]](https://arxiv.org/abs/2012.04178).
- [120] ATLAS Collaboration. "Searches for third-generation scalar leptoquarks in  $\sqrt{s} = 13$  TeV pp collisions with the ATLAS detector". In: *JHEP* 06 (2019), p. 144. doi: [10.1007/JHEP06\(2019\)144](https://doi.org/10.1007/JHEP06(2019)144). arXiv: [1902.08103 \[hep-ex\]](https://arxiv.org/abs/1902.08103).
- [121] B. Abi et al. "Measurement of the Positive Muon Anomalous Magnetic Moment to 0.46 ppm". In: *Physical Review Letters* 126.14 (2021). doi: [10.1103/physrevlett.126.141801](https://doi.org/10.1103/physrevlett.126.141801).
- [122] T. Aoyama et al. "The anomalous magnetic moment of the muon in the Standard Model". In: *Phys. Rept.* 887 (2020), pp. 1–166. doi: [10.1016/j.physrep.2020.07.006](https://doi.org/10.1016/j.physrep.2020.07.006). arXiv: [2006.04822 \[hep-ph\]](https://arxiv.org/abs/2006.04822).
- [123] L. Di Luzio et al. "Maximal flavour violation: a Cabibbo mechanism for leptoquarks". In: *JHEP* 11 (2018), p. 081. doi: [10.1007/JHEP11\(2018\)081](https://doi.org/10.1007/JHEP11(2018)081). arXiv: [1808.00942 \[hep-ph\]](https://arxiv.org/abs/1808.00942).
- [124] D. A. Faroughy, A. Greljo, and J. F. Kamenik. "Confronting lepton flavor universality violation in B decays with high- $p_T$  tau lepton searches at LHC". In: *Phys. Lett. B* 764 (2017), pp. 126–134. doi: [10.1016/j.physletb.2016.11.011](https://doi.org/10.1016/j.physletb.2016.11.011). arXiv: [1609.07138 \[hep-ph\]](https://arxiv.org/abs/1609.07138).
- [125] M. J. Baker et al. "High- $p_T$  signatures in vector-leptoquark models". In: *Eur. Phys. J. C* 79.4 (2019), p. 334. doi: [10.1140/epjc/s10052-019-6853-x](https://doi.org/10.1140/epjc/s10052-019-6853-x). arXiv: [1901.10480 \[hep-ph\]](https://arxiv.org/abs/1901.10480).
- [126] Glen Cowan et al. "Asymptotic formulae for likelihood-based tests of new physics". In: *Eur. Phys. J. C* 71 (2011). [Erratum: *Eur.Phys.J.C* 73, 2501 (2013)], p. 1554. doi: [10.1140/epjc/s10052-011-1554-0](https://doi.org/10.1140/epjc/s10052-011-1554-0). arXiv: [1007.1727 \[physics.data-an\]](https://arxiv.org/abs/1007.1727).
- [127] J. Alwall et al. "The automated computation of tree-level and next-to-leading order differential cross sections, and their matching to parton shower simulations". In: *JHEP* 07 (2014), p. 079. doi: [10.1007/JHEP07\(2014\)079](https://doi.org/10.1007/JHEP07(2014)079). arXiv: [1405.0301 \[hep-ph\]](https://arxiv.org/abs/1405.0301).
- [128] A. Alloul et al. "FeynRules 2.0 - A complete toolbox for tree-level phenomenology". In: *Comput. Phys. Commun.* 185 (2014), pp. 2250–2300. doi: [10.1016/j.cpc.2014.04.012](https://doi.org/10.1016/j.cpc.2014.04.012). arXiv: [1310.1921 \[hep-ph\]](https://arxiv.org/abs/1310.1921).
- [129] DELPHES 3 Collaboration. "DELPHES 3, A modular framework for fast simulation of a generic collider experiment". In: *JHEP* 02 (2014), p. 057. doi: [10.1007/JHEP02\(2014\)057](https://doi.org/10.1007/JHEP02(2014)057). arXiv: [1307.6346 \[hep-ex\]](https://arxiv.org/abs/1307.6346).
- [130] Georges Aad et al. "Search for high-mass dilepton resonances using  $139 \text{ fb}^{-1}$  of pp collision data collected at  $\sqrt{s} = 13$  TeV with the ATLAS detector". In: *Phys. Lett. B* 796 (2019), pp. 68–87. doi: [10.1016/j.physletb.2019.07.016](https://doi.org/10.1016/j.physletb.2019.07.016). arXiv: [1903.06248 \[hep-ex\]](https://arxiv.org/abs/1903.06248).

- [131] Albert M Sirunyan et al. "Search for resonant and nonresonant new phenomena in high-mass dilepton final states at  $\sqrt{s} = 13$  TeV". In: *JHEP* 07 (2021), p. 208. DOI: [10.1007/JHEP07\(2021\)208](https://doi.org/10.1007/JHEP07(2021)208). arXiv: [2103.02708 \[hep-ex\]](https://arxiv.org/abs/2103.02708).
- [132] S. Schael et al. "Measurement of the W boson mass and width in e+e- collisions at LEP". In: *The European Physical Journal C* 47.2 (2006), pp. 309–335. DOI: [10.1140/epjc/s2006-02576-8](https://doi.org/10.1140/epjc/s2006-02576-8).
- [133] T. Sjöstrand et al. "An introduction to PYTHIA 8.2". In: *Comput. Phys. Commun.* 191 (2015), pp. 159–177. DOI: [10.1016/j.cpc.2015.01.024](https://doi.org/10.1016/j.cpc.2015.01.024). arXiv: [1410.3012 \[hep-ph\]](https://arxiv.org/abs/1410.3012).
- [134] M. Cacciari, G. P. Salam, and G. Soyez. "FastJet User Manual". In: *Eur. Phys. J. C* 72 (2012), p. 1896. DOI: [10.1140/epjc/s10052-012-1896-2](https://doi.org/10.1140/epjc/s10052-012-1896-2). arXiv: [1111.6097 \[hep-ph\]](https://arxiv.org/abs/1111.6097).
- [135] NNPDF Collaboration. "Parton distributions for the LHC Run II". In: *JHEP* 04 (2015), p. 040. DOI: [10.1007/JHEP04\(2015\)040](https://doi.org/10.1007/JHEP04(2015)040). arXiv: [1410.8849 \[hep-ph\]](https://arxiv.org/abs/1410.8849).
- [136] G. Aad et al. "The ATLAS Experiment at the CERN Large Hadron Collider". In: *JINST* 3 (2008), S08003. DOI: [10.1088/1748-0221/3/08/S08003](https://doi.org/10.1088/1748-0221/3/08/S08003).
- [137] S. Chatrchyan et al. "The CMS Experiment at the CERN LHC". In: *JINST* 3 (2008), S08004. DOI: [10.1088/1748-0221/3/08/S08004](https://doi.org/10.1088/1748-0221/3/08/S08004).
- [138] Paul Lujan et al. *The Pixel Luminosity Telescope: A detector for luminosity measurement at CMS using silicon pixel sensors*. Tech. rep. CMS-DN-21-008. Accepted by *Eur. Phys. J. C*. 2022. arXiv: [2206.08870 \[physics.ins-det\]](https://arxiv.org/abs/2206.08870). URL: <https://arxiv.org/abs/2206.08870>.
- [139] F. Pedregosa et al. "Scikit-learn: Machine Learning in Python". In: *J. Mach. Learn. Res.* 12 (2011), pp. 2825–2830. ISSN: 1532-4435. DOI: [10.48550/arXiv.1201.0490](https://doi.org/10.48550/arXiv.1201.0490).
- [140] T. Chen and C. Guestrin. "XGBoost: A Scalable Tree Boosting System". In: *Proceedings of the 22nd ACM SIGKDD International Conference on Knowledge Discovery and Data Mining*. KDD '16. San Francisco, California, USA: ACM, 2016, pp. 785–794. ISBN: 978-1-4503-4232-2. DOI: [10.1145/2939672.2939785](https://doi.org/10.1145/2939672.2939785).
- [141] E. Bols et al. "Jet flavour classification using DeepJet". In: *Journal of Instrumentation* 15.12 (2020), P12012. DOI: [10.1088/1748-0221/15/12/P12012](https://doi.org/10.1088/1748-0221/15/12/P12012).
- [142] CMS Collaboration. "Identification of hadronic tau lepton decays using a deep neural network". In: *JINST* 17.07 (2022), Po7023. DOI: [10.1088/1748-0221/17/07/P07023](https://doi.org/10.1088/1748-0221/17/07/P07023). arXiv: [2201.08458 \[hep-ex\]](https://arxiv.org/abs/2201.08458).
- [143] Lyndon Evans and Philip Bryant. "LHC Machine". In: *Journal of Instrumentation* 3.08 (2008), S08001–S08001. DOI: [10.1088/1748-0221/3/08/S08001](https://doi.org/10.1088/1748-0221/3/08/S08001).

- [144] ATLAS Collaboration. “Observation of a new particle in the search for the Standard Model Higgs boson with the ATLAS detector at the LHC”. In: *Physics Letters B* 716 (2012). ATLAS Higgs-discovery paper; verify metadata if needed, pp. 1–29. doi: [10.1016/j.physletb.2012.08.020](https://doi.org/10.1016/j.physletb.2012.08.020).
- [145] CMS Collaboration. “Observation of a new boson at a mass of 125 GeV with the CMS experiment at the LHC”. In: *Physics Letters B* 716 (2012). CMS Higgs-discovery paper; verify metadata if needed, pp. 30–61. doi: [10.1016/j.physletb.2012.08.021](https://doi.org/10.1016/j.physletb.2012.08.021).
- [146] CMS Collaboration. *Study of the Discovery Reach in Searches for Supersymmetry at CMS with 3000/fb*. CMS Physics Analysis Summary CMS-PAS-FTR-13-014. Accessed on January 07, 2023. CERN, 2013. URL: <https://cds.cern.ch/record/1607141>.
- [147] G. Apollinari et al. *High-Luminosity Large Hadron Collider (HL-LHC): Technical and performance projections*. Tech. rep. CERN Yellow Report / TBD. HL-LHC technical design / projection report; please verify exact report number/title and replace placeholder fields as desired. CERN, 2017.
- [148] D. Bertolini et al. “Pileup Per Particle Identification”. In: *JHEP* 10 (2014). Introduces the PUPPI algorithm for per-particle pileup mitigation; ampliamente usado en ATLAS/CMS analyses., p. 59. arXiv: [1407.6013 \[hep-ph\]](https://arxiv.org/abs/1407.6013).
- [149] Matteo Cacciari, Gavin P. Salam, and Gregory Soyez. “The anti- $k_t$  jet clustering algorithm”. In: *Journal of High Energy Physics* 2008.04 (2008), p. 063. doi: [10.1088/1126-6708/2008/04/063](https://doi.org/10.1088/1126-6708/2008/04/063).
- [150] Izaak Neutelings. *CMS coordinate system*. URL: [https://tikz.net/axis3d\\_cms](https://tikz.net/axis3d_cms).
- [151] CMS Collaboration. “Particle-flow reconstruction and global event description with the CMS detector”. In: *JINST* 12 (2017). Resumen del algoritmo de reconstrucción particle-flow utilizado en CMS; útil para la discusión de PF en el texto., P10003.
- [152] A.M. Sirunyan et al. “Electron and photon reconstruction and identification with the CMS experiment at the CERN LHC”. In: *JINST* 16.05 (2021), Po5014. doi: [10.1088/1748-0221/16/05/P05014](https://doi.org/10.1088/1748-0221/16/05/P05014).
- [153] A.M. Sirunyan et al. “Performance of the reconstruction and identification of high-momentum muons in proton-proton collisions at  $\sqrt{s} = 13$  TeV”. In: *JINST* 15.02 (2020), Po2027. doi: [10.1088/1748-0221/15/02/P02027](https://doi.org/10.1088/1748-0221/15/02/P02027).
- [154] André Rubbia. *Phenomenology of Particle Physics*. Cambridge, UK: Cambridge University Press, June 2022. ISBN: 978-1-316-51934-9, 978-1-009-02342-9.

- [155] The CMS Collaboration. “Description and performance of track and primary-vertex reconstruction with the CMS tracker”. In: *Journal of Instrumentation* 9.10 (Oct. 2014), P10009–P10009. ISSN: 1748-0221. DOI: [10.1088/1748-0221/9/10/p10009](https://doi.org/10.1088/1748-0221/9/10/p10009).
- [156] John C. Collins, Davison E. Soper, and George F. Sterman. “Factorization of Hard Processes in QCD”. In: *Adv. Ser. Direct. High Energy Phys.* 5 (1989), pp. 1–91. DOI: [10.1142/9789814503266\\_0001](https://doi.org/10.1142/9789814503266_0001). arXiv: [hep-ph/0409313](https://arxiv.org/abs/hep-ph/0409313).
- [157] J. Butterworth, S. Carrazza, A. Cooper-Sarkar, A. De Roeck, J. Feltesse, S. Forte, J. Gao, S. Glazov, J. Huston, Z. Kassabov, R. McNulty, A. Morsch, P. Nadolsky, V. Radescu, J. Rojo and R. Thorne. “PDF4LHC recommendations for LHC Run II”. In: *J. Phys. G* 43 (2016), p. 023001. DOI: [10.1088/0954-3899/43/2/023001](https://doi.org/10.1088/0954-3899/43/2/023001). arXiv: [1510.03865 \[hep-ph\]](https://arxiv.org/abs/1510.03865).
- [158] Albert M Sirunyan et al. “Performance of missing transverse momentum reconstruction in proton-proton collisions at  $\sqrt{s} = 13$  TeV using the CMS detector”. In: *JINST* 14.07 (2019), Po7004. DOI: [10.1088/1748-0221/14/07/P07004](https://doi.org/10.1088/1748-0221/14/07/P07004). arXiv: [1903.06078 \[hep-ex\]](https://arxiv.org/abs/1903.06078).
- [159] Lawrence Lee et al. “Collider Searches for Long-Lived Particles Beyond the Standard Model”. In: *Prog. Part. Nucl. Phys.* 106 (2019). [Erratum: *Prog. Part. Nucl. Phys.* 122, 103912 (2022)], pp. 210–255. DOI: [10.1016/j.ppnp.2019.02.006](https://doi.org/10.1016/j.ppnp.2019.02.006). arXiv: [1810.12602 \[hep-ph\]](https://arxiv.org/abs/1810.12602).
- [160] William R. Leo. *Techniques for Nuclear and Particle Physics Experiments*. Springer, 1994. ISBN: 978-3-540-57280-0, 978-3-642-57920-2. DOI: [10.1007/978-3-642-57920-2](https://doi.org/10.1007/978-3-642-57920-2).
- [161] Alexander L. Read. “Presentation of search results: The  $CL_s$  technique”. In: *J. Phys. G* 28 (2002). Ed. by M. R. Whalley and L. Lyons, pp. 2693–2704. DOI: [10.1088/0954-3899/28/10/313](https://doi.org/10.1088/0954-3899/28/10/313).
- [162] Wolfgang A. Rolke, Angel M. López, and Jan Conrad. “Limits and confidence intervals in the presence of nuisance parameters”. In: *Nuclear Instruments and Methods in Physics Research Section A: Accelerators, Spectrometers, Detectors and Associated Equipment* 551.2–3 (Oct. 2005), 493–503. ISSN: 0168-9002. DOI: [10.1016/j.nima.2005.05.068](https://doi.org/10.1016/j.nima.2005.05.068).
- [163] Gary J. Feldman and Robert D. Cousins. “Unified approach to the classical statistical analysis of small signals”. In: *Physical Review D* 57.7 (Apr. 1998), 3873–3889. ISSN: 1089-4918. DOI: [10.1103/physrevd.57.3873](https://doi.org/10.1103/physrevd.57.3873).
- [164] Alejandro Segura and Angie Catalina Parra. “A Practical Guide to Statistical Techniques in Particle Physics”. In: (Nov. 2024). arXiv: [2411.00706 \[hep-ph\]](https://arxiv.org/abs/2411.00706).
- [165] Bo Andersson et al. “Parton Fragmentation and String Dynamics”. In: *Phys. Rept.* 97 (1983), pp. 31–145. DOI: [10.1016/0370-1573\(83\)90080-7](https://doi.org/10.1016/0370-1573(83)90080-7).

- [166] B. R. Webber. "A QCD Model for Jet Fragmentation Including Soft Gluon Interference". In: *Nucl. Phys. B* 238 (1984), pp. 492–528. doi: [10.1016/0550-3213\(84\)90333-X](https://doi.org/10.1016/0550-3213(84)90333-X).
- [167] Gavin P. Salam. "Towards Jetography". In: *Eur. Phys. J. C* 67 (2010), pp. 637–686. doi: [10.1140/epjc/s10052-010-1314-6](https://doi.org/10.1140/epjc/s10052-010-1314-6). arXiv: [0906.1833 \[hep-ph\]](https://arxiv.org/abs/0906.1833).
- [168] S. Catani et al. "Longitudinally invariant  $K_t$  clustering algorithms for hadron hadron collisions". In: *Nucl. Phys. B* 406 (1993), pp. 187–224. doi: [10.1016/0550-3213\(93\)90166-M](https://doi.org/10.1016/0550-3213(93)90166-M).
- [169] Stephen D. Ellis and Davison E. Soper. "Successive combination jet algorithm for hadron collisions". In: *Phys. Rev. D* 48 (1993), pp. 3160–3166. doi: [10.1103/PhysRevD.48.3160](https://doi.org/10.1103/PhysRevD.48.3160). arXiv: [hep-ph/9305266](https://arxiv.org/abs/hep-ph/9305266).
- [170] Yuri L. Dokshitzer et al. "Better jet clustering algorithms". In: *JHEP* 08 (1997), p. 001. doi: [10.1088/1126-6708/1997/08/001](https://doi.org/10.1088/1126-6708/1997/08/001). arXiv: [hep-ph/9707323](https://arxiv.org/abs/hep-ph/9707323).
- [171] Jesse Thaler and Ken Van Tilburg. "Identifying Boosted Objects with N-subjettiness". In: *JHEP* 03 (2011), p. 015. doi: [10.1007/JHEP03\(2011\)015](https://doi.org/10.1007/JHEP03(2011)015). arXiv: [1011.2268 \[hep-ph\]](https://arxiv.org/abs/1011.2268).
- [172] M. Cacciari, G. P. Salam, and G. Soyez. "The catchment area of jets". In: *JHEP* 04 (2008). Detalla conceptos de área de jets y técnicas relacionadas con la resta de pile-up., p. 005. doi: [10.1088/1126-6708/2008/04/005](https://doi.org/10.1088/1126-6708/2008/04/005).
- [173] Garvita Agarwal. "Jet Energy Scale and Resolution Measurements in CMS". In: *PoS ICHEP2022* (2022), p. 652. doi: [10.22323/1.414.0652](https://doi.org/10.22323/1.414.0652). arXiv: [2301.02175 \[hep-ex\]](https://arxiv.org/abs/2301.02175).
- [174] Jonathan M. Butterworth et al. "Jet substructure as a new Higgs search channel at the LHC". In: *Phys. Rev. Lett.* 100 (2008), p. 242001. doi: [10.1103/PhysRevLett.100.242001](https://doi.org/10.1103/PhysRevLett.100.242001). arXiv: [0802.2470 \[hep-ph\]](https://arxiv.org/abs/0802.2470).
- [175] Andrew J. Larkoski et al. "Soft Drop". In: *JHEP* 05 (2014), p. 146. doi: [10.1007/JHEP05\(2014\)146](https://doi.org/10.1007/JHEP05(2014)146). arXiv: [1402.2657 \[hep-ph\]](https://arxiv.org/abs/1402.2657).
- [176] A. M. Sirunyan et al. "Performance of reconstruction and identification of  $\tau$  leptons decaying to hadrons and  $\nu_\tau$  in pp collisions at  $\sqrt{s} = 13$  TeV". In: *JINST* 13.10 (2018), P10005. doi: [10.1088/1748-0221/13/10/P10005](https://doi.org/10.1088/1748-0221/13/10/P10005). arXiv: [1809.02816 \[hep-ex\]](https://arxiv.org/abs/1809.02816).
- [177] Georges Aad et al. "Identification and energy calibration of hadronically decaying tau leptons with the ATLAS experiment in pp collisions at  $\sqrt{s}=8$  TeV". In: *Eur. Phys. J. C* 75.7 (2015), p. 303. doi: [10.1140/epjc/s10052-015-3500-z](https://doi.org/10.1140/epjc/s10052-015-3500-z). arXiv: [1412.7086 \[hep-ex\]](https://arxiv.org/abs/1412.7086).
- [178] CMS Collaboration. "Performance of the CMS Level-1 trigger in proton-proton collisions at  $\sqrt{s} = 13$  TeV". In: *J. Inst.* 17.05 (2022), P05024. doi: [10.31526/lhep.2022.195](https://doi.org/10.31526/lhep.2022.195). arXiv: [2202.08678 \[hep-ex\]](https://arxiv.org/abs/2202.08678).

- [179] CMS Collaboration. “Identification of heavy-flavour jets with the CMS detector in pp collisions at 13 TeV”. In: *JINST* 13.04 (2018), P05011. doi: [10.1088/1748-0221/13/05/P05011](https://doi.org/10.1088/1748-0221/13/05/P05011). arXiv: [1712.07158](https://arxiv.org/abs/1712.07158) [hep-ex].
- [180] The CMS Collaboration. “The CMS experiment at the CERN LHC”. In: *Journal of Instrumentation* 3.08 (2008), S08004–S08004. doi: [10.1088/1748-0221/3/08/s08004](https://doi.org/10.1088/1748-0221/3/08/s08004).
- [181] N. D. Christensen and C. Duhr. “FeynRules - Feynman rules made easy”. In: *Comput. Phys. Commun.* 180 (2009), pp. 1614–1641. doi: [10.1016/j.cpc.2009.02.018](https://doi.org/10.1016/j.cpc.2009.02.018). arXiv: [0806.4194](https://arxiv.org/abs/0806.4194) [hep-ph].
- [182] Celine Degrande et al. “UFO - The Universal FeynRules Output”. In: *Comput. Phys. Commun.* 183 (2012), pp. 1201–1214. doi: [10.1016/j.cpc.2012.01.022](https://doi.org/10.1016/j.cpc.2012.01.022). arXiv: [1108.2040](https://arxiv.org/abs/1108.2040) [hep-ph].
- [183] Florian Staub. “SARAH 4: A tool for (not only SUSY) model builders”. In: *Comput. Phys. Commun.* 185 (2014), pp. 1773–1790. doi: [10.1016/j.cpc.2014.02.018](https://doi.org/10.1016/j.cpc.2014.02.018). arXiv: [1309.7223](https://arxiv.org/abs/1309.7223) [hep-ph].
- [184] Werner Porod. “SPheno, a program for calculating supersymmetric spectra, SUSY particle decays and SUSY particle production at e+ e- colliders”. In: *Comput. Phys. Commun.* 153 (2003), pp. 275–315. doi: [10.1016/S0010-4655\(03\)00222-4](https://doi.org/10.1016/S0010-4655(03)00222-4). arXiv: [hep-ph/0301101](https://arxiv.org/abs/hep-ph/0301101) [hep-ph].
- [185] P. Bechtle et al. “HiggsBounds-5: Testing Higgs Sectors in the LHC 13 TeV Era”. In: *Eur. Phys. J. C* 80 (2020), p. 1211. doi: [10.1140/epjc/s10052-020-08557-9](https://doi.org/10.1140/epjc/s10052-020-08557-9). arXiv: [2006.06007](https://arxiv.org/abs/2006.06007) [hep-ph].
- [186] Werner Porod, Florian Staub, and Avelino Vicente. “A Flavor Kit for BSM models”. In: *Eur. Phys. J. C* 74 (2014), p. 2992. doi: [10.1140/epjc/s10052-014-2992-2](https://doi.org/10.1140/epjc/s10052-014-2992-2). arXiv: [1405.1434](https://arxiv.org/abs/1405.1434) [hep-ph].
- [187] G. Bélanger et al. “micrOMEGAs5.2: A tool for dark matter studies”. In: *Comput. Phys. Commun.* 231 (2018), pp. 173–186. doi: [10.1016/j.cpc.2018.04.027](https://doi.org/10.1016/j.cpc.2018.04.027). arXiv: [1801.03509](https://arxiv.org/abs/1801.03509) [hep-ph].
- [188] J. Alwall et al. “Computing decay rates for new physics theories with FeynRules and MadGraph 5\_aMC@NLO”. In: *Comput. Phys. Commun.* 197 (2015), pp. 312–323. doi: [10.1016/j.cpc.2015.08.031](https://doi.org/10.1016/j.cpc.2015.08.031). arXiv: [1402.1178](https://arxiv.org/abs/1402.1178) [hep-ph].
- [189] Johan Alwall et al. “Comparative study of various algorithms for the merging of parton showers and matrix elements in hadronic collisions”. In: *Eur. Phys. J. C* 53 (2008), pp. 473–500. doi: [10.1140/epjc/s10052-007-0490-5](https://doi.org/10.1140/epjc/s10052-007-0490-5). arXiv: [0706.2569](https://arxiv.org/abs/0706.2569) [hep-ph].
- [190] Andy Buckley et al. “LHAPDF6: parton density access in the LHC precision era”. In: *Eur. Phys. J. C* 75 (2015), p. 132. doi: [10.1140/epjc/s10052-015-3318-8](https://doi.org/10.1140/epjc/s10052-015-3318-8). arXiv: [1412.7420](https://arxiv.org/abs/1412.7420) [hep-ph].

- [191] Rene Brun and Fons Rademakers. "ROOT — An object oriented data analysis framework". In: *Nucl. Instrum. Meth. A* 389.1-2 (1997). Ed. by M. Werlen and D. Perret-Gallix, pp. 81–86. DOI: [10.1016/s0168-9002\(97\)00048-x](https://doi.org/10.1016/s0168-9002(97)00048-x).
- [192] Wes McKinney. "Data structures for statistical computing in Python". In: *Proceedings of the 9th Python in Science Conference*. Vol. 445. Austin, TX. 2010, pp. 51–56.
- [193] T. Chen and C. Guestrin. "XGBoost: A scalable tree boosting system". In: *Proceedings of the 22nd ACM SIGKDD International Conference on Knowledge Discovery and Data Mining*. KDD '16. New York, NY, USA: Association for Computing Machinery, 2016, pp. 785–794. ISBN: 978-1-4503-4232-2. DOI: [10.1145/2939672.2939785](https://doi.org/10.1145/2939672.2939785). (Visited on 09/05/2022).
- [194] L. Moneta et al. "The RooStats Project". In: *PoS ACAT2010* (2010), p. 057. DOI: [10.22323/1.093.0057](https://doi.org/10.22323/1.093.0057). arXiv: [1009.1003 \[physics.data-an\]](https://arxiv.org/abs/1009.1003).
- [195] Steve Baker and Robert D. Cousins. "Clarification of the Use of Chi Square and Likelihood Functions in Fits to Histograms". In: *Nucl. Instrum. Meth.* 221 (1984), pp. 437–442. DOI: [10.1016/0167-5087\(84\)90016-4](https://doi.org/10.1016/0167-5087(84)90016-4).
- [196] Jerzy Neyman and Egon Sharpe Pearson. "On the Problem of the Most Efficient Tests of Statistical Hypotheses". In: *Phil. Trans. Roy. Soc. Lond. A* 231.694-706 (1933), pp. 289–337. DOI: [10.1098/rsta.1933.0009](https://doi.org/10.1098/rsta.1933.0009).
- [197] S. S. Wilks. "The Large-Sample Distribution of the Likelihood Ratio for Testing Composite Hypotheses". In: *Annals Math. Statist.* 9.1 (1938), pp. 60–62. DOI: [10.1214/aoms/1177732360](https://doi.org/10.1214/aoms/1177732360).
- [198] Dan Guest, Kyle Cranmer, and Daniel Whiteson. "Deep Learning and its Application to LHC Physics". In: *Ann. Rev. Nucl. Part. Sci.* 68 (2018), pp. 161–181. DOI: [10.1146/annurev-nucl-101917-021019](https://doi.org/10.1146/annurev-nucl-101917-021019). arXiv: [1806.11484 \[hep-ex\]](https://arxiv.org/abs/1806.11484).
- [199] Trevor Hastie, Robert Tibshirani, and Jerome Friedman. *The Elements of Statistical Learning*. Springer, 2009. ISBN: 978-0-387-84857-0, 978-0-387-84858-7. DOI: [10.1007/978-0-387-84858-7](https://doi.org/10.1007/978-0-387-84858-7).
- [200] A. Hoecker et al. *TMVA - Toolkit for Multivariate Data Analysis*. 2009. arXiv: [physics/0703039 \[physics.data-an\]](https://arxiv.org/abs/physics/0703039).
- [201] J. H. Friedman. "Greedy function approximation: A gradient boosting machine." In: *The Annals of Statistics* 29.5 (2001). Publisher: Institute of Mathematical Statistics, pp. 1189–1232. ISSN: 0090-5364, 2168-8966. DOI: [10.1214/aos/1013203451](https://doi.org/10.1214/aos/1013203451). (Visited on 09/05/2022).
- [202] Kyle Cranmer, Juan Pavez, and Gilles Louppe. "Approximating Likelihood Ratios with Calibrated Discriminative Classifiers". In: (June 2015). arXiv: [1506.02169 \[stat.AP\]](https://arxiv.org/abs/1506.02169).

- [203] John Platt. *Probabilistic Outputs for Support Vector Machines and Comparisons to Regularized Likelihood Methods*. Tech. rep. Microsoft Research, 1999.
- [204] Corinna Cortes and Vladimir Vapnik. "Support-vector networks". In: *Machine Learning* 20.3 (1995), pp. 273–297. doi: [10.1007/BF00994018](https://doi.org/10.1007/BF00994018).
- [205] Leo Breiman. "Random Forests". In: *Machine Learning* 45.1 (2001), pp. 5–32. doi: [10.1023/A:1010933404324](https://doi.org/10.1023/A:1010933404324).
- [206] Steven Weinberg. "Baryon and Lepton Nonconserving Processes". In: *Phys. Rev. Lett.* 43 (1979), pp. 1566–1570. doi: [10.1103/PhysRevLett.43.1566](https://doi.org/10.1103/PhysRevLett.43.1566).
- [207] Frank Wilczek and A. Zee. "Operator Analysis of Nucleon Decay". In: *Phys. Rev. Lett.* 43 (1979), pp. 1571–1573. doi: [10.1103/PhysRevLett.43.1571](https://doi.org/10.1103/PhysRevLett.43.1571).
- [208] Robert Eugene Marshak and Rabindra N. Mohapatra. "Quark - Lepton Symmetry and B-L as the U(1) Generator of the Electroweak Symmetry Group". In: *Phys. Lett. B* 91 (1980), pp. 222–224. doi: [10.1016/0370-2693\(80\)90703-6](https://doi.org/10.1016/0370-2693(80)90703-6).
- [209] Rabindra N. Mohapatra and Robert Eugene Marshak. "Local B-L Symmetry of Electroweak Interactions, Majorana Neutrinos and Neutron Oscillations". In: *Phys. Rev. Lett.* 44 (1980). Erratum: *Phys. Rev. Lett.* 44, 1643 (1980), pp. 1316–1319. doi: [10.1103/PhysRevLett.44.1316](https://doi.org/10.1103/PhysRevLett.44.1316).
- [210] W. Buchmuller, R. D. Peccei, and T. Yanagida. "Leptogenesis as the origin of matter". In: *Ann. Rev. Nucl. Part. Sci.* 55 (2005), pp. 311–355. doi: [10.1146/annurev.nucl.55.090704.151558](https://doi.org/10.1146/annurev.nucl.55.090704.151558). arXiv: [hep-ph/0502169](https://arxiv.org/abs/hep-ph/0502169).
- [211] Stephen L. Adler. "Axial vector vertex in spinor electrodynamics". In: *Phys. Rev.* 177 (1969), pp. 2426–2438. doi: [10.1103/PhysRev.177.2426](https://doi.org/10.1103/PhysRev.177.2426).
- [212] J. S. Bell and R. Jackiw. "A PCAC puzzle:  $\text{pio} \rightarrow \text{gamma gamma}$  in the sigma model". In: *Nuovo Cim. A* 60 (1969), pp. 47–61. doi: [10.1007/BF02823296](https://doi.org/10.1007/BF02823296).
- [213] Gerard 't Hooft. "Naturalness, chiral symmetry, and spontaneous chiral symmetry breaking". In: *NATO Sci. Ser. B* 59 (1980), pp. 135–157. doi: [10.1007/978-1-4684-7571-5\\_9](https://doi.org/10.1007/978-1-4684-7571-5_9).
- [214] H. Fritzsch and P. Minkowski. "Unified Interactions of Leptons and Hadrons". In: *Annals Phys.* 93 (1975), pp. 193–266. doi: [10.1016/0003-4916\(75\)90211-0](https://doi.org/10.1016/0003-4916(75)90211-0).
- [215] H. Georgi and S. L. Glashow. "Unity of all elementary particle forces". In: *Phys. Rev. Lett.* 32 (1974), pp. 438–441. doi: [10.1103/PhysRevLett.32.438](https://doi.org/10.1103/PhysRevLett.32.438).

- [216] J. C. Pati and A. Salam. "Lepton number as the fourth color". In: *Phys. Rev. D* 10 (1974). [Erratum: Phys.Rev.D 11, 703-703 (1975)], pp. 275–289. doi: [10.1103/PhysRevD.10.275](https://doi.org/10.1103/PhysRevD.10.275).
- [217] Rabindra N. Mohapatra and Jogesh C. Pati. "Left-Right Gauge Symmetry and an Isoconjugate Model of CP Violation". In: *Phys. Rev. D* 11 (1975), pp. 566–571. doi: [10.1103/PhysRevD.11.566](https://doi.org/10.1103/PhysRevD.11.566).
- [218] G. Senjanovic. "Spontaneous Breakdown of Parity in a Class of Gauge Theories". In: *Nucl. Phys. B* 153 (1979), pp. 334–364. doi: [10.1016/0550-3213\(79\)90604-7](https://doi.org/10.1016/0550-3213(79)90604-7).
- [219] N. Assad, B. Fornal, and B. Grinstein. "Baryon Number and Lepton Universality Violation in Leptoquark and Diquark Models". In: *Phys. Lett. B* 777 (2018), pp. 324–331. doi: [10.1016/j.physletb.2017.12.042](https://doi.org/10.1016/j.physletb.2017.12.042). arXiv: [1708.06350](https://arxiv.org/abs/1708.06350) [hep-ph].
- [220] R. N. Mohapatra and J. C. Pati. "'Natural' left-right symmetry". In: *Physical Review D* 11.9 (May 1975), pp. 2558–2561. doi: [10.1103/PhysRevD.11.2558](https://doi.org/10.1103/PhysRevD.11.2558).
- [221] G. Senjanovic and R. N. Mohapatra. "Exact left-right symmetry and spontaneous violation of parity". In: *Physical Review D* 12.5 (Sept. 1975), pp. 1502–1505. doi: [10.1103/PhysRevD.12.1502](https://doi.org/10.1103/PhysRevD.12.1502).
- [222] Bhaskar Dutta et al. "Explaining  $g_\mu - 2$  and  $R_{K^{(*)}}$  using the light mediators of  $U(1)_{T3R}$ ". In: *Physical Review D* 105.1 (Jan. 2022), p. 015011. doi: [10.1103/PhysRevD.105.015011](https://doi.org/10.1103/PhysRevD.105.015011).
- [223] Bhaskar Dutta, Sumit Ghosh, and Jason Kumar. "Sub-GeV dark matter model". In: *Physical Review D* 100.7 (Oct. 2019), p. 075028. doi: [10.1103/PhysRevD.100.075028](https://doi.org/10.1103/PhysRevD.100.075028).
- [224] Bhaskar Dutta, Sumit Ghosh, and Jason Kumar. "Contributions to  $N_{\text{eff}}$  from the dark photon of  $U(1)_{T3R}$ ". In: *Physical Review D* 102.1 (July 2020), p. 015013. doi: [10.1103/PhysRevD.102.015013](https://doi.org/10.1103/PhysRevD.102.015013).
- [225] Bhaskar Dutta, Sumit Ghosh, and Jason Kumar. " $U(1)_{T3R}$  Extension of Standard Model: A Sub-GeV Dark Matter Model". In: *Snowmass 2021*. Mar. 2022. arXiv: [2203.07786](https://arxiv.org/abs/2203.07786) [hep-ph].
- [226] Luca Di Luzio et al. "Maximal flavour violation: a Cabibbo mechanism for leptoquarks". In: *Journal of High Energy Physics* 2018.11 (Nov. 13, 2018), p. 81. ISSN: 1029-8479. doi: [10.1007/JHEP11\(2018\)081](https://doi.org/10.1007/JHEP11(2018)081). URL: [https://doi.org/10.1007/JHEP11\(2018\)081](https://doi.org/10.1007/JHEP11(2018)081).
- [227] Michael J. Baker et al. "High-\$p\_T\$ signatures in vector-leptoquark models". In: *The European Physical Journal C* 79.4 (2019), p. 334. ISSN: 1434-6052. doi: [10.1140/epjc/s10052-019-6853-x](https://doi.org/10.1140/epjc/s10052-019-6853-x).
- [228] Lisa Michaels and Felix Yu. "Probing new  $U(1)$  gauge symmetries via exotic  $Z \rightarrow Z'\gamma$  decays". In: *JHEP* 03 (2021), p. 120. doi: [10.1007/JHEP03\(2021\)120](https://doi.org/10.1007/JHEP03(2021)120). arXiv: [2010.00021](https://arxiv.org/abs/2010.00021) [hep-ph].

- [229] P. S. Bhupal Dev et al. "Searching for Z' bosons at the P2 experiment". In: *JHEP* 06 (2021), p. 039. DOI: [10.1007/JHEP06\(2021\)039](https://doi.org/10.1007/JHEP06(2021)039). arXiv: [2103.09067 \[hep-ph\]](https://arxiv.org/abs/2103.09067).
- [230] Z.G. Berezhiani. "The weak mixing angles in gauge models with horizontal symmetry — A new approach to quark and lepton masses". In: *Physics Letters B* 129.1 (1983), pp. 99–102. ISSN: 0370-2693. DOI: [10.1016/0370-2693\(83\)90737-2](https://doi.org/10.1016/0370-2693(83)90737-2).
- [231] Darwin Chang and Rabindra N. Mohapatra. "Small and calculable Dirac neutrino mass". In: *Phys. Rev. Lett.* 58 (16 1987), pp. 1600–1603. DOI: [10.1103/PhysRevLett.58.1600](https://doi.org/10.1103/PhysRevLett.58.1600).
- [232] Aharon Davidson and Kameshwar C. Wali. "Universal seesaw mechanism?" In: *Phys. Rev. Lett.* 59 (4 1987), pp. 393–395. DOI: [10.1103/PhysRevLett.59.393](https://doi.org/10.1103/PhysRevLett.59.393).
- [233] S. Rajpoot. "See-Saw Masses for quarks and leptons in an ambidextrous electroweak interaction model". In: *Modern Physics Letters A* 02.05 (1987), pp. 307–315. DOI: [10.1142/S0217732387000422](https://doi.org/10.1142/S0217732387000422).
- [234] K. S. Babu and Rabindra N. Mohapatra. "CP violation in seesaw models of quark masses". In: *Phys. Rev. Lett.* 62 (10 1989), pp. 1079–1082. DOI: [10.1103/PhysRevLett.62.1079](https://doi.org/10.1103/PhysRevLett.62.1079).
- [235] K. S. Babu and Rabindra N. Mohapatra. "Solution to the strong CP problem without an axion". In: *Phys. Rev. D* 41 (4 1990), pp. 1286–1291. DOI: [10.1103/PhysRevD.41.1286](https://doi.org/10.1103/PhysRevD.41.1286).
- [236] Akanksha Bhardwaj et al. "Roadmap to explore vectorlike quarks decaying to a new scalar or pseudoscalar". In: *Physical Review D* 106.9 (Nov. 2022). ISSN: 2470-0029. DOI: [10.1103/physrevd.106.095014](https://doi.org/10.1103/physrevd.106.095014).
- [237] Akanksha Bhardwaj et al. "Discovery prospects of a vectorlike top partner decaying to a singlet boson". In: *Physical Review D* 106.7 (Oct. 2022). ISSN: 2470-0029. DOI: [10.1103/physrevd.106.075024](https://doi.org/10.1103/physrevd.106.075024).
- [238] Jai Bardhan et al. "Machine learning-enhanced search for a vectorlike singlet B quark decaying to a singlet scalar or pseudoscalar". In: *Physical Review D* 107.11 (June 2023). ISSN: 2470-0029. DOI: [10.1103/physrevd.107.115001](https://doi.org/10.1103/physrevd.107.115001).
- [239] Shankha Banerjee et al. "Implications of a high-mass diphoton resonance for heavy quark searches". In: *Journal of High Energy Physics* 2016.11 (Nov. 2016). ISSN: 1029-8479. DOI: [10.1007/jhep11\(2016\)154](https://doi.org/10.1007/jhep11(2016)154).
- [240] João M. Alves et al. "Vector-like singlet quarks: A roadmap". In: *Physics Reports* 1057 (Mar. 2024), 1–69. ISSN: 0370-1573. DOI: [10.1016/j.physrep.2023.12.004](https://doi.org/10.1016/j.physrep.2023.12.004).
- [241] X. Ai et al. "Probing highly collimated photon-jets with deep learning". In: *JPCS* 2438.1 (2023), p. 012114. DOI: [10.1088/1742-6596/2438/1/012114](https://doi.org/10.1088/1742-6596/2438/1/012114).

- [242] ATLAS Collaboration. “Search for the standard model Higgs boson produced in association with top quarks and decaying into a  $b\bar{b}$  pair in pp collisions at  $\sqrt{s} = 13$  TeV with the ATLAS detector”. In: *Phys. Rev. D* 97.7 (2018), p. 072016. DOI: [10.1103/PhysRevD.97.072016](https://doi.org/10.1103/PhysRevD.97.072016). arXiv: [1712.08895 \[hep-ex\]](https://arxiv.org/abs/1712.08895).
- [243] A. Biswas et al. “Collider signature of  $U_1$  leptoquark and constraints from  $b \rightarrow c$  observables”. In: *J. Phys. G* 47.4 (2020), p. 045005. DOI: [10.1088/1361-6471/ab6948](https://doi.org/10.1088/1361-6471/ab6948). arXiv: [1808.04169 \[hep-ph\]](https://arxiv.org/abs/1808.04169).
- [244] Y. L. Chung, S. C. Hsu, and B. Nachman. “Disentangling boosted Higgs boson production modes with machine learning”. In: *JINST* 16 (2021), Po7002. DOI: [10.1088/1748-0221/16/07/P07002](https://doi.org/10.1088/1748-0221/16/07/P07002). arXiv: [2009.05930 \[hep-ph\]](https://arxiv.org/abs/2009.05930).
- [245] J. Feng et al. “Improving heavy Dirac neutrino prospects at future hadron colliders using machine learning”. In: *JHEP* 2022.9 (2022). DOI: [10.1007/jhep09\(2022\)141](https://doi.org/10.1007/jhep09(2022)141).
- [246] D. Barbosa et al. “Probing a  $Z'$  with non-universal fermion couplings through top quark fusion, decays to bottom quarks, and machine learning techniques”. In: *EPJC* 83.413 (2023). DOI: [10.1140/epjc/s10052-023-11506-x](https://doi.org/10.1140/epjc/s10052-023-11506-x).
- [247] S. Chigusa et al. “Deeply learned preselection of Higgs dijet decays at future lepton colliders”. In: *Phys. Lett. B* 833 (2022), p. 137301. DOI: [10.1016/j.physletb.2022.137301](https://doi.org/10.1016/j.physletb.2022.137301). arXiv: [2202.02534 \[hep-ph\]](https://arxiv.org/abs/2202.02534).
- [248] Ernesto Arganda et al. “LHC study of third-generation scalar leptoquarks with machine-learned likelihoods”. In: *Phys. Rev. D* 109 (5 2024), p. 055032. DOI: [10.1103/PhysRevD.109.055032](https://doi.org/10.1103/PhysRevD.109.055032).
- [249] S. Ajmal et al. “Searching for exclusive leptoquarks with the Nambu-Jona-Lasinio composite model at the LHC and HL-LHC”. In: *Journal of High Energy Physics* 2024.8 (Aug. 2024). ISSN: 1029-8479. DOI: [10.1007/jhep08\(2024\)176](https://doi.org/10.1007/jhep08(2024)176).
- [250] Bhaskar Dutta et al. “Probing compressed bottom squarks with boosted jets and shape analysis”. In: *Physical Review D* 92.9 (Nov. 2015). ISSN: 1550-2368. DOI: [10.1103/physrevd.92.095009](https://doi.org/10.1103/physrevd.92.095009).
- [251] CMS Collaboration. *Review of searches for vector-like quarks, vector-like leptons, and heavy neutral leptons in proton-proton collisions at  $\sqrt{s} = 13$  TeV at the CMS experiment*. 2024. arXiv: [2405.17605 \[hep-ex\]](https://arxiv.org/abs/2405.17605).
- [252] CMS Collaboration. *Search for production of a single vector-like quark decaying to tH or tZ in the all-hadronic final state in pp collisions at  $\sqrt{s} = 13$  TeV*. 2024. arXiv: [2405.05071 \[hep-ex\]](https://arxiv.org/abs/2405.05071).
- [253] Georges Aad et al. “Search for single production of a vectorlike T quark decaying into a Higgs boson and top quark with fully hadronic final states using the ATLAS detector”. In: *Phys. Rev. D* 105.9 (2022), p. 092012. DOI: [10.1103/PhysRevD.105.092012](https://doi.org/10.1103/PhysRevD.105.092012). arXiv: [2201.07045 \[hep-ex\]](https://arxiv.org/abs/2201.07045).

- [254] Georges Aad et al. “Search for singly produced vectorlike top partners in multilepton final states with 139 fb<sup>-1</sup> of pp collision data at s=13 TeV with the ATLAS detector”. In: *Phys. Rev. D* 109.11 (2024), p. 112012. DOI: 10.1103/PhysRevD.109.112012. arXiv: 2307.07584 [hep-ex].
- [255] Georges Aad et al. “Search for pair-production of vector-like quarks in pp collision events at s=13 TeV with at least one leptonically decaying Z boson and a third-generation quark with the ATLAS detector”. In: *Phys. Lett. B* 843 (2023), p. 138019. DOI: 10.1016/j.physletb.2023.138019. arXiv: 2210.15413 [hep-ex].
- [256] Georges Aad et al. “Search for pair-produced vector-like top and bottom partners in events with large missing transverse momentum in pp collisions with the ATLAS detector”. In: *Eur. Phys. J. C* 83.8 (2023), p. 719. DOI: 10.1140/epjc/s10052-023-11790-7. arXiv: 2212.05263 [hep-ex].
- [257] Georges Aad et al. “Search for single production of vector-like T quarks decaying into Ht or Zt in pp collisions at  $\sqrt{s} = 13$  TeV with the ATLAS detector”. In: *JHEP* 08 (2023), p. 153. DOI: 10.1007/JHEP08(2023)153. arXiv: 2305.03401 [hep-ex].
- [258] Georges Aad et al. *Exploration at the high-energy frontier: ATLAS Run 2 searches investigating the exotic jungle beyond the Standard Model*. Mar. 2024. arXiv: 2403.09292 [hep-ex].
- [259] Giacomo Cacciapaglia et al. “Exotic decays of top partners: mind the search gap”. In: *Phys. Lett. B* 798 (2019), p. 135015. DOI: 10.1016/j.physletb.2019.135015. arXiv: 1908.07524 [hep-ph].
- [260] Bhaskar Dutta, Sumit Ghosh, and Jason Kumar. “Opportunities for probing U(1)<sub>T3R</sub> with light mediators”. In: *Physical Review D* 102.7 (Oct. 2020), p. 075041. DOI: 10.1103/PhysRevD.102.075041.
- [261] Bhaskar Dutta et al. “Probing an MeV-scale scalar boson in association with a TeV-Scale top-quark partner at the LHC”. In: *Journal of High Energy Physics* 2023.3 (Mar. 2023), p. 164. ISSN: 1029-8479. DOI: 10.1007/JHEP03(2023)164.
- [262] A. C. Canbay and O. Cakir. “Investigating the single production of vectorlike quarks decaying into a top quark and W boson through hadronic channels at the HL-LHC”. In: *Phys. Rev. D* 108 (9 2023), p. 095006. DOI: 10.1103/PhysRevD.108.095006.
- [263] Giacomo Cacciapaglia, Aldo Deandrea, and Shahram Vatani. “Is the muon a third family lepton?” In: *Physical Review D* 108.1 (July 2023). ISSN: 2470-0029. DOI: 10.1103/physrevd.108.016010.
- [264] Joel Jones-Perez. “RGE behaviour of U(2)<sup>3</sup> symmetry in SUSY”. In: *J. Phys. Conf. Ser.* 447 (2013). Ed. by Gustavo C. Branco et al., p. 012060. DOI: 10.1088/1742-6596/447/1/012060. arXiv: 1302.6133 [hep-ph].

- [265] L. Calibbi et al. “SU(3) Flavour Symmetries and CP Violation”. In: *PoS EPS-HEP2009* (2009), p. 167. doi: [10.22323/1.084.0167](https://doi.org/10.22323/1.084.0167). arXiv: [0909.2501 \[hep-ph\]](https://arxiv.org/abs/0909.2501).
- [266] Matteo Cacciari, Gavin P Salam, and Gregory Soyez. “The anti-k<sub>T</sub>jet clustering algorithm”. In: *Journal of High Energy Physics* 2008.04 (Apr. 2008), 063–063. issn: [1029-8479](https://doi.org/10.1088/1126-6708/2008/04/063). doi: [10.1088/1126-6708/2008/04/063](https://doi.org/10.1088/1126-6708/2008/04/063).
- [267] Matteo Cacciari, Gavin P. Salam, and Gregory Soyez. “FastJet user manual: (for version 3.0.2)”. In: *The European Physical Journal C* 72.3 (Mar. 2012). issn: [1434-6052](https://doi.org/10.1140/epjc/s10052-012-1896-2). doi: [10.1140/epjc/s10052-012-1896-2](https://doi.org/10.1140/epjc/s10052-012-1896-2).
- [268] Albert M Sirunyan et al. “Identification of heavy, energetic, hadronically decaying particles using machine-learning techniques”. In: *JINST* 15.06 (2020), Po6005. doi: [10.1088/1748-0221/15/06/P06005](https://doi.org/10.1088/1748-0221/15/06/P06005). arXiv: [2004.08262 \[hep-ex\]](https://arxiv.org/abs/2004.08262).
- [269] Morad Aaboud et al. “Performance of top-quark and W-boson tagging with ATLAS in Run 2 of the LHC”. In: *Eur. Phys. J. C* 79.5 (2019), p. 375. doi: [10.1140/epjc/s10052-019-6847-8](https://doi.org/10.1140/epjc/s10052-019-6847-8). arXiv: [1808.07858 \[hep-ex\]](https://arxiv.org/abs/1808.07858).
- [270] A.M. Sirunyan et al. “Identification of heavy-flavour jets with the CMS detector in pp collisions at 13 TeV”. In: *JINST* 13 (2018), Po5011. doi: [10.1088/1748-0221/13/05/P05011](https://doi.org/10.1088/1748-0221/13/05/P05011). arXiv: [1712.07158 \[hep-ex\]](https://arxiv.org/abs/1712.07158).
- [271] Eric Conte, Benjamin Fuks, and Guillaume Serret. “MadAnalysis 5, a user-friendly framework for collider phenomenology”. In: *Computer Physics Communications* 184.1 (2013), pp. 222–256. issn: [0010-4655](https://doi.org/10.1016/j.cpc.2012.09.009). doi: [10.1016/j.cpc.2012.09.009](https://doi.org/10.1016/j.cpc.2012.09.009).
- [272] Adam Paszke et al. *PyTorch: An Imperative Style, High-Performance Deep Learning Library*. 2019. arXiv: [1912.01703 \[cs.LG\]](https://arxiv.org/abs/1912.01703).
- [273] A. Flórez et al. “Probing axionlike particles with  $\gamma\gamma$  final states from vector boson fusion processes at the LHC”. In: *Phys. Rev. D* 103.9 (2021), p. 095001. doi: [10.1103/PhysRevD.103.095001](https://doi.org/10.1103/PhysRevD.103.095001). arXiv: [2101.11119 \[hep-ph\]](https://arxiv.org/abs/2101.11119).
- [274] A. Flórez et al. “Anapole dark matter via vector boson fusion processes at the LHC”. In: *Phys. Rev. D* 100.1 (2019), p. 016017. doi: [10.1103/PhysRevD.100.016017](https://doi.org/10.1103/PhysRevD.100.016017). arXiv: [1902.01488 \[hep-ph\]](https://arxiv.org/abs/1902.01488).
- [275] A. Flórez et al. “Probing heavy spin-2 bosons with  $\gamma\gamma$  final states from vector boson fusion processes at the LHC”. In: *Phys. Rev. D* 99.3 (2019), p. 035034. doi: [10.1103/PhysRevD.99.035034](https://doi.org/10.1103/PhysRevD.99.035034). arXiv: [1812.06824 \[hep-ph\]](https://arxiv.org/abs/1812.06824).
- [276] A. Flórez et al. “Expanding the reach of heavy neutrino searches at the LHC”. In: *Phys. Lett. B* 778 (2018), pp. 94–100. doi: [10.1016/j.physletb.2018.01.009](https://doi.org/10.1016/j.physletb.2018.01.009). arXiv: [1708.03007 \[hep-ph\]](https://arxiv.org/abs/1708.03007).

- [277] A. Flórez et al. “Searching for new heavy neutral gauge bosons using vector boson fusion processes at the LHC”. In: *Phys. Lett. B* 767 (2017), pp. 126–132. DOI: [10.1016/j.physletb.2017.01.062](https://doi.org/10.1016/j.physletb.2017.01.062). arXiv: [1609.09765v2 \[hep-ph\]](https://arxiv.org/abs/1609.09765v2).
- [278] A. Flórez et al. “Probing the stau-neutralino coannihilation region at the LHC with a soft tau lepton and a jet from initial state radiation”. In: *Phys. Rev. D* 94.7 (2016), p. 073007. DOI: [10.1103/PhysRevD.94.073007](https://doi.org/10.1103/PhysRevD.94.073007). arXiv: [1606.08878 \[hep-ph\]](https://arxiv.org/abs/1606.08878).
- [279] R. Leonardi et al. “Phenomenology at the LHC of composite particles from strongly interacting Standard Model fermions via four-fermion operators of NJL type”. In: *The European Physical Journal C* 80.4 (Apr. 2020). ISSN: [1434-6052](https://doi.org/10.1140/epjc/s10052-020-7822-0). DOI: [10.1140/epjc/s10052-020-7822-0](https://doi.org/10.1140/epjc/s10052-020-7822-0).
- [280] Cardona Natalia et al. *Long-term LHC Discovery Reach for Compressed Higgsino-like Models using VBF Processes*. 2021. arXiv: [2102.10194 \[hep-ph\]](https://arxiv.org/abs/2102.10194).
- [281] Andrés Flórez et al. “Probing axionlike particles with  $\gamma\gamma$  final states from vector boson fusion processes at the LHC”. In: *Phys. Rev. D* 103 (9 2021), p. 095001. DOI: [10.1103/PhysRevD.103.095001](https://doi.org/10.1103/PhysRevD.103.095001).
- [282] B. Gripaios, M. Nardeccchia, and S. A. Renner. “Composite leptoquarks and anomalies in B-meson decays”. In: *JHEP* 05 (2015), p. 006. DOI: [10.1007/JHEP05\(2015\)006](https://doi.org/10.1007/JHEP05(2015)006). arXiv: [1412.1791 \[hep-ph\]](https://arxiv.org/abs/1412.1791).
- [283] S. Fajfer and N. Košnik. “Vector leptoquark resolution of  $R_K$  and  $R_{D^{(*)}}$  puzzles”. In: *Phys. Lett. B* 755 (2016), pp. 270–274. DOI: [10.1016/j.physletb.2016.02.018](https://doi.org/10.1016/j.physletb.2016.02.018). arXiv: [1511.06024 \[hep-ph\]](https://arxiv.org/abs/1511.06024).
- [284] D. Bećirević et al. “Palatable leptoquark scenarios for lepton flavor violation in exclusive  $b \rightarrow s\ell_1\ell_2$  modes”. In: *JHEP* 11 (2016), p. 035. DOI: [10.1007/JHEP11\(2016\)035](https://doi.org/10.1007/JHEP11(2016)035). arXiv: [1608.07583 \[hep-ph\]](https://arxiv.org/abs/1608.07583).
- [285] G. D’Amico et al. “Flavour anomalies after the  $R_{K^*}$  measurement”. In: *JHEP* 09 (2017), p. 010. DOI: [10.1007/JHEP09\(2017\)010](https://doi.org/10.1007/JHEP09(2017)010). arXiv: [1704.05438 \[hep-ph\]](https://arxiv.org/abs/1704.05438).
- [286] G. Hiller and I. Nisandzic. “ $R_K$  and  $R_{K^*}$  beyond the standard model”. In: *Phys. Rev. D* 96.3 (2017), p. 035003. DOI: [10.1103/PhysRevD.96.035003](https://doi.org/10.1103/PhysRevD.96.035003). arXiv: [1704.05444 \[hep-ph\]](https://arxiv.org/abs/1704.05444).
- [287] D. Bećirević et al. “Scalar leptoquarks from grand unified theories to accommodate the B-physics anomalies”. In: *Phys. Rev. D* 98.5 (2018), p. 055003. DOI: [10.1103/PhysRevD.98.055003](https://doi.org/10.1103/PhysRevD.98.055003). arXiv: [1806.05689 \[hep-ph\]](https://arxiv.org/abs/1806.05689).
- [288] Geneviève Belanger et al. “Leptoquark manoeuvres in the dark: a simultaneous solution of the dark matter problem and the  $R_{D^{(*)}}$  anomalies”. In: *JHEP* 02 (2022), p. 042. DOI: [10.1007/JHEP02\(2022\)042](https://doi.org/10.1007/JHEP02(2022)042). arXiv: [2111.08027 \[hep-ph\]](https://arxiv.org/abs/2111.08027).

- [289] J. Aebischer et al. “Confronting the vector leptoquark hypothesis with new low- and high-energy data”. In: *The European Physical Journal C* 83.2 (Feb. 16, 2023), p. 153. ISSN: 1434-6052. DOI: 10.1140/epjc/s10052-023-11304-5.
- [290] B. Schrempp and F. Schrempp. “Light leptoquarks”. In: *Phys. Lett. B* 153 (1985), pp. 101–107. DOI: 10.1016/0370-2693(85)91450-9.
- [291] M. Leurer. “A comprehensive study of leptoquark bounds”. In: *Phys. Rev. D* 49 (1994), pp. 333–342. DOI: 10.1103/PhysRevD.49.333. arXiv: hep-ph/9309266.
- [292] S. Davidson, D. C. Bailey, and B. A. Campbell. “Model independent constraints on leptoquarks from rare processes”. In: *Z. Phys. C* 61 (1994), pp. 613–644. DOI: 10.1007/BF01552629. arXiv: hep-ph/9309310.
- [293] M. Leurer. “Bounds on vector leptoquarks”. In: *Phys. Rev. D* 50 (1994), pp. 536–541. DOI: 10.1103/PhysRevD.50.536. arXiv: hep-ph/9312341.
- [294] J. L. Hewett and T. G. Rizzo. “Much ado about leptoquarks: A comprehensive analysis”. In: *Phys. Rev. D* 56 (1997), pp. 5709–5724. DOI: 10.1103/PhysRevD.56.5709. arXiv: hep-ph/9703337.
- [295] F. S. Queiroz, K. Sinha, and A. Strumia. “Leptoquarks, Dark Matter, and Anomalous LHC Events”. In: *Phys. Rev. D* 91.3 (2015), p. 035006. DOI: 10.1103/PhysRevD.91.035006. arXiv: 1409.6301 [hep-ph].
- [296] B. Diaz, M. Schmaltz, and Y. Zhong. “The leptoquark Hunter’s guide: Pair production”. In: *JHEP* 10 (2017), p. 097. DOI: 10.1007/JHEP10(2017)097. arXiv: 1706.05033 [hep-ph].
- [297] I. Doršner and A. Greljo. “Leptoquark toolbox for precision collider studies”. In: *JHEP* 05 (2018), p. 126. DOI: 10.1007/JHEP05(2018)126. arXiv: 1801.07641 [hep-ph].
- [298] N Vignaroli. “Seeking leptoquarks in the  $t\bar{t}$  plus missing energy channel at the high-luminosity LHC”. In: *Phys. Rev. D* 99 (3 2019), p. 035021. DOI: 10.1103/PhysRevD.99.035021. arXiv: 1808.10309 [hep-ph].
- [299] M. Schmaltz and Y. Zhong. “The leptoquark Hunter’s guide: large coupling”. In: *JHEP* 01 (2019), p. 132. DOI: 10.1007/JHEP01(2019)132. arXiv: 1810.10017 [hep-ph].
- [300] U. Haisch and G. Polesello. “Resonant third-generation leptoquark signatures at the Large Hadron Collider”. In: *JHEP* 05 (2021), p. 057. DOI: 10.1007/JHEP05(2021)057. arXiv: 2012.11474 [hep-ph].
- [301] A. Bhaskar et al. “Improving third-generation leptoquark searches with combined signals and boosted top quarks”. In: *Phys. Rev. D* 104.7 (2021), p. 075037. DOI: 10.1103/PhysRevD.104.075037. arXiv: 2106.07605 [hep-ph].

- [302] J. Bernigaud et al. “LHC signatures of  $\tau$ -flavoured vector leptoquarks”. In: *JHEP* 08 (2022), p. 127. doi: [10.1007/JHEP08\(2022\)127](https://doi.org/10.1007/JHEP08(2022)127). arXiv: [2112.12129 \[hep-ph\]](https://arxiv.org/abs/2112.12129).
- [303] R. Leonardi et al. “Phenomenology at the LHC of composite particles from strongly interacting Standard Model fermions via four-fermion operators of NJL type”. In: *EPJC* 80.309 (2020). doi: [10.1140/epjc/s10052-020-7822-0](https://doi.org/10.1140/epjc/s10052-020-7822-0). arXiv: [1810.11420 \[hep-ph\]](https://arxiv.org/abs/1810.11420).
- [304] CMS Collaboration. “Search for heavy neutrinos or third-generation leptoquarks in final states with two hadronically decaying  $\tau$  leptons and two jets in proton-proton collisions at  $\sqrt{s} = 13$  TeV”. In: *JHEP* 03 (2017), p. 077. doi: [10.1007/JHEP03\(2017\)077](https://doi.org/10.1007/JHEP03(2017)077). arXiv: [1612.01190 \[hep-ex\]](https://arxiv.org/abs/1612.01190).
- [305] CMS Collaboration. “Search for third-generation scalar leptoquarks and heavy right-handed neutrinos in final states with two tau leptons and two jets in proton-proton collisions at  $\sqrt{s} = 13$  TeV”. In: *JHEP* 07 (2017), p. 121. doi: [10.1007/JHEP07\(2017\)121](https://doi.org/10.1007/JHEP07(2017)121). arXiv: [1703.03995 \[hep-ex\]](https://arxiv.org/abs/1703.03995).
- [306] CMS Collaboration. “Search for third-generation scalar leptoquarks decaying to a top quark and a  $\tau$  lepton at  $\sqrt{s} = 13$  TeV”. In: *Eur. Phys. J. C* 78 (2018), p. 707. doi: [10.1140/epjc/s10052-018-6143-z](https://doi.org/10.1140/epjc/s10052-018-6143-z). arXiv: [1803.02864 \[hep-ex\]](https://arxiv.org/abs/1803.02864).
- [307] CMS Collaboration. “Constraints on models of scalar and vector leptoquarks decaying to a quark and a neutrino at  $\sqrt{s} = 13$  TeV”. In: *Phys. Rev. D* 98.3 (2018), p. 032005. doi: [10.1103/PhysRevD.98.032005](https://doi.org/10.1103/PhysRevD.98.032005). arXiv: [1805.10228 \[hep-ex\]](https://arxiv.org/abs/1805.10228).
- [308] CMS Collaboration. “Search for a singly produced third-generation scalar leptoquark decaying to a  $\tau$  lepton and a bottom quark in proton-proton collisions at  $\sqrt{s} = 13$  TeV”. In: *JHEP* 07 (2018), p. 115. doi: [10.1007/JHEP07\(2018\)115](https://doi.org/10.1007/JHEP07(2018)115). arXiv: [1806.03472 \[hep-ex\]](https://arxiv.org/abs/1806.03472).
- [309] CMS Collaboration. “Search for heavy neutrinos and third-generation leptoquarks in hadronic states of two  $\tau$  leptons and two jets in proton-proton collisions at  $\sqrt{s} = 13$  TeV”. In: *JHEP* 03 (2019), p. 170. doi: [10.1007/JHEP03\(2019\)170](https://doi.org/10.1007/JHEP03(2019)170). arXiv: [1811.00806 \[hep-ex\]](https://arxiv.org/abs/1811.00806).
- [310] CMS Collaboration. “Searches for additional Higgs bosons and for vector leptoquarks in  $\tau\tau$  final states in proton-proton collisions at  $\sqrt{s} = 13$  TeV”. In: (2022). doi: [10.48550/arXiv.2208.02717](https://doi.org/10.48550/arXiv.2208.02717). arXiv: [2208.02717 \[hep-ex\]](https://arxiv.org/abs/2208.02717).
- [311] CMS Collaboration. “The search for a third-generation leptoquark coupling to a  $\tau$  lepton and a b quark through single, pair and nonresonant production at  $\sqrt{s} = 13$  TeV”. In: (2022). URL: <https://inspirehep.net/literature/2110188>.

- [312] ATLAS Collaboration. “Search for a scalar partner of the top quark in the all-hadronic  $t\bar{t}$  plus missing transverse momentum final state at  $\sqrt{s} = 13$  TeV with the ATLAS detector”. In: *Eur. Phys. J. C* 80.8 (2020), p. 737. doi: [10.1140/epjc/s10052-020-8102-8](https://doi.org/10.1140/epjc/s10052-020-8102-8). arXiv: [2004.14060 \[hep-ex\]](https://arxiv.org/abs/2004.14060).
- [313] ATLAS Collaboration. “Search for pair production of third-generation scalar leptoquarks decaying into a top quark and a  $\tau$ -lepton in pp collisions at  $\sqrt{s} = 13$  TeV with the ATLAS detector”. In: *JHEP* 06 (2021), p. 179. doi: [10.1007/JHEP06\(2021\)179](https://doi.org/10.1007/JHEP06(2021)179). arXiv: [2101.11582 \[hep-ex\]](https://arxiv.org/abs/2101.11582).
- [314] ATLAS Collaboration. “Search for new phenomena in final states with b-jets and missing transverse momentum in  $\sqrt{s} = 13$  TeV pp collisions with the ATLAS detector”. In: *JHEP* 05 (2021), p. 093. doi: [10.1007/JHEP05\(2021\)093](https://doi.org/10.1007/JHEP05(2021)093). arXiv: [2101.12527 \[hep-ex\]](https://arxiv.org/abs/2101.12527).
- [315] ATLAS Collaboration. “Search for new phenomena in pp collisions in final states with tau leptons, b-jets, and missing transverse momentum with the ATLAS detector”. In: *Phys. Rev. D* 104.11 (2021), p. 112005. doi: [10.1103/PhysRevD.104.112005](https://doi.org/10.1103/PhysRevD.104.112005). arXiv: [2108.07665 \[hep-ex\]](https://arxiv.org/abs/2108.07665).
- [316] ATLAS Collaboration. “Search for leptoquarks decaying into the  $b\tau$  final state in pp collisions at  $\sqrt{s} = 13$  TeV with the ATLAS detector”. In: (2023). doi: [10.48550/arXiv.2305.15962](https://doi.org/10.48550/arXiv.2305.15962). arXiv: [2305.15962 \[hep-ex\]](https://arxiv.org/abs/2305.15962).
- [317] ATLAS Collaboration. *Search for pair production of third-generation leptoquarks decaying into a bottom quark and a  $\tau$ -lepton with the ATLAS detector*. 2023. doi: [10.48550/arXiv.2303.01294](https://doi.org/10.48550/arXiv.2303.01294). arXiv: [2303.01294 \[hep-ex\]](https://arxiv.org/abs/2303.01294).
- [318] A. Bhaskar et al. “Precise limits on the charge- $2/3$   $U_1$  vector leptoquark”. In: *Phys. Rev. D* 104.3 (2021), p. 035016. doi: [10.1103/PhysRevD.104.035016](https://doi.org/10.1103/PhysRevD.104.035016). arXiv: [2101.12069 \[hep-ph\]](https://arxiv.org/abs/2101.12069).
- [319] U. Haisch, L. Schnell, and S. Schulte. “Drell-Yan production in third-generation gauge vector leptoquark models at NLO+PS in QCD”. In: *JHEP* 2023.2 (2023). doi: [10.1007/jhep02\(2023\)070](https://doi.org/10.1007/jhep02(2023)070).
- [320] L. Calibbi, A. Crivellin, and T. Li. “Model of vector leptoquarks in view of the B-physics anomalies”. In: *Phys. Rev. D* 98.11 (2018), p. 115002. doi: [10.1103/PhysRevD.98.115002](https://doi.org/10.1103/PhysRevD.98.115002). arXiv: [1709.00692 \[hep-ph\]](https://arxiv.org/abs/1709.00692).
- [321] M. Blanke and A. Crivellin. “B Meson anomalies in a Pati-Salam model within the Randall-Sundrum background”. In: *Phys. Rev. Lett.* 121.1 (2018), p. 011801. doi: [10.1103/PhysRevLett.121.011801](https://doi.org/10.1103/PhysRevLett.121.011801). arXiv: [1801.07256 \[hep-ph\]](https://arxiv.org/abs/1801.07256).
- [322] S. Iguro et al. “TeV-scale vector leptoquark from Pati-Salam unification with vectorlike families”. In: *Phys. Rev. D* 104.7 (2021), p. 075008. doi: [10.1103/PhysRevD.104.075008](https://doi.org/10.1103/PhysRevD.104.075008). arXiv: [2103.11889 \[hep-ph\]](https://arxiv.org/abs/2103.11889).

- [323] M. Fernández-Navarro and S. F. King. “B-anomalies in a twin Pati-Salam theory of flavour including the 2022 LHCb  $R_{K^{(*)}}$  analysis”. In: *JHEP* 2023.2 (2023). doi: [10.1007/jhep02\(2023\)188](https://doi.org/10.1007/jhep02(2023)188).
- [324] M. Bordone et al. “A three-site gauge model for flavor hierarchies and flavor anomalies”. In: *Phys. Lett. B* 779 (2018), pp. 317–323. doi: [10.1016/j.physletb.2018.02.011](https://doi.org/10.1016/j.physletb.2018.02.011). arXiv: [1712.01368 \[hep-ph\]](https://arxiv.org/abs/1712.01368).
- [325] M. Bordone et al. “Low-energy signatures of the PS<sup>3</sup> model: from B-physics anomalies to LFV”. In: *JHEP* 10 (2018), p. 148. doi: [10.1007/JHEP10\(2018\)148](https://doi.org/10.1007/JHEP10(2018)148). arXiv: [1805.09328 \[hep-ph\]](https://arxiv.org/abs/1805.09328).
- [326] Javier Fuentes-Martín et al. “Flavor hierarchies, flavor anomalies, and Higgs mass from a warped extra dimension”. In: *Phys. Lett. B* 834 (2022), p. 137382. doi: [10.1016/j.physletb.2022.137382](https://doi.org/10.1016/j.physletb.2022.137382). arXiv: [2203.01952 \[hep-ph\]](https://arxiv.org/abs/2203.01952).
- [327] B. Gripaios. “Composite leptoquarks at the LHC”. In: *JHEP* 02 (2010), p. 045. doi: [10.1007/JHEP02\(2010\)045](https://doi.org/10.1007/JHEP02(2010)045). arXiv: [0910.1789 \[hep-ph\]](https://arxiv.org/abs/0910.1789).
- [328] R. Barbieri, C. W. Murphy, and F. Senia. “B-decay anomalies in a composite leptoquark model”. In: *Eur. Phys. J. C* 77.1 (2017), p. 8. doi: [10.1140/epjc/s10052-016-4578-7](https://doi.org/10.1140/epjc/s10052-016-4578-7). arXiv: [1611.04930 \[hep-ph\]](https://arxiv.org/abs/1611.04930).
- [329] R. Barbieri and A. Tesi. “B-decay anomalies in Pati-Salam SU(4)”. In: *Eur. Phys. J. C* 78.3 (2018), p. 193. doi: [10.1140/epjc/s10052-018-5680-9](https://doi.org/10.1140/epjc/s10052-018-5680-9). arXiv: [1712.06844 \[hep-ph\]](https://arxiv.org/abs/1712.06844).
- [330] J. Fuentes-Martín et al. “Vector leptoquarks beyond tree level. III. Vectorlike fermions and flavor-changing transitions”. In: *Phys. Rev. D* 102 (11 2020), p. 115015. doi: [10.1103/PhysRevD.102.115015](https://doi.org/10.1103/PhysRevD.102.115015).
- [331] A. Djouadi et al. “Interference effects in  $t\bar{t}$  production at the LHC as a window on new physics”. In: *JHEP* 03 (2019), p. 119. doi: [10.1007/JHEP03\(2019\)119](https://doi.org/10.1007/JHEP03(2019)119). arXiv: [1901.03417 \[hep-ph\]](https://arxiv.org/abs/1901.03417).
- [332] The ROOT team. “ROOT - An Object Oriented Data Analysis Framework”. In: *Nucl. Inst. & Meth. in Phys. Res. A* 389 (1997). Proceedings AIHENP’96 Workshop, Lausanne, Sep. 1996. See also “ROOT”[software], Release v6.18/02, and <https://root.cern/manual/roofit/>, pp. 81–86. doi: [10.5281/zenodo.3895860](https://doi.org/10.5281/zenodo.3895860).
- [333] D. Barbosa et al. “Probing a Z' with non-universal fermion couplings through top quark fusion, decays to bottom quarks, and machine learning techniques”. In: *Eur. Phys. J. C* 83.5 (2023), p. 413. doi: [10.1140/epjc/s10052-023-11506-x](https://doi.org/10.1140/epjc/s10052-023-11506-x). arXiv: [2210.15813 \[hep-ph\]](https://arxiv.org/abs/2210.15813).
- [334] B. Dutta et al. “Probing an MeV-Scale Scalar Boson in Association with a TeV-Scale Top-Quark Partner at the LHC”. In: *JHEP* 03.164 (2023). doi: [10.1007/JHEP03%282023%29164](https://doi.org/10.1007/JHEP03%282023%29164). arXiv: [2202.08234 \[hep-ph\]](https://arxiv.org/abs/2202.08234).

- [335] R. Arnowitt et al. "Determining the Dark Matter Relic Density in the Minimal Supergravity Stau-Neutralino Coannihilation Region at the Large Hadron Collider". In: *Phys. Rev. Lett.* 100 (2008), p. 231802. DOI: [10.1103/PhysRevLett.100.231802](https://doi.org/10.1103/PhysRevLett.100.231802). arXiv: [0802.2968 \[hep-ph\]](https://arxiv.org/abs/0802.2968).
- [336] B. Dutta et al. "Supersymmetry Signals of Supercritical String Cosmology at the Large Hadron Collider". In: *Phys. Rev. D* 79 (2009), p. 055002. DOI: [10.1103/PhysRevD.79.055002](https://doi.org/10.1103/PhysRevD.79.055002). arXiv: [0808.1372 \[hep-ph\]](https://arxiv.org/abs/0808.1372).
- [337] C. Avila et al. "Connecting Particle Physics and Cosmology: Measuring the Dark Matter Relic Density in Compressed Supersymmetry at the LHC". In: *Physics of the Dark Universe* 27 (2020), p. 100430. DOI: [10.1016/j.dark.2019.100430](https://doi.org/10.1016/j.dark.2019.100430). arXiv: [1801.03966 \[hep-ph\]](https://arxiv.org/abs/1801.03966).
- [338] B. Dutta et al. "Vector Boson Fusion Processes as a Probe of Supersymmetric Electroweak Sectors at the LHC". In: *Phys. Rev. D* 87 (2013), p. 035029. DOI: [10.1103/PhysRevD.87.035029](https://doi.org/10.1103/PhysRevD.87.035029). arXiv: [1210.0964 \[hep-ph\]](https://arxiv.org/abs/1210.0964).
- [339] A. Delannoy et al. "Probing Dark Matter at the LHC using Vector Boson Fusion Processes". In: *Phys. Rev. Lett.* 111 (2013), p. 061801. DOI: [10.1103/PhysRevLett.111.061801](https://doi.org/10.1103/PhysRevLett.111.061801). arXiv: [1304.7779 \[hep-ph\]](https://arxiv.org/abs/1304.7779).
- [340] B. Dutta et al. "Probing Compressed Sleptons at the LHC using Vector Boson Fusion Processes". In: *Phys. Rev. D* 91 (2015), p. 055025. DOI: [10.1103/PhysRevD.91.055025](https://doi.org/10.1103/PhysRevD.91.055025). arXiv: [1411.6043 \[hep-ph\]](https://arxiv.org/abs/1411.6043).
- [341] B. Dutta et al. "Probing Compressed Top Squarks at the LHC at 14 TeV". In: *Phys. Rev. D* 90 (2014), p. 095022. DOI: [10.1103/PhysRevD.90.095022](https://doi.org/10.1103/PhysRevD.90.095022). arXiv: [1312.1348 \[hep-ph\]](https://arxiv.org/abs/1312.1348).
- [342] B. Dutta et al. "Probing Compressed Bottom Squarks with Boosted Jets and Shape Analysis". In: *Phys. Rev. D* 92 (2015), p. 095009. DOI: [10.1103/PhysRevD.92.095009](https://doi.org/10.1103/PhysRevD.92.095009). arXiv: [1507.01001 \[hep-ph\]](https://arxiv.org/abs/1507.01001).